UNIVERSIDADE DE LISBOA
FACULDADE DE CIÊNCIAS
DEPARTAMENTO DE FÍSICA

Small Animal PET Imaging Using GATE Monte Carlo Simulations: implementation of physiological and metabolic information

Susana Evaristo de Oliveira Branco Silva

DOUTORAMENTO EM ENGENHARIA BIOMÉDICA E BIOFÍSICA

2010

UNIVERSIDADE DE LISBOA
FACULDADE DE CIÊNCIAS
DEPARTAMENTO DE FÍSICA

Small Animal PET Imaging Using GATE Monte Carlo Simulations: implementation of physiological and metabolic information

Susana Evaristo de Oliveira Branco Silva

Thesis supervised by:
Professor Dr. Pedro Miguel Dinis de Almeida
Instituto de Biofísica e Engenharia Biomédica
Departamento de Física da Faculdade de Ciências da Universidade de Lisboa
Dr. Sébastien Jan
Service Hospitalier Frédéric Joliot, Institut d'Imagerie Biomédicale
Direction des Sciences du Vivant, Commissariat à l'Énergie Atomique, Orsay, France

DOUTORAMENTO EM ENGENHARIA BIOMÉDICA E BIOFÍSICA

2010

Resumo

O rato/ratinho de laboratório é o modelo animal de escolha para o estudo dos processos fundamentais associados a determinadas patologias, como o cancro. Esta escolha deve-se a uma gama de factores que incluem uma grande homologia genética com o Homem. Assim sendo o rato/ratinho é amplamente utilizado em laboratórios por todo o Mundo para estudo dos processos celulares básicos associados á doença e à terapia. A comunidade laboratorial tem, nos últimos anos, desenvolvido um grande interesse pela imagiologia não-invasiva destes animais. De entre as diversas tecnologias de imagem aplicadas aos estudos*in vivo* de pequenos animais, a Tomografia por Emissão de Positrões (PET) permite obter informação sobre a distribuição espacial e temporal de moléculas marcadas com átomo emissor de positrões, de forma não invasiva.

Os traçadores utilizados para obter esta "imagem molecular" são administrados em baixas quantidades, de tal forma que os processos biológicos que envolvem concentrações da ordem do nano molar, ou mesmo inferiores, podem ser determinadas sem perturbar o processo em estudo. Muitas combinações de diferentes moléculas com diferentes radionúclidos permitem traçar uma gama de caminhos moleculares específicos (e.g. processos biológicos de receptores e síntese de transmissores em caminhos de comunicação em células, processos metabólicos e expressão genética). A imagem pode ser executada repetidamente antes e depois de intervenções permitindo o uso de cada animal como o seu próprio controlo biológico.

A investigação já realizada em curso que aplicam a PET ao estudos de pequenos animais, tem permitido compreender, entre outras coisas, a evolução de determinadas doenças e suas potenciais terapias. Contudo, existem algumas dificuldades de implementação desta técnica já que a informação obtida está condicionada pelos fenómenos físicos associados à interacção da radiação com a matéria, pelos instrumentos envolvidos na obtenção da informação e pela própria fisiologia do animal (por exemplo o seu movimento fisiológico). De facto, a fiabilidade da quantificação das imagens obtidas experimentalmente, em sistemas PET dedicados aos pequenos animais, é afectada ao mesmo tempo pelos limites de desempenho dos detectores (resolução espacial e em energia, sensibilidade, etc.), os efeitos físicos como a atenuação e a dispersão, que perturbam a reconstrução da imagem, e os efeitos fisiológicos (movimentos do animal). Na prática estes efeitos são corrigidos com métodos de correcção específicos com a finalidade de extrair parâmetros quantitativos fiáveis. Por outro lado, as características fisiológicas dos animais a estudar e a necessidade da existência de animais disponíveis, são factores adicionais de complexidade.

Recentemente, tem sido dedicada alguma atenção aos efeitos resultantes dos movimentos fisiológicos, nomeadamente do movimento respiratório, na qualidade das imagens obtidas no decurso de um exame PET. Em particular, no caso do estudo dos tumores do pulmão (algo infelizmente muito frequente em humanos), o movimento fisiológico dos pulmões é uma fonte de degradação das imagens PET, podendo comprometer a sua resolução e o contraste entre regiões sãs e doentes deste orgão. A precisão quantitativa na determinação da concentração de actividade e dos volumes funcionais fica assim debilitada, sendo por vezes impedida a localização, detecção e quantificação do radiotraçador captado nas lesões pulmonares. De modo a conseguir diminuir estes efeitos, existe a necessidade de melhor compreender a influência deste movimento nos resultados PET.

Neste contexto, as simulações Monte Carlo são um instrumento útil e eficaz de ajuda à optimização dos componentes dos detectores existentes, à concepção de novos detectores, ao desenvolvi-

mento e à avaliação de algoritmos de reconstrução e de métodos de correcção dos efeitos físicos. Baseados em modelos matemáticos dos processos físicos, químicos e, sempre que possível, biológicos, os métodos de simulação Monte Carlo são, desde há muito, uma ferramenta privilegiada para a obtenção de informação fiável da previsão do comportamento de sistemas complexos e por maioria de razão, para uma sua melhor compreensão.

No contexto da Imagiologia Molecular, a plataforma de simulação *Geant4 Application for Tomographic Emission* (GATE), validada para as técnicas de imagem de Medicina Nuclear, permite a simulação por Monte Carlo dos processos de obtenção de imagem. Esta simulação pode mesmo ser feita quando se pretende estudar a distribuição de emissores de positrões cuja localização varia ao longo do tempo. Adicionalmente, estas plataformas permitem a utilização de modelos computacionais para modelar a anatomia e a fisiologia dos organismos em estudo mediante a utilização de uma sua representação digital realista denominada de fantôma. A grande vantagem na utilização destes fantômas relaciona-se com o facto de conhecermos as suas características geométricas ("anatómicas") e de podermos controlar as suas características funcionais ("fisiológicas"). Podemos assim obter padrões a partir dos quais podemos avaliar e aumentar a qualidade dos equipamentos e técnicas de imagem.

O objectivo do presente trabalho consiste na modelação e validação de uma plataforma de simulação do sistema microPET® FOCUS 220, usado em estudos de PET para pequenos animais, utilizando a plataforma de simulação GATE. A metodologia adoptada procurou reproduzir de uma forma realista, o ambiente de radiação e factores instrumentais relacionados com o sistema de imagem, assim como o formato digital dos dados produzidos pelo equipamento. Foram usados modelos computacionais, obtidos por segmentação de imagem de exames reais, para a avaliação da quantificação das imagens obtidas. Os resultados obtidos indicam que a plataforma produz resultados reprodutíveis, adequados para a sua utilização de estudos de pequenos animais em PET.

Este objectivo foi concretizado estudando os efeitos combinados do tamanho das lesões, do rácio de concentração de actividade lesão-para-fundo e do movimento respiratório na recuperação de sinal de lesões esféricas localizadas no pulmão em imagens PET de pequenos animais. Para este efeito, foi implementada no código GATE uma representação digital em 4D de um ratinho de corpo inteiro (o fantôma MOBY). O MOBY permitiu reproduzir uma condição fisiológica que representa a respiração em condição de "stress", durante um exame típico de PET pequeno animal, e a inclusão de uma lesão esférica no pulmão tendo em conta o movimento da mesma. Foram realizadas um conjunto de simulações estáticas e dinâmicas usando *2-Deoxy-[^{18}F]fluoro-D-glucose* (FDG) tendo em consideração diferentes tamanhos das lesões e diferentes captações deste radiofármaco. O ruído da imagem e a resolução temporal foram determinadas usando imagens 3D e 4D. O rácio sínal-para-ruído (SNR), o rácio contraste-para-ruído (CNR), a relação lesão-fundo (*target-to-background activity concentration ratio*- TBR), a recuperação de contraste (CR) e a recuperação de volume (VR) foram também avaliados em função do tamanho da lesão e da actividade captada. Globalmente, os resultados obtidos demonstram que a perda de sinal depende tanto do tamanho da lesão como da captação de actividade na lesão. Nas simulações estáticas, onde não foi simulado movimento, os coeficientes de recuperação foram influenciados pelo efeito de volume parcial para os tamanhos mais reduzidos de lesão. Além disso, o aumento do contraste na lesão

produz um aumento significativo no desvio padrão da média de sinal recuperado resultando numa diminuição no CNR e no SNR. Também concluímos que o movimento respiratório diminui significativamente a recuperação do sinal e que esta perda depende principalmente do tamanho da lesão. A melhor resolução temporal e resolução espacial foram obtidas nas simulações estáticas, onde não existia movimento envolvido.

Os resultados simulados mostram que o efeito de volume parcial é dominante nas lesões mais pequenas devido à resolução espacial do sistema FOCUS, tanto nas imagens estáticas como nas dinâmicas. Além disso, para concentrações baixas de radiofármaco existe uma dificuldade inerente em quantificar a recuperação de sinal nas lesões comprometendo a análise quantitativa dos dados obtidos.

Palavras-chave: Tomografia por Emissão de Positrões (PET); PET de Pequenos Animais; *4D Mouse Whole-Body* (MOBY); *Geant4 Application for Tomographic Emission* (GATE); Detectabilidade de Lesões Pulmonares; Quantificação de Imagem.

Abstract

Organ motion has become of great concern in medical imaging only recently. Respiratory motion is one source of degradation of PET images. Respiratory motion may lead to image blurring, which may result in reduced contrast and quantitative accuracy in terms of recovered activity concentration and functional volumes. Consequently, the motion of lungs hinders the localization, detection, and the quantification of tracer uptake in lung lesions. There is, therefore, a need to better understand the effects of this motion on PET data outcome.

Medical imaging methods and devices are commonly evaluated through computer simulation. Computer generated phantoms are used to model patient anatomy and physiology, as well as the imaging process itself. A major advantage of using computer generated phantoms in simulation studies is that the anatomy and physiological functions of the phantom are known, thus providing a gold standard from which to evaluate and improve medical imaging devices and techniques.

In this thesis, are presented the results of a research studied the combined effects of lesion size, lesion-to-background activity concentration ratio and respiratory motion on signal recovery of spherical lesions in small animal PET images using Monte Carlo simulation. Moreover, background activity is unavoidable and it causes significant noise and contrast loss in PET images. For these purposes, has been used the Geant4 Application for Tomographic Emission (GATE) Monte Carlo platform to model the microPET®FOCUS 220 system. Additionaly, was implemented the digital 4D Mouse Whole-Body (MOBY) phantom into GATE. A physiological "stress breathing" condition was created for MOBY in order to reproduce the respiratory mouse motion during a typical PET examination. A spherical lung lesion was implemented within this phantom and its motion also modelled. Over a complete respiratory cycle of 0.37 s was retrieved a set of 10 temporal frames (including the lesion movement) generated in addition to a non-gated data set. Sets of static (non-gated data) and dynamic (gated data) *2-Deoxy-[*^{18}*F]fluoro-D-glucose* (FDG) simulations were performed considering different lesion sizes and different activity uptakes. Image noise and temporal resolution were determined on 3D and 4D images. Signal-to-Noise Ratio (SNR), Contrast-to-Noise Ratio (CNR), Target-to-Background activity concentration Ratio (TBR), Contrast Recovery (CR) and Volume Recovery (VR) were also evaluated as a function of lesion size and activity uptake.

Globally, the results obtained show that signal loss depends both on lesion size and lesion activity uptake. In the non-gated data, where was no motion included (perfect motion correction), the recovery coefficients were influenced by the partial volume effect for the smallest lesion size. Moreover, the increased lesion contrast produces a significant increase on the standard deviation of the mean signal recover. This led to a decrease in CNR and SNR. In addition, respiratory motion significantly deteriorates signal recovery and this loss depends mainly of the lesion size. Best temporal resolution (volume recovery) and spatial resolution was given by the non-gated data, where no motion is involved.

The simulated results show that the partial volume effect is dominant for small objects due to limited FOCUS system resolution in both 3D and 4D PET images. In addition, lower activity concentrations significantly deteriorates the lesion signal recovery compromising quantitative analysis.

Keywords: Positron Emission Tomography (PET); Small Animal PET; 4D Mouse Whole-Body

(MOBY) Phantom; Geant4 Application for Tomographic Emission (GATE); Lung Lesion Detectability; Image Quantification.

Acknowledgments

... 1589 days after ...

... my last words goes to those who have contributed for this moment!

First of all, I would like to express my deepest gratitude to my supervisor Professor Pedro Almeida for all the support. For the, sometimes hard but always productive, discussions about this work and for giving me the freedom and strength to explore new ideas. It has been an honour to work with him throughout these years.

I wish to thank to Doctor Sébastien Jan for being my supervisor and for welcoming me at the *Institut d'Imagerie BioMédicale* (I^2BM) research group of the *Service Hospitalier Frédéric Joliot* (SHFJ), a fantastic place to work with their advanced facilities and technologies which gave me the necessary tools to be able to complete my work and to achieve the results shown on this thesis.

I would also like to acknowledge my colleagues and all the persons with whom I had the privilege to work with at the SHFJ, namely Doctor Régine Trébossen, Doctor Claude Comtat, Frédéric Bataille, Florent Sureau and Yoann Fontyn.

To Doctor William Seagers who has guided my developments with the MOBY phantom.

To the OpenGATE collaboration and all the world wide GATE users.

To the teaching staff of the *Instituto de Biofísica e Engenharia Biomédica* (IBEB) *da Faculdade de Ciências da Universidade de Lisboa* (FCUL): Professor Eduardo Ducla Soares, Professor Pedro Cavaleiro Miranda and Professor Alexandre Andrade for their extraordinary dedication to the institute and to the constant care about students well-being and good work conditions.

I would also like to especially thank the friendship and support from Mónica Martins, Nuno Matela, Nuno Oliveira, Sofia Silva, Paula Faria, Ricardo Salvador, Sandra Tecelão, Patrícia Figueiredo, Teresa Montez, Luís Janeiro, Luís Freire, Sónia Gonçalves, Paula Santos, Mai Lu, Gilberto Almeida, Liliana Caldeira, Hugo Cordeiro, Marta Correia, ..., and to everyone who contribute to make IBEB such a nice place to work.

To Ana Sousa and Beatriz Lampreia. Besides the administrative help, for the friendship and care.

To my colleagues at the *Escola Superior de Tecnologia da Saúde de Lisboa* (ESTeSL). To Nuno Teixeira, Alexandra Carvalho, Luís Freire (again), Eduardo Alves and Nuno Machado, for their advices, help and friendship during the last year of this work.

Thanks to my friends and family who listened to my stories without ever understanding the logic behind them or why anyone would care to spend so much time trying to master it. To Ana Carina, Ana Margarida and Gabriela, for their support and friendship. A special thanks goes to António... for always being there.

To my son Pedro, who is my personal reminder of the fact that there are things by far more important in life than debugging a program or obtaining good quality simulated data.

And last, but not the least, I would like to express my thankfulness to Carlos for all the love, dedication and support during all these years. For the encouragements and for always believing in me. I could not have done it without you.

Lisboa, May 8th, 2010

This work was funded by the Fundação para a Ciência e a Tecnologia (FCT) under grant nº SFRH/BD/22723/2005. I would like to offer my sincere acknowledgments to FCT for this support.

... to the memory of my father... who always believed in me. Miss you.

... to my little one: Pedro! Love you!

Contents

I Introduction 1

1 Introduction 3

II Background 9

2 Positron Emission Tomography 11

2.1 Physics of Positron Emission and Annihilation . . . 13

2.1.1 Positron Emission and Annihilation . . . 13

2.1.2 Positron Range and Noncolinearity . . . 15

2.1.3 Photon Interactions with Matter . . . 17

2.1.3.1 Compton Scattering . . . 17

2.1.3.2 Photoelectric Effect . . . 18

2.1.3.3 Interaction Cross-Sections in Materials . . . 18

2.2 Imaging Technology for PET . . . 20

2.2.1 PET Detectors . . . 20

2.2.2 Photomultiplier Tubes (PMTs) . . . 23

2.2.3 Block Detector Readout . . . 23

2.3 Data Acquisition . . . 26

2.3.1 Coincidence Detection . . . 26

2.3.2 Type of Events . . . 27

2.3.3 2D and 3D Acquisitions . . . 28

2.3.4 Acquisition Protocols . . . 30

2.3.5 PET System Configurations . . . 30

2.4 Performance of PET Systems . . . 32

2.4.1 Spatial Resolution and Depth Of Interaction (DOI) . . . 32
2.4.2 System Sensitivity . . . 34
2.4.3 Noise Equivalent Count (NEC) . . . 35
2.4.4 Scatter Fraction (SF) . . . 35
2.5 Data Representation and Corrections . . . 36
2.5.1 Organizing the Data . . . 36
2.5.2 Data Normalization . . . 37
2.5.3 Photon Attenuation . . . 39
2.5.4 Scatter Correction . . . 41
2.5.5 Random Coincidences . . . 42
2.5.6 Dead Time . . . 43
2.5.7 Partial Volume Effect . . . 43
2.6 Image Reconstruction in PET . . . 44
2.6.1 Analytical Reconstruction Methods . . . 44
2.6.1.1 Backprojection . . . 44
2.6.1.2 Direct Fourier Reconstruction and Filtered Backprojection (FBP) . . . 45
2.6.2 Iterative Reconstruction Methods . . . 48
2.6.3 3D Reconstruction . . . 51
2.7 PET Radiopharmaceuticals . . . 51
2.7.1 Specific Activity . . . 52

3 Small Animal PET Imaging **55**
3.1 Challenges and Limitations of Small Animal PET Imaging Quantification . . . 56
3.1.1 Spatial Resolution . . . 56
3.1.2 System Sensitivity . . . 58
3.1.3 Radiation Exposure . . . 58
3.1.4 Specific Activity of Tracers . . . 59
3.1.5 Measurement of the Input Function . . . 59
3.1.6 Other Considerations... . . . 60
3.2 Implementation of Small Animal PET . . . 60
3.2.1 Anesthesia . . . 60
3.2.2 Immobilisation and Positioning . . . 61
3.2.3 ROI Identification . . . 61
3.3 Small Animal PET Scanners . . . 61
3.4 Applications of Small Animal PET . . . 64

4 Monte Carlo Simulations in Emission Tomography **67**

4.1 Random Numbers . . . 68

4.2 Sampling Methods . . . 69

4.2.1 The Distribution Method . . . 69

4.2.2 The Rejection Method . . . 69

4.2.3 The Mixed Methods . . . 70

4.2.4 Non Analog Samplig . . . 70

4.3 Photon Transport . . . 70

4.4 Variance Reduction Techniques . . . 72

4.5 Monte Carlo Packages for Nuclear Medicine . . . 72

III Materials & Methods **75**

5 The GATE Platform **77**

5.1 Main Features . . . 78

5.1.1 Software Architecture . . . 78

5.1.2 Geometry . . . 79

5.1.3 Systems . . . 80

5.1.4 Physics process . . . 80

5.1.4.1 Standard Energy Electromagnetic Processes (SEP) . . . 82

5.1.4.2 Low Energy Electromagnetic Processes (LEP) . . . 83

5.1.4.3 Production Cuts . . . 85

5.1.4.4 Positron Emission . . . 86

5.1.5 Radioactive Sources . . . 86

5.1.6 Voxellized Phantoms and Voxellized Sources . . . 87

5.1.7 Sensitive Detectors . . . 88

5.1.8 Time Management and Movements . . . 89

5.1.9 Digitizer and Readout Parameters . . . 90

5.1.9.1 From Particle Detection to Coincidences in GATE . . . 90

5.1.9.2 The Digitizer . . . 91

5.1.9.3 Digitizer Optimization . . . 94

5.2 GATE Modelled Systems . . . 94

5.3 Computing Resources . . . 94
5.3.1 CCRT @ CEA . . . 96
5.3.2 Cluster @ IBEB . . . 98
5.3.3 Instalation Procedure . . . 99
5.3.4 Cluster Computing for GATE Simulations . . . 99

6 The MicroPET® FOCUS 220 Scanner 103

6.1 Technical Specifications . . . 103
6.2 The Simulated Model . . . 105
6.2.1 The Geometry . . . 105
6.2.2 The Physical Process and the Acquisition Protocol . . . 108
6.2.3 Data Output and Reconstruction Set-Up . . . 112
6.2.4 Experiments . . . 114
6.2.5 Image Planes . . . 117

IV Results and Discussion 119

7 The Digital Mouse Phantoms 121

7.1 The Phantoms Used . . . 122
7.1.1 Phantoms Built from Real Data . . . 122
7.1.1.1 The [^{18}F]-fluoride mouse phantom . . . 122
7.1.1.2 FDG mouse phantom . . . 124
7.1.2 The MOBY Phantom . . . 126
7.1.2.1 Modelling of a Stress Breathing Condition and a Tumor Motion . . . 127
7.2 Phantom Simulation Process . . . 128

8 Enhancements to the GATE Platform 137

8.1 List Mode Format . . . 137
8.2 The microPET® Focus LMF . . . 138
8.3 The Class `GateToFOCUS` . . . 139
8.4 Configuration of the 48 bits LMF Output . . . 140

9 Small Animal PET with GATE **143**

9.1 Validation for the microPET® Focus Simulation 143

9.1.1 Spatial Resolution 143

9.1.2 Counting Rate 144

9.1.3 Contrast Recovering 146

9.2 Application for Small Animal PET Imaging 147

9.2.1 Bone Imaging Using [^{18}F]-Fluoride 147

9.3 Metabolic Imaging Using FDG 150

9.4 Physical Parameters Effects on the Quantification 153

10 Evaluation of the Respiratory Motion in Lung Lesion Quantification **157**

10.1 Data Analysis 157

10.2 Quantification Considerations... 159

10.3 Motion Blurring versus Spatial Resolution 162

10.4 Lesion Detectability 162

10.5 Evaluation of the Contrast Recovery and Volume Recovery Coefficient 169

V Main Discussion and Conclusions **173**

11 Main Discussion and Conclusions **175**

11.1 The Digital Mouse Phantoms 175

11.2 Enhancements to the GATE Platform 175

11.3 Small Animal PET with GATE 176

11.4 Evaluation of the Respiratory Motion in Lung Lesion Quantification 177

11.5 Perspectives for Future Work 178

11.6 Concluding Remarks 179

A MOBY files **181**

A.1 general.samp.par 181

A.2 Attenuation Coefficients 186

B GateToFOCUS New Class **193**

B.1 GateToFOCUS.cc . . . 193

B.2 GateToFOCUS.hh . . . 203

B.3 GateToFOCUSMessenger.cc . . . 206

B.4 GateToFOCUSMessenger.hh . . . 207

B.5 GateOutputMgr.cc . . . 208

B.6 GNUmakefile . . . 208

C Publications and Comunications **209**

C.1 List of Publications . . . 209

C.2 List of Comunications . . . 210

C.2.1 Oral communications . . . 210

C.2.2 Invited Oral communications . . . 211

C.2.3 Posters in conferences . . . 211

C.3 Scientific Committee . . . 212

C.4 Conference Chair . . . 212

C.5 Organizing Committee . . . 212

C.6 Honours and Awards . . . 213

Bibliography **215**

List of Figures

2.1 Positron Emission Tomography. 12

2.2 In a PET camera, each detector generates a timed pulse when it registers an incident photon. These pulses are then combined in coincidence circuitry, and if the pulses fall within a short time-window, they are deemed to be coincident. A coincidence event is assigned to a LOR joining the two relevant detectors. In this way, positional information is gained from the detected radiation without the need for a physical collimator. This is known as electronic collimation. Electronic collimation has two major advantages over physical collimation: improved sensitivity and improved uniformity of the Point Source Response Function (PSRF). 16

2.3 The process of positron emission and subsequent positron-electron annihilation results in two 511 keV annihilation photons emitted 180° apart. The positron range error is dependent on the energy of the emitted positrons resulting in variations of ~ 0.1 mm up to some mm. Accolinearity is independent of radionuclide, and the error is determined by the separation of the detectors. Because there is some residual momentum associated with the positron, the two annihilation photons are not emitted exactly at 180°, but at a slight deviation.Two detectors detect these photons in a straight line, which is slightly deviated of ±0.25° from the original annihilation line. . . 17

2.4 PET camera configuration: slits between crystals direct light photons toward PMTs. Adapted from [Powsner & Powsner, 2006]. 21

2.5 Photomultiplier tube and its preamplifier and amplifier. Adapted from [Powsner & Powsner, 2006]. 24

2.6 A schematic representation of a block detector: a) Standard PMT arrangement in a standard block detector and b) Quadrant-sharing detector. Adapted from [Zanzonico, 2004]. 25

2.7 Illustration of the main coincidence event types: a) true; b) multiple; c) single; d) random and e) scattered. 28

2.8 2D and 3D PET imaging. Adapted from [Powsner & Powsner, 2006]. 29

2.9 The three basic geometries found in modern dedicated PET systems: (a) Array of large detectors, either continuous detectors (flat or curve-plate NaI(Tl)) or plates of discrete crystals; (b) partial ring of detector blocks that rotates and (c) full ring of discrete crystals configured as small blocks or larger detector modules. Adapted from [Lewellen & Karp, 2004]. 31

2.10 In a ring geometry scanner, the point spread function becomes asymmetrical with increasing radial offsets due to detector penetration and the lack of information regarding the depth of interaction within the crystal. The result is a degrading spatial resolution and mispositioning of events towards the center of the FOV. The severity of these effects depends on detector ring diameter, detector depth, and the detector material. Adapted from [Cherry & Dahlbom, 2006]. 33

2.11 Representation of the coordinates of the Lines of Response in a 3D Sinogram. (a): view of a LOR in a plane parallel to the scanner rotation axis. (b): view of a LOR projected into the transaxial plane. Adapted from [Jacobson M. & G., 2000]. 37

2.12 A parallel projection, for a particular angle ϕ, of an object corresponds to a row in the sinogram. 38

2.13 Two 511 keV photons detected by two detectors after traversing different tissue thicknesses a and b. Attenuation is independent of location of annihilation, and depends on the total dimension of the body. Adapetd from [Saha, 2005]. 39

2.14 The projection slice theorem. Adapted from [Cherry & Dahlbom, 2006]. 46

2.15 Some filters currently used in FBP and their shape. Value on y-axis indicates to what extent contribution of each frequency to image is modified by filters. These filters reduce the amplitude at high frequencies, improving signal-to-noise but reducing spatial resolution. They also avoid “ringing” artifacts from the very sharp cut-off of the ramp filter at $\nu = \nu_{cut-off}$. All of them are defined as ”low-pass” filters. Adapted from [Bruyant, 2002]. 47

2.16 Images reconstructed by FBP from different numbers of equally spaced projections. The number of views included in each reconstruction is shown above its image. Adapted from [Wernick & Aarsvold, 2004]. 48

2.17 Flowchart of a generic iterative reconstruction algorithm. Adapted from [Lalush & Wernick, 2004]. 49

2.18 A projection data q_i in a sinogram is estimated from all pixels along the LOR and compared with the measured projection data p_i. Adapted from [Saha, 2005]. 50

2.19 Schematic representation of the principle of a rebinning algorithm for 3D PET data. Adapted from [Defrise *et al.* , 2003, 2005]. 52

2.20 FDG tracer uptake by metabolically active cells. Adapted from [Kappor *et al.* , 2004]. 53

3.1 Representation of a microPET (µPET) acquisition process. 56

3.2 Intrinsic spatial resolution of several existing tomographs as a function of detector size. Data have been labelled according to the type of position decoding scheme used to identify the crystal of interaction. Adapted from [Lecomte, 2004]. 57

3.3 Dedicated animal PET scanners: a) Hamamatsu SHR-7700 scanner, a PET system dedicated to non-human primate imaging. The position sensitive PMT-BGO detector-based ring has a diameter of 50.8 cm and an axial FOV of 11.4 cm. b) The microPET P4 scanner. This system uses fiberoptically coupled LSO scintillator elements and a position-sensitive PMT. The ring diameter is 27 cm and the axial FOV is 80 mm. c) The HIDAC system, an animal PET scanner which uses multiwire proportional chamber technology together with stacks of lead converters. All these detectors have an intrinsic spatial resolution of < 1 mm. Adapted from [Chatziioannou, 2002a]. 63

3.4 MicroPET imaging of bi-directional inducible therapeutic and reporter-gene expression. Sequential microPET imaging studies of a nude mouse carrying four tumours. Four tumour cell lines - two positive controls (constitutive reporter-gene expression), one negative control and one inducible line (reporter-gene expression induced by doxycycline - were injected subcutaneously into four separate sites in a single mouse. When tumours reached a size of at least 5 mm, the mouse was imaged with *9-(4-[^{18}F] fluoro-3-hydroxymethylbutyl)guanine* (FHBG). Doxycycline was then added to the water supply for 7 days. The mouse was then scanned again with FHBG. Doxycycline was removed from the water supply for the next 7 days, and the mouse was again scanned with FHBG. The locations of the four tumours and the mouse outline are shown by the dotted regions of interest. All images are 1 to 2 mm coronal sections through the four tumours. The %ID/g (% injected dose per gram tissue) scale for FHBG is shown on the right. The negative control tumours show no gene expression, and the positive control tumours show increased expression over the time course. The tumour on the top right, with inducible gene expression, initially does not accumulate FHBG, then at 7 days after addition of doxycycline, induction of reporter-gene expression traps FHBG. Seven days after withdrawal of doxycycline, there is decreased induction and minimal trapping of FHBG.The FHBG image signal correlates well with target-gene expression (not shown). Adapted from [Gambhir, 2002]. 65

3.5 Whole-body bone scans ([^{18}F]-fluoride ion) of a mouse acquired using the microPET scanner. The image on the left was reconstructed using standard 3D FBP technique with a high resolution ramp filter. The image on the right was reconstructed from the same raw data using a maximum a posteriori (MAP) algorithm that minimizes statistical error and models the detector response. A substantial improvement in spatial resolution without noise amplification is clearly demonstrated. Adapted from [Chatziioannou, 2002b]. 66

4.1 Principles and main components of a Monte Carlo program dedicated to the simulation of cylindrical multi-ring PET imaging systems. Adapted from [Zaidi, 2006]. . . . 68

5.1 Sketch of the layered architecture of GATE. Adapted from [Jan *et al.* , 2004b]. 79

5.2 Picture of a phantom and a `cylindricalPET` system composed of 5 `rsectors`, 4 `modules` (repeated along Z axis), 3 `submodules` (repeated along Y axis), 64 `crystals` (8×8) and 2 `layers` (red and yellow). Adapted from [Jan *et al.* , 2008]. . 82

5.3 Particle interactions in a sensitive detector. Adapted from [Jan *et al.* , 2008]. 88

5.4 Management of time-dependent phenomena with GATE. 90

5.5 The digitizer is organized as a chain of several modules that processes the hits to yield a single, which represents a physical observable. Adapted from [Staelens, 2004]. 92

5.6 Actions of both the `adder` and `readout` modules. The `adder` module transforms the hits into a pulse in each individual volume, and then the `readout` module sums a group of these pulses into a single pulse at the level of depth as defined by the user. Adapted from [Lazaro, 2003]. 92

5.7 Example of a readout scheme. The disk icons represents the data written to the GATE output files. Adapted from [Jan *et al.* , 2008]. 95

5.8 Tantale architecture. 97

5.9 IBEB Mini-Cluster architecture. 100

5.10 The job splitter is used to generate fully resolved, non-parameterized macro files together with a platform specific submit file and a split file for error handling in the merging step. Adapted from [Beenhouwer *et al.* , 2005]. 101

5.11 A GATE simulation consisting of 3 runs. The parallelization introduces virtual time slices that update the geometry based on the original time schedule. Adapted from [Beenhouwer *et al.* , 2005]. 102

5.12 The output merger is used to merge the ROOT output data into a single output file. Adapted from [Beenhouwer *et al.* , 2005] 102

6.1 The microPET® FOCUS 220. Adapted from [microPET FOCUS, 2010]. 105

6.2 Illustration of the microPET® FOCUS geometry performed by GATE. 109

6.3 Example of a set of plots produced by a ROOT macro, for the FOCUS system. The three plots in the upper row show the detection coordinates of the annihilation photons in the system's detector heads. The first two plots (`Transaxial detection position`) are 2D histograms of the respective X and Y coordinates, one per frame. The third plot (`Axial detection position`) is a 1D histogram of the Z coordinate. In the left plot of the middle row illustrate the decay time curve of the F^{18} source. The second plot in the middle row (`Axial sensitivity`) illustrates the axial sensitivity of the scanner. For all unscattered coincidences, the axial position of the corresponding LOR is histogramed. The third plot in the middle row (`Axial scatter fraction`) shows the scatter fraction as a function of the axial position. The plot in the lower row (`Acollinearity Angle Distribution (deg)`) shows the distribution of the deviation to 180 degrees. of the angle between the two annihilation gammas. The second to last plot compare the delay coincidences generated with the real random selected in the prompts coincidences, and the last one shows the different type of decay events as a function of the time acquisition. Adapted from [Branco, 2005]. 115

6.4 Illustration of a simulation process. 116

6.5 Image planes. 118

7.1 Coronal, sagital and transaxial slices for the activity distribution of [^{18}F]-fluoride mouse phantom. 123

7.2 The curve shows the radioactive decay of the [^{18}F]-fluoride with a half-life of 6585.2 s, along the exam acquisition time. 123

7.3 Coronal, sagital and transaxial slices for the activity distribution of the FDG mouse phantom. 124

7.4 The curve shows the radioactive decay for the FDG study, with a half-life of 6585.2 s. 125

7.5 Measured TACs used as input for the FDG uptake simulation. 125

7.6 Anterior (left) and lateral (right) views of the MOBY digital mouse phantom. Adapted from [Segars *et al.* , 2004]. 127

7.7 Inspiratory motions of the liver (diaphragm), stomach, spleen, heart, and kidneys simulated in the mouse phantom. Expiratory motion was simulated as the reverse of the inspiratory motion. Adapted from [Segars *et al.* , 2004]. 129

7.8 (Top) Anterior view of end-expiration (left) and end-inspiration (right) in new mouse phantom. (Bottom) Left lateral view at end-expiration (left) and end-inspiration (right). The dotted line indicates the movement of the diaphragm. Adapted from [Segars *et al.* , 2004]. 129

7.9 Parameter curves for both respiratory (normal and abnormal breathing condition) and lesion motion in the MOBY phantom (as a function of the non normal tidal breathing condition). 130

7.10 Slices of the emission map of the MOBY phantom including a spherical lesion in middle region of the left lung, generated by the MOBY program. 131

8.1 Systran listmode data packets. 138

8.2 LMF 48 bits. 138

8.3 Packet translation for the microPET LMF formats. 138

9.1 Evaluation of the FWHM and full width at the FWTM, with GATE compared with experimental values. Adapted from [Jan *et al.* , 2005b]. 144

9.2 Defined parameters, in the digitizer chain, to measure the counting rate performances.145

9.3 Evaluation of the counting rate, for single events, of the microPET®Focus with GATE compared with experimental values. Adapted from [Jan *et al.* , 2005b]. 145

9.4 Evaluation of the counting rate, for prompt and delay coincidences, of the microPET FOCUS with GATE compared with experimental values. Adapted from [Jan *et al.* , 2005b]. 145

9.5 Contrast recovering with the FOCUS system. Adapted from [Jan *et al.* , 2005b]. . . 146

9.6 Coronal, sagital and transaxial slices representing [^{18}F]-fluoride uptake: acquired data (top) and GATE simulation using the real data phantom as input (bottom). . . . 148

9.7 Comparison between PET image quantification using a real exam and GATE simulation, for the [^{18}F]-fluoride radiotracer with the mouse phantom generated from real data. Black bars represent the ROI statistical error measured as the ratio standard deviation over mean for all voxels considered. 149

9.8 Maximum Intensity Projection (MIP) of the MOBY phantom after a simulation with an activity distribution representative of the real [^{18}F]-fluoride distribution. 149

9.9 Comparison between PET image quantification and the GATE measurements, for the [^{18}F]-fluoride radiotracer with the MOBY phantom. Black bars represent the ROI statistical error measured as the ratio standard deviation over mean for all voxels considered. 150

9.10 TACs used as input in the simulations for the FDG functional model, expressed in %ID/cc. 151

9.11 Slices from the real FDG exam (top) and the simulated exam (bottom) for the FDG mouse phantom, with an activity map distribution close to the last activity frame. . . 152

9.12 Comparison between PET image quantification and the GATE measurements, for the FDG radiotracer with the mouse phantom generated from real data. Black bars represent the ROI statistical error measured as the ratio standard deviation over mean for all voxels considered. 153

9.13 Coronal, sagital and transaxial slices for FDG simulation using MOBY: top - first activity frame (the first 60 s of the real exam), bottom - last activity frame (the last 900 s releated to the real exam). 154

9.14 Measured TACs from a complete FDG simulation with the MOBY phantom. 155

9.15 Relative differences between the quantification values obtained in the measured TACs for the MOBY phantom, and the TACs from the real FDG exam. 155

9.16 Physical parameters effects on the quantification. Left: Sagital slice of the simulated MOBY phantom with a gamma-gamma emission source. Right: Sagital slice of the simulated MOBY phantom for the ^{18}F emission source (with the inclusion of positron range and gamma accolinearity effects). Bottom: Maximum concentration profiles which illustrate the blurring or smearing effect for the ^{18}F emission source caused by the physical parameters effects. 156

10.1 Lesion size definition. To obtain this definition there were several steps that were executed. The first was to carefully place the lesion in the lungs and not on any other organ. Secondly there was the need to try different sizes in order to define a lesion that was entirely inside the lungs. The images on the first column of the figure show this steps using ROOT. In order to achieve this outcome we had to define activity in the lesion as well as in the lungs (in a FDG exam there is no lungs activity uptake in the image). The middle column presents the images for the static FDG simulations (for the last frame), and in the rightmost column there is presented the images for the dynamic FDG simulations (for the last farme). For the higher diameter lesions (1.25 mm, 1.5 mm and 2.0 mm) in the dynamic mode images are not show due to lesion blending into the liver. 160

10.2 Sagital slices through the MOBY phantom containing a 1.0 mm diameter lung lesion or only background, illustrating the placement of the background and lesion ROIs used for data analysis. 161

10.3 Sagital slices, of the reconstructed MOBY phantom, for a static acquisition, where no motion was simulated, and for the simulation of a dynamic acquisition, where respiratory and lesion motions were considered, with a lung lesion of 1.0 mm diameter and an FDG uptake of 0.05 μCi. The maximum concentration profiles from 3D and 4D simulated exams: where the blurring or smearing effect induced by respiratory motion are represented in the right. 163

10.4 Coronal slices of the MOBY phantom corresponding to the simulation of a “stress” condition breathing motion (see section 7.1.2.1) including a lung motion lesion of 1.5 mm diameter and an FDG uptake of 1.35 μCi. These coronal slices represent one respiratory cycle for an FDG exam in the last time frame. The dynamic 3D emission assumed an event collection during 900 s, where 5.65×10^9 particles were generated. 164

10.5 Transaxial, coronal and sagital slices of the reconstructed lung lesion, in the MOBY phantom, with 2.0 mm diameter and an FDG uptake of 0.08 μCi. No motion was simulated. 164

10.6 FWHM of the line spread function through the lesion centroid as a function of the lesion diameter defined for the static acquisitions schemes. 165

10.7 FWHM of the line spread function through the lesion centroid as a function of the FDG activity defined for static and dynamic acquisitions schemes, for the 1.0 mm diameter lesion. Data from dynamic acquisitions are represented by dashed curves and static acquisition data are represented by solid curves. 166

10.8 SNR of the 0.01 μCi, 0.03 μCi, 0.05 μCi, 0.08 μCi, 1.08 μCi and 1.35 μCi FDG uptakes for the spherical lesions as a function of the lesion diameter. Results obtained for the static simulations. 167

10.9 CNR of the 0.01 μCi, 0.03 μCi, 0.05 μCi, 0.08 μCi, 1.08 μCi and 1.35 μCi FDG uptakes for the spherical lesions as a function of the lesion diameter. Results obtained for the static simulations. 168

10.10TBR of the 0.01 μCi, 0.03 μCi, 0.05 μCi, 0.08 μCi, 1.08 μCi and 1.35 μCi FDG uptakes for the spherical lesions as a function of the lesion diameter. Results obtained for the static simulations. 169

10.11TBR of a set of a dynamic and a static acquisition as a function of the FDG activity concentration for the 1.0 mm diameter lesion. Data from dynamic acquisitions are represented with the dashed curve and static acquisition data are represented by the solid curve. 170

10.12Contrast of the 0.01 μCi, 0.03 μCi, 0.05 μCi, 0.08 μCi, 1.08 μCi and 1.35 μCi FDG uptakes for the spherical lesions as a function of the lesion diameter. Results obtained for the static simulations. 171

10.13Contrast recover of a set of dynamic and static acquisitions as a function of the FDG activity concentration for the 1.0 mm diameter lesion. Data from dynamic acquisitions are represented by the dashed curve and static acquisition data are represented by the solid curve. The red line represents the mean simulated contrast. 172

List of Tables

2.1 Selected list of radionuclides, and their physical properties, that decay by positron emission and are relevant to PET Imaging. 14

2.2 Linear Attenuation Coefficients for soft tissue, bone, Bismuth Germanate - BGO (a detector material), lead, and tungsten at 511 keV. Adapted from [Cherry & Dahlbom, 2006]. 19

2.3 Properties of some scintillators used in PET detectors. Note that some of these specifications are subject to change as developers change dopants and trace elements in the scintillator growth. For example, the light output, peak wavelength, decay time and density for LYSO and LFS will vary somewhat for different versions of the basic scintillator. Adapted from [Lewellen, 2008]. 22

2.4 Some radiopharmaceuticals used in PET and their applications. Adapted from [Saha, 2005]. 53

5.1 Different systems available in GATE and their characteristics. In the second column are listed some of the keywords that are also used in a simulation (see also [Jan *et al.* , 2008] for a complete list). The shape in the third column describes the mother volume, composed of daughter volumes: a box means a box shaped mother volume containing an array of daughter boxes, a cylinder mother volumes will contains cylinders. Cylinders are understood here as tube sectors defined by an inner and outer radius. Adapted from [Jan *et al.* , 2008]. 81

6.1 Specifications and features of the microPET® FOCUS system. Adapted from [microPET FOCUS, 2010]. 104

6.2 Relationship between the physical components of the scanner and the hierarchical levels of the system. 105

9.1 CR results for each rod. The activity ratio with the background is 2:1 for the Rod1, 3:1 for the Rod2, 4:1 for the Rod3 and 5:1 for the Rod4. Adapted from [Jan *et al.* , 2005b]. 146

9.2 Activity distribution in the MOBY phantom at the last frame, in the case of the [^{18}F]-fluoride. 147

9.3 Input activity distribution for the first and the last frame in the MOBY structure for the FDG. 151

10.1 Statistical error obtained for the defined ROIs in the lung lesion implementation in the MOBY phantom, from the static and the dynamic simulation modes. 161

10.2 SNR and CNR values in the lesion with 1.0 mm diameter as a function of the FDG activity concentration. The first columns show the CNR and the SNR from the images of the phantom in a static mode. The other results correspond to data obtained from the images of the phantom in the dynamic mode. 168

10.3 VRC in the static and dynamic acquisitions as a function of the lesion diameter. The mean percent errors in volume estimates measured on simulated lesions as a function of the real lesion volume are also shown. (Note: N/A - ”not available” - is this context means that the VRC value was not possible to measure due to the blurring and to the smearing effect resulting from the respiratory motion.) 171

Abbreviations

ACF Attenuation Correction Factor

AMIDE Amide is a Medical Imaging Data Examiner

APD avalanche photodiode

ART Algebraic Reconstruction Technique

BaF2 Barium Fluoride

BGO Bismuth Germanate

BGO Bismuth Germanate

BPF BackProjection Filtering

CCRT Centre de Calcul Recherche et Technologie

CLHEP Class Library for High Energy Physics

CNR contrast-to-noise ratio

CR Contrast Recovery

CT Computed Tomography

DOI Depth Of Interaction

DRM Distributed Resource Management

EADL Evaluated Atomic Data Library

EEDL Evaluated Electron Data Library

EGS Electron Gamma Shower

EPDL Evaluated Photon Data Library

FBP Filtered Backprojection

FDG 2-Deoxy-[18F]fluoro-D-glucose

FEE Front End Electronics

FHBG 9-(4-[18F]fluoro-3hydroxymethylbutyl)guanine

fMRI functional Magnetic Resonance Imaging

FOM Figure of Merit

FORE FOurier REbinning

FOV Field Of View

FT Fourier Transform

FWHM Full Width at Half Maximum

FWTM Full Width at Tenth Maximum

GATE Geant4 Application for Emission Tomography

Geant GEometry ANd Tracking

GPS General Particle Source

GSO Gadolinium Orthosilicate

LaBr3 Lanthanum Bromide

LEP Low Energy Electromagnetic Processes

LFS Lutetium Fine Silicate

LGPL Lesser General Public License

LMF List Mode Format

LOR Line Of Response

LSF Load Sharing Facility

LSO Leutetium Orthosilicate

LuAP Cerium doped Lutetium Orthoaluminate

LuI3 Lutetium Iodide

LYSO Cerium doped Lutetium Yttrium Orthosilicate

MAP MAximum a Posteriori

MCNP Monte Carlo N-Particle

MIP Maximum Intensity Projection

MLEM Maximum Likelihood Expectation Maximization

MOBY 4D Mouse Whole-Body

MPI Message Passing Interface

MRI Magnetic Resonance Imaging

MRM Magnetic Resonance Microscopy

MSB Most Significant Bit

MWPC MultiWire Proportional Chambers

NaI(TI) Sodium Iodide

NEC Noise Equivalent Count

NEMA National Electrical Manufacturers Association

NURBS Non-Uniform Rational B-Splines

OSEM Ordered Subset Expectation Maximization

PDF Probability Density Function

PE Photoelectron

PENELOPE Code System to Perform Monte Carlo Simulation of Electron Gamma-Ray Showers in Arbitrary Materials

PET Positron Emission Tomography

PMT Photomultiplier Tube

PSPMT Position Sensitive Photomultiplier Tube

PSRF Point Source Response Function

PV Partial Volume

PVI positron volume imaging

RatCAP Rat Conscious Animal PET

RC Recovery Coefficient

RDM Radioactive Decay Module

Rmax maximum or extrapolated ranges

ROI Region Of Interest

Rrms root-meansquare ranges

RT Radiation Therapy

SA Specific Activity

SEP Standard Energy Electromagnetic Processes

SF Scatter Fraction

SimSET Simulation System for Emission Tomography

SNR signal-to-noise ratio

SORTEO Simulation Of Realistic Tridimensional Emitting Objects

SPECT Single Photon Emission Computed Tomography

SSRB Single Slice Rebinning Algorithm

TAC Time Activity Curve

TBR Target to Background Ratio

TOF Time-Of-Flight

US UltraSound

VOI Volume Of Interest

VRC Volume Recovery Coefficient

VRT Variance Reduction Technique

Part I

Introduction

Chapter 1

Introduction

Non-invasive diagnostic imaging can be performed with different technologies: X-ray radiography, computed radiography, direct radiography, mammography, Computed Tomography (CT), UltraSound (US), and Magnetic Resonance Imaging (MRI), which all give anatomical information, and also with functional MRI (fMRI), optical imaging, thermography, planar isotope imaging, Single Photon Emission Computed Tomography (SPECT), Positron Emission Tomography (PET), and gamma camera PET which return functional information [Kane, 2009; Wernick & Aarsvold, 2004; Gambhir, 2002; Nutt, 2002]. Since biochemical changes precede morphologic changes, PET has the potential to provide diagnostic information earlier than, for example, X-Ray, CT or MRI. Recent devices combine two modalities on the same gantry in order to achieve hardware fusion of anatomical and functional images, as PET/CT [Mawlawi & Townsend, 2009; Cherry, 2009; Townsend *et al.* , 2004].

In nuclear medicine examinations, a radiopharmaceutical is administered to the patient, which is marked with a radionuclide emitting one single photon with an energy of 100 - 200 keV in SPECT and a positron emitting radionuclide in PET. Positron emitting radionuclides, such as ^{11}C, ^{13}N, ^{15}O, and ^{18}F, have been used in medicine for decades. These radionuclides are used to synthesize an ever growing number of tracer compounds that enable measurement of regional biology and biochemistry. The emission of a positron results in two annihilation photons of 511 keV. With the advent of tomographic reconstruction methods and the development of detector technologies, images generated from the detection of the two 511 keV photons from the subsequent positronium decay have become common place. Such images allow us to follow the dynamics of the tracers in the body with high sensitivity, producing quantitatively accurate images of the distribution of tracer concentration [Zanzonico & Heller, 2007; Zanzonico, 2004]. These methods are minimally invasive, repeatable, reproducible, and have been applied widely in the fields of oncology, cardiology and neuroscience. *2-Deoxy-[^{18}F]fluoro-D-glucose* (FDG) is the most common radiotracer used in PET to stage cancer and metastasis in many regions of the body. FDG is analogous to glucose and is taken up by living cells through the normal glucose pathway. Tumor imaging with FDG relies on the fact that malignant cells possess high metabolic rates and therefore take up greater amounts of FDG than healthy tissues [Larson & Schwartz, 2006; Couturier, 2004; Kubota, 2001; Guhlke *et al.* , 2007]. PET functional imaging using FDG is widely considered as the state of the art in diagnosis for a number of oncology applications [Bomanji *et al.* , 2001].

The rapid growth in genetics and molecular biology combined with the development of techniques for genetically engineering small animals has led to increased interest in in vivo small animal imaging [Cherry & Gambhir, 2001; Riemann *et al.* , 2008; Rowland & R., 2008]. Small animal imaging has been applied frequently to the imaging of small animals (mice and rats), which are ubiquitous in modeling human diseases and testing treatments. The use of PET in small animals allows the use of subjects as their own control, reducing the interanimal variability. This allows performing longitudinal studies on the same animal and improves the accuracy of biological models [Cherry, 2004]. However, small animal PET still suffers from several limitations. The amounts of radiotraces needed, limited scanner sensitivity, image resolution and image quantification issues, all could clearly benefit from additional research [Chatziioannou, 2002b; Tai & Laforest, 2005].

Because nuclear medicine imaging deals with radioactive decay, the emission of radiation energy through photons and particles alongside with the detection of these quanta and particles in different materials make Monte Carlo method an important simulation tool in both nuclear medicine research and clinical practice. In order to optimize the quantitative use of PET in clinical practice, data- and image-processing methods are also a field of intense interest and development. The evaluation of such methods often relies on the use of simulated data and images since these offer control of the ground truth. Monte Carlo simulations are widely used for PET simulation since they take into account all the random processes involved in PET imaging, from the emission of the positron to the detection of the photons by the detectors. Simulation techniques have become an importance and indispensable complement to a wide range of problems that could not be addressed by experimental or analytical approaches [Rogers, 2006].

Monte Carlo methods are numerical calculation methods based on random variable sampling. This approach has been used to solve mathematical problems since 1770 and has been named “Monte Carlo” by Von Neumann because of the similarity of statistical simulations to games of chance, represented by the most well known center for gambling: the Monte Carlo district in the Monaco principality. The general idea of Monte Carlo analysis is to create a model, which is as similar as possible to the real physical system of interest, and to create interactions within that system based on known probabilities of occurrence, with random sampling of the Probability Density Functions (PDFs). As the number of individual events (called histories) increase, the quality of the reported average behavior of the system improves, meaning that the statistical uncertainty decreases. Virtually, any complex system can in principle be modeled: if the distribution of events that occur in a system is know from experience, a PDF can be generated and sampled randomly to simulate the real system. A detailed description of the general principles and applications of the Monte Carlo method can be found elsewhere:[Andreo, 1991; Zaidi, 1999; Ljungberg, 1998, 2004; Zaidi & Sgouros, 2002; Zaidi, 2006].

The simulation of PET imaging using Monte Carlo allows the optimization of system design for new scanners, the study of factors affecting image quality, the validation of correction methodologies for effects such as scatter, attenuation and partial volume, for improved image quantification, as well as the development and testing of new image reconstruction algorithms. Another major advantage of simulations in nuclear medicine imaging is that they allow studying parameters that are not measurable in practice. The fraction of photons that are scattered in a phantom and their contribution to the image are examples of such parameters, and they can only be measured indirectly

for a very limited number of geometries. In addition, in a computer model it is possible to turn off certain effects, such as photon attenuation and scattering in the phantom, which means that ideal images, which include camera-specific parameters, can be created and used as reference images. In combination with patient-like phantoms, the Monte Carlo method can be used to produce simulated images very close to those acquired from real measurements. In this context, Monte Carlo simulations are becoming an essential tool for assisting this research and some specific Monte Carlo simulation packages have been evaluated for nuclear medicine applications [Andreo & Ljungberg, 1998; Buvat & Castiglioni, 2002; Buvat *et al.* , 2005; Buvat & Lazaro, 2006]. Recently, the Geant4 Application for Tomographic Emission (GATE) platform has been developed [Jan *et al.* , 2004b; GATE, 2010a] and validated for the simulation of the microPET® FOCUS 220 system [Jan *et al.* , 2005b].

An important aspect of simulation is the possibility of having a realistic model (phantom) of the subject's anatomy and physiological functions from which imaging data can be generated using accurate models of the imaging process [Ljungberg, 2004; Zaidi, 2006; Zubal, 1998; Poston *et al.* , 2002; Peter *et al.* , 2000]. Conceptually, the purpose of a physical or computerized phantom is to represent an organ or body region of interest, to allow modeling the biodistribution of a particular radiotracer and the chemical composition of the scattering medium, which absorbs and scatters the emitted radiation in a manner similar to biological tissues. In other terms, a phantom is a mathematical model designed to represent an organ or tissue of the body, an organ system, or the whole-body.

The widespread interest in molecular imaging spurred the development of more realistic 3D to 5D computational models based on the actual anatomy and physiology of individual humans and small animals. The advantage in using such phantoms in simulation studies is that the exact anatomy and physiological functions are known, thus providing a gold standard or truth in order to evaluate and improve imaging devices, data acquisition techniques, and imaging processing and reconstruction methods. Moreover, computer phantoms can be altered in order to model different anatomies and pathological situations. A review of the fundamental and technical challenges of designing computational models of the human anatomy can be found in [Zaidi & Xu, 2007; Zaidi & Tsui, 2009]. These reviews summarizes the latest efforts and future directions in the development of computational anthropomorphic models for application in radiological sciences.

Based on state-of-the-art computer graphics techniques, the 4D Mouse Whole Body (MOBY) phantoms provide a realistic model of the mouse anatomy and physiology for imaging studies [Segars *et al.* , 2004]. The phantom, when combined with accurate models for the imaging process, is capable of providing realistic imaging data from subjects with various anatomies and motions (cardiac and respiratory) in health and disease. With this ability, the phantom has enormous potential to help studying the effects of anatomical, physiological, physical, and instrumentation factors on small animal imaging and to research new instrumentation, image acquisition strategies, image processing and reconstruction methods as well as image visualization and interpretation techniques.

It is known that the localization and detection of thoracic and abdominal lesions in PET imaging is often perturbed due to the displacement of the organs during normal breathing [Bajc *et al.* , 2007]. The respiratory motion compromise image quality and quantification in PET [Buvat, 2007],

and affect clinical diagnosis. Motion can actually introduce large biases, for instance tracer uptake underestimation greater than 50% in the case of lung lesions [Nehmeh *et al.* , 2002]. Moreover, respiratory motion can induce resolution degradation (blurring effect) for PET imaging. Contrast loss of small lesions in PET images due to the above motion blurring effect can adversely affect the lesion detection sensitivity for PET imaging in the case of lung or liver cancer imaging [Visvikis *et al.* , 2004, 2006a]. The degree of motion blurring and contrast loss depends on the lesion size and location [Visvikis, 2004]. To compensate respiratory motion, simulation using software packages may provide a valuable tool for the assessment of respiratory motion detection and correction.

In order to contribute for the full understanding of this problem, the GATE Monte Carlo platform was used to model the microPET® FOCUS 220 system and the MOBY phantom to produce realistic simulated mouse scans. GATE is a well validated and very versatile application for Monte Carlo simulations in emission tomography that can be used for highly realistic simulations. MOBY was developed to provide a realistic and flexible model of the mouse anatomy and physiology to be used in molecular imaging research.

Time Activity Curves (TACs), for the FDG radiotracer, were extracted from mouse studies and activity was transposed in the MOBY phantom. The dynamic respiratory feature available in the MOBY phantom, was used, and a lung lesion was modelled in order to evaluate the effect of the respiratory motion on image quantification. These simulated data will be useful to evaluate the degradation on lesion detection due to normal breathing in whole-body mouse PET imaging, and hopefully shed some additional light on dealing with this problem in human exams.

The major aim of the work discussed in this dissertation was to contribute for the full understanding of this problem in small animal PET imaging, and hopefully shed some additional light on dealing with this problem in human exams.

This thesis is composed for eleven main chapters, organized in five parts, as follows:

The **Part I – Introduction**is composed of the present **Chapter 1 – Introduction**, where the context, motivations and general organization of the work are provided.

The **Part II – Background**, comprises three chapters, which include a review of the state of the art on the main knowledge fields that are related to the work developed in the present thesis. In **Chapter 2 – Positron Emission Tomography**, are present an overview of PET:how PET has developed both as a tracer method and as a physical tomographic detection method. Basic labelling and physiological aspects are touched upon in the choice of suitable positron emitting nuclides and how gamma emission in the decay may affect detection. The physics of the PET detector is described in some detail as well as data collection and data handling. **The Chapter 3 – Small Animal PET Imaging**, presents the challenges facing PET technology as applied to small animal imaging, provides a historical overview of the development of small animal PET systems, and discusses the current state of the art in small animal PET technology. The final chapter of the second part of this work, **Chapter 4 – Monte Carlo Simulations in Emission Tomography**, presents an overview of the fundamental characteristics of the Monte Carlo method and details the relevance of accurate Monte Carlo modelling in emission tomography.

The **Part III – Materials & Methods**, is composed of two chapters that describe the materials that were used in the development of this research and the methods used to achieve the aims of this

work. **Chapter 5 – The GATE platform**, is devoted to providing a detailed overview of the GATE software package and its features and capabilities. A description of the computer resources used is also provided. **Chapter 6 – The microPET® FOCUS 220Scanner**, describes the development of an accurate model of the microPET®FOCUS 220 system using GATE based on system performance measurements. It includes a general overview of the design of the FOCUS system.

The **Part IV – Results and Discussion**begins with **Chapter 7 – The Digital Mouse Phantoms**, describes the mouse phantoms generated from real data, and provides a detailed description of the physiological and metabolic information implemented in the MOBY phantom. The simulation settings used and the image reconstruction process are described in these chapters. The following chapter, **Chapter 8 – Enhancements to the GATE Platform**, describes the new features that were introduced in the GATE platform in order to provide the data output format of the microPET® FOCUS 220 system: the LMF 48 bits. The **Chapter 9 – Small Animal PET with GATE**, describes a validation and a verification of the GATE simulation package versus measurements in the microPET® FOCUS 220 system, as well as the results obtained for the simulations of the different mouse phantoms. The final chapter of Part IV is **Chapter 10 – Evaluation of the Respiratory motion in Lung Lesion Quantification**, which describes the quantitative evaluation of the degradation on lesion detection due to normal breathing in whole body mouse PET imaging.

Finally, the work presented in this thesis and related conclusions are summarized in **Chapter 11 – Main Discussion and Conclusions, Part V – Main Discussion and Conclusions**, together with a discussion of the main findings and the perspectives of future work.

Detail information about parameters choose in the digital MOBY phantom are presented in **Appendix A**. Moreover, all the attenuation coefficients related to the mouse phantom is listed in the same appendix.

A separate appendix section - **Appendix B** - includes all the code files implemented inside the GATE platform to provide the data output format of the microPET® FOCUS 220 system.

Research performed within the context of this PhD thesis resulted in 2 articles as a first author in peer reviewed high-impact international journals and in 9 publications (8 as a first author) in international conference proceedings. References to these publications are given in **Appendix C** at the end of this dissertation. Moreover, a list of all comunications, honours and awards are presented.

Part II

Background

Chapter 2

Positron Emission Tomography

Positron emission tomography (PET) is a noninvasive imaging technique that uses the unique decay characteristics of radionuclides that decay by positron emission (*e.g.* ^{11}C, ^{13}N, ^{15}O, ^{18}F, ^{64}Cu, etc.). These radionuclides are produced in a cyclotron and are then used to label compounds of biological interest. The labeled compound is introduced into the body, usually by intravenous injection, and is distributed in tissues in a manner determined by its biochemical properties. The required concentration of radiotracers can be extremely low, in the order of 10^{-9} Mole, in contrast with radiographic or magnetic resonance agents that require much higher concentrations, in the range of 10^{-3} Mole. When the radioactive atom on a particular molecule decays, a positron is ejected from the nucleus. These proton rich radionuclides spontaneously convert a proton to a neutron, resulting in the emission of a positron and a neutrino. The emitted positron, equal in mass and opposite in charge to an electron, slows down through a series of collisions with the surrounding matter, then combines with an electron before it annihilates. The mass of positron and electron is converted to two high energy photons of 511 keV each that travel in approximately opposite directions. Coincidence detection of these gamma rays, which are highly penetrating and can escape from the subject, and reconstruction of the location of the annihilation events using analytical or statistical methods form the basis of PET. The output of the reconstruction process is a 3D image volume, where the signal intensity in any particular image voxel is proportional to the amount of the radionuclide (and, hence, the amount of the labeled molecule to which it is attached) in that voxel. By taking a time sequence of images, the tissue concentration of the radiolabeled molecules as a function of time is measured, and with appropriate mathematical modeling, the rate of specific biological processes can be determined (Figure 2.1).

With its dynamic imaging capability, PET provides both spatial and temporal measurements of the distribution of biomolecules within a living subject. Combined with kinetic modeling, PET provides quantitative measurements of biological processes *in vivo* without disturbing the underlying biochemical process. This unique feature and the wide variety of biomolecules that can be labeled with positron emitting nuclides of different half-lifes make PET an extremely powerful tool to study normal development (e.g. maping normal human brain and heart function) and diseases in humans (e.g. linical diagnosis of certain diffuse brain diseases such as those causing various types of dementias). PET is also used in pre-clinical studies using animals models of human disease, where

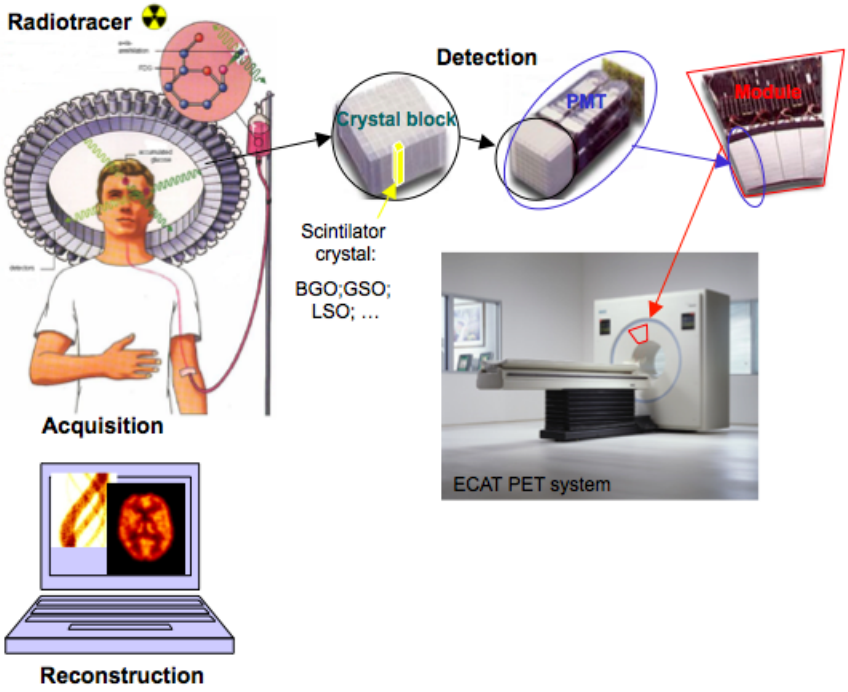

(a) Schematic representation of a PET scanner and data processing principles.

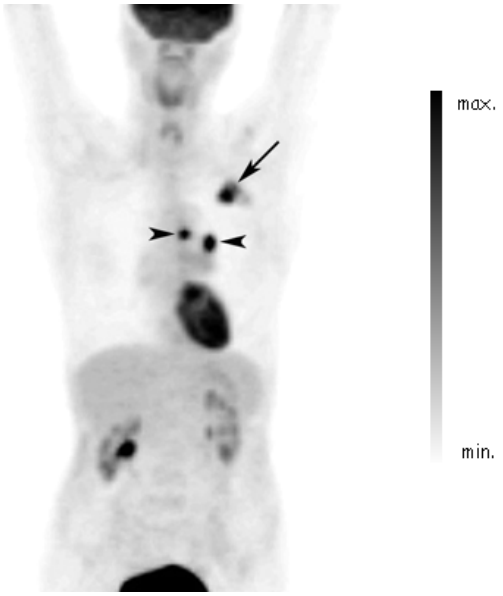

(b) Maximum intensity projection (MIP) image from a FDG PET scan demonstrates intense uptake in known lung cancer in left upper lobe (arrow) as well as within 2 small ipsilateral mediastinal lymph nodes (arrowheads). Adapted from [of a PET exam, 2010].

Figure 2.1: Positron Emission Tomography.

it allows repeated investigations into the same subjects. This is particularly valuable in cancer research, and in the study of the *in vivo* pharmacokinetics of new drugs, as it results in an increase in the statistical quality of the data (subjects can act as their own control) and substantially reduces the numbers of animals required for a given study. Other key applications include the assessment on how far a cancer has spread from the initial focus, evaluating and guiding early treatment response and assessment of tumor response to therapy (either chemotherapy or radiotherapy) [Ben-Haim & Ell, 2009].

An overview of the physical principles, basic features and performance parameters of nuclear medicine instrumentation, and some of the practical issues involved in optimizing system design aspects can be found in: [Phelps, 2000; Ollinger & Fessler, 1997; Zaidi & Hasegawa, 2006a; Wernick & Aarsvold, 2004; Lewellen & Karp, 2004; Christian, 2007a; Shukla & Kumar, 2006; Pomper & Hammoud, 2004].

2.1 Physics of Positron Emission and Annihilation

2.1.1 Positron Emission and Annihilation

The nucleus of an atom is held together by two opposing forces: the strong force is an attractive force between nucleons and is balanced by the repulsive coulomb (electrical) force between the positively charged protons. If a nucleus has either an excess number of protons or neutrons, it is unstable and prone to radioactive decay, leading to a change in the number of protons or neutrons in the nucleus and a more stable configuration. Decay nucleus are known as radionuclides. For a specific element with atomic number Z, isotopes that are unstable and which undergo radioactive decay are known as radioisotopes of that element.

One common method by which nuclei with an excess of protons may decay is through positron emission (also known as β^+ or *beta-plus decay*). Essentially, a proton in the nucleus of the atom is converted into a neutron (n) and a positron (e^+). The positron is ejected from the nucleus, along with a neutrino (ν) that is not detected. An example of a radionuclide that decays by positron emission is ^{11}C:

$$^{11}\mathrm{C} \rightarrow ^{11}\mathrm{B} + e^+ + \nu \tag{2.1}$$

The energy released during positron emission is shared between the daughter nucleus, the positron, and the neutrino. Positrons are therefore emitted with a range of energies, from zero up to a maximum endpoint energy E_{max}. This endpoint energy is determined by the difference in atomic masses between the parent atom and the daughter atom, taking into account gamma-ray emission from excited states that may occur if the transition is not between the ground states of the two nuclei. The mean kinetic energy of the emitted positrons is approximately $0.33 \times E_{max}$ [Christian, 2007b].

Many radionuclides decay by positron emission. Table 2.1 presents a selection of these radionuclides that are commonly encountered in relation to PET imaging. Included in the table are the maximum kinetic energy of the emitted positrons, E_{max}, and the branching ratio (the percentage

radionuclide	$T_{1/2}$	$E_{max}\,(\mathrm{MeV})$	R_{max}	R_{rms}	β^+ branching ratio
^{11}C	20.4 min	0.96	3.9	0.4	99%
^{13}N	9.97 min	1.20	5.1	0.6	100%
^{15}O	122 s	1.73	8.0	0.9	100%
^{18}F	109.8 min	0.63	2.3	0.2	97%
^{22}Na	2.60 y	0.55	15	1.6	98%
^{62}Cu	9.74 min	2.93	2.0	0.2	19%
^{64}Cu	12.7 h	0.65	20	3.3	56%
^{68}Ga	67.6 min	1.89	9.0	1.2	88%
^{76}Br	16.2 h	Various	19	3.2	54%
^{82}Rb	1.27 min	2.60, 3.38	18	2.6	95%
^{86}Y	14.7 h	1.4	6.0	0.7	32%
^{124}I	4.17 d	1.53, 2.14	7.0	0.8	22%

Table 2.1: Selected list of radionuclides, and their physical properties, that decay by positron emission and are relevant to PET Imaging.

of total decays resulting in positron emission instead of electron capture) that occur by positron emission. For positrons emitters used in PET, the maximum energies vary from 0.58 MeV to 3.7 MeV, the maximum (or extrapolated) ranges, (R_{max}), from 2 mm to 20 mm, and the root-meansquare ranges(R_{rms}) from 0.2 mm to 3.3 mm [Sanchez-Crespo *et al.* , 2004]. This latter parameter is important since the positron range distributions are cusp-like shaped, with long tails, and, therefore, the FWHM is not the best indicator of positron range.

The table 2.1 also lists the half-life of the radionuclides. A sample of identical radioactive atoms will decay in an exponential fashion, and the half-life is the time required for half the atoms in the sample to decay. This process continues until the number of nuclide atoms eventually comes so close to zero thatwecan consider the process complete. The relationship between the activity A of a sample at time t, and the half-life, $T_{1/2}$, is given by the decay equation:

$$A(t) = A(0)\, e^{-\lambda t} \tag{2.2}$$

where $A(0)$ is the initial number of radioactive atoms, and $\lambda$is the decay constant which is described by:

$$\lambda = \frac{\ln 2}{T_{1/2}} = \frac{0.693}{T_{1/2}} \tag{2.3}$$

The amount of activity of any radionuclide may be expressed as the number of decays per unit time. Common units for measuring radioactivity are the Curie (after Marie Curie) or the newer SI unit, the becquerel (after another nuclear pioneer, Henri Becquerel). One Becquerel (Bq) is defined as one radioactive decay per second. One Curie (Ci) is defined as 3.7×10^{10} decays per second (this is

approximately equal to the radioactivity emitted by 1 g of radium in equilibrium with its daughter nuclides).

The positron that is ejected following β^+ decay has a very short lifetime in electron rich material such as tissue. It rapidly loses its kinetic energy in inelastic interactions with atomic electrons in the tissue, and once most of its energy is dissipated (typically within 10^{-1} to 10^{-2} cm, depending on its energy), it will combine with an electron. The combined mass of the two particles is instantly converted to energy in the form of two oppositely directed photons. This is referred to as an annihilation reaction.

The two photons are emitted simultaneously in opposite directions, 180° apart, carrying an energy of 511 keV (because the positron and electron are almost at rest when this occurs, the energy released comes largely from the mass of the particles and can be computed from Einstein's mass energy equivalence), ensuring that both energy and momentum are conserved. The annihilation process forms the basis for PET imaging. A PET scanner is designed to detect and localize the simultaneous back-to-back annihilation photons that are emitted following decay of a radionuclide by positron emission.The detectors are designed to record as many of the annihilation photons as possible and to locate the line along which the decay occurred by determining the two interaction vertices. Each detector is in electronic coincidence (also known as electronic collimation) with a fan of detectors on the opposite side of the ring, named Line Of Response (LOR), so the object is simultaneously sampled from many different angles. Typically, 10^6 to 10^9 events (detections of annihilation photon pairs) are needed in a PET scan to reconstruct a statistically meaningful image of the distribution of radioactivity in the body [Bailey *et al.* , 2003; Cherry & Dahlbom, 2006; Bailey *et al.* , 2005]. A conceptualised diagram of this process is shown in Figure 2.2.

2.1.2 Positron Range and Noncolinearity

There are two effects in PET imaging systems that lead to errors in determining the line along which a positron emitting radionuclide is to be found. These effects place some finite limits on the spatial resolution in PET and manifest themselves as a blurring of the reconstructed images. The first of these effects is positron range. As shown in Figure 2.3, positron range is the distance from the site of positron emission to the site of its annihilation. A PET scanner detects the annihilation photons which define the line along which the annihilation takes place, not the line along which the decaying atom is located. Because the positrons follow a tortuous path in tissue, undergoing multiple direction-changing interactions with electrons prior to annihilation, the total path length the positron travels is considerably longer than the positron range. From the perspective of PET imaging, it is the perpendicular distance from the emission site to the line defined by the annihilation photons that matters, the effective positron range, and which causes mispositioning. Some radionuclides emit, on average, higher energy positrons than others, making the positron range effect radionuclide-dependent: For example: broader distribution for ^{15}O (a high energy positron emitter with E_{max} of 1.72 MeV) compared to ^{18}F ($E_{max}$of 0.64 MeV). As a consequence, the blurring effect on the final PET image ranges from a few tenths of a millimeter up to several millimeters, depending on the radionuclide and its E_{max} [Levin, 2004; Bailey *et al.* , 2005, 2003].

The second effect comes from the fact that the positron and electron are not completely at rest when

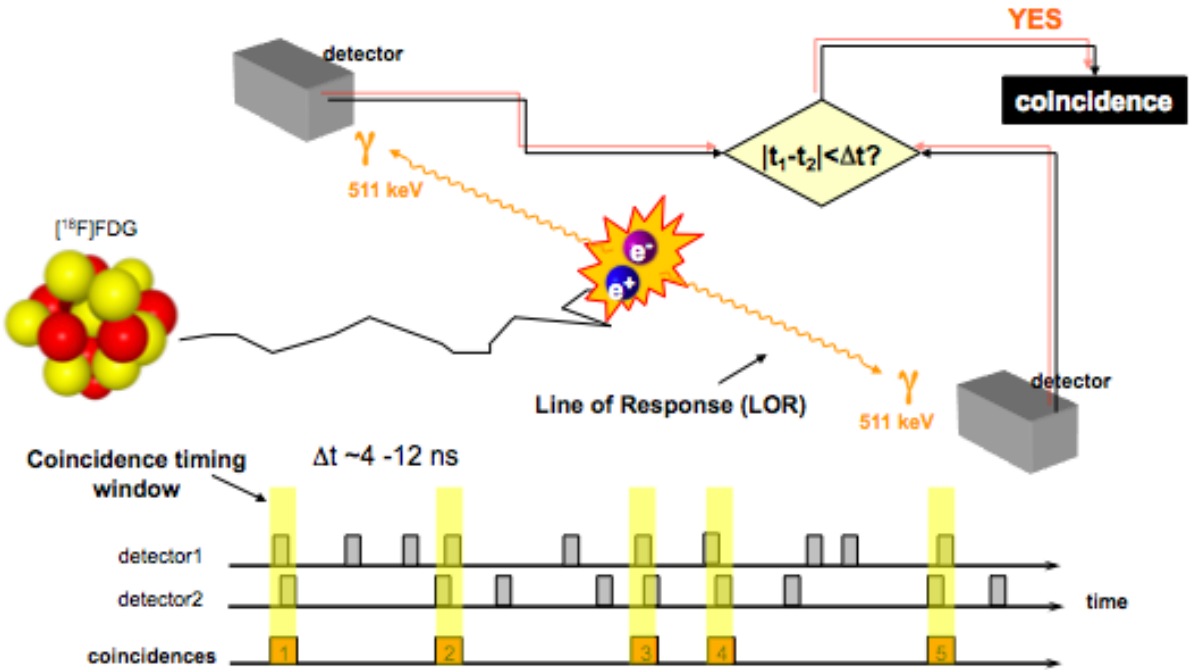

Figure 2.2: In a PET camera, each detector generates a timed pulse when it registers an incident photon. These pulses are then combined in coincidence circuitry, and if the pulses fall within a short time-window, they are deemed to be coincident. A coincidence event is assigned to a LOR joining the two relevant detectors. In this way, positional information is gained from the detected radiation without the need for a physical collimator. This is known as electronic collimation. Electronic collimation has two major advantages over physical collimation: improved sensitivity and improved uniformity of the Point Source Response Function (PSRF).

they annihilate. The small net momentum of these particles means that the annihilation photons will not be at exactly 180° and will, in fact, be emitted with a distribution of angles around 180°. This is known as noncolinearity or accolinearity, and is illustrated in Figure 2.3. This effect is independent of radionuclide because the positrons must lose most of their energy before they can annihilate; hence, the initial energy is irrelevant. The distribution of emitted angles is roughly Gaussian in shape, with a Full Width at Half Maximum (FWHM)[1] of 0.5° [Cherry *et al.* , 2003a; Zanzonico, 2004; Wernick & Aarsvold, 2004]. After detecting the annihilation photons, PET assumes that the emission was exactly back to back, resulting in a small error in locating the line of annihilation. Assuming a Gaussian distribution and using the fact that the angles are small, the blurring effect due to noncolinearity, Δ_{nc}, can be estimated as:

$$\Delta_{nc} = 0.0022 \times D \tag{2.4}$$

where D is the diameter of the PET scanner. The error increases linearly as the diameter of the PET scanner increases [Cherry & Dahlbom, 2006; Bailey *et al.* , 2003, 2005].

[1] FWHM is often used to characterize a distribution that is Gaussian or nearly Gaussian and involves measuring the width of the distribution at the point where it reaches half the maximum amplitude. A related measure, full width at tenth maximum (FWTM), identifies the width of the distribution where it reaches one tenth of its maximum amplitude.

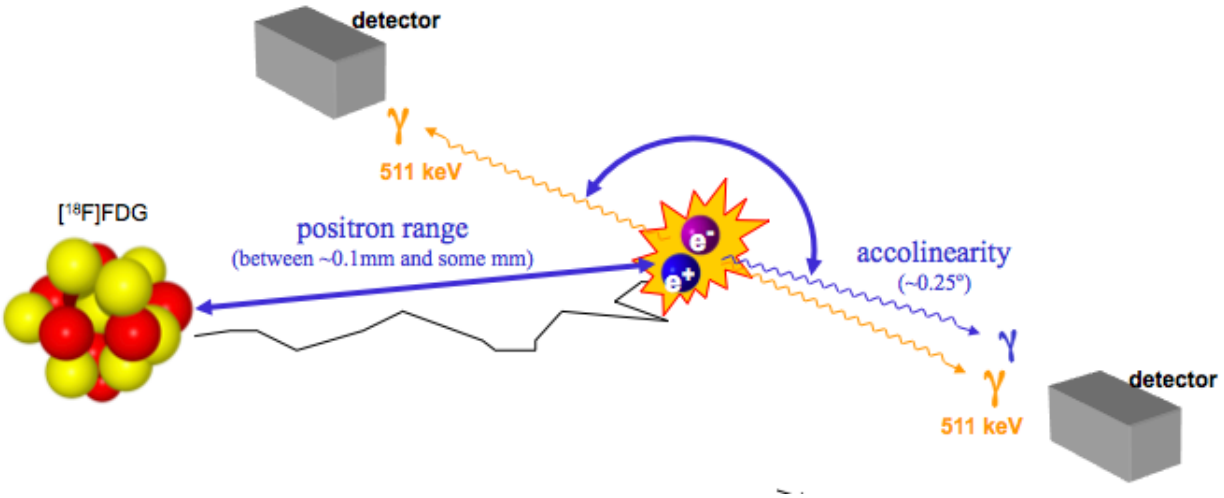

Figure 2.3: The process of positron emission and subsequent positron-electron annihilation results in two 511 keV annihilation photons emitted 180° apart. The positron range error is dependent on the energy of the emitted positrons resulting in variations of ~ 0.1 mm up to some mm. Accolinearity is independent of radionuclide, and the error is determined by the separation of the detectors. Because there is some residual momentum associated with the positron, the two annihilation photons are not emitted exactly at 180°, but at a slight deviation.Two detectors detect these photons in a straight line, which is slightly deviated of ±0.25° from the original annihilation line.

2.1.3 Photon Interactions with Matter

It is important to understand how the 511 keV photons emitted following annihilation interact with the tissue surrounding them, with the detector material of the PET scanner, and with materials such as lead and tungsten that may be used for shielding or slice collimation purposes.

As they pass through matter, photons interact with atoms. The type of interaction is a function of the energy of the photons and the atomic number (Z) of elements composing the matter. In the practice of nuclear medicine, where gamma rays with energies between 50 keV and 550 keV are used, Compton scattering is the dominant type of interaction in materials with lower atomic numbers, such as human tissue (Z = 7.5). The photoelectric effect is the dominant type of interaction in materials with higher atomic numbers, such as lead (Z = 82). A third type of interaction of photons with matter, pair production, only occurs with very high photon energies (greater than 1020 keV) and is therefore not important in clinical nuclear medicine [Powsner & Powsner, 2006; Bailey *et al.* , 2005, 2003].

2.1.3.1 Compton Scattering

In Compton scattering the incident photon transfers part of its energy to an outer shell or (essentially) “free” electron, ejecting it from the atom. Upon ejection this electron is called a Compton electron. The photon is scattered at an angle that depends on the amount of energy transferred from the photon to the electron. The scattering angle can range from nearly 0º to 180º. Imposing conservation of momentum and energy leads to a simple relationship between the energy of

the original photon, E, the energy of the scattered photon, E_{sc},and the angle through which it is scattered, θ:

$$E_{sc} = \frac{m_e c^2}{\frac{m_e c^2}{E} + 1 - \cos\theta} \tag{2.5}$$

In this equation, m_e is the mass of the electron and c is the speed of light (2.998×10^8 m/s). Using units of electron volts for energy, the term $m_e c^2$ is equal to 511 keV. In PET, the incoming photon of interest has an energy level of 511 keV; the equation, therefore, reduces further to:

$$E_{sc}\,(keV) = \frac{511}{2 - \cos\theta} \tag{2.6}$$

The recoil energy that is transferred to the electron, E_{re}, which is dissipated in the medium, is equal to $E - E_{sc}$. The maximum energy that can be imparted to the electron (and, therefore, the medium) occurs when the photon is scattered through 180°. The probability of Compton scattering per unit length of absorbing medium is linearly proportional to the atomic number of the medium [Sorenson & Phelps, 1987; Turkington, 2001; Levin, 2004].

The angular distribution of the scattered photons is given by the Klein-Nischina equation [Cherry & Dahlbom, 2006]. It is independent of the scattering medium but strongly dependent on the energy of the photons. The angular distribution for a range of energies can be found in [Cherry *et al.* , 2003a].

2.1.3.2 Photoelectric Effect

A gamma ray of low energy, or one that has lost most of its energy through Compton interactions, may transfer its remaining energy to an orbital (generally inner-shell) electron. This last process is called the photoelectric effect and the ejected electron is called a photoelectron (PE). This electron leaves the atom with an energy equal to the energy of the incident gamma ray diminished by the binding energy of the electron. An outer-shell electron then fills the inner-shell vacancy and the excess energy is emitted as an X-ray. The probability of photoelectric absorption per unit distance in a medium strongly depends on the atomic number of the medium in which the photon is propagating [Levin, 2004; Bailey *et al.* , 2005, 2003].

2.1.3.3 Interaction Cross-Sections in Materials

The interaction (absorption or scattering) of 511 keV photons by matter can be described with a simple exponential relationship:

$$I(x,y,x) = I(0)\,e^{-\mu(x,y,z)} \tag{2.7}$$

where $I(0)$ is the 511 keV photon flux impinging on the medium, x is the thickness of the medium, and $I(x,y,z)$ is the flux of 511 keV photons that passes through the medium without interaction.

	$\mu_{compton}$	$\mu_{photoelectric}$	μ	half-value thickness
	(cm^{-1})	(cm^{-1})	(cm^{-1})	(cm)
soft tissue	~0.096	~0.00002	~0.096	7.2
bone	~0.169	~0.001	~0.17	4.1
BGO	0.51	0.40	0.96	0.76
lead	0.76	0.89	1.78	0.42
tungsten	1.31	1.09	2.59	0.29

Table 2.2: Linear Attenuation Coefficients for soft tissue, bone, Bismuth Germanate - BGO (a detector material), lead, and tungsten at 511 keV. Adapted from [Cherry & Dahlbom, 2006].

The parameter μ is the linear attenuation coefficient and is the probability per unit distance that an interaction will occur. In the context of diagnostic imaging, the attenuation coefficient reflects, essentially, the sum of the probabilities associated with the photon interaction by photoelectric absorption and Compton scattering, Equation 2.8. Since PET imaging occurs at 511 keV, photon attenuation is determined by Compton scattering [Kinahan *et al.* , 2003] and Table 2.2.

$$\mu \approx \mu_{compton} + \mu_{photoelectric} \tag{2.8}$$

For PET imaging, three media are of potential interest: tissue in the body, the detector material, and any material used for shielding or collimation. The attenuation coefficients for soft tissue, bone, for a typical detector material and for lead and tungsten are shown in Table 2.2. The half-value thickness, the thickness of material that is required to cause half of the 511 keV photons to interact, is also given.

The annihilation photons must pass through the body so that they can be detected. Therefore, photon interactions in the body attenuate the signal by redirecting annihilation photons that would have struck a particular detector pair. The angular correlation between the annihilation photons is randomized by the scattering process, so if the redirected photons still escape the body and are detected in the PET scanner, they will be incorrectly located. This results in a background of scattered events in the images. Unfortunately, even at the high energies of the annihilation photons, substantial numbers are scattered in the body because the Compton scatter cross-section is quite high.

The function of the PET scanner is to detect those 511 keV photons that escape the body without interacting. The detector material should, therefore, be something that has a high probability of stopping these photons, that is, very dense materials, with large values of μ. An example of such a material is BGO. Photoelectric interactions are preferred in a detector because they result in all of the energy being deposited locally. Compton scattering can result in multiple interactions within a detector or interactions in adjacent detectors. It can, therefore, be difficult to unambiguously define the location of the interaction.

2.2 Imaging Technology for PET

2.2.1 PET Detectors

A common PET detector system consists of rings of crystals. The rings may or may not be separated by septa[2]. The individual detector contains one or more large segmented crystals or a collection of small crystals. A standard detector unit or block consists of a small crystal or small portion of a larger crystal watched by four Photomultiplier Tubes (PMTs), Figure 2.4.

To obtain the best quality image for a given injected dose of radioactivity, the detectors must have a very high efficiency for detecting 511keV photons that impinge on their surface (the more photon pairs that are detected, the better the signal-to-noise ratio (SNR) in the image) and must also give precise information on the spatial location of the interaction (this relates directly to the spatial resolution of the images). The latter is generally achieved in one of two ways, either by using arrays of small detector elements, in which case the precision of localization is related to the size of the detector elements, or by using a larger area detector that has position sensing capability built in. It is also important to be able to determine when a photon struck the detectors, so that the time of all detected events can be compared to determine which ones arrived closely enough in time to correspond to an annihilation pair. The ability of a pair of detectors to determine the time difference in arrival of the annihilation photons is known as the timing resolution and is typically on the order of 2 to 6 ns. A typical timing window that is used in PET scanners so as not to accidentally reject annihilation photon pairs is typically 2 to 3 times the timing resolution, leading to values in the range of 4 to 18 ns. The detectors should indicate the energy of the incoming annihilation photon such that those that have scattered in the body can be rejected. The ability of the detector to determine the energy of the photon is known as the energy resolution. Finally, the index of refraction of the scintillator is also important as this determines how efficiently optical photons can be transmitted from the scintillator to the photodetector. Large mismatches in index result in significant internal reflection at the scintillator/photodetector boundary and reduce light transmission to the photodetector.

Scintillation detectors are widely used gamma ray detectors that form the basis for almost all PET scanners in use today. These detectors consist of a dense crystalline scintillator material that serves as an interacting medium for gamma rays and high energy photons and which emits visible light when energy is deposited inside of them. This light is then subsequently detected by some form of visible light photon detector and converted into an electrical current [Wilkinson, 2004; Melcher, 2000].

To further complicate an ideal scintillation detector wish list, the attributes that should be emphasized depend on the final target application. For simplicity, one can group applications into three main categories: (1) pre-clinical imaging (e.g. small animal), (2) dedicated neuro-imaging and (3) whole-body imaging. For all three categories, there is a need to strive for higher sensitivity. For pre-clinical imaging, the parameter getting the most attention is spatial resolution with newer designs striving to achieve < 1 mm^3 volume resolution. Timing resolution is not as important for pre-clinical

[2]Septal rings are used, to reduce the number of scattered events collected, and to minimize other effects of radiation originating outside the FOV, including dead time and random events, discussed later.

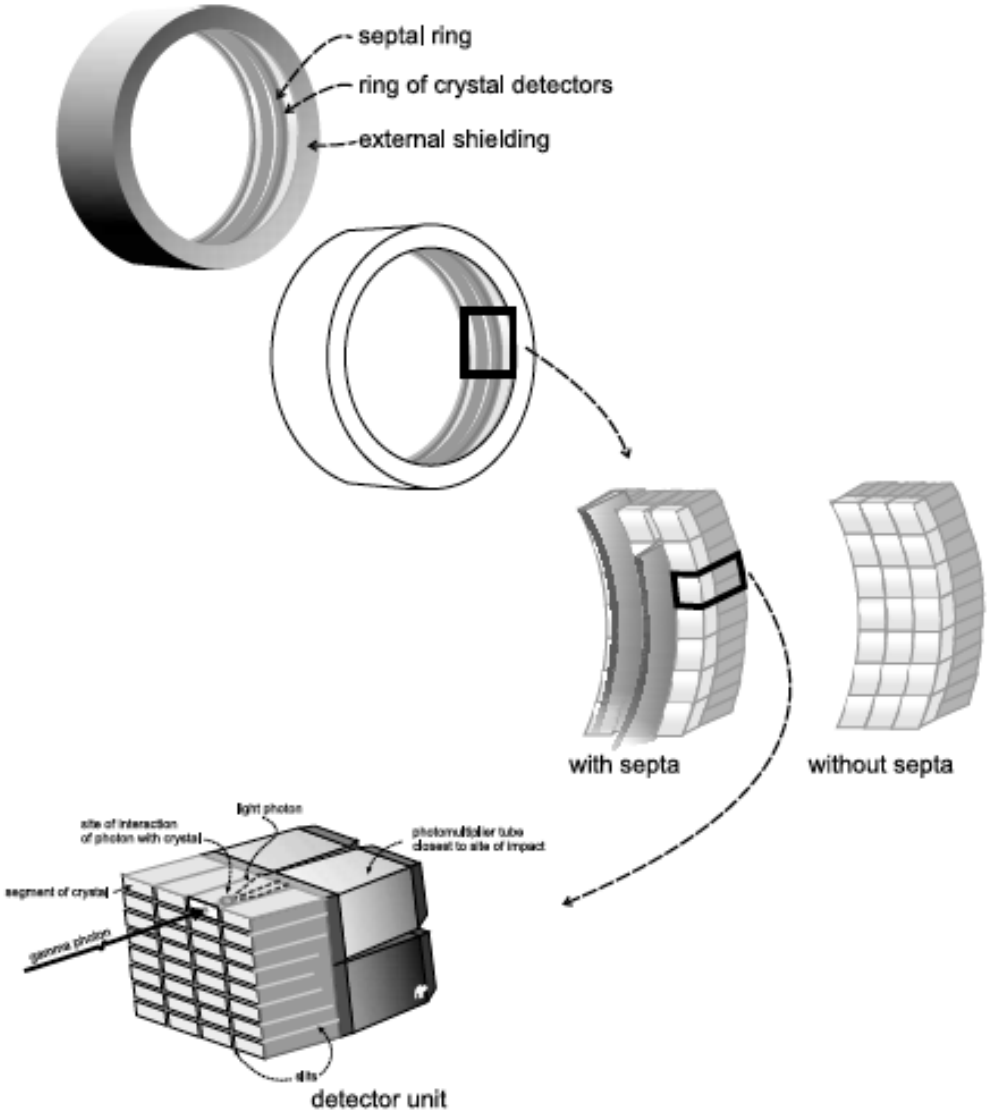

Figure 2.4: PET camera configuration: slits between crystals direct light photons toward PMTs. Adapted from [Powsner & Powsner, 2006].

	NaI(Tl)	BaF_2	LSO	GSO	LYSO	$LaBr_3$	LFS	LuAP	LuI_3
Effective atomic no. (Z)	51	54	66	59	60	47	63	65	60
μ (cm^{-1})	0.34	0.44	0.87	0.62	0.86	0.47	0.82	0.9	~0.56
Density ($gm\ cm^{-3}$)	3.67	4.89	7.4	6.7	7.1	5.3	7.3	8.34	5.6
Index of refraction	1.85	-	1.82	1.85	1.81	1.88	1.78	1.95	-
Light yield (% NaI(Tl))	100	5	75	30	80	160	77	16	190
Peak wavelength (nm)	410	220	420	430	420	370	430	365	470
Decay constant (ns)	230	0.8	40	65	41	25	35	18	30
Hygroscopic	yes	slight	no	no	no	no	no	no	yes

Table 2.3: Properties of some scintillators used in PET detectors. Note that some of these specifications are subject to change as developers change dopants and trace elements in the scintillator growth. For example, the light output, peak wavelength, decay time and density for LYSO and LFS will vary somewhat for different versions of the basic scintillator. Adapted from [Lewellen, 2008].

imaging since the count rates are such that randoms rates are generally low. For neuroimaging, the spatial resolution target can be relaxed (perhaps ~3 mm^3). Many brain imaging applications want both high spatial resolution and good dynamic imaging, and thus sensitivity is particularly important. Sensitivity is also important if effects such as non-collinearity of annihilation gamma rays are to be addressed in the image reconstruction algorithm. Further, timing resolution is important for randoms rejection. Current whole body imaging commercial systems have crystal cross section dimensions as small as 4×4 mm^2. The realities of dose limitations and the number of gamma rays detected make going to smaller detector dimensions for body imaging generally not a goal in most detector designs. Current systems cannot generally reach their spatial resolution limits due to the amount of variance in the images. Thus, one of the current major areas of development for body systems is that of pushing the Time-Of-Flight (TOF) resolution to achieve an improvement in the final SNR in the images. It should be no surprise that the ideal detector is yet to be developed for any of these applications and is an area of very active research [Zanzonico, 2004; Humm *et al.* , 2003; Bailey *et al.* , 2005, 2003]. In general, a scintillator should be fast, dense, have high light output and be cheap to produce. Table 2.3 lists some of the properties of scintillators found in many PET detector designs.

2.2.2 Photomultiplier Tubes (PMTs)

A PMT is a device that produces a pulse of electrical current when stimulated by very weak light signal, such as those produced by a scintillation crystal. A cross-section through a typical photomultiplier tube is shown in Figure 2.5. Light from the scintillator is transmitted through the glass entrance window of the PMT and excites the photocathode. The photocathode is made from a thin layer of material that can easily liberate electrons as energy is deposited in it. Each light photon from the scintillator has roughly a 15% to 25% chance (depending on wavelength) to liberate an electron. This probability is called the quantum efficiency of the PMT. A high potential difference accelerates the electron from the photocathode and directs it to strike a positively charged electrode called the first dynode. This dynode is also coated with an emissive material that readily releases electrons, and each impinging electron has acquired sufficient energy to release on the order of 3 to 4 secondary electrons from the dynode. These electrons are in turn accelerated to the second dynode and so forth, ultimately creating an avalanche of photoelectrons. After 10 stages of amplification, each initial electron has created on the order of 10^6 electrons, which, occurring over a period of a few nanoseconds, lead to an easily detectable current in the milliamp range. PMTs come in a wide range of shapes and sizes and also are available as multichannel and position sensitive models. Most PET scanners use round or square single-channel PMTs in the range of 1 to 5 cm in diameter. The advantages of PMTs are their high gain (amplification), which leads to high signal-to-noise pulses, their stability and ruggedness, and their fast response (the output pulse from a PMT rises in approximately a nanosecond for a step function input of light into the PMT). The disadvantages are that they are quite bulky and fairly expensive [Pichler & Ziegler, 2004; Bailey *et al.* , 2005, 2003].

An alternative to PMTs is a special type of semiconductor photodiodes, know as avalanche photodiodes (APDs). An APD is a *p-n* junction in a silicon wafer that can be operated near breakdown voltage under reverse bias. The distinctive feature of such device is the acceleration electrons generated by interactions with ionizing radiation are subject to, due to the high electric field. These electrons gain enough velocity to generate free carriers by impact ionization, which are themselves sufficiently accelerated between collisions to create additional electron-hole pairs along the collection path. This process results in gains of 10^2 to 10^3, yielding improved SNR over photodiodes. The quantum efficiency is in the 60% to 80% range. When combined with the relatively high gain, this leads to roughly equivalent performance in terms of energy and timing performance when compared to PMT-based detectors [Zanzonico, 2004; Humm *et al.* , 2003; Bailey *et al.* , 2005, 2003].

2.2.3 Block Detector Readout

The majority of dedicated PET scanners in use in the early part of the 21st century have detectors based on the block design proposed originally by Casey and Nutt [Casey & Nutt, 1986]. A schematic of the block detector is shown in Figure 2.6. A relatively large block of scintillator material (typically 4×4 cm in area by 3 cm deep) is segmented into an array of smaller detector elements (typically 8×8). The saw cuts are filled with a white reflective material that helps to optically isolate individual elements within the block. The scintillator block is coupled to four single-channel PMTs.

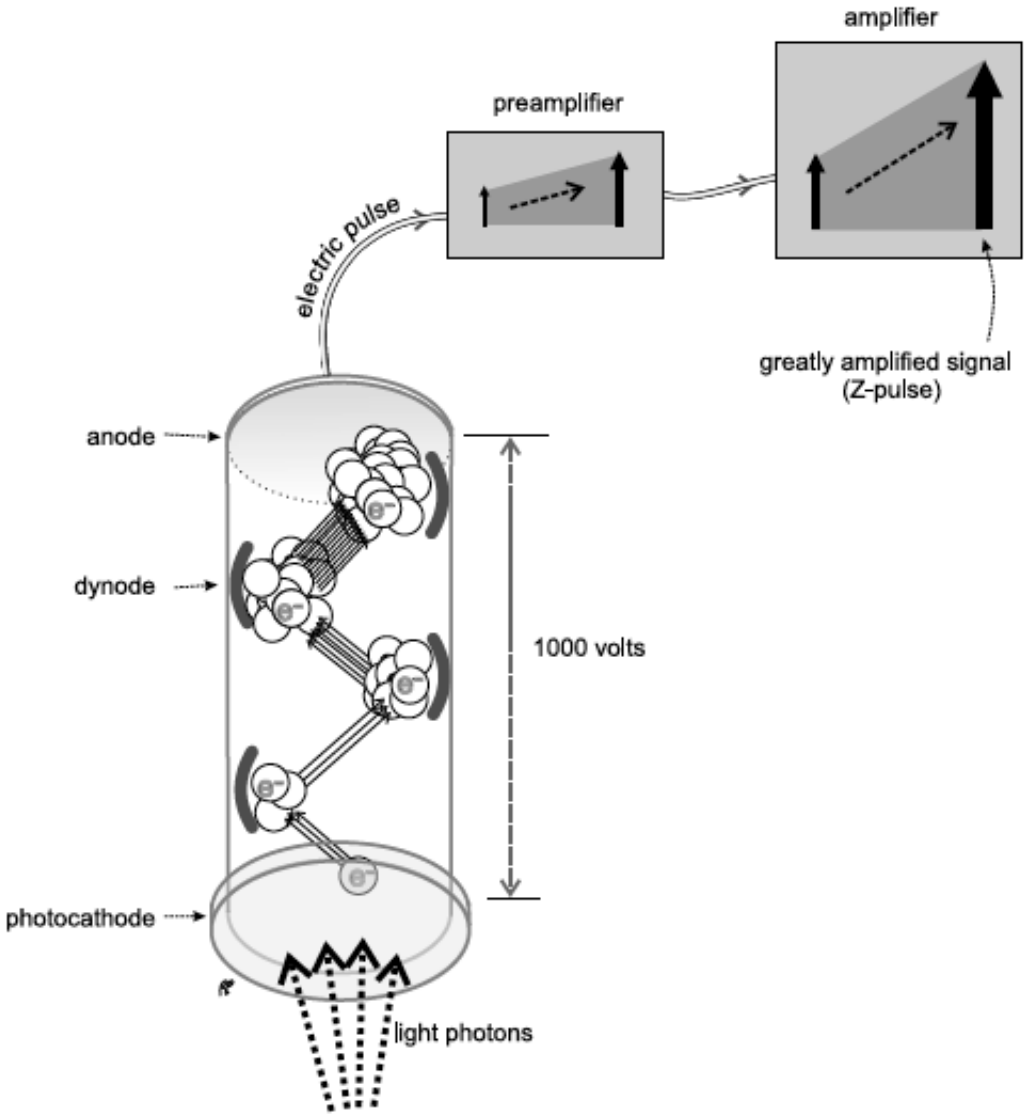

Figure 2.5: Photomultiplier tube and its preamplifier and amplifier. Adapted from [Powsner & Powsner, 2006].

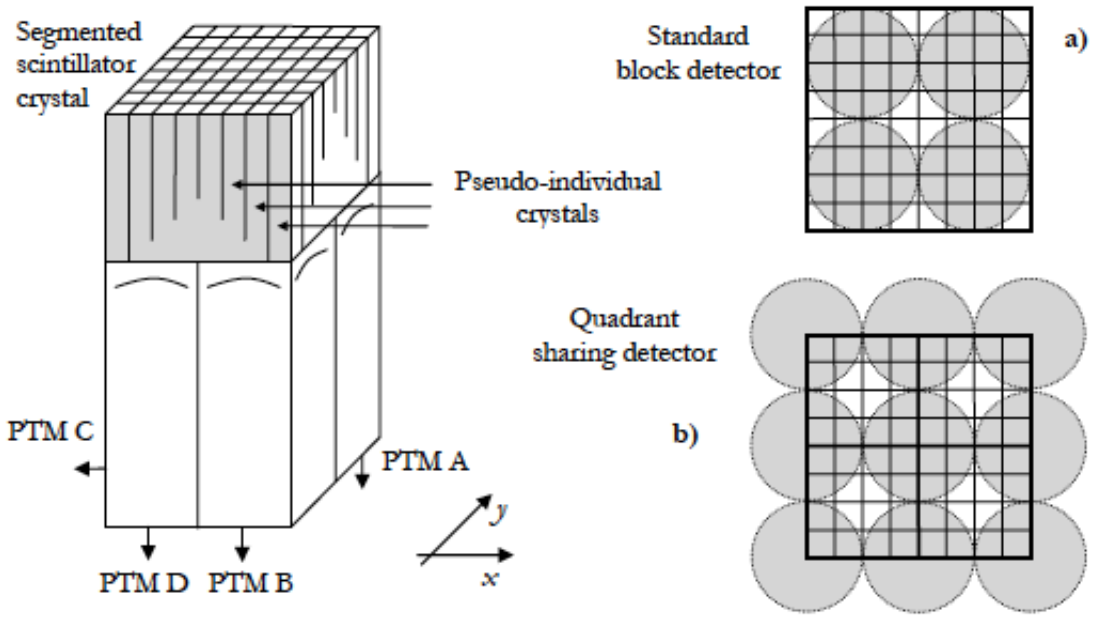

Figure 2.6: A schematic representation of a block detector: a) Standard PMT arrangement in a standard block detector and b) Quadrant-sharing detector. Adapted from [Zanzonico, 2004].

The depth of the saw cuts is empirically determined to share scintillation light in a linear fashion between the four PMTs as a function of the position of the annihilation photon interaction within the block. For example, if an annihilation photon interacts in the corner detector element, the deep cuts ensure that virtually all the scintillation light photons that are produced from the interaction end up in the PMT sitting directly underneath that element. Alternatively, an event interacting towards the middle of the block, where the cuts are shallower, results in a roughly equal spread of scintillation light among all four PMTs. By careful design of the depth of the cuts, and with sufficient scintillation light, interactions in each detector element will produce a unique distribution of scintillation light and, therefore, signals on the four PMTs. In practice, an X and Y coordinate is calculated for each annihilation photon that interacts in the block detector based on:

$$X = \frac{(A+B)-(C+D)}{A+B+C+D} \tag{2.9}$$

$$Y = \frac{(A+C)-(B+D)}{A+B+C+D} \tag{2.10}$$

The standard arrangement for coupling the PMTs assembly with the block detector is represented in Figure 2.6 a): the light from each block is collected by 4 PMT, centered over each quadrant. The block detector is a very cost-effective approach to PET, as it allows on the order of 64 crystals to be decoded from just four PMTs. Because the photodetectors are one of the most expensive components of a PET scanner, this 16:1 multiplexing is the key to developing PET scanners with thousands of detector elements at a reasonable cost. A large number of detector elements implies

good solid angle coverage. The block design also leads to detector elements that are smaller than the PMTs themselves. Smaller detector elements allow gamma-ray interactions to be better localized leading to improved spatial resolution as well. The spatial resolution of the block detector is primarily determined by the width of the detector elements (assuming scintillation light is sufficient to resolve each of the elements). This width is commonly 3 to 5 mm in current generation block detectors designed for clinical PET scanners.

Another approach is called quadrant sharing (Figure 2.6 b)): each block is also monitored by four PMTs, but each of these PMTs is centered in the corner of four different blocks. Four PMTs are still being used to decode each block, but each PMT now actually serves four different scintillator blocks. The block in which the interaction occurs is determined by which four PMTs show a significant signal is determined from equations 2.9 and 2.10. This approach, when extended to large area detector panels, leads to almost another fourfold reduction in the number of PMTs required per detector element, giving a total multiplexing approximately 64:1, and lower overall detector cost. Alternatively, this approach can be used to decode smaller detector elements for the same sized photomultiplier tubes used in the original block detector [Humm *et al.* , 2003; Zanzonico, 2004; Bailey, 2003, 2005].

2.3 Data Acquisition

2.3.1 Coincidence Detection

A simple coincidence detection system is illustrated in Figure 2.3, which consists of a pair of radiation detectors with associated electronics (amplifiers, pulse height analyzers, high voltage) and a coincidence circuit. If an annihilation occurs somewhere between two high-efficiency detectors, and the direction of the two 511 keV photons is such that each will have a chance to interact with one of the two detectors, it is very likely that a coincidence event will be recorded. Because all annihilation photons are emitted approximately 180° apart, a recorded coincidence indicates an annihilation occurred somewhere along the LOR. To reconstruct a complete cross-sectional image of the object, data from a large number of LORs are collected at different angles and radial offsets that cover the field of view of the system. The two detectors and associated circuitry should, under ideal circumstances, simultaneously generate the logic pulses necessary to generate a coincidence. However, due to stochastic processes in the emission of light in the scintillation detectors, a random time delay occurs exactly when the detectors respond following the absorption of the annihilation photons in the detectors. This uncertainty in response or time resolution depends on the characteristics of the detector, primarily scintillation decay time constant and light output (Table 2.3).

To avoid missing coincidence events, the logic pulses must have a certain finite width to ensure that the pulses overlap despite the finite time resolution. Typically, the width of the logic pulses, τ, should be at least as wide as the timing resolution of a pair of detectors (measured in FWHM). It is important to keep the pulses as narrow as possible to minimize the detection of events from unrelated decays that happen to strike the detectors within the time window determined by the overlap of the two logic pulses.

2.3.2 Type of Events

A true coincidence occurs when a single positron annihilates and both of the gamma rays are detected without either of them scattering in the object being scanned. However, due to limitations of the detectors used in PET and the possible interaction of the 511 keV photons in the body before they reach the detector, the coincidences measured are contaminated with undesirable events which includes scattered, random and multiple coincidences (Figure 2.7).

All these events have a degrading effect on the measurement and need to be corrected to produce an image that represents as closely as possible the true radioactivity concentration under measurement. Another point to consider is that the vast majority (typically 90% or more) of photons detected by the PET scanners are single events, in which only one of the two annihilation photons is registered. The partner photon may be on a trajectory such that it does not intersect a detector (most PET scanners provide relatively modest solid angle coverage around the object), or the photon may not deposit sufficient energy in a detector to be registered or may not interact at all. These single events are not accepted by the PET scanner, but they are responsible for random and multiple coincidence events. Because they must still be processed by the electronics to see if they form part of a coincidence pair, they are the determining factor in issues related to detector dead time

A scattered coincidence occurs when one or both of the 511 keV annihilation photons from a single positron decay scatter in the object being scanned. This is a true coincidence since it came from single positron annihilation, but the resulting LOR will be misplaced, resulting in reduction of spatial resolution and image contrast. If not corrected, the scattered events produce a low spatial frequency background that reduces contrast. The distribution of scattered events depends on the distribution of the radioactivity and the shape of the scattering medium (i.e., the patient). The fraction of scattered events detected can range from 10% to well over 40% in typical PET studies, depending on the size of the object and the geometry and energy resolution of the PET scanner [Cherry *et al.* , 2003a].

A random, or accidental, coincidence occurs when two positrons annihilate and one gamma ray from each annihilation is detected. If the two events occur close enough in time, then the tomograph electronics will register the event as a coincidence (or a prompt event). However, such randoms are distributed uniformly in time and only the portion of random events included in the prompt window contaminates the primary data set. If the individual photon detection rates (counts per second) in a pair of detectors are given by N_1 and N_2, then it can be shown that the rate of random coincidences, N_R (randoms per second) is given by:

$$N_R = 2\tau N_1 N_2 \tag{2.11}$$

where τ is the width of the logic pulses produced when a photon is absorbed in the detector. The term 2τ is often referred to as the coincidence timing window. Because the individual detection rates N_1 and N_2 are directly proportional to the activity in the field of view (FOV) of the scanner, the rate of random coincidences is proportional to the square of the activity in the FOV. During image reconstruction, randoms corrections can be made in a scanner by either sampling the randoms

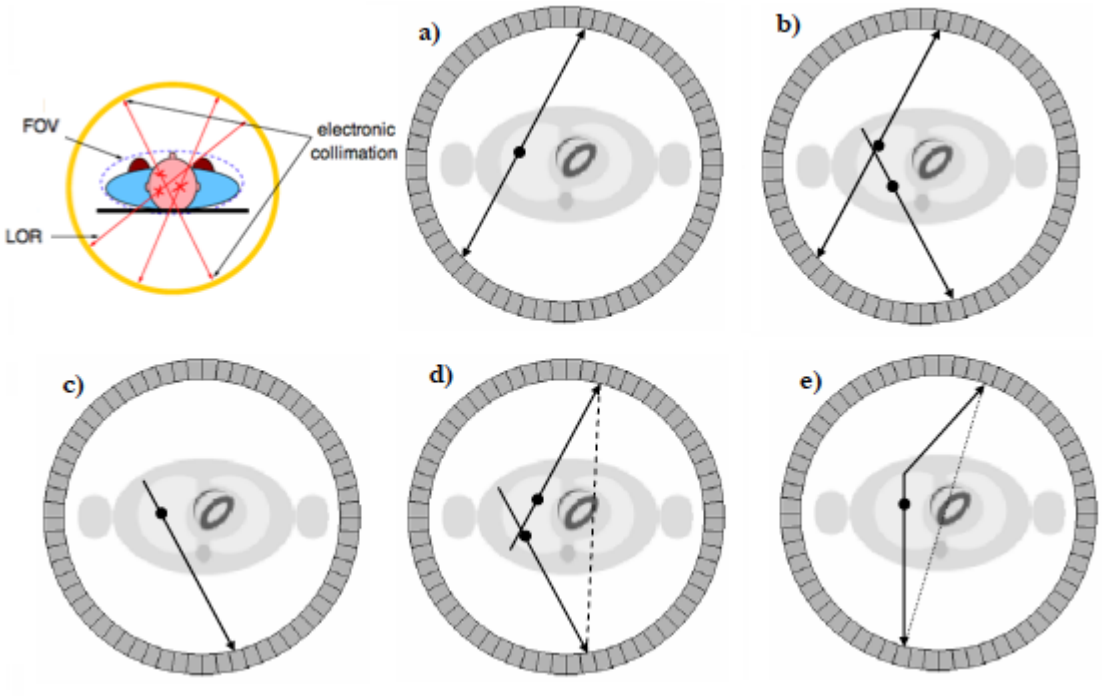

Figure 2.7: Illustration of the main coincidence event types: a) true; b) multiple; c) single; d) random and e) scattered.

for each LOR by applying a timing acceptance window that is delayed from the prompt window (accepting events that are not true coincidence or scattered events) or measuring the single event rates in each detector unit and calculating the randoms.

Multiple events result from more than one annihilation and correspond to the detection, within the same coincidence window, of three or more gamma rays. Since there is an ambiguity in deciding which photons make a valid pair (result from the same annihilation), these events are usually discarded by the system.

The total number of events detected by the coincidence circuit in a PET scanner are referred to as prompt coincidences. These events consist of true, scattered, and accidental coincidences where the true coincidences are the only ones that carry spatial information regarding the distribution of the radiotracer. It is, therefore, necessary to estimate what fraction of the measured prompt coincidences arise from scattered and accidental coincidences for each of the LORs [Sorenson & Phelps, 1987; Tarantola *et al.* , 2003; Bailey, 2003, 2005].

2.3.3 2D and 3D Acquisitions

Septal rings, of tungsten, can be used to improve resolution by reducing the amount of scatter from photons originating outside the plane of one ring of crystals. The sensitivity of the scanner is reduced, however, because a significant fraction of true coincidence events are rejected. Removal of the septa will increase sensitivity and decrease resolution. Scans obtained with the septa in place are called two-dimensional (2D) scans. Without septa the scans are called three-dimensional (3D)

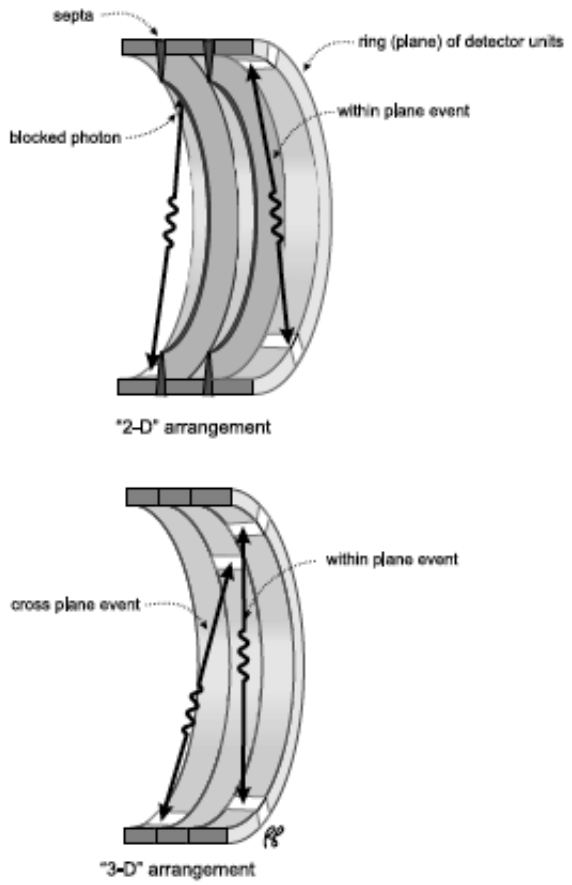

Figure 2.8: 2D and 3D PET imaging. Adapted from [Powsner & Powsner, 2006].

scans. In the 2D mode illustration in Figure 2.8, the septa block out of plane photons, allowing only within-plane coincidence events to be recorded. The 3D configuration permits coincident registration of cross-plane events, those in which the two 511 keV photons are detected in different rings. Septa reduces the number of random coincidence events. The effect of septa is to reduce the scatter from 30% to 60% of all collected events to approximately 10% to 20% [Turkington, 2001].

To increase the axial sampling, the length of the septum is adequately chosen in order to allow, even under a 2D acquisition mode, the acquisition of data along LORs connecting detector elements belonging to first neighbor rings. These LORs lie within planes corresponding to polar angles slightly different from zero – the cross planes or inter-planes. Two cross planes corresponding to two adjacent detector rings cross the scanner axis at a point exactly halfway between the points of intersection of the scanner axis and the transaxial planes associated with each of these two rings. Thus, these cross planes can be added together to form a single virtual transaxial plane located halfway between the real adjacent transaxial planes. This is the strategy for incrementing the axial sampling: if the scanner has n detector rings, the use of cross planes leads to a total of $2N-1$ transaxial planes.

Using 3D mode raises a different question: if, theoretically, with a N ring scanner, it is possible to define N^2 data planes, in practice, however, due to the large amount of data this would produce,

there are groups of planes that are mashed (added together) into a single plane. This compression strategy corresponds to a loss of information, but it guarantees that the large amounts of data can be stored and processed within reasonable times [Schoder *et al.* , 2003; Fahey, 2002; Bailey, 2005].

2.3.4 Acquisition Protocols

The end point in all PET studies is to produce an image, from which diagnostic or quantitative parameters can be derived. These parameters can be as simple as a qualitative comparison of activity concentration in different tissue regions or more complex biologic parameters such as metabolic rate or levels of gene expression. The information that is to be extracted from the image will dictate how the PET data are collected (i.e., static or dynamic sequence) [Ferreira, 2001; Wernick & Aarsvold, 2004].

The most basic data acquisition protocol in PET is the collection of a single data set or static frame over a fixed length of time. The image reconstructed from such a data set represents the average tissue activity concentration during the acquisition. This is the typical acquisition mode used in studies where the tissue activity distribution remains relatively static during the collection of the data. An example is the use of *2-Deoxy-[^{18}F]fluoro-D-glucose* (FDG) studies, where the tracer concentration remains fairly stable following an initial uptake period of 30 to 40 minutes [Boellaard *et al.* , 2009]. In these types of studies, the biologic parameter of interest (in this case the metabolic rate for glucose) is then assumed to be directly proportional to the measured activity concentration.

For some radiotracers, it is necessary to follow the dynamic changes in concentration to extract a particular parameter of interest. In these studies, the data are collected as a sequence of dynamic time frames, where the PET images provide information about the changes in activity concentration distribution over time. This information represents the tissue response to the time course of the radiotracer in the plasma following intravenous injection. The tissue time activity curve (TAC) can then be processed with a compartmental model to determine the parameters of interest. These types of studies typically also require additional data such as the blood plasma radioactivity concentration and the blood plasma concentration of labeled metabolites, which can be determined from blood samples.

2.3.5 PET System Configurations

Current detector module designs use either large continuous NaI(Tl) crystals or arrays of discrete crystals. The NaI(Tl) systems offer a lower price due to the lower cost of the scintillator and the use of fewer electronics channels, whereas the discrete crystal machines offer higher sensitivity due to the higher stopping power of the scintillators used (e.g., BGO, LSO, or GSO) and much higher count-rate performance (e.g., lower dead time and less pulse pileup). In either case, the detectors can be configured as full rings that completely surround the patient or as partial rings with rotational motion to obtain the needed angular sampling (Figure 2.9).

Current designs with NaI(Tl) use either six large 25 mm thick curve plates (full ring) or SPECT systems with two or three detector heads with 18 to 25 mm thick detectors (partial ring). Current

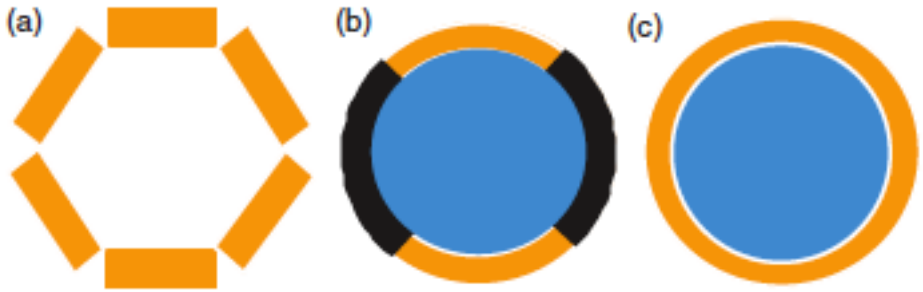

Figure 2.9: The three basic geometries found in modern dedicated PET systems: (a) Array of large detectors, either continuous detectors (flat or curve-plate NaI(Tl)) or plates of discrete crystals; (b) partial ring of detector blocks that rotates and (c) full ring of discrete crystals configured as small blocks or larger detector modules. Adapted from [Lewellen & Karp, 2004].

discrete crystal designs use BGO (25 to 30 mm thick), LSO (typically 25 mm thick), or GSO (typically 20 mm thick) arranged in full or partial rings about the patient. Full-ring NaI(Tl) systems are currently being built with an axial extent of 25 cm. Because the NaI(Tl) system use continuous detectors, the axial sampling is determined by the intrinsic spatial resolution of the system and the choice in how the data are collected. These systems typically sort the data into 128 axial image planes (2 mm thick) for brain studies, and 64 axial planes (4 mm thick) for whole-body studies. These full-ring NaI(Tl) systems are operated exclusively in positron volume imaging (PVI) mode (also known as 3D mode) to achieve better sensitivity [Lewellen & Karp, 2004; Bailey, 2005].

Full-ring discrete crystal systems currently all use BGO, LSO, or GSO. Some common block sizes include 6×6 arrays of 4×8×30 mm^3 BGO crystals (GE Advance) or 6.25×6.25×30 mm^3 BGO crystals (GE Discovery ST) and 8×8 arrays of 6.75×6.75×20 mm^3 BGO crystals (Siemens/CTI EXACT) or 4.5×4.8×30 mm^3 BGO crystals (EXACT HR^+). In addition, the ECAT ACCEL uses an 8×8 array of 6.75×6.75×25 mm^3 LSO crystals. The Phillips Allegro uses 4×6×20 mm^3 GSO crystals assembled in 28 modules that are optically coupled to one another and viewed by a hexagonal array of PMTs.

BGO and LSO systems have ring diameters of 80 to 90 cm and are equipped with removable axial collimators (septa), allowing the systems to operate in either 2D or 3D mode [Gunter, 2004]. The GSO systems do not include axial collimators and only operate in 3D mode, as do the NaI(Tl) scanners. Discrete BGO and LSO systems are also available in partial-ring designs, the Siemens/CTI ECAT ART (BGO) and EMERGE (LSO). Because block detectors generally use smaller PMTs than the continuous crystal designs, they are more expensive (due to the increased number of PMTs and electronic channels). In an effort to reduce the cost of these systems, partial-ring designs were developed. These machines essentially take a portion of the blocks used in a full-ring system and mount them on a rotating plate. Current designs use blocks with 8×8 arrays of 6.75×6.75×20 mm^3 (BGO) or 6.75×6.75×25 mm^3 (LSO) crystals. A typical arrangement uses 66 blocks arranged with three blocks in the axial direction providing 24 partial rings of crystals and an axial extent of 16.2 cm. The ring diameters are 82.5 cm. To compensate for the loss of sensitivity from only using partial rings of detectors, these systems operate only in PVI mode.

2.4 Performance of PET Systems

To objectively compare the performance of different clinical PET systems, the National Electrical Manufacturers Association (NEMA) has developed guidelines on how certain performance parameters should be obtained. These guidelines allow a user, in the process of selecting a PET system, to obtain a relatively unbiased comparison of system parameters. The NEMA NU2-2001 (last update) takes some of these shortcomings into account and adds an image quality measurement appropriate for whole-body imaging [Association, 2001].

Several parameters associated with the scanner are critical to good quality image formation, which include spatial resolution, sensitivity, noise equivalent count rate and scatter fraction. Comparation of these parameters for different comercial PET scanners can be found in these references: [Tarantola *et al.* , 2003; Saha, 2005].

2.4.1 Spatial Resolution and Depth Of Interaction (DOI)

The spatial resolution of a system represents its ability to distinguish between two point sources in an image, i.e., it corresponds to the shortest distance these point sources can be placed at so they will be identified in the image as two separated sources.

As discussed in section 2.1.2 an ultimate resolution limit can be achieved in PET due to the physics of the positron decay. The noncolinearity related blurring for a 80 cm diameter whole-body PET scanner is about 2 mm, but for a 12 cm diameter small animal PET scanner this reduces to 0.3 mm [Zanzonico, 2004]. In a PET camera with 3 mm system resolution, the loss of spatial resolution due to the positron distance of flight accounts for 1.3% in bone and 3.5% in soft tissue but up to 22.5% in lung tissue for ^{18}F. The corresponding values are, respectively, 2.9%, 9.3% and 45.0% for ^{11}C and 37.9%, 68.9% and 167% for ^{82}Rb, which has a much higher positron range [Sanchez-Crespo & Larsson, 2006].

In addition to this limit, the design and properties of the detector used in the PET scanner, and the system geometry, will also contribute to the final image resolution. The intrinsic detector resolution can be divided into two main components: geometric and physical. The geometric component can be seen as the best possible resolution that can be attained for a particular design using a scintillation material with ideal detection properties (100% detection efficiency). The physical component is caused by nonideal properties of the detectors (e.g., detector scatter, light sharing, cross-talk, and so on). Comparison of the FWHM of the coincidence response function for discrete and continuous detectors can be found, for example, in [Cherry & Dahlbom, 2006].

Another important factor that should be taken into account is the depth at which each photon interacts with the crystal, named depth of interaction effect (DOI), or parallax error, Figure 2.10. This effect is due to the finite distance a photon travels within a crystal before depositing all of its energy. For a source located at the centre of the scanner and a discrete detector, the intrinsic spatial resolution is essentially determined by the width of the detector element, d : $FWHM_{det} = \frac{d}{2}$. However, for a source in a location with an offset from the centre of the FOV, the apparent width of the detector increases. The result is a decrease of the spatial resolution along the radial direction, as

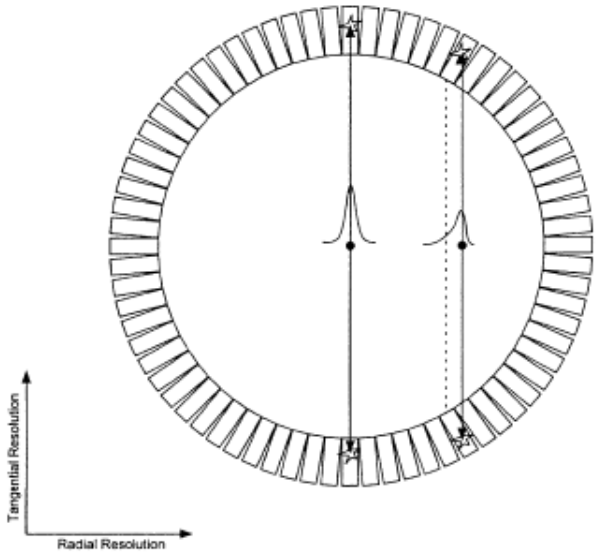

Figure 2.10: In a ring geometry scanner, the point spread function becomes asymmetrical with increasing radial offsets due to detector penetration and the lack of information regarding the depth of interaction within the crystal. The result is a degrading spatial resolution and mispositioning of events towards the center of the FOV. The severity of these effects depends on detector ring diameter, detector depth, and the detector material. Adapted from [Cherry & Dahlbom, 2006].

one moves away from the centre to the borders of the FOV. For a whole-body PET scanner with 4 mm wide detectors and a diameter of 80 cm, the DOI effect contributes to a 40% degradation of the resolution at a distance of 10 cm from the center of the FOV. A thin crystal with a high stopping power will contribute for the reduction of the distance traveled by the photon inside the detector and, therefore, to the reduction of the parallax effect. It should also be noted that the DOI effect depends on the scanner geometry, being different for a ring, hexagonal or octagonal system. One possible strategy to deal with the DOI effect is to use the phoswich detector method that involves stacking thin layers of different detector materials with different decay times. The signal decay time may then used to identify the layer in which the interaction took place.

In 1993, Derenzo and Moses have developed a parameterized expression that relates the relative contribution of each of these factors to the observed spatial resolution. Spatial resolution in PET imaging systems is characterized as the FWHM of a profile that runs through the center of a point or perpendicular to a line source image. The parameterized expression of PET spatial resolution is described by Equation 2.12:

$$FWHM = \alpha \left[\left(\frac{d}{2} \right)^2 + b^2 + (0.0022D)^2 + r^2 \right]^{\frac{1}{2}} \tag{2.12}$$

The first term inside the square brackets is related to the geometry of the individual detector crystals, where d is the dimension of the square face of a crystal. In most PET scanners the size of the crystal is a dominant component of the achievable spatial resolution. The term b, represents the uncertainty associated with identifying individual crystals with secondary detection devices such as PMTs. This factor typically contributes only a fraction of a millimeter to the spatial resolution. The

term $\left[(0.0022D)^2\right]$ describes the noncolinearity of the 511 keV photons. The spatial resolution degradation caused by noncolinearity is dependent on the spacing between the detectors, D, which are operated in coincidence. The last term, r^2, relates to the effective size of the object, which includes the positron range factors discussed above. Finally, the multiplicative factor accounts for resolution degradation that occurs in the image reconstruction process: for conventional filtered backprojection reconstruction algorithms this term is typically set to $\alpha = 1.2$ [Derenzo *et al.* , 1993].

Spatial resolution affects the level of detail that can be visualized in an image and limits the size of structures for which accurate quantification of radionuclide concentrations can be achieved. If an object is smaller (in any dimension) than approximately $2.5 \times FWHM$ spatial resolution of the PET scanner, a distortion called partial volume effect (PV) occurs. This term describes the condition in which the cross-sectional area of the object being imaged is smaller than that of the sensitive region of the detector pairs used to detect the 511 keV annihilation photons [Bailey, 2003, 2005].

2.4.2 System Sensitivity

The system sensitivity is the efficiency with which the PET scanner detects a coincidence event when a radionuclide located in the FOV of the scanner emits a positron. System sensitivity is defined as the number of events (in counts per second) detected per unit of radioactive concentration (cps/Bq/mL) in a source. It is sometimes also expressed as the fraction of radioactive decays that produce a valid coincidence event (cps/Bq). The system sensitivity is a product of several factors, which include the efficiency of the detectors at 511 keV, the solid angle coverage of the detectors, the location of the radioactivity with respect to the detectors, and the timing and energy windows applied to the data.

The detection efficiency, ε, of an individual detector is given by the product of the detection probability of the incoming photon in the detector volume and the fraction of these events, Φ, that fall within the selected energy window (typically set at 350 - 650 keV). The energy window helps to reduce the influence of scattered events by only accepting events that deposit energy close to 511 keV. The efficiency is given by Equation 2.13:

$$\varepsilon = \left(1 - \varepsilon^{-\mu d}\right) \times \Phi \tag{2.13}$$

where μ is the attenuation coefficient of the detector material (table 2.3), and d is the thickness of the detector. A valid event requires that both photons be detected in opposing detectors and be within the appropriate energy range. The coincidence detection efficiency, ε^2, is, therefore, given by the square of Equation 2.13.

The scanner geometry establishes the total solid angle covered by the scanner over its FOV. For a ring scanner with diameter D and detectors whose thickness is h, if the small interdetectors area is ignored, the geometric efficiency decreases linearly from approximately d/D, at the centre of the scanner, to 0, at its borders, resulting in an average geometry efficiency given by $d/2D$ [Cherry *et al.* , 2003a]. So, small diameter scanners with a large extension in the axial direction usually have higher sensitivities.

For a point source located at the centre of the FOV, PET systems sensitivities range from 0.2% to 0.5% (0.002 to 0.005 cps/Bq) in 2D mode, to 2% to 10% (0.02 to 0.10 cps/Bq) in fully 3D mode [Cherry *et al.* , 2003a; Bailey, 2005, 2003].

2.4.3 Noise Equivalent Count (NEC)

3D mode greatly improves the sensitivity for any scanner design, but it comes at the cost of nonuniform axial sensitivity, increased scatter fraction, and increased impact of activity outside the FOV. One measurement that has been used to give some insight into the quality of the primary data is the noise equivalent count rate (NEC) [Strother *et al.* , 1990]. Although this metric does not directly relate to final image quality, it does demonstrate the impact of dead time, randoms rates, and scatter on the overall ability of the scanner to measure the true events count rate. Generally, the NEC is defined as:

$$NEC = \frac{T^2}{T + S + kR} \tag{2.14}$$

where T is the trues count rate, S the scatter count rate, R the randoms count rate, and k is a factor that depends on the method used for randoms correction. In general, the real-time subtraction of randoms leads to the largest variances thus $k = 2$ is often used for real-time subtraction, whereas $k = 1$ is used when the randoms have first been smoothed before subtraction.

The randoms and scatter rates are given by:

$$R = R_T - \frac{T}{1 - SF} \tag{2.15}$$

$$S = \frac{SF}{1 - SF} \times T \tag{2.16}$$

where SF is the intrinsic scatter fraction and R_T is the total count rate. For 3D scanners, since the trues and scatter count rates are proportional to the activity, while the randoms count rate is proportional to the square of the activity, there exists an optimum activity for each scanner that corresponds to the maximum of the NEC [Zanzonico, 2004; Defrise & Kinahan, 1998; Bailey, 2005, 2003].

2.4.4 Scatter Fraction (SF)

The scatter fraction (SF) is often used to compare the performances of different PET scanners. It is given by:

$$SF = \frac{S}{R_T} \tag{2.17}$$

where S and R_T are e scattered and prompt count rates, as previously stated. The lower the SF value, the better the performance of a scanner and better the quality of images. Comparative SF

values for different PET scanners can be found in [Tarantola *et al.* , 2003; Saha, 2005; Bailey *et al.* , 2005; Bailey, 2003].

2.5 Data Representation and Corrections

The projection data acquired in the form of sinograms are affected by a number of factors, namely variations in detector efficiencies between detector pairs, random coincidences, scattered coincidences, photon attenuation, dead time, and parallax error (also called radial elogation or DOI, section 2.4.1). Each of these factors contributes to the sinogram to a varying degree depending on the 2D or 3D acquisition. A large number of methodologies to correct these sources of error, their relative merits and impact on the quantitative accuracy of PET images, can be found in [Cherry *et al.* , 2003a; Cherry & Dahlbom, 2006; Meikle & Badawi, 2003, 2005; Lewellen & Karp, 2004].

2.5.1 Organizing the Data

A LOR in a cylindrical PET scanner may be specified in a set of four coordinates (s, ϕ, z, θ), where s is the transaxial distance from the LOR to the scanner axis, ϕ is the azimuthal angle of the LOR, θ measures the axial distance between the points intersected by the scanner and z measures the axial distance relative to the scanner mid-plane. Figure 2.11 shows a graphical interpretation of the LOR coordinates.

Consider a simple PET system scanning an object with a 2D distribution of radioactivity denoted by $f(x,y)$: the raw data, which consists of the detection of annihilation photon pairs, usually is histogrammed into a 2D matrix, where each element in the matrix corresponds to the number of events recorded by a particular pair of detectors (or along a specific LOR). The matrix is arranged such that each row represents parallel line integrals or a projection of the activity at a particular angle, ϕ. Each column represents the radial offset from the center of the scanner, s. The relationship that relates which elements in this matrix (s,ϕ) record data from radioactivity in the object at location (x,y) is given by:

$$s = x\cos\phi + y\sin\phi \tag{2.18}$$

This 2D matrix (s,ϕ) is known as a sinogram (or histogram) because a point source at a location (x,y) traces a sinusoidal path in the matrix as given by Equation 2.18. This is represented in Figure 2.12. The LORs that cross a point source not centered in the FOV describe a sinusoidal curve on the sinogram, whereas a point source located in the center of the FOV corresponds to a straight line in the sinogram [Bailey, 1998; Lewitt & Matej, 2003].

The sinograms described above correspond either to LORs contained in a same detector ring, in which case the sinogram is called a direct sinogram, or to LORs in two different detector rings. In this later case, the sinogram is known as an oblique sinogram. For a scanner of N detector rings, there are N direct sinograms and $N(N-1)$ oblique sinograms, for a total of N^2 sinograms. Depending on the ring difference associated with a sinogram, the sinogram is said to belong to

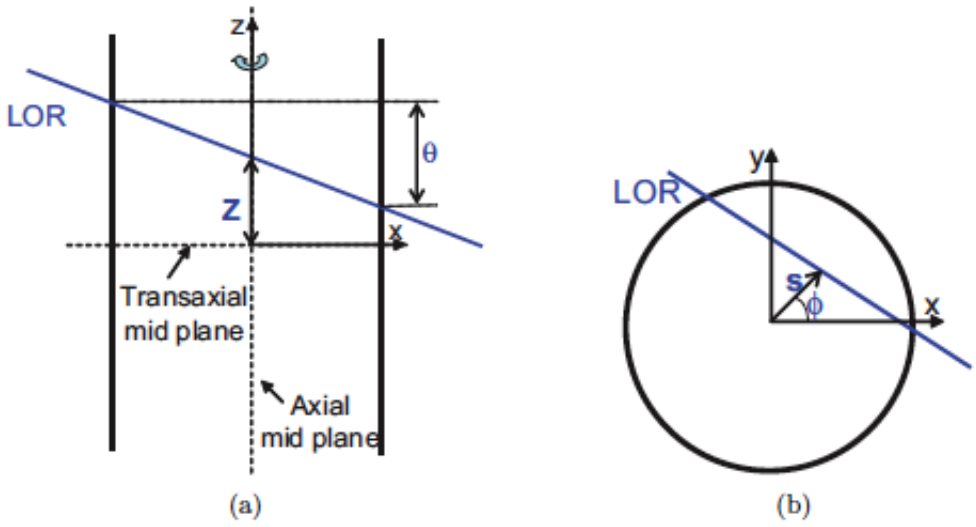

Figure 2.11: Representation of the coordinates of the Lines of Response in a 3D Sinogram. (a): view of a LOR in a plane parallel to the scanner rotation axis. (b): view of a LOR projected into the transaxial plane. Adapted from [Jacobson M. & G., 2000].

a given segment. The segment of a sinogram is indexed by the LOR coordinate θ. A segment is a set of sinograms with a given average ring difference, $ringB - ringA$. For instance, a direct sinogram belongs to segment 0, while LORs between ring 1 and ring 4 belong to segment 3 and LORs between ring 4 and ring 1 belong to segment -3.

In 3D PET, the projections are two-dimensional (x_r, y_r) parallel line-integrals with azimuthal angle ϕ and oblique, or polar, angle θ. The full set of 3D projection data are then represented as a set of sinograms, with one sinogram per polar angle θ. In each sinogram, each row represents the projected intensity across a single oblique plane (at polar angle θ) and each column the projected intensity at the same position across the projection at successive azimuthal angles ϕ. A complete 3D sinogram of a scanner with N detector rings contains $2N-1$ segments: one direct segment plus $N-1$ positive oblique segments plus $N-1$ negative oblique segments.

A more general data format than sinograms is named the list mode format (LMF). In the LMF, the activated detector coordinates, along with other kind of information such as the deposited energy or a time stamp, are stored sequentially as the photons are detected. The data can then be binned to the histogram mode and reconstructed with the conventional algorithms that will be presented in the following sections. Alternatively, iterative statistical algorithms that were developed for list mode data can be used-

2.5.2 Data Normalization

PET scanners can have 10.000 to 20.000 detectors arranged in blocks and coupled to several hundred PMTs. Because of the variations in the gain of PMTs, location of the detector in the block, and the physical variation of the detector, the detection sensitivity of a detector pair varies from pair to pair, resulting in nonuniformity count rates. The method of correcting for this effect is termed

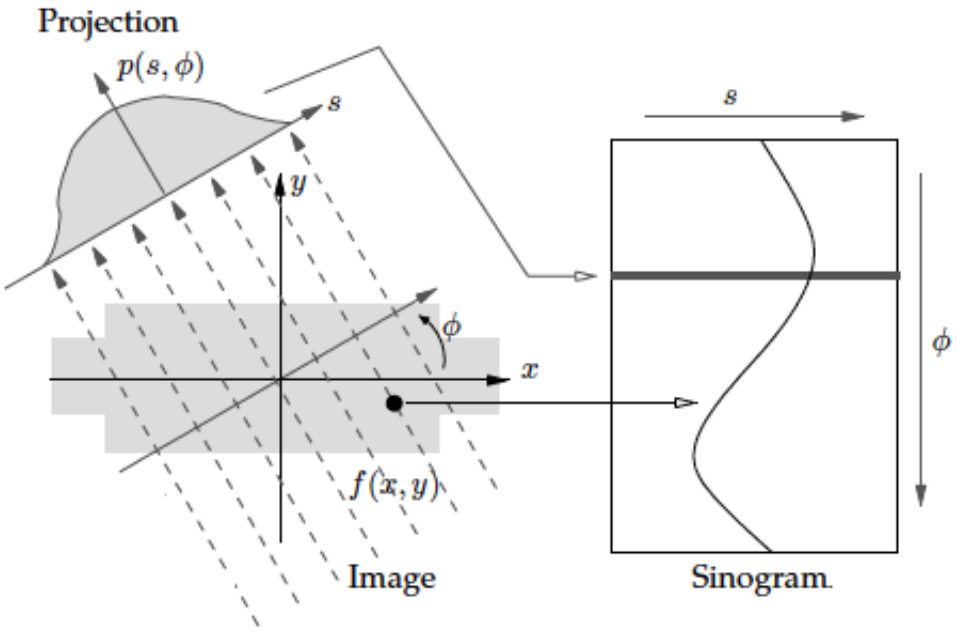

Figure 2.12: A parallel projection, for a particular angle ϕ, of an object corresponds to a row in the sinogram.

the normalization. Normalization of the acquired data is accomplished by exposing uniformly all detector pairs to a 511 keV photon source (e.g., ^{68}Ge source with a very uniform activity concentration to grant a uniform exposure of all LORs), without a subject in the FOV. Data are collected for all detector pairs in both 2D and 3D modes, and normalization factors are calculated for each pair by dividing the average of counts of all LORs by the individual detector pair count. Thus, the normalization factor F_i for each LOR is calculated as:

$$F_i = \frac{A_{mean}}{A_i} \tag{2.19}$$

where A_{mean} is the average coincidence counts for all LORs in the plane and A_i the counts in the ith LOR. The normalization factor is then applied to each detector pair data in the acquisition sinogram of the patient as follows:

$$C_{norm,i} = C_i \times F_i \tag{2.20}$$

where C_i is the measured counts and $C_{norm,i}$ is the normalized counts in ith LOR in the patient scan. This method is known as direct normalization.

A problem with this method is the long duration (~6 hours) of counting required for meaningful statistical accuracy of the counts in the blank scan, and hence overnight counting is carried out. Otherwise, the resultant normalization coefficients will be biased: since the amount of scatter and its distribution in the normalization scan may be very different from that associated with a regular emission scan, this can result in bias and artifacts [Cherry *et al.* , 2003a; Zanzonico, 2004; Townsend & Bendriem, 1998; Bailey, 1998].

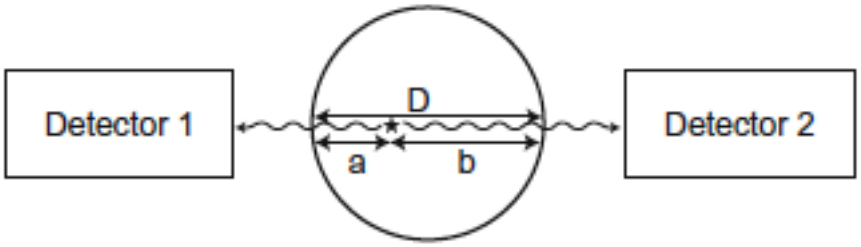

Figure 2.13: Two 511 keV photons detected by two detectors after traversing different tissue thicknesses a and b. Attenuation is independent of location of annihilation, and depends on the total dimension of the body. Adapetd from [Saha, 2005].

A different approach is to split the normalization into different components and treat each one of them separately: the so-called component-based model for normalization [Badawi & Marsden, 1999; Casey *et al.* , 1995]. The central idea is to express the normalization coefficients as a product of factors associated with the effects normalization should account for. Detailed models based on this principle can be found in the following references: [Badawi & Marsden, 1999; Badawi *et al.* , 2000; Ferreira, 2001; Ollinger, 1995; Bailey, 1998; Meikle & Badawi, 2003, 2005].

2.5.3 Photon Attenuation

The 511keV annihilation photons originating from different locations in the body are attenuated by tissue, as they traverse different thicknesses to reach the detector pair in coincidence, as discussed earlier in section 2.1.3.3. Attenuation of the signal from a given LOR can be corrected either by a direct measurement or using a mathematical model or a combination of the two.

Consider a point source located at an unknown depth in a uniformly attenuating medium: if μ is the linear attenuation coefficient of 511keV photons in the tissue, and a and b are the tissue thicknesses traversed by the two 511 keV photons along the LOR (Figure 2.13), then the probability P of a coincidence detection is given by:

$$P = e^{-\mu a} \times e^{-\mu b} = e^{-\mu(a+b)} = e^{-\mu D} \tag{2.21}$$

where D is the total thickness of the body. Equation 2.21 is applicable to organs or tissues of uniform density.

When photons travel through different organs or tissues with different μ values, then Equation 2.21 becomes:

$$P = e^{-\sum_{i=0}^{n} \mu_i D_i} \tag{2.22}$$

where μ_i and D_i are the linear attenuation coefficient and thickness of ith organ or tissue, and n is the number of organs or tissues the photon travels through. Photon attenuation causes nonuniformities in the images, because of the loss of relatively more coincidence events from the central tissues

than the peripheral tissues of an organ and also because the two photons may transverse different organs along the LOR. The probability P is the attenuation correction factor, which is independent of the location of positron annihilation and depends on the total thickness of the tissue. If an external radiation passes through the body, the attenuation of the radiation will be determined by the attenuation coefficient μ and the thickness of the body, as expressed by Equation 2.21.

The most accurate method to determine the attenuation correction is through direct measurements. As was shown in Equations 2.21 and 2.22, the amount of attenuation is independent of the location of the source. This means that if a source is placed outside the object along the LOR of interest, the amount of attenuation would be the same as for a source inside the object. Therefore, by placing a positron emitting source outside the object, the amount of attenuation can be measured directly. In measured attenuation correction, either a set of ring sources, or a set of rotating rod sources, is placed just inside the detectors, enabling the attenuation factors for all LORs in the scanner to be measured in a single scan. Initially, a reference or a blank scan (without the patient in the scanner) is measured, in which data from these external sources are acquired with no object in the scanner. Then the object is placed in the scanner, and a transmission scan is acquired. The attenuation correction factors (ACFs) for each LOR are simply given by taking the ratio between the blank sinograms and the transmission sinograms:

$$ACF_i = \frac{Blanck_i}{Trans_i} \tag{2.23}$$

where $Blanck_i$ and $Trans_i$ are the counts in the blank and transmission scans for LOR i. The normalized emission sinogram is multiplied by these factors to obtain attenuation corrected sinograms [Cherry *et al.* , 2003a; Zanzonico, 2004; Townsend & Bendriem, 1998; Bailey, 1998].

The transmission scan can be acquired before the patient has been injected with the radiopharmaceutical, after the patient has been injected with the radiopharmaceutical but before or after the emission scan, or after the patient has been injected with the radiopharmaceutical and at the same time as the emission scan. Pre-injection transmission scanning avoids any interferences between the emission and transmission data but requires that the patient remain on the imaging table before, during, and after injection of the radiotracer. It is the least efficient operationally and is rarely used in practice. Postinjection transmission scanning minimizes the effects of patient motion, relying on the much higher external source count rates for reliable subtraction of the emission counts from the transmission counts. It is probably the most commonly used approach in PET scanners. Simultaneous emission/transmission scanning is obviously the most efficient (fastest) approach but may result in excessively high randoms and scatter counter rates in the emission data [Cherry & Dahlbom, 2006; Zanzonico, 2004; Saha, 2005; Zaidi & Hasegawa, 2006b].

In order to obtain the transmission scans referred above there are three types of sources that can be used: positron sources, γ-ray sources and X-ray sources. The usual positron source for transmission scans is the ^{68}Ge source ($t_{1/2} = 287 days$). One advantage is the possibility to reject random or scattered events, based on the knowledge of the source location (named triple-point method or sinogram windowing). The main difficulty in these transmission scans is to collect an adequate number of counts along each attenuated LOR. The most common method to process the transmission data is to apply a spatial smoothing filter to the blank and transmission scans prior to

computing the attenuation correction [Kinahan *et al.* , 2003; Meikle & Badawi, 2003, 2005; Zaidi & Hasegawa, 2006b]. In the group of γ- ray sources, ^{137}Cs ($t_{1/2} = 30 years$) is the most used. For equal activity sources, ^{68}Ge results in much lower count rates and longer transmission scan times than ^{137}Cs because coincidence counting of the ^{68}Ge results in rejection of most of its annihilations. In addition, ^{137}Cs has a much longer half-life than ^{68}Ge, and therefore a ^{137}Cs transmission source does not have to be replaced while a ^{68}Ge source must be replaced periodically. At the same time, the energy of the ^{137}Cs, 662 keV, is significantly higher than the 511 keV annihilation rays and there is less interference of a ^{137}Cs transmission scan by activity in the patient. As a result, transmission scans can be acquired more quickly since the counting statistics requirements are considerably less than for reliable subtraction of equal energy transmission and emission counts. However, because of the difference in energies, 662 keV versus 511 keV, the attenuation correction factors derived from a ^{137}Cs transmission scan must be scaled slightly to adjust for the differential attenuation between 662 KeV and 511 keV [Kinahan *et al.* , 2003]. The third possible type of transmission sources are X-ray sources. Among the advantages of this last type is a low statistical noise and a fast acquisition; as disadvantage, there is the need to convert the measured attenuation coefficients into the appropriate values for 511 keV [Kinahan *et al.* , 2003]. A summary of transmission sources for different PET scanners can be found in [Saha, 2005; Tarantola *et al.* , 2003].

In alternative to the transmission approach, there is also the possibility of using CT reconstructed images of the object and proceed with a conversion method (such as segmentation or scaling), to convert the Hounsfield units into attenuation correction factors [Kinahan *et al.* , 2003; Meikle & Badawi, 2003, 2005].

2.5.4 Scatter Correction

Scatter results in generally diffuse background counts in reconstructed PET images, reducing contrast and distorting the relationship between image intensity and activity concentration.

The use of scatter correction is especially important since the fraction of scattered events in PET is usually very high, especially in 3D mode: for a scan of the abdomen, it can be 60% to 70% [Cherry *et al.* , 2003a; Zanzonico, 2004; Townsend & Bendriem, 1998; Zaidi & Koral, 2006].

The scatter contribution increases with the density and depth of the body tissue, the density of the detector material, the activity in the patient, and the window width of pulse height analyzer for the PET system. Since both scattered and true coincidence rates vary linearly with the administered activity, the scatter-to-true ratio does not change with the activity. Also, this ratio does not change with the width of the time window, because scatter events arise from the same annihilation event and the two similar photons arrive at the two detectors almost at the same time. The pulse height window cuts off a large fraction of the scattered radiations, which is limited by the width of the window.

In 2D acquisition, the use of septa in multiring PET systems removes additional scattered events, whereas in 3D acquisition, they become problematic because of the absence of septa. Typically, the scatter fraction ranges from 10% in 2D mode to more than 30% to 40% in 3D mode in modern PET scanners [Cherry *et al.* , 2003a; Townsend & Bendriem, 1998]. In practice, the correction for

scatter is made by taking the counts just outside the FOV, where no true coincidence counts are expected. The outside counts contain both random and scatter events. After subtracting random counts, the scatter counts are subtracted from the prompt counts across the field of view to give true coincidence counts.This assumes that scattering is uniform throughout the FOV. Other approaches for quantitative scatter corrections are being considered, such as dual energy window (based on scatter correction techniques developed originally for SPECT) and simulation methods [Cherry & Dahlbom, 2006; Zaidi & Koral, 2006; Bailey, 1998; Meikle & Badawi, 2003, 2005].

2.5.5 Random Coincidences

Coincidence prompt counts include random or accidental coincidences that raise the background on the images. They increase with increasing width of the energy window as well as the coincidence timing window, and with increasing activity (varies as the square of activity, see Equation 2.11 in section 2.3.2). Random events add to the background causing artifacts and loss of image contrast and are more problematic in low efficiency detectors such as thin NaI(Tl) crystals and in 3D acquisition.

Efforts have been made to minimize random events by using the faster electronics and shorter time window, e.g.: BGO system (12 ns), GSO and NaI(Tl) systems (8 ns) and LSO system (6 ns). Still, further corrections are needed to improve the image contrast.

Two main approaches correct random or accidental coincidences in PET. A common method of correcting for random events is to employ two coincidence circuits: one with the standard time window (e.g., 6 ns for LSO) and another with a delayed time window (e.g., 50 to 56 ns) using the same energy window.The counts in the standard time window include both the randoms plus trues, whereas the delayed time window represents the randoms. For a given source, the random events in both time windows are the same within statistical variations. Thus, correction for random coincidences is made by subtracting the delayed window counts from the standard window counts [Cherry *et al.* , 2003a; Zanzonico, 2004; Townsend & Bendriem, 1998; Meikle & Badawi, 2003, 2005].

The random counting rate can be estimated from the singles counting rate for a given detector pair and coincidence time window, was shown in Equation 2.11. In theory, the number of random events for every detector pair in the scanner can be estimated and subtracted. To implement this singles method, one would need a data acquisition system that can, in addition to recording coincidences, also accurately monitor the singles rate for each detector element. In addition, the coincidence time window needs to be accurately known for each detector pair.

In both methods, the correction for randoms is not a correction on an event-by-event basis, because a random event is indistinguishable from a true event for the coincidence circuit. This leads to an increase in the statistical uncertainty of the true coincidence rate [Cherry & Dahlbom, 2006]. An overview of variance reduction methods is given in [Brasse *et al.* , 2005].

2.5.6 Dead Time

When a 511keV photon interacts within the detector and is absorbed in the crystal, light photons are produced, which strike the photocathode of the PMT. A pulse is generated at the end of the PMT and amplified by an amplifier; the energy and the spatial position of the photon are determined and finally a count is recorded. When two such events are detected by two detectors in the time window, a coincidence event is recorded. The total time required to complete the above steps is defined as the dead time, τ, and during this time the detection system is unable to process a second event, which will be lost. This loss (called the dead-time loss) is a serious problem at high count rates and varies with different PET systems.

It is obvious that the dead-time loss can be reduced by using detectors with shorter scintillation decay time and faster electronics components in the PET scanners. In scintillation counting, two 511 keV photons may arrive at and be absorbed completely in the detector simultaneously and, therefore, a photopeak of 1.022 MeV will be produced, which will fall outside the energy window of 511 keV photopeak. If, however, two Compton scattered photons are summed up simultaneously in the detector and the resultant peak falls within the window, then the event will be counted but be mispositioned because of the two unrelated events.These events are called the pulse pile-ups, which can cause image distortion at high count rates. Multiple coincidences do also contribute to dead time, because the impossibility to ascertain which is the correct coincidence pair forces the rejection of all the events [Cherry *et al.* , 2003a; Zanzonico, 2004; Townsend & Bendriem, 1998; Meikle & Badawi, 2003, 2005].

Dead time correction is made by empirical measurement of observed count rates as a function of increasing concentrations of activity. From these data, the dead time is calculated and a correction is applied to compensate for the dead-time loss. Various techniques such as use of buffers, in which overlapping events are held off during the dead time, use of pulse pile-up rejection circuits, and use of high-speed electronics, have been applied to improve the dead time correction [Cherry *et al.* , 2003a; Meikle & Badawi, 2003, 2005].

2.5.7 Partial Volume Effect

In PET imaging, the reconstructed images should depict the radiotracer distribution uniformly and accurately throughout the field of view. However, because of the limit of the spatial resolution of current PET scanners, “hot” spots (structures) relative to a “cold” background that are smaller than twice the resolution of the scanner show partial loss of intensity, and the activity around the structure appears to be smeared over a larger area than it occupies in the reconstructed image. While the total counts are preserved, the object appears to be larger and to have a lower activity concentration than it actually has. Similarly, a cold spot relative to a hot background would appear smaller with high activity concentration. Such underestimation and overestimation of activities around smaller structures in the reconstructed images is called the partial-volume effect, and this reduces the contrast between high and low uptake regions. However, this effect also contains the so-called spillover effect due to contamination of activity from the neighboring tissues to these hot or cold areas. This is of particular importance in the quantitative characterization of small lesions or structures.

A correction factor, called the recovery coefficient (RC), is the ratio of the reconstructed count density to the true count density of the region of interest (ROI) that is smaller than twice the spatial resolution of the system. The RC is determined by measuring the count density of different objects containing the same activity but with sizes larger as well as smaller than the spatial resolution of the system. Normally, the RCs would be 1 for larger objects [Saha, 2005; Cherry & Dahlbom, 2006]. These RC values are then applied to the images of small structures for partial volume corrections. However, the sizes of the *in vivo* structures are not precisely known, and so the phantom RC data may not be accurate for these structures. Other methods using point-spread functions of the activity distribution around the object have been investigated with limited success [Rousset & Zaidi, 2006; Saha, 2005; Meikle & Badawi, 2003].

2.6 Image Reconstruction in PET

The goal of image reconstruction is to provide quantitatively accurate cross-sectional images of the distribution of positron-emitting radiopharmaceuticals in the object that is being scanned, using the externally detected radiation along with the mathematical algorithms of computed tomography. A review about some of the methods used can be found in [Defrise & Gullberg, 2006; Zeng, 2001]

A PET scan consists of the detection of a large number of pairs of annihilation photons (typically 10^6 to 10^8). During the course of the PET scan, the total number of counts measured by a particular detector pair will be proportional to the integrated radioctivity along the line joining the two detectors. This data are commonly referred to as line integral data. The role of image reconstruction is to convert the line integrals measured at many different angles around the object into a 2D image that quantitatively reflects the distribution of positron-emitting atoms (and, therefore, the molecule to which it is attached) in a slice through the object parallel to the detector plane.

There are two basic approaches to image reconstruction. One approach is analytic in nature and utilizes the mathematics of computed tomography that relates line integral measurements to the activity distribution in the object. These algorithms have a variety of names, including Fourier reconstruction and filtered backprojection (FBP). The second approach is to use iterative methods that model the data collection process in a PET scanner and attempt, in a series of successive iterations, to find the image that is most consistent with the measured data.

2.6.1 Analytical Reconstruction Methods

2.6.1.1 Backprojection

In 2D acquisition, activity in a given line of response in a sinogram is the sum of all activities detected by a detector pair along the line through the depth of the object. The principle of backprojection is employed to reconstruct the images from these acquired LORs. A reconstruction matrix of a definite size (e.g., 128×128 pixels) is chosen. An image pixel in (x, y) position is related to polar coordinates in the sinogram data, section 2.5.1 (Equation 2.18). The measured counts in the projection sinogram corresponding to the calculated s are added to the (x, y) pixel in the reconstruction

matrix. This is repeated for all projection angles. Thus, the backprojected image pixel $A'(x, y)$ in the reconstruction matrix is given by:

$$A'(x, y) = \frac{1}{N}\sum_{N=1}^{N} p(s, \phi) = \frac{1}{N}\sum_{N=1}^{N} p(x\cos\phi + y\sin\phi, \phi) \tag{2.24}$$

where $p(s, \phi)$ is the count density in the sinogram element in the acquired matrix, and N is the number of projection angles.When all pixels are computed, a reconstructed image results from this simple backprojection. In another approach of simple backprojection, in the reconstruction matrix of chosen size, the counts along an LOR in a sinogram detected by a detector pair are projected back along the line from which they originated. The process is repeated for all LORs. Thus, the counts from each subsequent LOR are added to the counts of the preceding backprojected data, resulting in a backprojected image of the original object.

Simple backprojection of the data does result in an image that resembles the true distribution of radioactivity in the object, but it is only an approximation, hence the designation $A'(x, y)$. Backprojection places counts outside the boundaries of the object which is clearly incorrect, and for any complex object, it is readily apparent that backprojection will result in a blurred representation of the object because counts are distributed equally along the line from which they originated. The blurring in backprojection is proportional to $\frac{1}{s}$, where s is the distance from the source. Mathematically, it can be shown that the relationship between the backprojected image $A'(x, y)$ and the true activity distribution $A(x, y)$ is given as:

$$A'(x, y) = A(x, y) \otimes \frac{1}{s} \tag{2.25}$$

where $\otimes$ denotes the operation of convolution [Tsui & Frey, 2006; Kinahan *et al.* , 2004; Defrise *et al.* , 2005].

2.6.1.2 Direct Fourier Reconstruction and Filtered Backprojection (FBP)

The blurring effect, described in previous section, is minimized by applying a filter to the acquisition data, and filtered projection data are then backprojected to produce an image that is more representative of the original object. Such methods are called the filtered backprojection, and are accomplished by the Fourier method or projection slice theorem (sometimes also known as the central section theorem).

According to the Fourier method, the measured projection data $p(s, \phi)$ in a sinogram is related to the count density distribution $A(x, y)$ in the object by the Fourier transformation. The projection data obtained in the spatial domain can be expressed in terms of a Fourier series in the frequency domain as the sum of a series of sinusoidal waves of different amplitudes, spatial frequencies and phase shifts running across the image. This conversion of data from spatial domain to frequency domain is called the Fourier transformation. Similarly the reverse operation of converting the data from frequency domain to spatial domain is termed the inverse Fourier transformation. In the Fourier method of backprojection, the projection data in each profile are subjected to the Fourier transformation from spatial domain to frequency domain, which is symbolically expressed as:

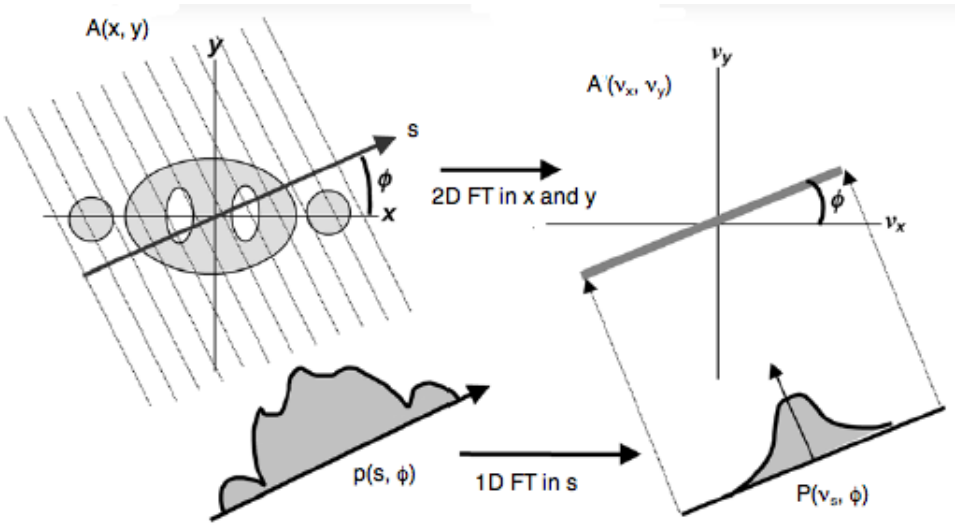

Figure 2.14: The projection slice theorem. Adapted from [Cherry & Dahlbom, 2006].

$$F(\nu_x, \nu_y) = \mathscr{F} f(x, y) \tag{2.26}$$

where $F(\nu_x, \nu_y)$ is the Fourier transform of $f(x, y)$ and $\mathscr{F}$ denotes the Fourier transformation. In essence, the Fourier transform $F(x_\nu, y_\nu)$ of each row in the sinogram of the 2D projection data is taken and added together. Figure 2.14 illustrates an example of the projection slice theorem: the1D Fourier transform (FT) of a projection at angle ϕ is equal to the 2D Fourier transform of the image evaluated along a radial profile at angle ϕ with respect to the x-axis, which can be written as:

$$P(\nu_s, \phi) = A(\nu_x, \nu_y)_{|\, \nu_x = \nu_s \cos\phi,\, \nu_y = \nu_s \sin\phi} \tag{2.27}$$

where $P(\nu_s, \phi)$ is the 1D Fourier transform of $p(s, \phi)$ with respect to s, and $A(\nu_x, \nu_y)$ is the 2D Fourier transform of the activity distribution $A(x, y)$ which is the quantity desired to reconstruct in the image.

A more elegant approach, named filtered backprojection (FBP), to reconstruction can be achieved by reformulating Equation 2.26 in the spatial rather than frequency domain. The result is:

$$F'(\nu) = H(\nu) \bullet F(\nu) \tag{2.28}$$

where $F'(\nu)$ is the filtered projection which is obtained as the product of $H(\nu)$, a filter function in the spatial frequency domain, and $F(\nu)$. The reconstruction filter, $H(\nu)$, is known as the ramp filter because of its shape in the frequency domain which results in a larger weighting factor for higher spatial frequencies. The blurring that occurs in images reconstructed with backprojection can be thought of as suppressing high-spatial frequency information. The shape of the ramp filter, therefore, makes sense intuitively, as it amplifies the high-spatial frequencies with respect to the low-spatial frequencies, reversing the effects of the $\frac{1}{s}$ blurring. Finally, the inverse Fourier transformation is performed to obtain filtered projection data, which are then backprojected in the same way as in

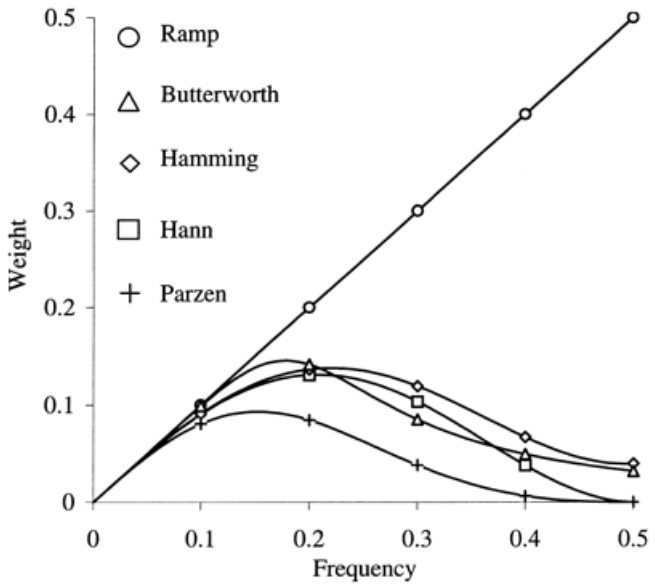

Figure 2.15: Some filters currently used in FBP and their shape. Value on y-axis indicates to what extent contribution of each frequency to image is modified by filters. These filters reduce the amplitude at high frequencies, improving signal-to-noise but reducing spatial resolution. They also avoid “ringing” artifacts from the very sharp cut-off of the ramp filter at $v = v_{cut-off}$. All of them are defined as ”low-pass” filters. Adapted from [Bruyant, 2002].

the simple backprojection [Wilson, 1998; Tsui & Frey, 2006; Kinahan *et al.* , 2004; Defrise *et al.* , 2005].

A number of Fourier filters have been designed and used in the reconstruction of tomographic images in nuclear medicine. All of them are characterized by a maximum frequency, called the Nyquist frequency, which gives an upper limit to the number of frequencies necessary to describe the sine or cosine curves representing an image projection.

An undesirable characteristic of the ramp filter is that it amplifies the noise associated with high frequencies in the image even though it removes the blurring effect of simple backprojection. To eliminate the highfrequency noise, various filters have been designed by including a window in them (Figure 2.15). Such filters are basically the products of the ramp filter with a sharp cut-off at the Nyquist frequency (0.5 cycle/pixel) and a window with amplitude 1.0 at low frequencies but gradually decreasing at higher frequencies. The effect of a decreasing window at higher frequencies is to eliminate the noise associated with the images. The frequency above which the noise is eliminated is called the cut-off frequency, v_c.

Many commercial software packages are available, offering a variety of choices for filters and cut-off values. The selection of a cut-off value is important so that noise is reduced, while image detail is preserved. Reducing a cut-off value will increase smoothing and degrade spatial resolution [Wilson, 1998; Tsui & Frey, 2006].

Figure 2.16 shows the backprojection of noise free projections that have been sharpened with a ramp filter. As the number of projections (number of viewing angles) increases, the fidelity of the

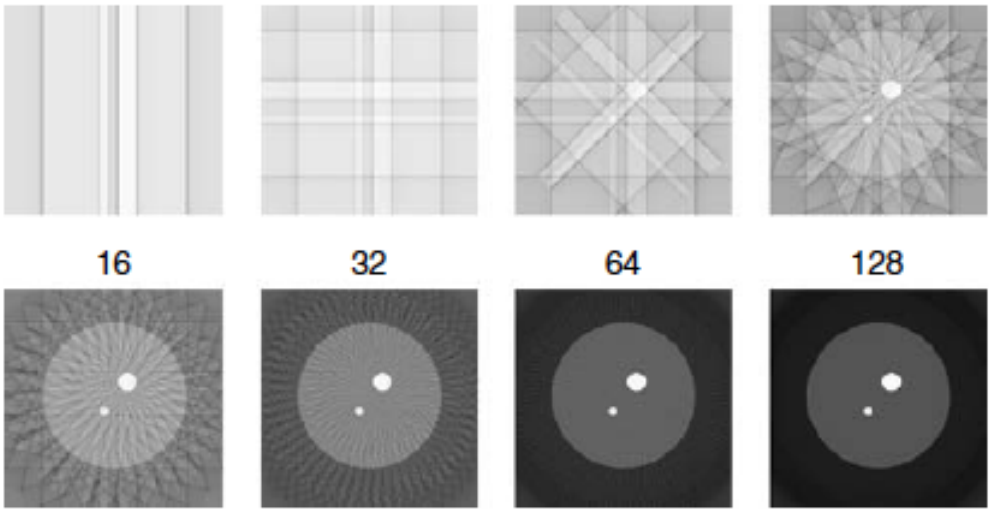

Figure 2.16: Images reconstructed by FBP from different numbers of equally spaced projections. The number of views included in each reconstruction is shown above its image. Adapted from [Wernick & Aarsvold, 2004].

reconstructed image improves. An image slice can be exactly reconstructed by FBP, provided that the data indeed follow the parallel projection imaging model and that sufficiently many projections are acquired.

2.6.2 Iterative Reconstruction Methods

In iterative methods of image reconstruction, an initial estimate of an image is made, and the projections are computed from the image and compared with the measured projections. If there is a difference between the estimated and measured projections, corrections are made to improve the estimated image, and a new iteration is performed to assess the convergence between the estimated and measured projections. Iterations are continued until a reasonable agreement between the two sets of projections is achieved, Figure 2.17.

There are many different types of iterative algorithms each differing in some aspect of their formulation and implementation. They differ primarily in the manner in which the projections are computed from the estimated image, the order in which the corrections are applied, and the type of error corrections to be applied to the estimated projections.

Unfolding of the estimated image into a set of projections is considered as the forward projection, as opposed to the backprojection, and is accomplished by determining the weighted sum of the activities in all pixels along a LOR across the estimated image. Thus, a projection q_i from an estimated image is given by:

$$q_i = \sum_{j=1}^{N} a_{ij} C_j \tag{2.29}$$

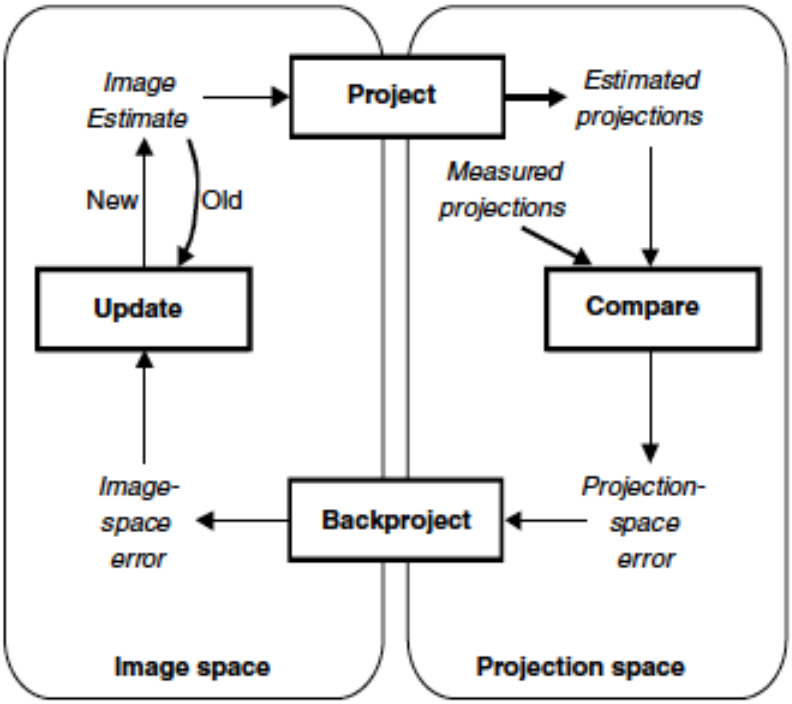

Figure 2.17: Flowchart of a generic iterative reconstruction algorithm. Adapted from [Lalush & Wernick, 2004].

where C_j is the activity counts in the j^{th} pixel and a_{ij} is the probability that an emission from pixel j is recorded in the i^{th} LOR, Figure 2.18. The weight, a_{ij}, is equal to the fraction of activity in the j^{th} pixel out of the total activity along the ith LOR. If p_i is the measured projection, then the error is calculated as the difference, $(p_i - q_i)$. The weighting factors are then applied to distribute this error into all pixels, N, along the i^{th} LOR according to:

$$\triangle C_j = \frac{a_{ij}\,(p_i - q_i)}{\sum_{j=1}^{N} a_{ij}} \tag{2.30}$$

where $\triangle C_j$ is the error from the i^{th} LOR distributed into the j^{th} pixel [Lalush & Wernick, 2004; Hutton *et al.* , 2006].

There are three ways of calculating and applying error corrections. In a point-by-point correction technique, the errors for all LORs passing through a single pixel are calculated and used to correct that point before proceeding to the next point. In the projection-by-projection (LOR by LOR) correction technique, the error is computed and the image is updated for each LOR before proceeding to the next LOR. In the simultaneous iteration reconstruction technique, all errors for all comparison LORs are calculated and then the image is updated.

The principle of the basic algebraic reconstruction technique (ART) algorithm consists of describing every iteration point by point (row-action method), and in correcting all voxels in the image which are found on a projection ray, so as to minimise the difference between the values of the calculated

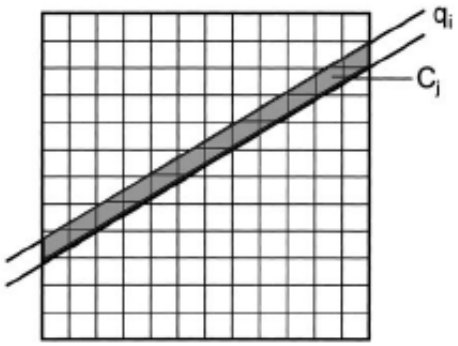

Figure 2.18: A projection data q_i in a sinogram is estimated from all pixels along the LOR and compared with the measured projection data p_i. Adapted from [Saha, 2005].

and measured projections at the point under consideration. The process comes to a stop when a certain criterion becomes relatively small. For example the sum of squared differences between the calculated and measured projections can be used as such a criterion.

The most widely used iterative algorithms in PET are maximum likelihood expectation maximization (MLEM) algorithm and ordered subset expectation maximization (OSEM) algorithm. The main feature of the MLEM algorithm is to update the image during each iteration using Equations 2.29 and 2.30. This method requires many iterations to achieve an acceptable agreement between the estimated image and the measured image demanding a lengthy computation time. To circumvent this problem, the OSEM algorithm has been introduced, which is a modification of MLEM, in that projections are grouped into subsets around the object to be imaged, separated by some fixed angle.

For noiseless projections, it has been shown that each OSEM estimate based on one subset of projections converges to a maximum likelihood solution as close as a full iteration of MLEM using all projections. In other words, if there are n subsets of projections, then once all projections are used in a single iteration of OSEM, the resulting estimate of the image is similar to that obtained by n iterations of MLEM. It is this feature of OSEM that accelerates the computation process, and in general, the computation time decreases with the increasing number of subsets. Corrections for factors such as detector efficiency variations, noise component, random coincidences, scatter coincidences, and attenuation are made prior to reconstruction in the FBP method. In the MLEM or OSEM method, these factors are incorporated a priori in the estimated image and need not be applied separately. A current modification in the forward projection technique is that each image pixel is considered to contribute in varying probabilities to virtually all LORs instead of only a single LOR, but it adds to the computing time. In general, iterative reconstruction methods do not produce artifacts observed with FBP methods, and provide a better SNR in regions of low tracer uptake. Overall, the MLEM and OSEM iterative methods reduce noise providing high-quality images and are currently included in many PET and SPECT systems.

Detailed description of the iterative methods can be found in the following references: [Bruyant, 2002; Hutton *et al.* , 2006; Lalush & Wernick, 2004].

2.6.3 3D Reconstruction

Reconstruction of images from 3D data is complicated by a very large volume of data, particularly in a multiring scanner. In a multiring scanner having N rings, a full 3D acquisition would generate N direct (perpendicular to the axis of the scanner) and $N(N-1)$ oblique sinograms (N^2 total) in the absence of septa, compared to $2N-1$ as in the case of 2D acquisition. Processing and storage of such a large amount of data is challenging for routine clinical applications. The FBP can be applied to 3D image reconstruction with some manipulations. The 3D data sinograms are considered to consist of a set of 2D parallel projections, and the FBP is applied to these projections by the Fourier method. The iteration methods also can be generally applied to the 3D data. However, the complexity, large volume, and incomplete sampling of the data due to the finite axial length of the scanner are some of the factors that limit the use of the FBP and iterative methods directly in 3D reconstruction.

To circumvent these difficulties, a modified method of handling 3D data is commonly used. A method of 3D reconstruction involves the rebinning of the 3D acquisition data into a set of 2D equivalent projections, Figure 2.19. Rebinning is achieved by assigning axially tilted LORs to transaxial planes[3] intersecting them at their axial midpoints. This is equivalent to collecting data in a multiring scanner in 2D mode, and is called the single slice rebinning algorithm (SSRB). This method works well along the central axis of the scanner, but steadily becomes worse with increasing radial distance. In another method, called the Fourier rebinning (FORE) algorithm, rebinning is performed by applying the 2D Fourier method to each oblique sinogram in the frequency domain. This method is more accurate than the SSRB method because of the more accurate estimate of the source axial location. After rebinning of 3D data into 2D data sets, the FBP or iterative method is applied. Several approximate and exact rebinning methods have been published [Defrise *et al.* , 2003, 1997; Defrise & Kinahan, 1998; Defrise *et al.* , 2005].

2.7 PET Radiopharmaceuticals

Nuclear medicine imaging relies on the detection of gamma photons produced by the decay of radioactive isotopes. The radionuclides used in PET (Table 2.1) decay by emitting positrons and can be chemically incorporated in to biologically active compounds (ligands[4]) forming a so called radiopharmaceutical. During a PET exam, these compounds are injected into the patient, in order to take part of specific physiological processes.

The radioisotope most commonly used in clinical PET is fluorine-18[5] [^{18}F] labeled with *fluorodeoxyglucose* (FDG). This modified glucose molecule behaves like normal glucose and allows the imaging of glucose metabolism. Just as glucose, FDG is actively transported into the cells of tissues that use glucose as their main energy source. This transport is performed by a group of glucose transport proteins and once intracellular, FDG is phosphorylated or breakup apart by especialized

[3] A transaxial plane is a plane perpendicular to the scanner axis.

[4] The ligands used in radiopharmaceuticals are common analogs of biological molecules, and therefore, often depict a true representation of biological processes after *in vivo* administration.

[5] The ^{18}F is preferred most, since it has a relatively longer half-life (~110min) that allows its supply to remote places.

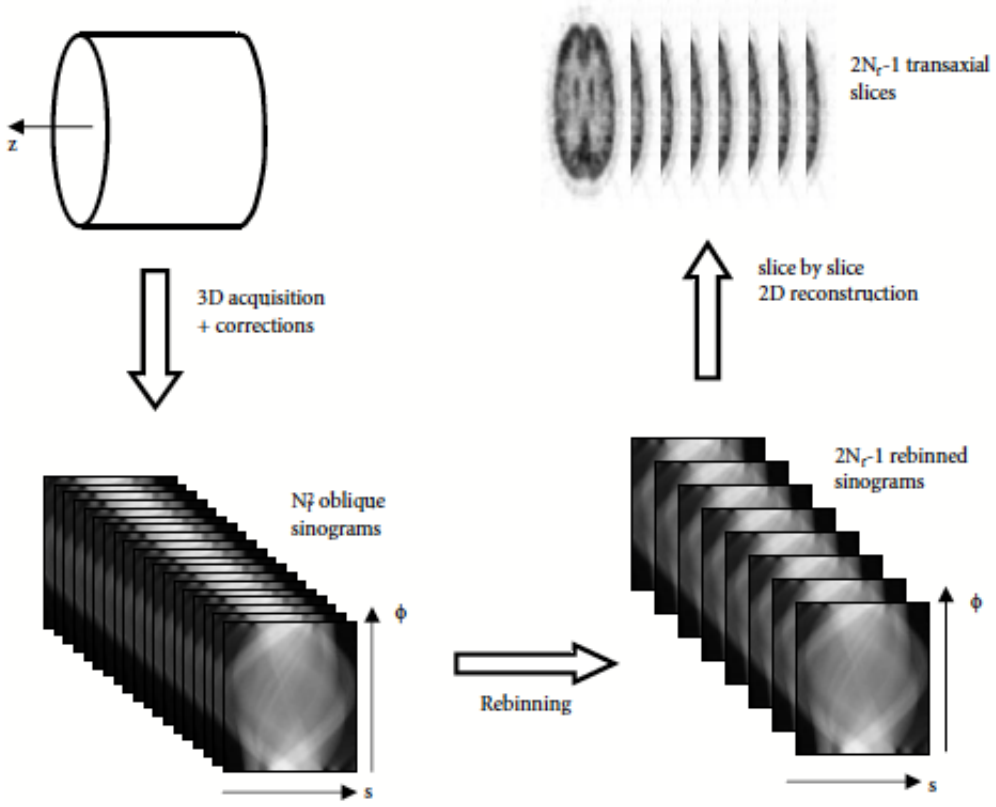

Figure 2.19: Schematic representation of the principle of a rebinning algorithm for 3D PET data. Adapted from [Defrise *et al.* , 2003, 2005].

enzimes in the cells, hexokinases, as the first step toward to glycolysis. However, FDG cannot continues along the glycolytic metabolism pathway for energy production and so it becomes trapped intracellularly as a sub-product called *FDG–6–phosphate,* Figure 2.20. Many malignant tumors and cancer metastases consume glucose more avidly than normal tissues or benign tumors due to the presence of a larger number of glucose transporters, as well as higher levels of hexokinase, which is a good indicator of abnormal metabolism or cell proliferation. This mechanism allows to obtain information on how certain organs or tissues in the body are functioning at the cellular level, making FDG PET especially effective in detecting and staging a variety of cancers.

Many radiopharmaceuticals have been used for PET imaging (Table 2.4); however, only a few are routinely utilized for clinical purposes. In all cases, a suitable synthesis method is adopted to provide a stable product with good labeling yield, high specific activity, high purity, and most importantly, high *in vivo* tissue selectivity [Schwarz & Anderson, 2007; Saha, 2005; Valk *et al.* , 2006; Cherry *et al.* , 2003a; Guhlke *et al.* , 2007; Vallabhajosula, 2007].

2.7.1 Specific Activity

The specific activity (SA) of a radiotracer is related to the fraction of the molecules in the tracer solution which are radiolabeled at a given time and is expressed in Bq/g or Ci/g or, more commonly, in concentration units (Bq/mol or Ci/mol). The specific activity declines over time as the radionuclide

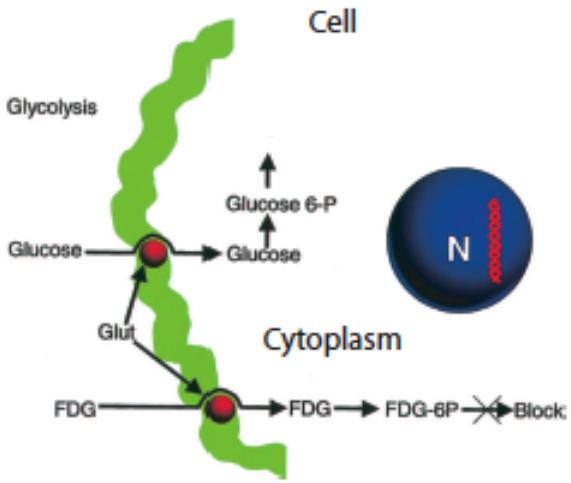

Figure 2.20: FDG tracer uptake by metabolically active cells. Adapted from [Kappor *et al.* , 2004].

Radiopharmaceutical	Application
2-[F-18] Fluoro-2-deoxy-D-glucose (FDG)	glucose metabolism
[O-15] water, [N-13] ammonia, [O-15] butanol, [O-15] CO2	blood flow
[F-18] Fluoride	bone metabolism
[C-11] O-methylglucose	glucose transport
6-[F-18] Fluoro-L-DOPA	dopamine metabolism
L-[metil-C-11] Methionine	aminoacids metabolism
[C-11] Raclopride, N-[C-11] methylspiperone	dopamine receptors
[C-11] Flumazenil	$GABA_A$ receptors
[F-18] Fluoromisonidazol	ischemia/hypoxia
[C-11] Acetate	metabolism (Krebs cycle)
8-[F-18] Fluoroganciclovir, 8-[F-18] fluoropenciclovir	genetic expression
8-[F-18] fluoropenciclovir	inflammation

Table 2.4: Some radiopharmaceuticals used in PET and their applications. Adapted from [Saha, 2005].

decays. Specific activity can be critical in animal PET studies that are mass limited because it directly determines the activity of the tracer that can be administered. The theoretical maximum specific activity for a radionuclide with a half-life (in hours) of $T_{1/2}$ is:

$$SA_{max}\,(Bq/mole) = \frac{1.16 \times 10^{20}}{T_{1/2}} \tag{2.31}$$

The specific activity is an important parameter to consider in radiolabeling and in vivo biodistribution of tracers. Cold molecules in low specific activity radiopharmaceuticals compete with radioactive molecules and lower the uptake of the tracer in different organs. Similarly, lowspecific- activity radionuclides yield poor radiolabeling. The SA of [^{18}F]-fluoride is in the order of about 1×10^4 Ci/mmol (3.7×10^5 GBq/mmol) [Saha, 2005].

Chapter 3

Small Animal PET Imaging

The exponential advances in the biological inquiry in the recent years, focused in the molecular bases of the functions of the systems of the body (*e.g.* cells, agencies and entire organism), had increased the necessity of the instrumentation of the molecular image.

Small animal experiments (with rats and mice) are an integral part of biomedical and pharmacological research. Because of their genetic and resemblance with humans and the feasibility of gene transfer or modification, many different genetically modified small animal models have been developed to study the mechanism of human diseases.

For a long time already, the methods based on the tracing of molecules marked radioactively in low concentrations, combining with the dissection of the bodies are used. In parallel, the cryosection of the body entirety followed by numerical autoradiography provides also anatomical images of very high spatial resolution (about ~50 µm), while correlating them in a quantitative way with the concentrations of the tracer used. The principal limitation of these methods lies in the fact that the analysis takes place for one given time and cannot thus take account for the temporal evolution of an individual process. Then, it is impossible to study the same animal, during and after one intervention. To carry out this kind of study, it is necessary to resort to noninvasive methods, like PET (Figure 3.1) and SPECT, that can assess molecular pathways using small amounts of radioactive labeled molecules *in vivo*. These instruments, until the nineties, exclusively employed for clinical applications since their spatial resolution didn't allow their use within the framework of small animal research (the volume of the mouse is inferior to that of a human adult by a factor of about 2'500).

During the past few years, dedicated small animal PET scanners with enhanced spatial resolution were developed to overcome the limitation of using human PET scanners with small species. The first dedicated small animal scanner RATPET was introduced in 1995. Since then, the development of small animal PET has become a promising area for technological innovation. To date, the spatial resolution has exceeded the 1 mm value.

Small animal PET imaging, namely in mice, rats, or small nonhuman primates, offers the added benefit that the animals can be their own control, reducing the interanimal variability, and making repeat studies on the same animal possible. It is particularly useful for testing hypotheses during

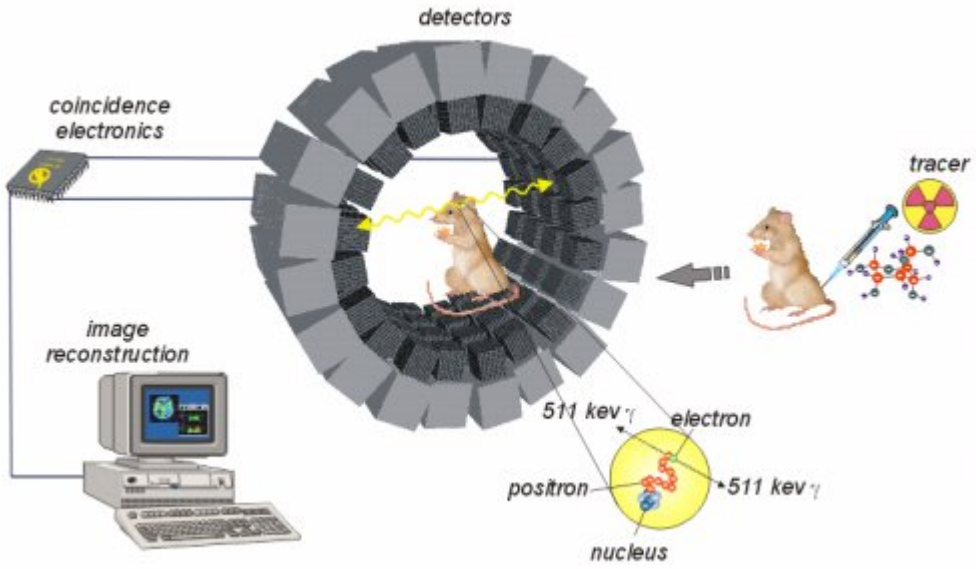

Figure 3.1: Representation of a microPET (µPET) acquisition process.

the study of diseases and the development of new imaging and therapeutic drugs. It is thus not surprising that small animal PET now provides the best tool for the accurate measurement of the pharmacokinetics of imaging agents *in vivo*.

3.1 Challenges and Limitations of Small Animal PET Imaging Quantification

Challenges common to all imaging techniques include:

a) the design of probes or probing techniques that are highly specific to the biological processes of interest,

b) optimization of imaging systems to provide the highest sensitivity and image resolution, and

c) minimization of perturbation to the biological processes under observation so that the experimental outcomes correlate to the biology and not to the probing process [Balaban & Hampshire, 2001; Cherry & Chatziioannou, 2004; Tai & Laforest, 2005; Hutchins *et al.* , 2008].

3.1.1 Spatial Resolution

A mouse is more than three orders of magnitude smaller than a human based on body weight (70 Kg for a human and 20 to 30 g for a mouse). Because of this, an animal PET system must have very

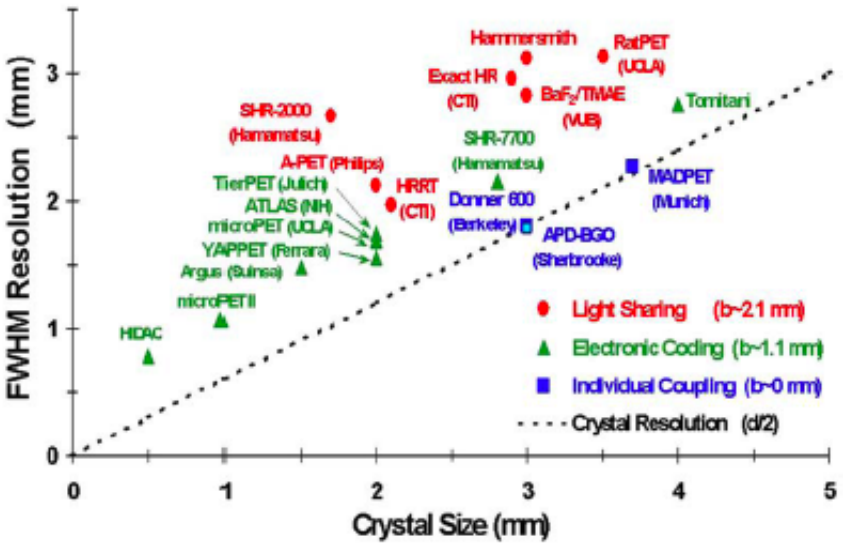

Figure 3.2: Intrinsic spatial resolution of several existing tomographs as a function of detector size. Data have been labelled according to the type of position decoding scheme used to identify the crystal of interaction. Adapted from [Lecomte, 2004].

high spatial resolution and sensitivity to achieve the same level of details and accuracy currently achievable in human PET studies. Current human clinical PET scanners have a typical image resolution ranging from 4 to 10 mm FWHM and an absolute sensitivity of 0.5% to 5%, depending on the mode of operation (2D versus 3D). To improve the volumetric resolution of human PET systems by three orders of magnitude, the image resolution of animal PET systems needs to be reduced to 1 mm FWHM or less in each of the three dimensions. A number of factors, including statistical and technological issues, affect this improvement.

The published resolution data of several existing tomographs have been analyzed to remove the effects of noncollinearity and positron range (or effective source size used for resolution measurements) and were plotted as a function of crystal size, Figure 3.2. The scanners can be grouped into three different categories (light-sharing[1]; electronic coding[2]; individual coupling[3]), depending on the type of coupling between scintillators and photodetectors and on the positioning algorithm used to identify the crystal of interaction.

These data suggest that there is some inherent loss of positioning accuracy associated with all types of decoding schemes. The positioning accuracy can be improved by limiting the light exchange between individual crystals, but charge spread within the multiplying structure of the PMT and the readout circuit still adds some uncertainty to crystal identification.

[1]Mostly consisting of block type detectors, uses light-sharing and Anger-like logic to decode the crystal of interaction. The positioning accuracy calculated as the quadratic difference between the measured intrinsic resolution and the geometric resolution.

[2]Uses a direct coupling of crystals to the photodetectors and attempts to avoid as much as possible the spread of scintillation light between crystals. Position decoding is performed using a charge division readout scheme of the signals from position-sensitive or multiple-anode PMTs.

[3]Uses true pixel detectors (crystals individually coupled to photodetectors and independent electronic signal processing channels) and achieves an intrinsic resolution that is exactly equal to the geometric resolution.

3.1.2 System Sensitivity

Imaging techniques based on radionuclide decay rely on photon counting for signal detection. Photon counting is a stochastic process that follows Poisson statistics. With Poisson statistics, the variance equals the mean, thus the SNR ratio of photon counting measurement is proportional to the square root of the number of counts detected. When the image resolution of a PET system is improved, the volume of each image voxel is reduced accordingly. If the radiotracer concentration remains the same, the number of coincidence events originating from each image voxel is reduced proportionally. So, to improve the counting statistics of an animal study, one may increase the radiotracer concentration, extend the scan duration, or improve the sensitivity of the PET scanner itself. Extending the acquisition time is feasible only for a static imaging protocol where the process under observation is assumed to have reached a steady state prior to the scan. However, in many animal experiments, the objective is to measure the dynamics of a specific biological process. To provide adequate temporal resolution of the measurements, the number of counts collected per unit time is more critical than the total number of counts collected. Ideally, to accomplish this, one would like to improve the sensitivity of an animal PET scanner to a value much higher than that of a human PET system.

Whole-body human PET scanners detect on the order of 0.3 to 0.6% of the coincident annihilation photons in 2D mode and 2 to 5% in 3D acquisition mode. Based on the same argument of scale presented for spatial resolution and to preserve the number of counts per resolution element, the sensitivity for mouse imaging would need to improve by a factor of 1000 relative to human imaging, which is clearly not possible. Even with perfectly efficient detectors and complete solid angle coverage around the animal, the best that can be achieved is about a 200-fold increase in 2D mode and a 30-fold increase in 3D mode.

Although this relative reduction in sensitivity from mouse to human can partly be dealt with by injecting larger amounts of radioctivity. Another approach to compensate for the sensitivity problem is to use more sophisticated reconstruction algorithms that make better use of the available counts. Iterative statistical algorithms that accurately model the physics of the scanner and the statistics of the raw data will probably play an important role in very high resolution PET studies because they can produce improvements in either resolution or SNR relative to analytic reconstruction algorithms.

Most recent animal PET systems have equal or less sensitivity compared to human PET systems. It remains a major challenge in animal PET scanner design to improve both image resolution and system sensitivity at the same time.

3.1.3 Radiation Exposure

The amount of activity that can be administered during a small animal imaging study is limited by the specific activity of the radiochemical (the ratio of labeled to unlabeled chemical in the injection), by the total volume that can be injected into a mouse, by the radiotoxicity effects of the radiotracer, and by the maximum counting rate capability of a PET system. A fundamental requirement of imaging is to not disturb the biological systems under observation either through pharmacological effects or radiation dose to tissues. For example, a typical animal PET imaging protocol administers

7.4 MBq (200 µCi) radiotracer into a 20 g mouse, and a typical clinical PET study administers 370 to 555 MBq (10 to 15 mCi) into a 70 Kg patient. What appears to be a small amount of radiotracer in an animal experiment can result in a radiotracer concentration 40 to 70 times higher than that of a typical human study. This amount of radiotracer, if using FDG, results in a radiation dose of 13.1 cGy (rad) to a 20 g mouse, assuming no biological excretion, whereas the typical 555 MBq, injected dose in human, delivers a radiation dose of 0.67 cGy (rad). This large radiation dose in a small animal yields a radiobiological effect that cannot be neglected. Although the potential gain in radiotracer concentration is advantageous from the point of view of SNR, one needs to ensure that biology is not altered, in particular for repeated studies such as those monitoring the progression of cancerous tumor growth or those evaluating neurological receptors with tracers competing with endogenous molecules.

3.1.4 Specific Activity of Tracers

Increases in specific activity would allow more radioactivity to be injected into an animal and thus improve counting statistics and SNR in the images. To ultimately achieve adequate SNR in sub-millimeter resolution images from mass-limited tracers, it is likely that significant improvements in specific activity (of an order of magnitude or so) will need to be acomplished.

3.1.5 Measurement of the Input Function

In addition to achieving adequate spatial resolution and counting statistics, the performance of fully quantitative studies in small animals dictates the need for measurement of the blood input function and, in many cases, labeled metabolites in the blood. In the case of humans, blood samples may be an inconvenience, but are easily obtained. The rat has a blood volume of just ~30 mL, of which roughly 3 mL may be safely withdrawn over a period of an hour or so for external counting. Nevertheless, it has been possible to implant arterial lines into rats for blood withdrawal and to carry out longitudinal studies in these animals. A microsampling system for the rat that continuously draws small blood samples, separated by air bubbles, into plastic tubing and passes the samples through a plastic scintillation detector has also been developed. In the mouse, direct sampling becomes extremely difficult. The blood volume is just 1.3 mL, allowing only 0.13 mL to be safely removed and the vessels are tiny, requiring fairly sophisticated microsurgery for routine and repeated cannulation. Direct cardiac puncture and sampling has been successfully employed for a limited number of samples in the mouse, but remains difficult to implement routinely. It may be possible to estimate the input function in the mouse by rapid imaging of the left ventricular blood pool. This requires high-resolution, high-sensitivity, and rapid dynamic imaging along with appropriate corrections for spillover, partial volume effects, and heart motion. Similar techniques have been used successfully in the human and can probably be adapted for the mouse. Studies that require metabolite analysis are still problematic and may require additional modeling or assumptions such that only a small number of arterial or, preferably, venous blood samples will suffice. A practical approach to this difficulty in neuroreceptor studies is to use regions of the brain that have no specific binding as reference regions. This allows receptor kinetics to be measured without requiring the input function[Green *et al.* , 1998; Chatziioannou, 2002a,b; Huang *et al.* , 2004].

3.1.6 Other Considerations...

Other factors, such as energy resolution, dead time characteristics, the ability to perform attenuation correction, and imaging FOV impose, different constraints to the design of the detector and system need to be taken into consideration. The accuracy of the biological models derived from animal PET experiments depends on the quantitative accuracy of imaging. PET data needs to be corrected, notably for normalization, attenuation, scatter, and dead time, to achieve quantitative images. The implementation of these correction techniques can be affected by the choices of system design. Compromises in performance characteristics are often necessary, and should consider the targeted applications of the system, the availability and cost of the technologies, and the ease and cost of operation.

In the review available in [Weber & Bauer, 2004] a description of the current methods of evaluation of physical performance parameters of small animal PET scanners can be found. Differences in performance measurement methods are described with regard to commercially available systems. Moreover, consequences of differences in scanner performance parameters are rated with respect to applications of small animal PET, see section 3.3.

Given the variation in animal size and types of experiments, it is unreasonable to expect that a single animal PET system would be optimal for all studies. Because of this, it is important to understand current state-of-the-art animal PET technologies and the impacts of different designs on system performance [Cherry & Chatziioannou, 2004].

3.2 Implementation of Small Animal PET

3.2.1 Anesthesia

The animal must be kept still during the imaging study and therefore almost all animal PET studies involve anesthesia. This can be a major confounding variable, particularly in brain studies. Further characterization of the effects of different anesthetics on biological systems and careful anesthetic selection will be required to minimize this difficulty. In some cases, tracers that are irreversibly trapped can be used, thus enabling distribution and uptake of the tracer to occur while the animal is conscious, followed by scanning of the anesthetized animal after uptake is complete. FDG is a good example of a tracer that can be used in this way. This approach also permits activation-stimulation-type studies in awake animals.

An alternative to anesthesia is to use complete restraint of the animal in a tube or body cast or to use paralyzing drugs that prevent motion but do not interfere with brain function. However, these methods cause enormous stress to the animal and also lead to highly unphysiological conditions that can confound experimental results just as much as anesthesia does. A number of groups are in the early stages of exploring the use of motion detection systems or mounting a ring of counterbalanced detectors directly onto a rat's head, the Rat Conscious Animal PET (RatCAP) allowing PET studies in freely moving animals [RatCAP, 2010; Woody *et al.* , 2004; Vaska *et al.* , 2007; Park *et al.* , 55].

3.2.2 Immobilisation and Positioning

Even anaesthetised animals move a little by virtue of their breathing and other random motion. When working with ROIs so close in size to the resolution of the scanner, motion should be eliminated and a firm fixing device is now commonly used for rat brain studies [Rubins *et al.* , 2001]. These devices take the form of a stereotaxic frame which, if ideally implemented, positions the rat head in the same, flat-skull orientation as the Paxinos and Watson (1986) rat brain atlas. This greatly facilitates both the development and application of ROI templates and also the averaging of data from different scans, for the purpose of group comparisons. Such holding and positioning devices have yet to be developed for animal PET scans outside of the brain.

3.2.3 ROI Identification

PET imaging provides functional, rather than anatomical, information. All too frequently, accurate identification of ROIs[4] is confounded by poor quality images. The identification of a tumour with a low tracer signal, for instance, may be difficult where other organs in the FOV have much higher retention or accumulation of counts. The use of low radioactivity fiducial markers, placed close to the site of the tumour, may help. In human PET, the problem is addressed by using multimodality imaging devices combining, for example, PET and CT. The first similar devices are now available for animals, like the Inveon multimodality system [Inveon, 2010; Bao *et al.* , 2009].

3.3 Small Animal PET Scanners

The first animal PET tomographs were designed for imaging nonhuman primates and were constructed around 1990. The SHR-2000 was developed by Hamamatsu and installed in their Central Research Laboratory; the other, ECAT-713, was developed by CTI PET Systems Inc. and installed at UCLA. They offered a relatively large ring diameter and transaxial field of view, which was sufficient to accommodate adult vervet and rhesus monkeys and dogs. Both these systems were based on bismuth germanate (BGO) scintillator. The UCLA tomograph used an adaptation of the block detector designed for the ECAT HR scanner, configured in a 64 cm diameter detector ring. The detector elements were 3.5×6.25×30 mm deep in a 6×8 matrix and mounted on two dual anode PMTs. The axial FOV was 5.4 cm. The Hamamatsu tomograph used individual 1.7×10×17 mm deep BGO crystals mounted on a position sensitive photomultiplier tube (PSPMT). Four rows of 33 crystals were mounted to each PSPMT. Fifteen of these modules were arranged to form a 34.8 cm diameter scanner. The axial FOV was 4.6 cm. Both scanners were designed to be used in 2D mode and had interplane septa, although the UCLA system was later modified to enable the septa to be removed, allowing full 3D acquisition. The reconstructed spatial resolution of the systems at the center of the FOV were reported as 3.8 mm transaxial and 4.2 mm axial for the UCLA system, and 3.0 mm transaxial and 4.4 mm axial for the Hamamatsu system. This leads to volumetric resolutions[5] of 0.061 cc for the ECAT-713 system and 0.040 cc for the SHR-2000 system. The reported

[4] Region of Interest (ROI) - number of counts within the image of the target organ.
[5] volumetric resolution = (transaxial resolution)^2×(axial resolution)

sensitivities were 20.7 kcps/μCi/cc at a 300 keV lower energy discriminator measured with a 10 cm diameter cylinder for the Hamamatsu system and 58.1 kcps/μCi/cc at 350 keV lower energy discriminator with a 20 cm diameter cylinder for the UCLA system. Hamamatsu have more recently developed a higher resolution PET scanner, the SHR-7700, for nonhuman primate imaging, which is an extension of their previous design, see Figure 3.3.

The first PET system developed specifically for rodent imaging was the RATPET scanner developed at the Hammersmith Hospital in collaboration with CTI PET Systems Inc.. This system used an almost identical detector to the ECAT-713 already described, but with the BGO block segmented into an 8×7 matrix. This gives individual element dimensions measuring 3.5×5.95×30 mm^3. Sixteen of these block detectors are arranged in a 11.5 cm diameter ring to form the scanner. The axial FOV is 50 mm and the system has no interplane septa, operating entirely in 3D mode. The measured spatial resolution in 3D at the center of the FOV is 2.4 mm transaxially by 4.6 mm axially, giving a volumetric resolution of 0.026 cc. The absolute sensitivity of the scanner is 4.3% for a lower energy threshold of 250 keV.

This pioneering system demonstrated for the first time the potential utility of a dedicated small animal PET scanner. Some of the challenges raised by this system relate to the large angular gaps where the detectors meet, which, if not treated correctly, can lead to artifacts in the reconstructed images. The resolution is also very nonuniform and degrades rapidly as you move away from the center of the FOV, due to depth of interaction effects. These effects are particularly pronounced in this scanner due to the large depth of the crystals (30 mm) and the small ring diameter (11.5 cm).

With the introduction of LSO detectors and fiberoptic readouts of individually cut crystals, small animal scanners with higher resolution have been developed. Siemens MicroPET® Focus™ 120 [Cherry *et al.* , 1997; Tai *et al.* , 2005] and GE eXplore Vista systems [Wang *et al.* , 2006] represent the state-of-the-art in high-resolution small animal PET scanners. These systems offer very high resolution and a good sensitivity. For both systems, special care is devoted to keep the spatial resolution as constant as possible over the whole FOV. Two different approaches are used: MicroPET® Focus™ 120 uses thinner crystal elements with a larger gantry aperture, while GE eXplore Vista makes use of a more complex phoswich technology to limit the parallax error. The performance of these systems offers a spatial resolution of 1.3 and 1.4 mm FWHM and a sensitivity of 6.5% and 4% for the Siemens and GE scanners, respectively. A detailed description of the Focus system can be found in chapter 6.

Concorde Microsystems Inc. have recently developed similar microPET systems with four rings of detector modules, increasing the axial FOV to almost 8 cm. The P4 model, shown in Figure 3.3, has a 26 cm ring diameter to accommodate brain imaging in small nonhuman primates in addition to whole-body rodent imaging [Tai *et al.* , 2001]. The R4 model, for small rodents only, has a 15 cm ring diameter [Knoess *et al.* , 2003]. The larger axial FOV, in addition to allowing whole-body mouse positioning in a single bed position improves sensitivity at the center of the scanner to approximately 1.2% and 2.2% for the P4 and R4 systems, respectively.

The HIDAC PET, Figure 3.3, has an unsurpassed spatial resolution by using an unconventional detector technology based on gas multiwire proportional chambers (MWPC) coupled to solid, high Z converters [Jeavons *et al.* , 1999]. The drawbacks of this system are tricky tuning and poor sensitivity, both due to the gas chamber detector technology. The HIDAC PET system consists of

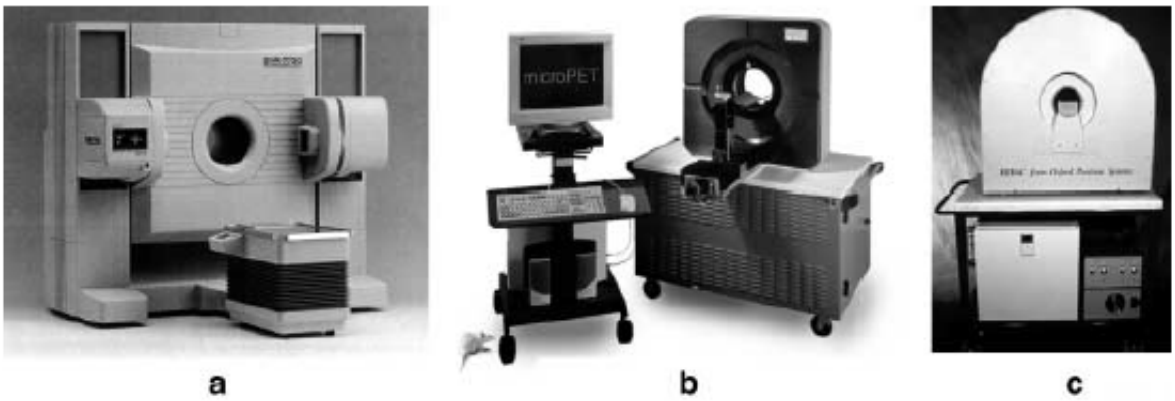

Figure 3.3: Dedicated animal PET scanners: a) Hamamatsu SHR-7700 scanner, a PET system dedicated to non-human primate imaging. The position sensitive PMT-BGO detector-based ring has a diameter of 50.8 cm and an axial FOV of 11.4 cm. b) The microPET P4 scanner. This system uses fiberoptically coupled LSO scintillator elements and a position-sensitive PMT. The ring diameter is 27 cm and the axial FOV is 80 mm. c) The HIDAC system, an animal PET scanner which uses multiwire proportional chamber technology together with stacks of lead converters. All these detectors have an intrinsic spatial resolution of < 1 mm. Adapted from [Chatziioannou, 2002a].

two such detector heads that are rotated around the object in order to acquire complete projection data. The scanner has a variable detector separation between 10 and 20 cm and an axial FOV of 21 cm and operates exclusively in 3D mode. The reconstructed spatial resolution of the tomograph at the center of the FOV is 0.95 mm FWHM in the transverse direction and 1.2 mm FWHM in the axial direction using FBP. A newer version of the system, the quad-HIDAC, is available and has four detector heads, thus providing better solid-angle coverage and increased sensitivity. The main advantages of these detectors are their high intrinsic spatial resolution and the depth of interaction information they provide. The relative inefficiency of the detectors is compensated for by large solid-angle coverage around the animal. The drawbacks of these detectors come from the conversion process that does not provide energy information, thus making it difficult to discriminate against scatter, and the large coincidence timing window of 60 ns, which ultimately limits count rate performance. Both these factors will degrade the NEC performance of the system.

A critical discussion on some aspects related to the use of these systems, namely the parameters characterizing the imaging capability, is reported in [Larobina *et al.* , 2006].

Because of the importance of animal work in drug development that later translates into clinical use in humans, further improvement of the small animal scanners is being pursued by manufacturers such as CTI/Siemens, GE Medical, and Philips Medical Systems, and several small animal PET scanners are now commercially available [Cherry & Chatziioannou, 2004; Myers, 2001; Myers & Hume, 2002; Tai & Laforest, 2005; Rowland & R., 2008; Guerra & Belcari, 2007; Chatziioannou, 2002a,b].

3.4 Applications of Small Animal PET

There are now a number of reports documenting the use of dedicated small animal PET scanners for different applications. These include studies of the dopaminergic system in the rat brain, longitudinal studies of glucose metabolism in rat brain, investigation of the effect of photodynamic therapy in a mouse tumor model, and the development of methods for imaging reporter gene expression *in vivo*. Examples from studies performed on the small animal PET systems are shown in Figures 3.4 and 3.5.

Several excellent review articles including extensive reference lists that give a more detailed presentation of each subfield of small animal PET imaging: [Kornblum *et al.* , 2000; Phelps, 2000; Pomper, 2001; Weissleder & Mahmood, 2001; Cherry & Gambhir, 2001; Myers, 2001; Rowland, 2002; Schelbert, 2003; Herschman, 2003; Cherry, 2004; Laforest, 2005; Rowland & R., 2008; Lewis *et al.* , 2002; Riemann *et al.* , 2008; Lammertsma, 2004; Blasberg, 2002; Blasberg & Tjuvajev, 2002; MacLaren *et al.* , 2000; Vassaux & Wassink, 2003; Gambhir *et al.* , 1999, 2000; Hume & Jones, 1998; Chatziioannou, 2005]

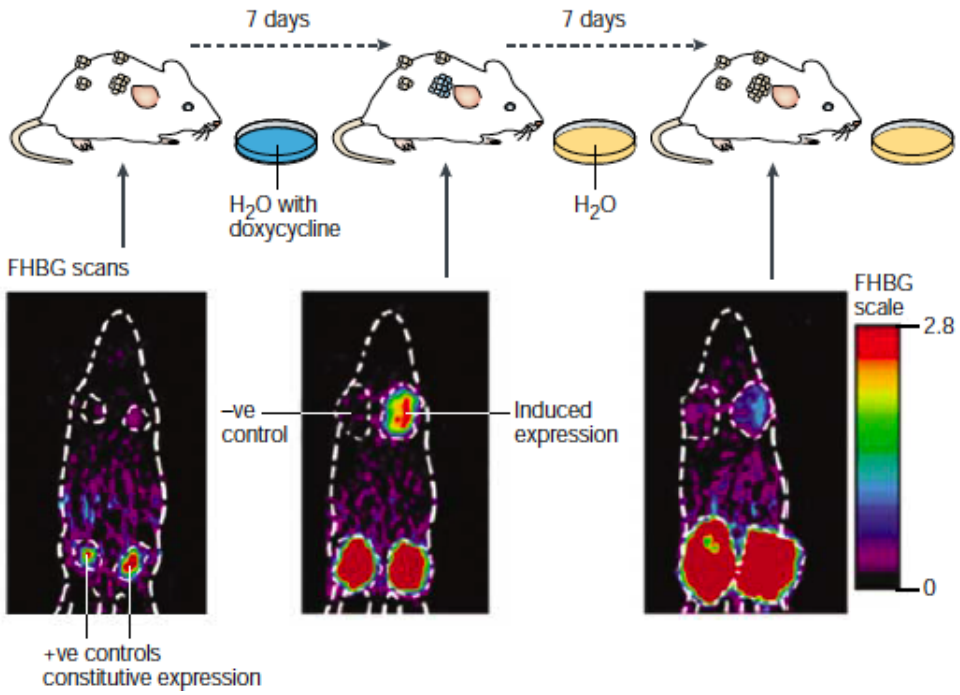

Figure 3.4: MicroPET imaging of bi-directional inducible therapeutic and reporter-gene expression. Sequential microPET imaging studies of a nude mouse carrying four tumours. Four tumour cell lines - two positive controls (constitutive reporter-gene expression), one negative control and one inducible line (reporter-gene expression induced by doxycycline - were injected subcutaneously into four separate sites in a single mouse. When tumours reached a size of at least 5 mm, the mouse was imaged with *9-(4-[^{18}F] fluoro-3-hydroxymethylbutyl)guanine* (FHBG). Doxycycline was then added to the water supply for 7 days. The mouse was then scanned again with FHBG. Doxycycline was removed from the water supply for the next 7 days, and the mouse was again scanned with FHBG. The locations of the four tumours and the mouse outline are shown by the dotted regions of interest. All images are 1 to 2 mm coronal sections through the four tumours. The %ID/g (% injected dose per gram tissue) scale for FHBG is shown on the right. The negative control tumours show no gene expression, and the positive control tumours show increased expression over the time course. The tumour on the top right, with inducible gene expression, initially does not accumulate FHBG, then at 7 days after addition of doxycycline, induction of reporter-gene expression traps FHBG. Seven days after withdrawal of doxycycline, there is decreased induction and minimal trapping of FHBG.The FHBG image signal correlates well with target-gene expression (not shown). Adapted from [Gambhir, 2002].

Figure 3.5: Whole-body bone scans ([^{18}F]-fluoride ion) of a mouse acquired using the microPET scanner. The image on the left was reconstructed using standard 3D FBP technique with a high resolution ramp filter. The image on the right was reconstructed from the same raw data using a maximum a posteriori (MAP) algorithm that minimizes statistical error and models the detector response. A substantial improvement in spatial resolution without noise amplification is clearly demonstrated. Adapted from [Chatziioannou, 2002b].

Chapter 4

Monte Carlo Simulations in Emission Tomography

Monte Carlo simulation methods can be described as statistical methods that use random numbers as a base to solving problems involving stochastic processes. The name of the technique was chosen during the World War II Manhattan Project due to the close connection to games of chance and the location of the famous casino in Monte Carlo. The general concept of Monte Carlo simulation is to create a model, as similar as possible to the real system and to simulate interactions with that system based on *a priori* known probabilities of occurrence through random sampling of Probability Density Functions (PDFs). Due to the stochastic nature of radiation emission and detection processes, the Monte Carlo method is particular interesting for medical physics in areas such as radiotherapy, radiation protection and nuclear medicine [Andreo, 1991]. In fact, this simulation technique is nowadays an essential research tool in nuclear medicine to study the response of imaging systems, like PET and SPECT scanners, predicting the performance of new detectors and optimizing their design [Zaidi, 1999]. In addition, Monte Carlo data is currently essential for the development, validation and comparative evaluation of image reconstruction techniques and for the assessment of correction methods such as photon attenuation and scattering. One of the advantages of Monte Carlo simulations, is the possibility to change different parameters and to investigate the effects of such modifications on the performance of scanners, allowing to test several detection configurations that may be impracticable using an experimental approach. Following the development of more powerful computing systems, Monte Carlo has recently been used to produce simulation data that allows to anticipate the lesion detectability performance of an imaging system under development as well as to calculate the system matrix to be incorporated in image reconstruction algorithms, as an alternative to the standard analytical models.

The success of this approach is due to the ability of Monte Carlo techniques to accurately describe the physics of the interaction of particles with matter by using pseudo–random number generators, and rules to sample probability distributions and cross–sections to determine the interaction probability of particle traveling through a given material. When simulating photon interactions, the partial and total cross section data (based on the material constitution) represent such information and are used to calculate the path length and type of interaction for this particle. Afterwards, the PDFs are

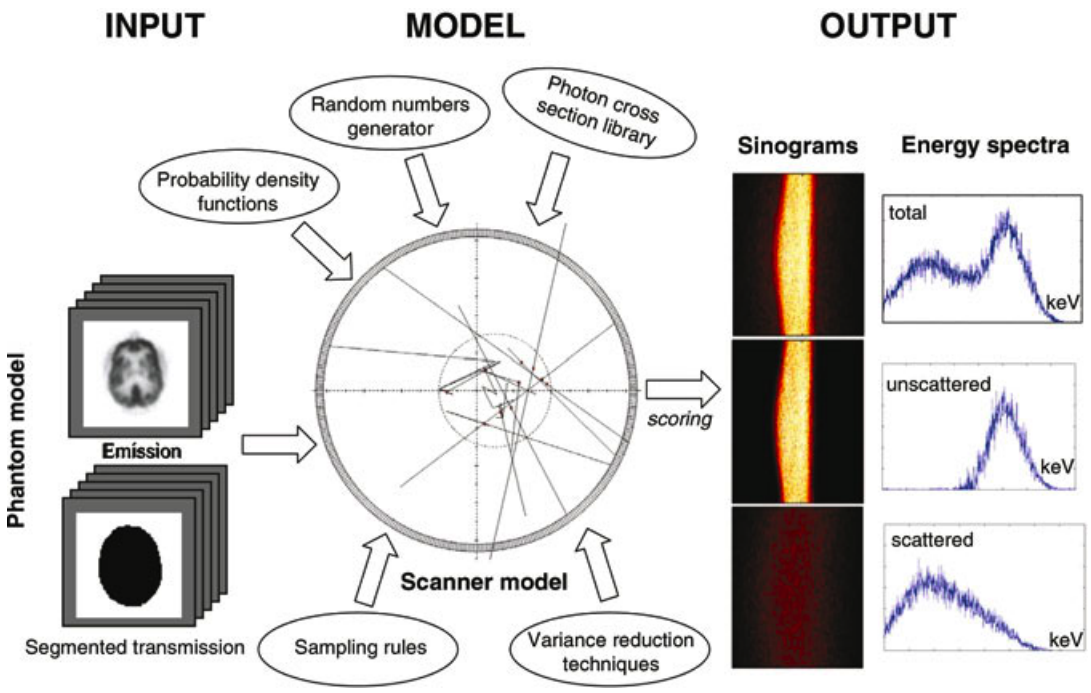

Figure 4.1: Principles and main components of a Monte Carlo program dedicated to the simulation of cylindrical multi-ring PET imaging systems. Adapted from [Zaidi, 2006].

sampled by predefined sampling rules using randomly generated numbers. The energy of such a photon can be dissipated along its path or the photon can penetrate all scattering and attenuating media to reach the detector where a new PDF sampling decides whether it should be accounted for in the scoring region or whether it should be discarded [Zaidi, 1999; Buvat & Castiglioni, 2002].

Figure 4.1 illustrates the principles and main components of Monte Carlo applied to a cylindrical multi-ring PET imaging system. Some of these principles will be described in the following sections.

A detailed description of the general principles and applications of the Monte Carlo method can be found in [Andreo, 1991; Ljungberg, 1998; Zaidi, 1999; Ljungberg, 2004; Zaidi & Sgouros, 2002; Zaidi, 2006].

4.1 Random Numbers

Random numbers are of key importance when modeling a physical system using a statistical model. Every random number generator has to deliver uncorrelated, uniform and reproducable sequences with a very long period in a short amount of time. A computer algorithm can be used to generate that random number from seed numbers. An example of such an algorithm is the linear congruental algorithm where a series of random numbers I_n is calculated from a first seed value I_0, according to the relationship:

$$I_{n+1} = (aI_n + b) \bmod \left(2^k\right), \tag{4.1}$$

where a and b are constants and k is the integer word size of the computer. The seed value must

be randomly changed, for instance by triggering a value from a call to the system clock [Andreo, 1991].

4.2 Sampling Methods

To obtain a stochastic variable that follows a particular PDF three different sampling methods can be used: the distribution function method, the rejection method and the mixed method [Zaidi, 1999; Ljungberg, 1998; Lazaro, 2003].

4.2.1 The Distribution Method

With the distribution function method a cumulated distribution function $cpdf(x)$ is constructed from the integral of $pdf(x)$ over the interval $[a, x]$ according to:

$$cpdf(x) = \int_a^x pdf\left(x'\right) dx'. \tag{4.2}$$

The variable x is then sampled by replacing $cpdf(x)$ with a uniformly distributed random number in the range of $[0, 1]$ and solving for x. This sampling method is used if the inverse of the $cpdf(x)$ is easily obtainable.

4.2.2 The Rejection Method

The rejection method possibly can lead to some mathematical difficulties in calculating the inverse of the $cpdf$. In the latter case the rejection method can be used. Let the $pdf(x)$ be defined in the range $[a, b]$ and calculate the normalized $pdf^*(x)$ as in:

$$pdf^*(x) = \frac{pdf(x)}{max[pdf(x)]'}, \tag{4.3}$$

so the maximum of $pdf(x)$ is 1. Then sample a uniform distributed value of x within the range $[a, b]$ from the relation:

$$x = a + R_1(b - a), \tag{4.4}$$

where R_1 is a random number. Let a second random number decide whether the sampled x should be accepted. This is done by checking:

$$R_2 < pdf^*(x). \tag{4.5}$$

If this relation is fulfilled, then x is accepted as a properly distributed stochastic value, otherwise x needs to be resampled.

4.2.3 The Mixed Methods

When the previous two methods are impractical, a mixture of the two methods above is used. Accordingly, the $pdf^*(x)$ is the product of two probability distribution functions $pdf^*A(x) \cdot pdf^*B(x)$, both normalized to unity. Now one determines an x value using the distribution method on $pdf^*A(x)$ and applies then (with that x) the rejection method to $pdf^*B(x)$ [Ljungberg, 1998, 2004].

4.2.4 Non Analog Samplig

A direct Monte Carlo simulation using true $pdfs$ may require an unacceptable long time to produce statistically relevant results. It may thus be desirable to bias the sampling by introducing stratification (limit source distribution), importance sampling (splitting or Russian Roulette using production tables) or by implementing forced detection (by imposing a registration in a scoring region).

4.3 Photon Transport

Compton incoherent scattering and photoelectric effect are the two most important interaction mechanisms in nuclear medicine simulations. The total photoelectric cross section for a given energy, E, is calculated using discretized libraries by means of interpolation. The incident photon is absorbed and an electron is emitted in the same direction of the incident photon. The kinetic energy of the electron is defined as the difference between the energy of the original photon and the binding energy of the electron. The subshell of emission is again randomly sampled, thereby using cross sectional data for all subshells. When simulating the Compton scattering of a photon from an atomic electron on the other hand, an empirical cross section formula is used and sampling of the final state is done by a variant of the mixed Monte Carlo method as noted in section 5.3. The quantum mechanical Klein-Nishina differential cross section per atom is:

$$\frac{d\sigma}{d\varepsilon} = \pi r_e^2 \frac{m_e c^2}{E_0} Z \left[\frac{1}{\varepsilon} + \varepsilon\right] \left[\frac{1 - \varepsilon \sin^2\theta}{1 + \varepsilon^2}\right], \tag{4.6}$$

where:

r_e = classical electron radius;

$m_e c^2$ = electron mass;

E_0 = energy of the incident photon;

E_1 = energy of the scattered photon:

$\varepsilon = \frac{E_1}{E_0}$.

Assuming an elastic collision, the scattering angle θ is defined by the Compton formula:

$$E_1 = E_0 \frac{m_e c^2}{m_e c^2 + E_0 (1 - \cos\theta)}. \tag{4.7}$$

The value ε of corresponding to the minimum photon energy (backscatter) is given by:

$$\varepsilon_0 = \frac{m_e c^2}{m_e c^2 + 2E_0}, \tag{4.8}$$

hence $\varepsilon \in [\varepsilon_0, 1]$. One may state that:

$$\Phi_\varepsilon \approx \left[\frac{1}{\varepsilon} + \varepsilon\right]\left[\frac{1 - \varepsilon \sin^2\theta}{1 + \varepsilon^2}\right]$$

$$= f(\varepsilon) \cdot g(\varepsilon)$$

$$= \left[\alpha_1 f_1(\varepsilon) + \alpha_2 f_2(\varepsilon)\right] \cdot g(\varepsilon) \tag{4.9}$$

where

$$\alpha_1 = \ln\left(\frac{1}{\varepsilon_0}\right)$$

$$f_1(\varepsilon) = \frac{1}{\alpha_1 \varepsilon}$$

$$\alpha_2 = \frac{\left(1 - \varepsilon_0^2\right)}{2}$$

$$f_2(\varepsilon) = \frac{\varepsilon}{\alpha_2}. \tag{4.10}$$

f_1 and f_2 are probability density functions defined on the interval $[\varepsilon_0, 1]$, and $g(\varepsilon)$ is set to:

$$g(\varepsilon) = \left[\frac{1 - \varepsilon \sin^2\theta}{1 + \varepsilon^2}\right], \tag{4.11}$$

being the rejection function $\forall \varepsilon \in [\varepsilon_0, 1] \Longrightarrow 0 < g(\varepsilon) \leq 1$. Given a set of 3 random numbers r, r', r'' uniformly distributed on the interval $[0, 1]$, the sampling procedure for ε is the following:

1. decide whether to sample from $f_1(\varepsilon)$ or $f_2(\varepsilon)$: if $r < \frac{\alpha_1}{\alpha_1 + \alpha_2}$ select $f_1(\varepsilon)$ otherwise select $f_2(\varepsilon)$;
2. sample ε from the distributions to f_1 or f_2:
   - for f_1: $\varepsilon = \varepsilon_0^{r'}$ $(\equiv \exp(-r'\alpha_1))$,
   - for f_2: $\varepsilon^2 = \varepsilon_0^2 + \left(1 - \varepsilon_0^2\right) r'$;
3. calculate $\sin^2\theta = t(t-1)$ where $t \equiv (1 - \cos\theta) = \frac{m_e c^2 (1-\varepsilon)}{E_0 \varepsilon}$;
4. test the rejection function: if $g(\varepsilon) \geq r''$ accept ε, otherwise go to (i).

The polar angle θ is deduced from the sampled ε value and in the azimuthal direction the angular distributions of both the scattered photon as the recoil electron are considered to be isotropic.

4.4 Variance Reduction Techniques

Variance reduction is a procedure used to increase the precision of the estimates that can be obtained for a given number of iterations and to decrease the time required to compute a given number of events at the detector. Every output random variable from the simulation is associated with a variance which limits the precision of the simulation results. In order to make a simulation statistically efficient, i.e., to obtain a greater precision and smaller confidence intervals for the output random variable of interest, variance reduction techniques can be used. Detailed description of some techniques used can be found in: [Zaidi, 1999; Haynor, 1998; Zubal & Harrell, 1991; Salvat *et al.* , 1999].

4.5 Monte Carlo Packages for Nuclear Medicine

Several Monte Carlo computer codes for the simulation of radiation transport are available in the public domain. The majority of Monte Carlo codes were initially designed for high energy physics experiments or nuclear physics that later found applications also outside their original domain. For that reason, there is a large community of researchers continuously maintaining and improving these codes as well as contributing to their validation.

Two types of Monte Carlo codes can be used for simulating SPECT and PET: the general purpose codes, which simulate particle transportation and were developed for high energy physics or for dosimetry, and the dedicated codes, designed specifically for SPECT or PET simulations [Buvat & Castiglioni, 2002; Buvat *et al.* , 2005; Buvat & Lazaro, 2006; Andreo & Ljungberg, 1998]. Among the most popular Monte Carlo codes for medical applications are the Electron Gamma Shower (EGS) simulation code [EGS, 2010], the Monte Carlo N-Particle (MCNP) [MCNP, 2010], transport code, the GEometry ANd Tracking (Geant) toolkit [Barca *et al.* , 2003], and the Code System to Perform Monte Carlo Simulation of Electron Gamma-Ray Showers in Arbitrary Materials (PENELOPE) [PENELOPE, 2010]. As an alternative to the general purpose Monte Carlo codes, dedicated codes specifically designed to nuclear medicine simulations are currently also available such as SimSPECT derived from MCNP transport code, PET-EGS based on the EGS4 code [EGS4, 2010], or even the Geant4 Application for Emission Tomography (GATE) [Jan *et al.* , 2004b; GATE, 2010a; Assie *et al.* , 2004; Strul *et al.* , 2003]. Simulation System for Emission Tomography(SimSET) [SimSET, 2010], is one of the most powerful dedicated codes enabling PET and SPECT simulations, has the capability to precisely and efficiently model physics phenomena and basic detector designs (e.g. ring detectors and planar detectors), but it also has limitations with respect to the range of detector geometries that can be simulated. Simulation Of Realistic Tridimensional Emitting Objects (SORTEO) [SORTEO, 2010], and SIMIND [SIMIND, 2010], are other examples of powerful simulation codes for specific applications in PET and SPECT respectively. They have the advantage of being fast with a precise geometry modelling but are less precise than GATE as far as the physics

modelling is concerned. Although, GATE offers additional precision considering physics modelling but is also much more computationally demanding.

Dedicated packages are very powerful due to their specific design-goal but are both not detailed nor flexible enough to allow realistic simulations of emission tomography detector geometries. Moreover, they do not account for time explicitly, which limits their use for modeling time dependent processes such as decay, tracer kinetics, patient and bed motion, dead time or detector orbits. One may therefore prefer to use general purpose nuclear physics codes. The main advantages of these general purpose codes are: they are widely used and extensively tested, they can be regarded as long-term existent as well as supported, and they are continuously evolving and therefore use the best of current hardware and software capabilities. There are fewer limitations on their possible applications, and fewer simplifying assumptions are made: for example, the processes taking place in a collimator can be thoroughly simulated whereas dedicated codes often use a parametric model. Next to that, time-dependent processes can be simulated and their non-specific design also offers the opportunity to implement future developments in SPECT and PET cameras, whereas dedicated codes are limited by the time of their design. Therefore a new code-concept was designed as an upper layer for the Geant4 nuclear physics code [Geant4, 2010; Agostinelli *et al.* , 2003; Barca *et al.* , 2003], and was tuned for use in nuclear medicine, more specifically to fulfill its role as a simulation platform for PET and SPECT incorporating all Geant4 features including well-validated physics models, basic event timing information, geometry modeling tools, visualization, and a scripting language for commanding the simulation. Object-oriented software design was envisaged to ensure high modularity and re-usability and the implementation effort was shared by a large research community in order to provide long-term support and maintenance.

Chapter 5 will provide a detailed discussion demonstrating the flexibility and accuracy of this simulation platform named GATE.

Following the review by Zaidi [Zaidi, 1999], the applications of the Monte Carlo method in nuclear medical imaging cover almost all topics including detector modelling and systems design, image correction and reconstruction techniques, internal dosimetry and pharmacokinetic modelling, with an increasing enthusiastic interest in exotic and exciting new applications such as online PET monitoring of radiation therapy beams. The use of Monte Carlo techniques in the last two areas falls outside the scope of this thesis whereas applications in other fields are only briefly summarized in the following sections given the huge amount of literature available today. With the rapid development of computer technology, Monte Carlo-based modelling in a clinical setting is becoming practical.

Part III

Materials & Methods

Chapter 5

The GATE Platform

GATE is a Monte Carlo simulator (object-oriented simulation platform) based on Geant4 libraries (a generic Monte Carlo code), providing a scripting interface with a number of advantages for the simulation of SPECT and PET systems, including the description of source decay phenomena, moving detector components and time management [Assie *et al.* , 2004; Jan *et al.* , 2004b]. Since the code is based on Geant4, it profits from the validation of the underlying physics components including testing from a very large scientific community. At the same time, the scripting interface provides a convenient platform for most of the users to create their own simulation of emission tomography experiments and complicated emission tomography system designs.

The use of GATE facilitates the description of the different components necessary for the accurate modelling of a PET system, starting from the geometry configuration, up to the creation of a processing chain for the detected events. Analytical phantoms can also be defined through the use of these basic structures, while voxelized sources can be equally employed in order to represent realistic patient imaging conditions. The physics processes are based on Geant4 libraries including the modelling of radioactive source decays and particles interactions for standard and low energies. Users may also interactively select which gamma-ray interactions should be considered (photoelectric effect, Compton and Rayleigh scattering, and gamma-ray conversion), and may specify the energy cuts applied to the production of secondary gamma-rays and electrons. In addition, Geant4 material libraries in combination with user defined material tables are used to cover all of the object compositions necessary for the modelling of a system. A number of modules are available for modelling the detection process, going from the detection of the gamma-rays by the scintillating crystals (singles) to the detection of coincidences in PET. Simulation data results may be stored into multiple output files with different file formats. Time-dependence is taken into account at all steps of the simulation, so that realistic simulations of the acquisitions count rates and source decay can be achieved under dynamic configurations (e.g. rotation detectors or evolving bio-distributions).

GATE has been developed since 2001 by a consortium of international institutes/laboratories without any specific financial support, and has been publicly released in 2004. A public release of GATE licensed under the GNU Lesser General Public License (LGPL) can be downloaded at the electronic address: `http://www.opengatecollaboration.org`.

GATE simulation framework constitutes the basis for the studies carried out through this thesis. The present chapter focus on the description of the GATE tools, its organization and main capabilities. The research presented in this thesis was developed using different versions of GATE from version 2.2.0, released in 3 August 2005 to version 4.0.0, released in 20 August 2008. Therefore, in this chapter we will describe the main features of these versions of GATE. The recent version of GATE is the 6.0.0, released in 25 February 2010, which includes some specific tools for radiation therapy (RT) applications [GATE, 2010b]. The documentation in which this chapter is based in the GATE's documentation, source code comments and the GATE code itself [Jan *et al.* , 2008; GATE, 2010a; Jan *et al.* , 2004b].

5.1 Main Features

5.1.1 Software Architecture

GATE code is written in C++. It's design is a modular structure built on three fundamental layers:

1. the core layer defines the basic mechanisms available in GATE for geometry definition, time management, source definition, digitization, and data output;

2. the application layer is composed of classes derived from the base classes to model specific objects or processes;

3. and the user layer which enables the user to simulate a setup through the use of scripting, Figure 5.1. Each of these functionalities has its own messenger that translates the command to a straightforward instruction. Accordingly, a complete nuclear medicine experiment, including the camera geometry, the phantom geometry, detector electronics, the passing of time and the kinematic parameters, the output format, the physics processes, and the radioactive sources, can be defined using this particular script language.

The GATE developer layer consists of the core layer and the application layer. It is built from the various classes that provide the most general features of GATE. These classes define which tools are available, what developers can do, and how they can do it. The core layer includes some base classes that are common or even mandatory in all Geant4 based simulations, such as those involved in the construction of the geometry, the interaction physics, the event generation, and the visualization management. In addition, the core layer includes classes that are specific to GATE simulations, such as the GATE virtual clock for time management. Thus, the core layer defines the basic mechanisms available in GATE for geometry definition, time management, source definition, detector electronics modelling, and data output. The application layer is composed of classes derived from the base classes of the core layer to model specific objects or processes. Thus, the range of features available in GATE can increase as new application classes are developed, while the general structure remains unaffected [Jan *et al.* , 2003; Rodrigues *et al.* , 2004; Lazaro *et al.* , 2004; Archambault *et al.* , 2003].

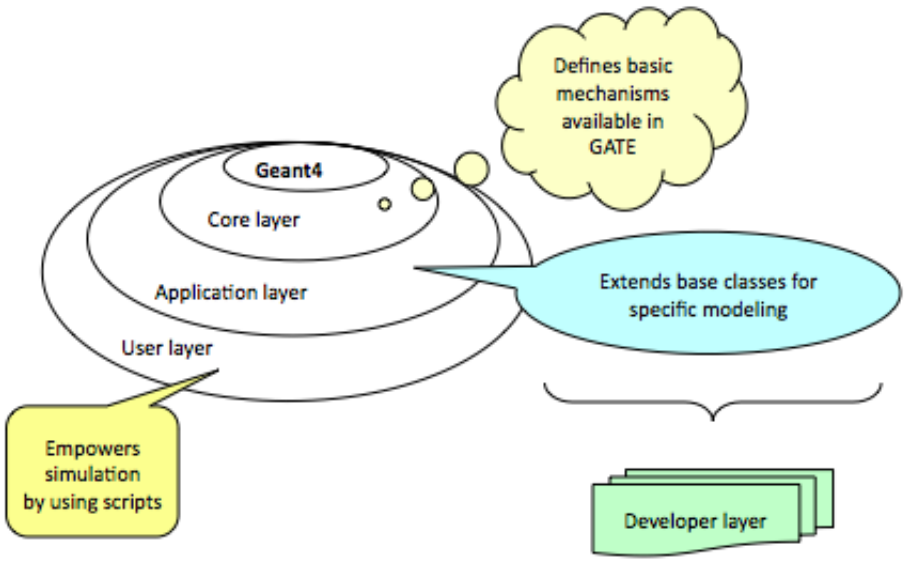

Figure 5.1: Sketch of the layered architecture of GATE. Adapted from [Jan *et al.* , 2004b].

5.1.2 Geometry

The definition of geometry is a key step in designing a simulation because it is through the geometry definition that the imaging device and object are described. Particles are then tracked through the components of the geometry.

The world is the only volume already defined in GATE when starting a macro. All volumes are defined as daughters or grand-daughters of the world. The world volume is a typical example of a GATE volume and has predefined properties. The world volume is a box centred at the origin. For any particle, tracking stops when it escapes from the world volume. The world volume can be of any size and has to be large enough to include all volumes involved in the simulation.

A logical volume is defined by all its properties except its position in the world. These properties include its name, shape, size, and material composition. When logical volumes are placed at specific positions they form physical volumes. Repeaters replicate and then place logical volumes at multiple positions and orientations to form physical volumes. Repeaters are basically elementary geometrical transformations such as rotations and translations applied in succession.

Complex structures are created by combining ring, linear, quadrant and cubicarray repeaters. Accessing a material database file is the primary method for assigning material properties to volumes. This file contains all material parameters required by Geant4 to calculate the interaction cross-sections.

The GEANT geometry architecture requires the geometry to be static during a simulation. However, the typical duration of a single event (e.g. ps for the particle transport, μs for scintillation, or ms for the response of the electronics) is very short when compared to most of the geometrical changes to be modelled (e.g. movements of the phantom or of the detector or bio-kinetics). Therefore, the elements of the geometry are considered to be at rest during each time-step. Between every time-

step, the position and the orientation of a subset of daughter volumes can be changed to mimic a movement such as a rotation or a translation. These displacements are parametrized by their velocity. Hence, the amplitude of the volume displacement is deduced from the duration of the time-step multiplied by the velocity of the displacement. Given the speed of the components of the geometry, it is the responsibility of the user to set the time step duration short enough in order to produce smooth changes. A volume can be moved during a simulation using five types of motion: rotation, translation, orbiting, wobbling and eccentric rotation.

Specific guidelines with respect to the geometrical hierarchy must be followed. Most PET scanners are built following comparable concepts: one or more rings, each ring consisting of several scintillator blocks, each block being subdivided in crystal pixels, etc. This means that most of these geometrical concepts are common to many different imaging systems. To facilitate the geometry definition process and to provide a dedicated hierarchical output, predefined global systems are used.

5.1.3 Systems

A System is a key-concept of GATE. It provides a template of a predefined geometry to simulate a scanner. Families of geometry like systems sharing the same general geometrical characteristics can be so derived from these templates. Each system can be described by components organized in a tree level structure, each component having its own specific role or ordering. As for an example of the `cylindricalPET` scanner system, the geometrical volumes containing crystals are grouped in matrices, themselves assembled in submodules and modules. At the top level of this structure, the sectors composed of modules are `repeated` on a cylindrical surface to build up the whole device. Thus, one familly of PET scanners as shown in Figure 5.2 can be composed of such volumes called `rsectors`, `modules`, `submodules`, `crystal` and `layer`. Different systems are available in GATE : `scanner`, `SPECTHead`, `cylindricalPET`, `ecat`, `CPET` and `OPET`, which can be used to simulate most of the existing tomographic imagery devices.

From the user's point of view, the main property of a system is that its geometric hierarchy is automatically accepted by the corresponding data output formats (see Table 5.1).

5.1.4 Physics process

The simulation proceeds by steps and the purpose of the implementation of the physics is to decide where these steps take place and which interactions are to be invoked at each step. This is done by using pseudorandom numbers which are uniformly distributed in the interval $[0, 1]$ to calculate the mean free path or interaction length for each interaction that the particle is allowed to undergo. The interaction that proposes the shortest mean free path is chosen. The step length can also be restricted to preserve precision or to prevent the particle from crossing a boundary in the geometry in a single step.

The electromagnetic interactions used in GATE are derived from Geant4 [Agostinelli *et al.* , 2003; Allison *et al.* , 2006]. There are two types of packages available to simulate electromagnetic

System	Components and its shape		Available outputs
scanner	level1 level2 level3 level4 level5	geometry not fixed	Basic output : Ascii or ROOT, coincidences only for PETscanner.
CTScanner	block pixel	box box	Binary CT image; Basic output : Ascii or ROOT.
cylindricalPET	rsector module submode crystal layer	box box box box box	Basic output : Ascii, ROOT and Raw. Specific: LMF.
CPET	crystal	cylinder	Basic output : Ascii, ROOT and Raw.
SPECThead	crystal pixel	geometrynot fixed	Basic output : Ascii, ROOT and Raw. Specific: PROJECTIONSET or INTERFILE, no coincidences.
ecat	block crystal	box box	Basic output : Ascii, ROOT and Raw. Specific: SINOGRAM or ECAT7.
ecatAccel	block crystal	box box	Basic output : Ascii, ROOT and Raw. Specific: SINOGRAM or ECAT7
OPET	rsector module submode crystal layer	box box box box wedge	Basic output : Ascii, ROOT and Raw. Specific: LMF.

Table 5.1: Different systems available in GATE and their characteristics. In the second column are listed some of the keywords that are also used in a simulation (see also [Jan *et al.* , 2008] for a complete list). The shape in the third column describes the mother volume, composed of daughter volumes: a box means a box shaped mother volume containing an array of daughter boxes, a cylinder mother volumes will contains cylinders. Cylinders are understood here as tube sectors defined by an inner and outer radius. Adapted from [Jan *et al.* , 2008].

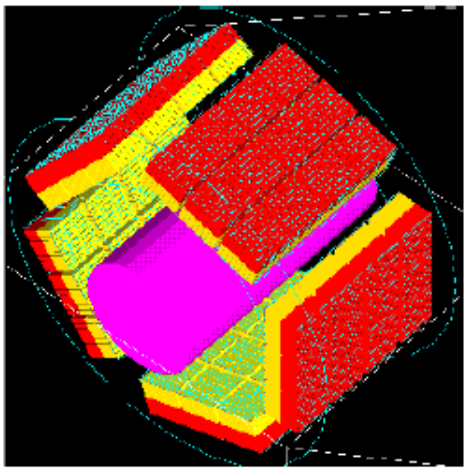

Figure 5.2: Picture of a phantom and a `cylindricalPET` system composed of 5 `rsectors`, 4 `modules` (repeated along Z axis), 3 `submodules` (repeated along Y axis), 64 `crystals` (8×8) and 2 `layers` (red and yellow). Adapted from [Jan *et al.* , 2008].

processes: the Standard Energy Electromagnetic Processes (SEP) and the Low Energy Electromagnetic Processes (LEP). By low-energy is meant the regime below 100 GeV, in which respect both models are, in principle, applicable in the present context. Both packages manage electrons, positrons, γ-rays, X-rays, optical photons, muons, hadrons, and ions. When using the LEP package, the treatment of photons and electrons is extended and verified down to 250 eV and includes Rayleigh scattering. This is the most accurate package for biomedical applications but comes at the price of increased computing time.

A complete description of the physics used in Geant4 can be found in [Manual, 2010]. Overview reports of the physics models and their validation are given e.g. in [Amako *et al.* , 2004; Chauvie *et al.* , 2000, 2001; Cirrone *et al.* , 2003].

5.1.4.1 Standard Energy Electromagnetic Processes (SEP)

In general, the standard electromagnetic physics model of Geant4 covers the energy range from 10 keV to several PeV and is mainly used for high-energy and nuclear physics applications. In the standard electromagnetic physics model, the photon induced processes are Compton scattering, photon conversion and photoelectric effect. The electron/positron induced processes are ionisation, bremsstahlung and positron-electron annihilation. The ionisation class for electrons and positrons calculates the continuous energy loss due to ionisation and simulates the discrete part of the ionisation, i.e. Moller scattering, (e^-e^-), Bhabha scattering , (e^+e^-), and δ-ray production. The bremsstrahlung class calculates the continuous energy loss due to soft bremsstrahlung and simulates discrete bremsstrahlung.

The multiple scattering model is based on the Lewis theory [Lewis, 1950]. This model is a condensed multiple scattering algorithm which is invoked at the end of the step to compute a correction to the mean path length and also the lateral displacement of the track. The model uses functions to determine the angular and spatial distributions after the step. The functions are chosen as to give

the same moments of the angular and spatial distributions as the Lewis theory.

A special case of process in Geant4 is the transportation process. This class is responsible for determining the geometrical limits of a step and handles the crossing of geometric boundaries. It calculates the distance to the next volume in the geometry and proposes this distance as a possible step length in the same way as the physics processes propose the 'physical' step lengths using their cross sections. The transportation process requires that the particle should always stop at a boundary, thus setting an additional restriction on the step length, as was mentioned above.

5.1.4.2 Low Energy Electromagnetic Processes (LEP)

The low-energy electromagnetic physics package is an extension to the standard physics code and uses shell cross section data rather than their parametrizations (as they are used in the standard model). A lowest validity limit of 250 eV was chosen to allow for the treatment of characteristic K-shell emission down to Z=6. The model covers the interactions of photons and electrons in materials with atomic number between 1 and 100. This package does not provide a new implementation of processes induced by positrons. They are treated by the same classes as in the standard electromagnetic physics package. The extended classes of the model treat the following interactions: Compton Scattering, Rayleigh Scattering, Photoelectric Effect, Ionisation and Bremsstrahlung. Photon conversion has also been implemented with the same methodology for the total cross section calculation as the processes above. The model also provides implementations for atomic relaxation (fluorescence and Auger electrons).

The implementation of all processes is done in two phases: (a) calculation of the total cross sections and (b) generation of the final state. Both phases are based on data from the following libraries: Evaluated Photon Data Library (EPDL), Evaluated Electron Data Library (EEDL) and Evaluated Atomic Data Library (EADL) [Libraries, 2010].

The energy dependence of the total cross section is derived for each process from the evaluated data libraries. The total cross-section at a given energy is calculated by interpolation between the closest lower and higher energies for which data are available [Apostolakis *et al.* , 1999]:

$$\log(\sigma(E)) = \log(\sigma_1)\frac{\log(E_2)-\log(E)}{\log(E_2)-\log(E_1)} + \log(\sigma_2)\frac{\log(E)-\log(E_1)}{\log(E_2)-\log(E_1)} \tag{5.1}$$

The final state is defined by the four-momenta of the final state products. These are determined according to distributions derived from the evaluated data.

Compton Scattering

The total cross section at energy E is calculated by Equation 5.1. The scattered photon energy is sampled using the distribution:

$$P(\varepsilon, q) = \Phi(\varepsilon)\cdot F(q) \tag{5.2}$$

where Φ is the Klein-Nishina formula:

$$\Phi(\varepsilon) \cong \left(\frac{1}{\varepsilon} + \varepsilon\right)\left(1 - \frac{\varepsilon \sin^2(\theta)}{1+\varepsilon^2}\right) \tag{5.3}$$

where $F(q)$ are scattering functions, ε is the ratio between the scattered photon energy and the incident photon energy, θ is the scattering angle and q is the momentum transfer:

$$q = E \sin^2\left(\frac{\theta}{2}\right) \tag{5.4}$$

The form factors are calculated from the data in the EPDL library. The angular distribution of the scattered photon is obtained in the same way.

Rayleigh Scattering

The total cross section at energy E is calculated by Equation 5.1. The angular distribution of the scattered photon is given by the relation:

$$\Phi(E, \theta) = \left[1 + \cos^2(\theta)\right] F^2(q) \tag{5.5}$$

where q is the momentum transfer, given by Equation 5.4, and $F(q)$ is a form factor obtained from the EPDL library.

Photoelectric Effect

The total cross section at kinetic energy T is calculated by Equation 5.1. The cross sections of the subshells are calculated in the same way and they are used to select the subshell from which the electron will be emitted. The electron is emitted at the direction of the incident photon. The interaction leaves the atom in an excited state with excitation energy equal to the binding energy of the emitted electron. The atom returns to the ground state by emitting fluorescence photons. The probabilities for a transition to lower energy subshells are extracted from the EADL library. The fluorescence photons are emitted isotropically[1].

Bremsstrahlung

The total cross section at kinetic electron energy T is calculated by Equation 5.1. The probability for the emission of a photon of kinetic energy t is calculated from:

$$P(T, t) = \frac{a(T)}{t} + b(T) \tag{5.6}$$

[1] Isotropic radiation has the same intensity regardless of the direction of measurement

The coefficients a and b are obtained by fitting the energy distributions of the emitted photons at few T values as they are available at the EEDL library. The values of the coefficients at different incident electron energies are calculated by interpolation. The direction of motion of the electron is not changed in the interaction. There are three models for the angular distribution of the emitted photons. In the present simulations, the Tsai cross section was used [Tsai, 1974].

Ionisation

In the case of ionisation, the total cross section for an incident electron of kinetic energy T is calculated as the sum of the partial cross sections for all the subshells of an element. The partial cross sections are calculated by Equation 5.1 using the cross section data in the EEDL library. The partial cross sections are also used to select the shell from which the secondary electron will be emitted. The probability of emission of a δ-ray with kinetic energy t from a subshell of binding energy B_i is given by:

$$P(T,t,B_i) = \sum_{j=2}^{7} \frac{a_j(T)}{(t+B_i)^j} \tag{5.7}$$

for $T < T_0$ and

$$P(T,t,B_i) = \frac{c(T)}{t^2} \tag{5.8}$$

for $T > T_0$, where T_0 is a parameter. The coefficients in Equations 5.7 and 5.8 are calculated by fitting EEDL data and their energy dependence is calculated by interpolating from the values resulting from the fits. The angles of emission of the primary and secondary electrons are calculated by energy and momentum conservation. The deexcitation of the atom proceeds as in the case of the photoelectric effect (fluorescence photons and Auger electrons).

5.1.4.3 Production Cuts

The Geant4 does not use tracking cuts, i.e. all particles are tracked to zero kinetic energy unless they reach the limits of the World. Photons and secondary electrons are, however, generated only above a given kinetic energy threshold (production cut-off). This is done as to avoid the production of a large number of secondary particles, which would deteriorate the performance of the simulation without enhancing the accuracy of the calculations [Agostinelli *et al.* , 2003].

The cut functions in GATE define some thresholds for the production of secondary particles. It has 2 sorts of cuts, the cut in range and the cut in energy. Concerning the cut in range, this is the definition of the minimal distance for allowing production. This cut is not applied close to the volume boundaries and it is not applied for some particles. The cut in energy defines the minimum energy for allowing production. This cut is always applied for low energy processes. GATE allows the user to set three types of cuts that are applied on electron, X-ray and δ-ray (low-energy electrons which are produced by some atomic interactions).

5.1.4.4 Positron Emission

GATE includes 2 modules dedicated to PET. The first uses the von Neumann algorithm to randomly generate the positron energy according to the measured β^+ spectra. This method greatly increases the speed of the simulation by bypassing the decay of radionuclides process used by Geant4. The β^+ spectra of 3 commonly used radionuclides (^{11}C, ^{15}O and ^{18}F) have been parametrized in GATE according to the Landolt-Börnstein tables. The second module deals with the acollinearity of the two annihilation photons, which is not accounted for in Geant4. In GATE, acollinearity is modelled using a 0.58º FWHM Gaussian blur. This width corresponds to experimental values measured in water.

5.1.5 Radioactive Sources

The Geant4 General Particle Source (GPS) [GPS, 2010] is used to shoot particles of a given type to a given direction with a given kinetic. A source in GATE is defined by its particle type (e.g. radionuclide, gamma, positrons, etc.), position (volume), direction (solid angle), energy (spectrum), and activity. The lifetime of a radioactive source is usually obtained from the Geant4 database, but it can also be set by the user to approximate a decay source through the emission of its decay products (e.g. positrons or gammas).

The activity determines the decay rate for a given source during the simulated acquisition time. Radioactive decay of radionuclides with secondary particle emission is performed by the Geant4 Radioactive Decay Module (RDM) [RDM, 2010] which has been modified so that GATE source manager maintains control over the definition of decay time. Continuous event time flow is obtained by using a virtual clock that defines an absolute time t used to initialize the Geant4 internal tracking time. Random time intervals δt between events that occur at time t are sampled from a exponential distribution:

$$p(\delta t) = A(t)\, e^{(-A(t)\delta t)} \tag{5.9}$$

where $A(t) = A_0 e^{\left(\frac{(t-t_0)}{\tau}\right)}$ is the source activity at time t, A_0 is the user defined source activity at time t_0 and τ the lifetime. When the resulting decay time exceeds the end of the current time step, the run is terminated and a new one is started, allowing for the synchronization of the sources with the geometrymovements. Multiple sources can be defined with independent properties. For each event, a proposed time interval is sampled for each source according to Equation 5.9, and the shortest one is chosen for the primary generation. The overall behavior of this mechanism is such that, at all times, the relative importance of each source is proportional to its activity, while the overall time interval sampling is determined by the total activity of all sources.

Voxelized phantom or patient data can be used as sources to reproduce realistic acquisitions: emission data are converted into activity levels, and GATE can read in voxelized attenuation map and converts the gray scale into material definitions using an analogous translator.

5.1.6 Voxellized Phantoms and Voxellized Sources

GEANT4 offers two convenient methods to describe multiple copies of a volume inside a mother volume: replicas and parameterized volumes. The parameterized volumes method offers several advantages over replicas such as: voxels that can be varied in size, shape and material, voxels not entirely filling the envelope, and visualization attributes. The parameterized volume method is available in GATE for voxellized phantoms and is preferred over replicas.

To create a parameterized object it's needed to use the option `parameterizedBoxMatrix`. The `parameterizedBoxMatrix` supports the `imageReader` and the `interfileReader` as well as the range or tabulated translator. As with other objects, placement and moves commands can be specified. To introduce a phantom two possibilities as able: one can choose to read in a ASCII file or an Interfile image. In the first way is need to declare (by scripting) that the voxelized phantom will be entered using image data (ASCII format) before insert the ASCII file that contains all necessary numbers for all pixels (using the `imageReader` option). Moreover is necessary to specify the material attenuations by using the tabulated translator that it's able to interpret the data table materials. The phantom is then converted to material definitions. The Interfile input is more user friendly, and it's necessary to use when the phantoms doesn't have a header within your image file. In this case it's necessary use the `InterfileReader` to read the interfile data file. In the same way that the ASCII format, with the interfile reader the users need to specify the phantom material, in this case by using the range translator option. The material database can be update with the phantom materials or new materials related to the scanner geometry in use (the file `GateMaterials.db` contains all material parameters required by Geant4 to calculate the interaction cross-section and can be modify). A detailed descritpion about phantoms usage within GATE can be found in Chapter 7 and in reference [Jan *et al.* , 2008].

The current implementation of voxellized phantoms using Geant4 parameterization supports phantom dose calculations and voxel visualization attributes on a per material basis. As an output it's possible to have binary files with the dose expression in the phantom (binary file writing in 4 bytes number format containing the dose in cGy) and emission maps (ROOT file) [Taschereau & Chatziioannou, 2007; Visvikis *et al.* , 2006b; R. & Chatziioannou, 2005].

Depending on the phantom dimensions, the use of a `parameterizedBoxMatrix` may increase memory usage by up a factor of 2 and increase CPU time by 5 to 50%. As phantom resolution increases, the number of voxels can become very large and a significant amount of memory may be required. For most applications however, high resolution is not required everywhere in the phantom but only where necessary to keep smooth boundaries between phantom structures. The `compressedMatrix` phantom object can be used instead of the`parameterizedBoxMatrix` to generate a compressed phantom where voxel size is variable. With the compression algorithm, all adjacent voxels of the same material are fused together to form the largest possible rectangular voxel. A compressed phantom uses less memory and also less CPU.

To save time when simulating voxelized phantoms, new navigation algorithms are often developed. Here the new one is called the Regular Navigator (developed in Geant4.9.1 version) and has been implemented in GATE version 4.0.0 (not used in the results presented) [Jan *et al.* , 2008].

The voxelized attenuation geometries (phantoms) can be the emission sources following the two

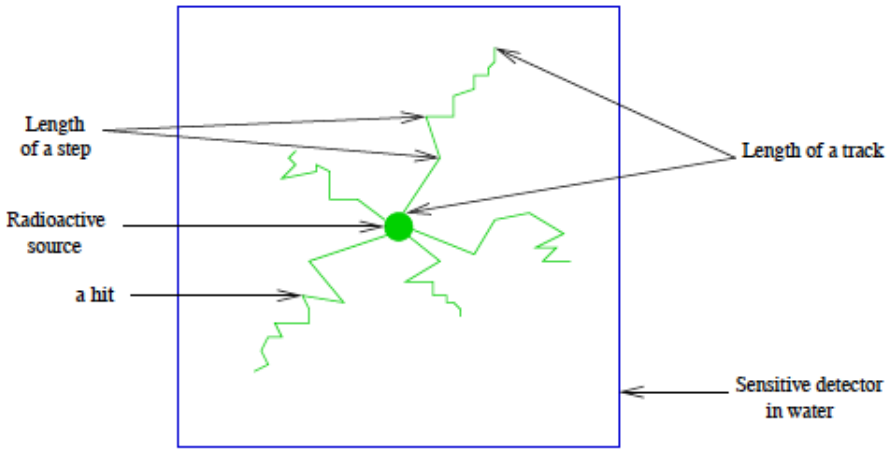

Figure 5.3: Particle interactions in a sensitive detector. Adapted from [Jan *et al.* , 2008].

strategies described. The scales have is translated to activity distributions, in this case is need to use an analogous translator. In an activity table or range is need to define the number of subdivisions followed by their range and the actual activity for that voxel or voxels range (in Bq units).

From the second to last release (version 5.0.0 from 10 June 2009) new commands to define in the simulation set-up and TACs in a voxelized phantom are available. With this approach, users could combine and manage organ motions and tracer kinetics. More information can be found in [Jan *et al.* , 2009; GATE, 2010b].

5.1.7 Sensitive Detectors

Once a model has been defined for the scanner through the construction of a system, the next step is to attach a sensitive detector to some volumes of the geometry. As in any Geant4 simulation, these sensitive detectors are used to store information on interactions of a particle in the matter (hits) using information from steps along a particle track. A hit is a snapshot of a physical interaction of a track in a sensitive region of the detector, Figure 5.3 illustrates these notions. Hits store various information associated to a step object, the information can be: the energy deposition of a step, geometrical information, position and time of a step, etc.

GATE records and stores information related to the hits only for those volumes that are attached to a sensitive detector. All the information regarding the interactions occuring in non-sensitive volumes is lost. Two sensitive detectors are defined in GATE:

- The `crystalSD` allows to record information on interactions inside the volumes belonging to a scanner for instance, crystals or collimators.
- The `phantomSD` may be used to record information on Compton and Rayleigh interactions taking place in the scanner FOV. This information is then used to estimate whether a photon reaching a detector is a direct or a Compton-scattered photon. Thus, in PET, the `phantomSD`

is currently the only way to discriminate scattered from true coincidences. To simulate low energy X-ray acquisitions (for example: mammography acquisitions from 7 to 28 keV), information concerning Rayleigh interactions is significant. Using this type of sensitive detector.

A complete definition of the simulation context normally involves performing both series of attachments: one series of volumes is attached to the `phantomSD`, another series of volumes is attached to the `crystalSD`.

5.1.8 Time Management and Movements

One of the distinctive features of GATE is the management of time-dependent phenomena [Strul *et al.* , 2003; Santin *et al.* , 2003]. The synchronization of the source kinetics with the movement of the geometry thus allows for the simulation of realistic acquisition conditions including patient movement, respiratory and cardiac motions, scanner rotation, or changes in activity distribution over time. Dealing with time in GATE includes: (a) defining the movements associated with the physical volumes that describe the detector and phantom; (b) describing the radioactive sources; and (c) specifying the start and stop times of the acquisition (which are equivalent to the start and stop times in a real experiment).

The Geant4 geometry architecture requires the geometry to be static during a simulation. However, the typical duration of a single event is very short when compared to movements in the geometry model or bio-kinetics. Movements are synchronized with the evolution of the source activities by subdividing the acquisition time frames (typically of the order of minutes or hours) into smaller time steps. At the beginning of each time step, the geometry is updated according to the requested movements. During each time step, the geometry is held at rest and the simulation of the particle transport proceeds. Within the time steps, the source is allowed to decay so that the number of events decreases exponentially from one time step to the next, and within the time steps themselves. The proper timing of the simulated event sequence is a key feature for modeling time-dependent processes such as count rates, random coincidences, event pile-up, and detector deadtime [Simon *et al.* , 2004]. Between time steps, the position and the orientation of a subset of daughter volumes can be changed to mimic a movement such as a rotation or a translation. These displacements are parametrized by their velocity. It is the responsibility of the user to set the time step duration short enough to produce smooth changes. Combinations of translations and rotations allow the simulation of complex acquisition trajectories of the detectors such as parameterized eccentric rotations.

Geant4 does not allow the movement of sources[2]. Therefore, in GATE, an emission volume is defined so that it encompasses the actual source's volume throughout its range of displacement. To enable movement of the activity distribution, an additional volume is defined to confine the emission within the intersection of the emission and the confinement volumes. This confinement volume defines the shape and size of the actual source and moves within the emission volume.

[2]Real time motion management for voxellized source and phantom is available in the last GATE version: version 5.0.0 released in 10 June 2009 [GATE, 2010a].

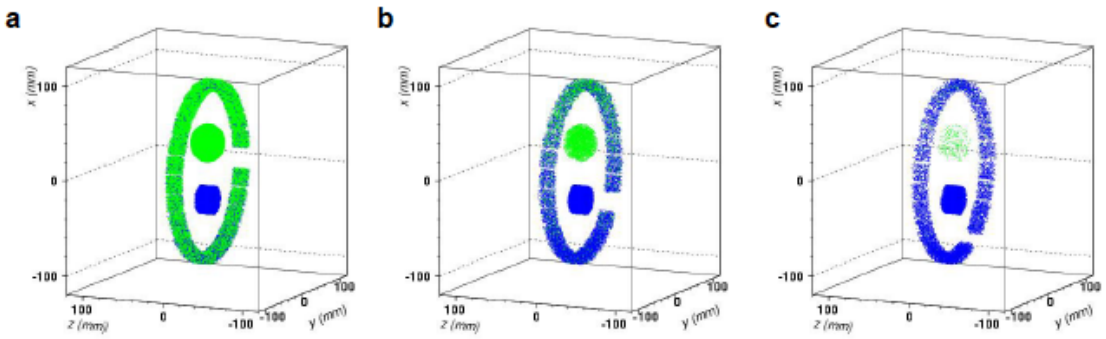

(a) Distributions of counts registered for the two decaying sources throughout three time-frames: (a) 0-2 min, (b) 7-9 min (c) 14-16 min. On all time-frames, one detector has been hidden (gap in the detector ring) to show the scanner rotation steps. Adapted from [Santin *et al.* , 2003].

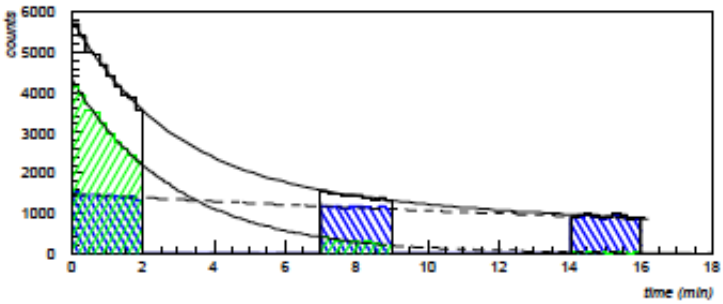

(b) Counts registered for the decay of sources of ^{15}O (rightward filling pattern) and ^{11}C (leftward pattern) throughout three time-frames (0-2, 7-9 and 14-16 min). The dashed lines are theoretical decay curves from the isotope half-lives. The top curve shows the total number of counts from both sources. Adapted from [Santin *et al.* , 2003].

Figure 5.4: Management of time-dependent phenomena with GATE.

5.1.9 Digitizer and Readout Parameters

The purpose of the digitizer module is to simulate the behavior of the scanner's detectors and signal processing chain. This involves the conversion of the charged particle and photon interactions into energy bins, detection positions, and coincidences [Kerhoas-Cavata & Guez, 2006]. To do this, portions of the scanner geometry are designated as sensitive detectors, which record interactions within these regions. The digitizer chain then processes these recorded interactions and produces counts and coincidences. Sensitive detectors are used to store information about particle interactions (hereafter referred to as hits) within volumes. GATE only stores hits for those volumes that have a sensitive detector attached.

5.1.9.1 From Particle Detection to Coincidences in GATE

GATE makes use of Geant4 to generate particles and transport them through the different materials. This mimics the physical interactions between particles and matter. The information generated during this process is used by GATE to simulate the detector pulses (digits), which correspond to

the observed data. The digitizer represents the series of steps and filters that make up this process. The typical data-flow for an event is composed as follows:

1. A particle is generated, with its parameters, such as initial type, time, momentum, and energy.
2. An elementary trajectory step (referred to in Geant4 simply as a step) is applied. A step corresponds to the trajectory of a particle between discrete interactions (i.e. photoelectric, Compton, pair production, etc). During a step the changes to particle's energy and momentum are calculated. The length of a step depends upon the nature of interaction, the type of particle and material, etc. The calculation of step length is complex and is mentioned here only briefly.
3. If a step occurs within a volume corresponding to a sensitive detector, the interaction information between the particle and the material is stored. For example, this information may include the deposited energy, the momentum before and after the interaction, the name of the volume where the interaction occurred, and so on. This set of information is referred to as a hit.
4. Steps 2 and 3 are repeated until the energy of the particle becomes lower than a predefined value, or the particle position goes outside the predefined limits. The entire series of steps form a simulated trajectory of a particle, that is called a track in Geant4.
5. The amount of energy deposited in a crystal is filtered by the digitizer module. The output from the digitizer corresponds to the signal after it has been processed by the Front End Electronics (FEE). Generally, the FEE are made of several processing units, working in a serial and/or in parallel. This process of transforming the energy of a hit into the final digital value is called digitization, and is done by the digitizer portion of the GATE architecture. Each processing unit in the FEE is represented in GATE by a corresponding digitizer module. The final value obtained after filtering by a set of these modules is called a single. Each transient value, between two modules, is called a pulse.

This process is repeated for each event in the simulation in order to produce one or more sets of singles. These singles can be stored into an output file (as a ROOT tree, for example). Once this list is created, a second processing stage can be inserted to sort the singles list for coincidences (in case of PET systems). To do this, the algorithm searches in this list for a sets of singles, that are detected within a given time interval (the called coincident events). Finally, the coincidences data can be filtered-out (if so required) to mimic any possible data loss which could occurs in the coincidence logical circuit or during the data transportation. As for the singles data, the treatment is done by specifying a list of generic modules to apply to the coincidence data flow.

5.1.9.2 The Digitizer

The information contained in the hit does not correspond to what is accessible by a real detector. To simulate the digital values (pulses) that result from the output of the FEE, the sampling methods of the signal must be specified. In order to do this, a number of digitizer modules are available and are described below. Moreover, in the case of PET analysis, the trigger logic is based on one

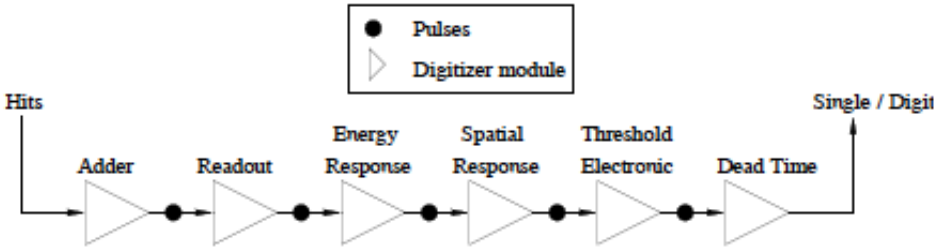

Figure 5.5: The digitizer is organized as a chain of several modules that processes the hits to yield a single, which represents a physical observable. Adapted from [Staelens, 2004].

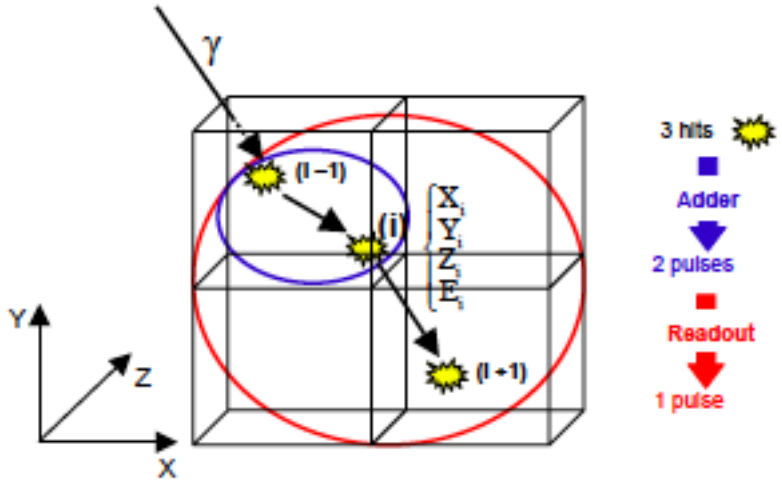

Figure 5.6: Actions of both the `adder` and `readout` modules. The `adder` module transforms the hits into a pulse in each individual volume, and then the `readout` module sums a group of these pulses into a single pulse at the level of depth as defined by the user. Adapted from [Lazaro, 2003].

or more decisions defined by the user that depend upon physically observable quantities such as, energy thresholds and coincidence times.

The role of the digitizer is to build, from the hits information, the physical observables, which include energy, position, and time of detection for each particle. In addition, the digitizer must implement the required logic to simulate coincidences during PET simulations. Typical usage of digitizer module includes the following actions: simulate detector response, simulate readout scheme and simulate the trigger logic. The digitization consists of a series of signal processors, Figure 5.5. The output at each step along the series is defined as a pulse. Figure 5.6 illustrates the actions of both the `adder` and `readout` modules. Following the hit adder and the pulse reader, which regroup the hits into pulses and then sum pulses, the remaining modules of the digitizer chain transform these pulses into the physical observables of the scanner: the singles. These singles realistically simulate the physical observables of a detector's response to a particle interacting with it. These modules are discussed below.

Energy resolution

The blurring pulse-processor module simulates Gaussian blurring of the energy spectrum of a pulse after the `readout` module. This is accomplished by introducing a resolution, R_0 (FWHM), at a given energy, E_0. By examining a Poisson process, it is seen that the resolution is a function of energy, $R(E)$, that is proportional to $1/\sqrt{E}$. The resolution is equal to:

$$R = \frac{R_0\sqrt{E_0}}{\sqrt{E}} \tag{5.10}$$

To define Gaussian distribution determined by its mean, m, and its standard deviation, σ. The resolution of a Gaussian distribution is given by:

$$R = 2\sqrt{2\ln 2}\frac{\sigma}{m} \approx 2.35\frac{\sigma}{m} \tag{5.11}$$

A more elaborate model is available that propagates the relative variances of the physical processes involved with light collection and detection [Jan *et al.* , 2008].

Energy window

Upper and lower energy thresholds can be set for several energy windows by using multiple processor chains. These thresholds are applied using either a step or sigmoid function.

Spatial Resolution

In PET analysis, coincidence events provide the LORs needed for the image reconstruction. Only the two crystal numbers are transferred by the simulation. The determination of this crystal is based on the crystal with the highest energy deposited. Without additional spatial blurring of the crystal, simulation results will always have a smaller spatial resolution than experimental measurements. This module is only available for the ecat system. The spatial blurring is based on a 2D Gaussian function.

Time resolution

Simulation of time jitter can be obtained using a Gaussian blur of the pulse time.

Noise

Different sources of background noise could exist in a PET/SPECT architecture. For example, the electronic can carry out its own noise, or some crystals used for the detection, such as LSO, contains radioactive nucleus, which can participate to the background detection count rate. Within GATE, the noise module is aimed to add such background events, in a totally generic way, so that any kind of source of noise can be simulated. To achieve this, the energy, as well as the inter-event time interval are chosen randomly, for each event, into user defined distributions.

Deadtime

Both paralyzable (the detector is dead for a period t after every event, even if the event arrives during the dead period of the previous event) and non-paralyzable dead times (the detector is dead for a period t after every event) can be modeled on an event-by-event basis [Simon *et al.* , 2004]. The detailed workings of these models can be found in reference [Knoll, 2000].

Other user defined modules can be added individually to model more specific properties: pile-up[3], light yield, transfer and quantum efficiency and so on. Moreover, at the end of a digitizer chain a coincidence sorter can be added to find pairs of singles that are in coincidence (whenever the time interval between the singles is less than a user-defined coincidence window). Using the event number and the Compton flag, randoms and scatter events can be differentiated from trues. Multiple coincidences and auto-coincidences are also taken into account. A complete readout scheme is shown in Figure 5.7.

5.1.9.3 Digitizer Optimization

In GATE standard operation mode, primary particles are generated by the source manager, and then propagated through the attenuating geometry before generating hits in the detectors, which feed into the digitizer chain. While this operation mode is suited for production simulations, it is inefficient when trying to optimize the parameters of the digitizer chain. In this case, the user needs to compare the results obtained for many different sets of digitizer parameters that are based upon the same series of hits. Thus, repeating the particle generation and propagation stages of a simulation are unnecessary.

The optimization of the digitizer chain parameters is very time-consuming. This is best done by comparing the results from different sets of digitizer parameters using the same series of hits. To perform this specific task, GATE offers an operating mode named DigiGATE. In this mode, hits are read from a data file generated by GATE and fed directly into the digitizer chain. All conditions are kept identical in the simulations including time dependencies.

5.2 GATE Modelled Systems

Validation of Monte Carlo simulated data against real data obtained with PET and SPECT cameras is essential to assess the accuracy of the simulation of nuclear medicine examinations. Several commercial PET systems have been modelled with GATE, as the ECAT EXACT HR+ [Jan *et al.* , 2005a], the ECAT HRRT [Bataille *et al.* , 2004], Hi-Rez [Michel *et al.* , 2006], Philips Allegro [Lamare *et al.* , 2006], General Electric Advance [Schmidtlein *et al.* , 2006], MicroPET P4 [Vandervoort *et al.* , 2005, 2007], microPET® Focus 220 [Jan *et al.* , 2005b] and the Mosaic [Merheb *et al.* , 2007]. The previously cited references provide detailed information about the figures of merit (FOM) used for assessing the consistency between simulated and real data, as well as the major validation results. Overall, these studies illustrate the flexibility and the reliability of GATE for accurate modelling of various detector designs.

5.3 Computing Resources

An important disadvantage of GATE Monte Carlo simulations is the fundamental burden of computation time. Diferent variance reduction techniques (VRTs) are available in order to improve the

[3] Response time of the detector, which is the time that the detector takes to form the signal after the arrival of the radiation.

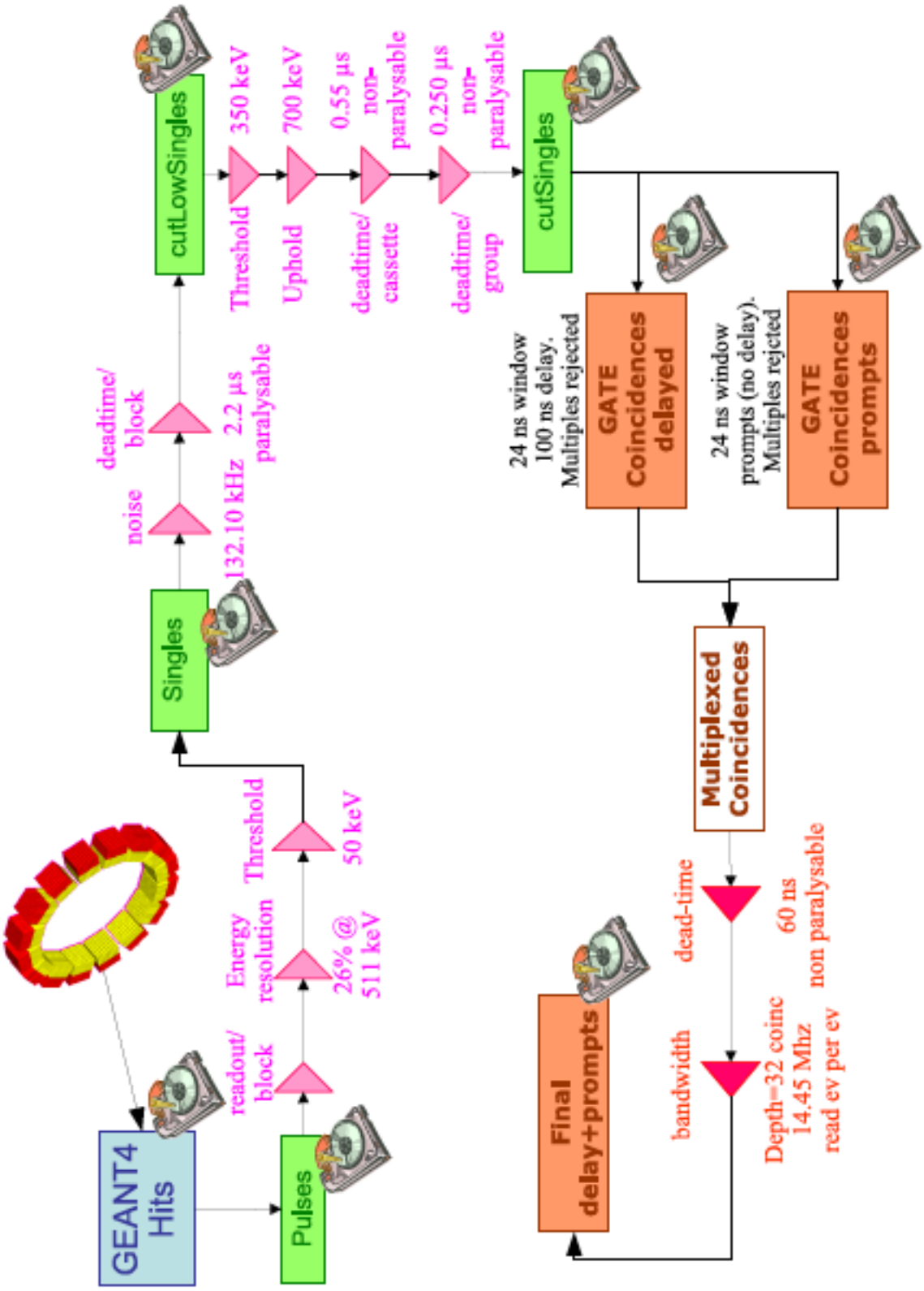

Figure 5.7: Example of a readout scheme. The disk icons represents the data written to the GATE output files. Adapted from [Jan *et al.* , 2008].

efficiency of those simulations. Classical ways to decrease Monte Carlo simulation time are the application of energy and path length cuts, as well as limiting the emission angle. Another technique consists in the incorporation of geometrical importance sampling [Staelens *et al.* , 2006]. Another possible approach is the use of a grid computing environment. A grid environment consists of physical resources (computers, disks and networks) and middleware software that ensures the access and the coordinated use of such resources. The next subsections describes, in full detail, the computing resources used for this work research.

5.3.1 CCRT @ CEA

At the Centre de Calcul Recherche et Technologie (CCRT) the cluster Tantale, Figure 5.8, is part of a bigger cluster environment of an entire research community [CCRT, 2010]. This big cluster environment holds 3 clusters and a common storage system. Tantale is the second largest cluster in terms of processing power (up to 800 GigaFlops), memory capacity (300 GBytes) and local disks capacity (8 TBytes). Tantale is a cluster based on HP hardware with 64 bits Opteron processors. Tantale has 512 computational CPUs distributed over more than 100 servers. All of the servers are interconnected by gigabit interfaces and infiniband[4] [Infiniband, 2010], interfaces in order to be able for users to connect to each server (by means of the gigabit network) and for the servers to connect to the storage system (via Infiniband network) in order to execute Message Passing Interface (MPI) communication (latency of 5 ms and 1GBytes/sec in terms of debit). Regarding hardware the Tantale cluster holds the following:

- Quad-Core AMD Opteron processor running at 1.8 GHz and Quad-Core AMD Opteron processor running at 2.4 GHz (64 bits architecture);
- 4 GBytes of RAM memory or 32 GBytes of RAM memory;
- 18 GBytes of Hard Disk (SCSI Ultra320).

Tantale cluster uses Load Sharing Facility (LSF) to execute the batch management of the jobs and MPI to allow for parallel execution of the jobs that are submitted using LSF system. Each server in Tantale runs the following common software:

- Operating System: Linux Red Hat Enterprise server 3 update 4;
- Kernel version: 2.4.21-27;
- gcc version: 4.0.2.

[4] InfiniBand is a switched fabric communications link primarily used in high-performance computing. The InfiniBand architecture specification defines a connection between processor nodes and high performance I/O nodes such as storage devices.

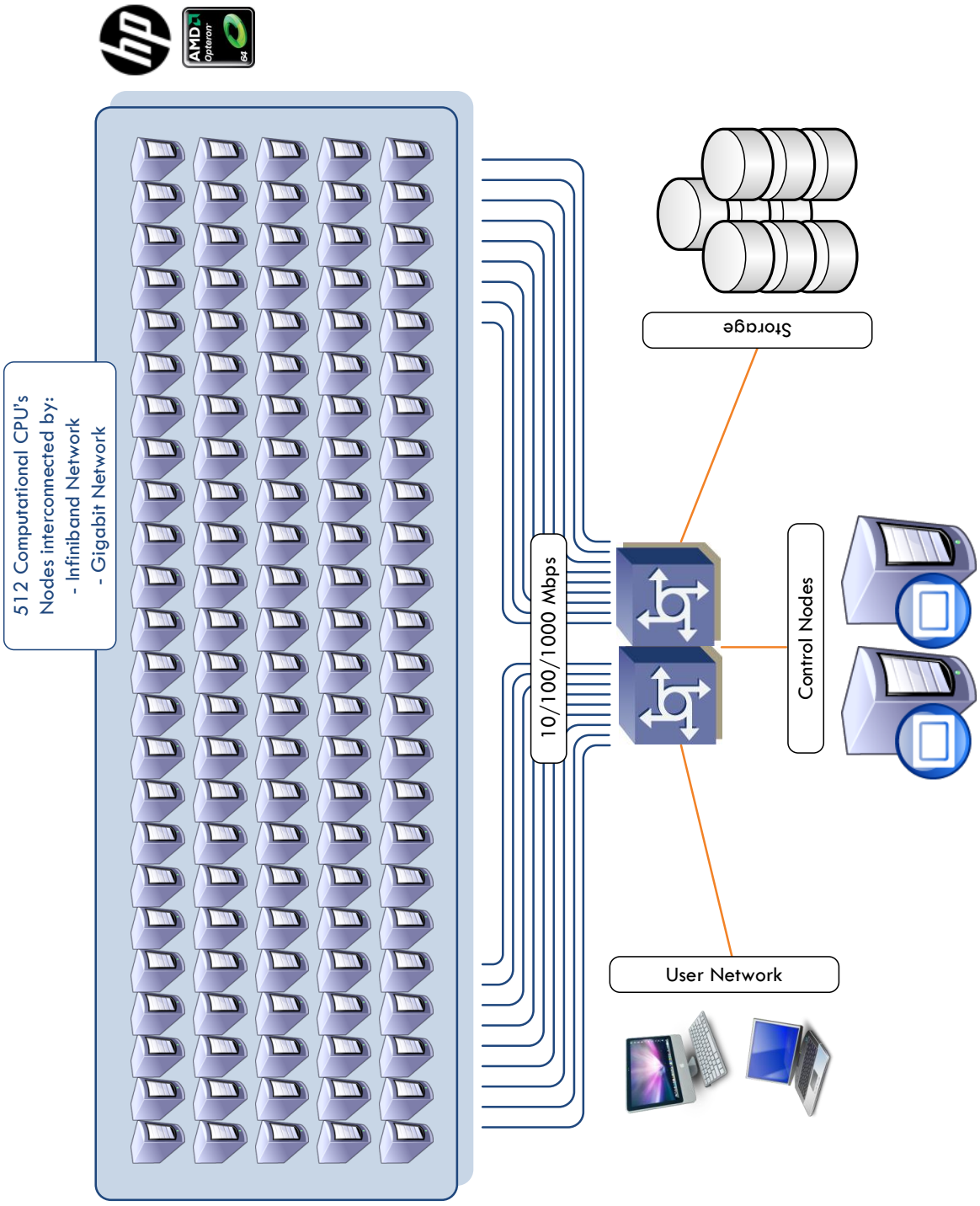

Figure 5.8: Tantale architecture.

5.3.2 Cluster @ IBEB

We developed the major part of our simulations studies at IBEB where we used two main computational resources: the IBEB Mini-Cluster and a standalone server. The latter is a server with the following hardware characteristics:

- Dual-Core Intel Xeon processor running at 3.2 GHz (64 bits architecture);
- 4 GBytes of RAM memory;
- 250 GBytes of Hard Disk;

Regarding the software installed in this server the current versions are:

- Operating System: Red Hat Enterprise Server 4, version 4.6-10;
- Kernel version: 2.6.9-78;
- gcc version: 3.4.6.

The mini-cluster at the IBEB facilities is a Sun platform with Intel processors, Figure 5.9. The mini-cluster works using two fundamental pieces of software, the Sun Grid Engine [Microsystems, 2007; Engine, 2010] and the MPICH2 [Gropp *et al.* , 2008; MPICH2, 2010]. The former is the Distributed Resource Management (DRM) system, designed to maximize resource utilization by matching incoming workload to available resources according to the needs of the workload and the business policies that are in place. It can be considered as the middleware that allows for the cluster to work with all the nodes and their processors. The latter is the environment software that allows that all the processors can be involved in tasks, which can communicate between them using this protocol, the MPI protocol. The versions in use for both these software are:

- Sun Grid Engine: version 6.1, update 4;
- MPICH2: version 1.0.7.

Four of these five computational nodes included in the IBEB mini-cluster have the following hardware characteristics:

- 2 × Quad-Core Intel Xeon processor running at 2.33 GHz (64 bits architecture);
- 2 GBytes of RAM memory;
- 146 GBytes of hard disk.

Regarding the software installed on these 4 nodes (as well as the fifth node mentioned above) the current versions are:

- Operating System: CentOS 5.4;

- Kernel version: 2.6.18-164;
- gcc version: 4.1.2.

The fifth computational node have the same hardware characteristics as the control node which are:

- 2 × Quad-Core Intel Xeon processor running at 2.33 GHz (64 bits architecture);
- 8 GBytes of RAM memory;
- 146 GBytes of Hard Disk Regarding the software installed on the control node;
- Operating System: CentOS 5.4;
- Kernel version: 2.6.18-164;
- gcc version: 4.1.2.

Storage component of this mini-cluster is based on a Sun platform with 2.5 TBytes of disk capacity directly connected to the control node by means of two 4 Gbits fibre channel interfaces.

5.3.3 Instalation Procedure

The installation procedure of GATE comprises two steps: the installation of the Geant4 package and all helper tools required (e.g. the CLHEP, a Class Library for High Energy Physics, and all the Geant4 libraries) and the GATE installation itself. It should be highlighted that tools needing external libraries or packages may only be activated if the corresponding external system is installed. Detailed information about the instalation procedure and the definition of the environement variables can be found in: [Jan *et al.* , 2007; GATE, 2010b].Moreover, more information about CLHEP can be found in [CLHEP, 2010], and about the Geant4 package and corresponding libraries in [Installation, 2010b]. To install GATE some careful is needed about the required specific version for each dependency (CLHEP, Geant4, ROOT, etc.). A brief table with all specific versions of each dependency, for a given GATE version, is available in [Installation, 2010a].

Two benchmarks, one for PET and one for SPECT, are included in the Gate distribution. These benchmarks check the integrity of a Gate installation or upgrade. Each benchmark consists of the macros required to run the simulation, analyze the simulation output, and generate figures. In addition, a set of baseline figures are included to compare the users results with those from a correct run. Detailed information can be found in [Jan *et al.* , 2007].

5.3.4 Cluster Computing for GATE Simulations

A distributed computing approach for running the highly scalable GATE experiments in a cluster of computers is an appropriate solution to reduce the overall computing time. The approach is platform independent in the sense that the simulations are partitioned in virtual time slices so that

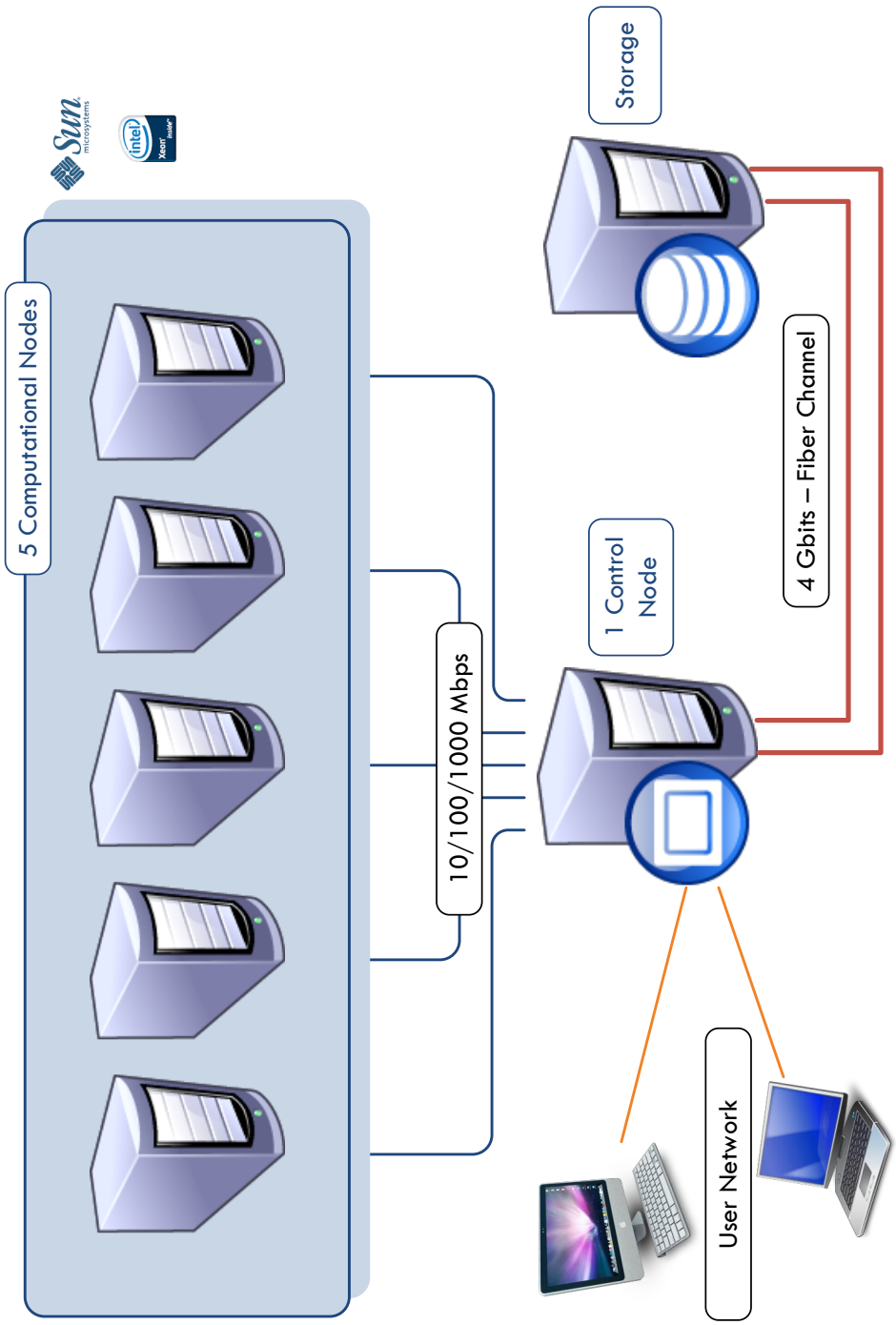

Figure 5.9: IBEB Mini-Cluster architecture.

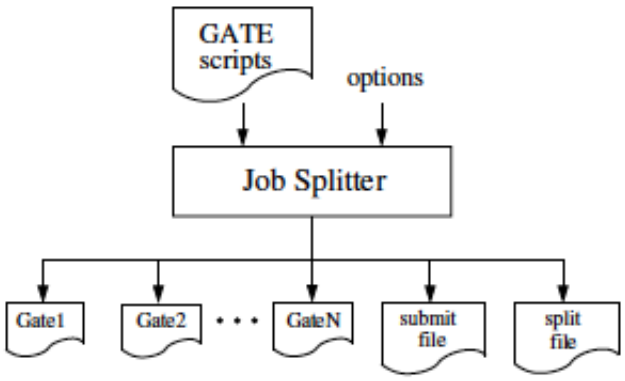

Figure 5.10: The job splitter is used to generate fully resolved, non-parameterized macro files together with a platform specific submit file and a split file for error handling in the merging step. Adapted from [Beenhouwer *et al.* , 2005].

the user obtains a number of fully resolved independent job execution macros accompanied by a platform specific submit file.

The parallelized simulations are made up of 3 steps: the job splitting, the actual simulations (on a number of CPUs) and the file merging. The most natural, simple and general scheme for splitting simulations is the time-domain decomposition approach, in which the acquisition time of the experiment is split into a number of smaller experiments of the same duration.

Typically, an experiment of length T and initial source activity A_0 is partitioned into N independent simulations, such that simulation i lasts $\frac{T}{N}$ with initial activity $A_0 \exp\left\{-\lambda i \frac{T}{N}\right\}$, where λ is the isotope half-life. This approach does not involve any approximation nor simplification. Moreover, since the singles rates for each interval are unchanged, measures such as randoms, scatter rates, and system deadtime will be effectively the same as in a single-node run. As shown in Figure 5.10 the input to the job splitter are the GATE scripts, parameters and command-line options which mainly specify the cluster platform, the number of jobs and the output directories. The output is a collection of non-parameterized macro files.

Finally, a split file is generated that contains all information about the partitioned simulation to facilitate the merging of the output files and error handling. GATE does not allow any volume movement during data acquisition and only updates the geometry at the start of each frame (the equivalent of a Geant4 run). Each frame is defined by its time length. A PET simulation of a 60 seconds acquisition with a time slice length of 1 second would therefore result in 60 frames and thus 60 projections, for example. If the time-domain based decomposition would be restricted to the number of frames, then this would limit the maximum number of CPUs that can be used. To allow for independent time-domain based partitioning, virtual time slices were introduced which can span a shorter or longer time length than that of a single run in the original simulation, while the original geometry updates remain in place.

Figure 5.11 shows a simulation consisting of 3 frames. Although the activity is updated continuously throughout the simulation, the geometry is only updated at the beginning of each run. In this case the simulation is split into four virtual time slices. The geometry updates take place within virtual

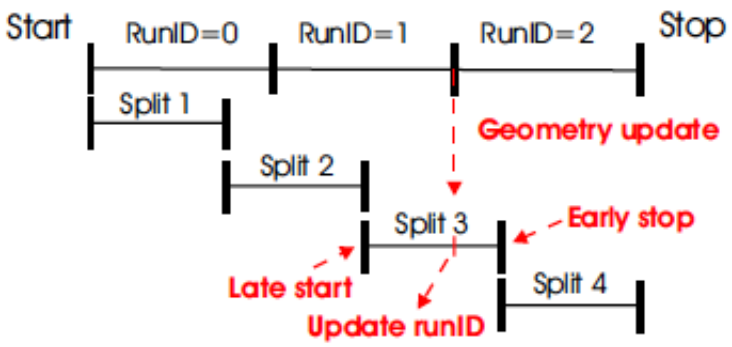

Figure 5.11: A GATE simulation consisting of 3 runs. The parallelization introduces virtual time slices that update the geometry based on the original time schedule. Adapted from [Beenhouwer *et al.* , 2005].

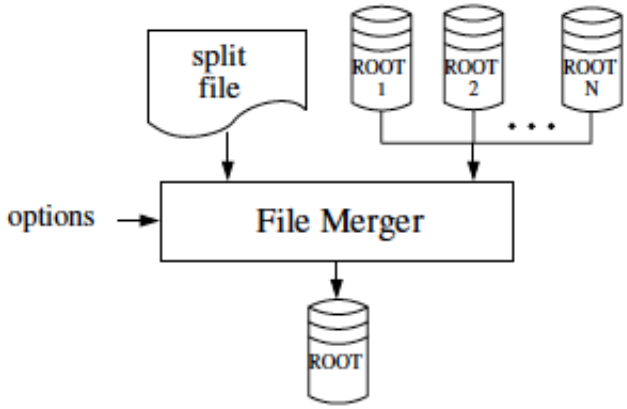

Figure 5.12: The output merger is used to merge the ROOT output data into a single output file. Adapted from [Beenhouwer *et al.* , 2005]

time slices 2 and 3. The virtual slices are updated with a new runID to accommodate the geometry updates in the original time schedule. Figure 5.11 shows how the third virtual slice is actually a late start of the original time slice with runID 1 and an early end of the time slice with runID 2.

As shown in Figure 5.12, the output merger takes as input the ROOT output files from the parallelized simulations and uses the information in the split file to merge them. Detailed information about this approach can be found in [Beenhouwer *et al.* , 2007, 2005; Staelens *et al.* , 2006].

Chapter 6

The MicroPET® FOCUS 220 Scanner

The Siemens microPET® Focus 220 preclinical PET scanner is the second generation large-bore PET system expanding the capabilities of its predecessor, the microPET® P4 PET scanner. The microPET® Focus 220 is designed specifically to accommodate a range of animal sizes, allowing you to visualize and quantify disease and the action of novel therapies in living animals. Enables the evaluation of pharmacokinetics, pharmacodynamics, and tissue target occupancy by using labeled drugs and other molecular imaging probes in non-human primates and rodents. It allows quantitative, non-invasive and repeated studies of the spatial and temporal distribution of a molecular radiotracer in one animal in contrast to other techniques, such as tissue dissection and autoradiography, where the animal has to be sacrificed (as stated above). The large bore gantry design permits imaging of nonhuman primates but also provides high-resolution images for rodent studies.

6.1 Technical Specifications

The microPET® FOCUS 220 system is a commercial scanner consisting in 4 detector rings: each ring is made of 42 detector blocks. Each detector block is composed of a matrix of 12×12 LSO[1] crystals with the dimensions 1.5 mm×1.5 mm×10.0 mm. Its axial Field of View (FOV) is 7.6 cm and has a diameter of 26.0 cm. The FOCUS system has a volume resolution of 2.5 μL and an absolute sensitivity of 3.4%, both measured at the center of the FOV [Tai *et al.* , 2005]. With computer controlled vertical and horizontal bed motion, the microPET® Focus 220 can perform whole-body biodistribution or dynamic imaging with an effective axial FOV of up to 50 cm (using primate bed pallet) using continuous bed motion acquisition and support for animals up to 25 Kg in weight [microPET FOCUS, 2010]. Table 6.1 summarizes the system geometry and acquisition conditions.

[1] LSO offers a very good combination of properties of any PET scintillator used today— fast scintillation decay time, high light output, and effective atomic number.

Specifications	
Detector diameter (cm)	22
Bore size (cm)	22/26[2]
Transaxial active Field of View (FOV in cm)	19
Axial Field of View (cm)	7.6
Axial FOV continuous bed motion	30/50[3] cm
Number of detector blocks	168
Number of acquisition channels	168
Total number of LSO elements	24 192
Pixel element size (mm^3)	1.5×1.5×10.0
Peak absolute system sensitivity (%)[4]	≥ 4
Resolution at center of FOV (mm)	≤ 1.4
Average energy resolution (%)	≤ 18
Volumetric resolution (Center FOV) (μL)	≤ 3.0
Volumetric resolution (Central 8 cm) (μL)	≤ 9

Features	
Variable timing window: 2, 6, 10, 14, nsec	Normalization (point source or cylinder acquisition)
Variable energy window: 0–814 keV	Deadtime correction
Reconstruction algorithms: 2D OSEM, 3D OSEM, 2D FBP, 3D RP, 3D MAP, 3D OSEM + MAP	Scatter correction
Point source holder with computer-controlled helical trajectory	Decay correction ($\geq$ 24 isotopes supported)
Computer-controlled bed (horizontal and vertical)	Dynamic framing (variable from 1msec to static)
Data acquisition software: microPETManager™	Simultaneous respiratory and cardiac gating
Data analysis tool: ASIPro™ (unlimited number of seats)	Interchangeable bed pallet
Attenuation Correction (both measured and calculated)	Mobile (does not require new setup)
Post Emission Transmission	Wholebody imaging in a single bed position

Table 6.1: Specifications and features of the microPET® FOCUS system. Adapted from [microPET FOCUS, 2010].

Figure 6.1: The microPET® FOCUS 220. Adapted from [microPET FOCUS, 2010].

Physical component	`cylindricalPET system`
head	`rsector`
module	`module`
crystal	`crystal`
LSO	`layer0`

Table 6.2: Relationship between the physical components of the scanner and the hierarchical levels of the system.

6.2 The Simulated Model

The system modeling instructions (from the geometry of the system to the acquisition protocol), for the GATE platform, will be demonstrated hereafter while comment the implemented functionality.

6.2.1 The Geometry

In accordance with the real tomograph, the simulated microPET®Focus scanner has a 26 cm diameter detector ring, which gives a transaxial FOV of 19 cm and an axial FOV of 7.6 cm. The detector ring contains 24 192 individual LSO crystal elements in 168 detector blocks. Each detector block is arranged in a 12×12 array, with each pixel element measuring 1.5×1.5×10 mm^3. The cylindricalPET system is used to describe the logical organization of the scanner. The relationship between the physical components of the scanner and the hierarchical levels of the system is described in Table 6.2. The geometry description of the scanner is illustrated in Figure 6.2.

```
# G E O M E T R Y: microPET FOCUS #
```

```
/gate/geometry/enableAutoUpdate

# W O R L D #
/gate/world/geometry/setXLength 40.  cm
/gate/world/geometry/setYLength 40.  cm
/gate/world/geometry/setZLength 40.  cm

# C Y L I N D R I C A L with cylindralPET system #
/gate/world/daughters/name cylindricalPET
/gate/world/daughters/insert cylinder
/gate/cylindricalPET/setMaterial Air
/gate/cylindricalPET/geometry/setRmax 149 mm
/gate/cylindricalPET/geometry/setRmin 128 mm
/gate/cylindricalPET/geometry/setHeight 80 mm
/gate/cylindricalPET/vis/forceWireframe
/gate/geometry/update

# B L O C K #
/gate/cylindricalPET/daughters/name rsector
/gate/cylindricalPET/daughters/insert box
/gate/rsector/geometry/setXLength 19.1 mm
/gate/rsector/geometry/setYLength 10.  mm
/gate/rsector/geometry/setZLength 76.6 mm
/gate/rsector/setMaterial Air
/gate/rsector/vis/forceWireframe
/gate/rsector/vis/setColor gray
/gate/rsector/placement/setTranslation 0 135.6 0 mm
#/gate/rsector/placement/setRotationAxis 0 0 1
#/gate/rsector/placement/setRotationAngle 180 deg
/gate/geometry/update

# M O D U L E #
```

```
/gate/rsector/daughters/name module
/gate/rsector/daughters/insert box
/gate/module/geometry/setXLength 19.  mm
/gate/module/geometry/setYLength 10.  mm
/gate/module/geometry/setZLength 19.  mm
/gate/module/setMaterial Water
/gate/module/vis/forceWireframe
/gate/module/vis/setColor gray

# C R Y S T A L #
/gate/module/daughters/name crystal
/gate/module/daughters/insert box
/gate/crystal/geometry/setXLength 1.5 mm
/gate/crystal/geometry/setYLength 10.  mm
/gate/crystal/geometry/setZLength 1.5 mm
/gate/crystal/placement/setTranslation 0 0 0 mm
/gate/crystal/setMaterial Air
/gate/crystal/vis/forceWireframe
/gate/geometry/update

# L A Y E R #
/gate/crystal/daughters/name LSO
/gate/crystal/daughters/insert box
/gate/LSO/geometry/setXLength 1.5 mm
/gate/LSO/geometry/setYLength 10.  mm
/gate/LSO/geometry/setZLength 1.5 mm
/gate/LSO/placement/setTranslation 0 0 0 mm
/gate/LSO/setMaterial LSO
/gate/LSO/vis/setColor yellow
/gate/geometry/update

# R E P E A T  C R Y S T A L #
```

```
/gate/crystal/repeaters/insert cubicArray
/gate/crystal/cubicArray/setRepeatNumberX 12
/gate/crystal/cubicArray/setRepeatNumberY 1
/gate/crystal/cubicArray/setRepeatNumberZ 12
/gate/crystal/cubicArray/setRepeatVector 1.6 0.  1.6 mm
/gate/geometry/update

# R E P E A T  M O D U L E #
/gate/module/repeaters/insert cubicArray
/gate/module/cubicArray/setRepeatNumberZ 4
/gate/module/cubicArray/setRepeatVector 0.  0.  19.2 mm

# R E P E A T  R S E C T O R #
/gate/rsector/repeaters/insert ring
/gate/rsector/ring/setRepeatNumber 42

# A T T A C H  S Y S T E M #
/gate/systems/cylindricalPET/rsector/attach rsector
/gate/systems/cylindricalPET/module/attach module
/gate/systems/cylindricalPET/crystal/attach crystal
/gate/systems/cylindricalPET/layer0/attach LSO

# A T T A C H  L A Y E R  SD #
/gate/LSO/attachCrystalSD
```

6.2.2 The Physical Process and the Acquisition Protocol

The selection of the physics processes is described by the scripted lines below and can be found in [Tai *et al.* , 2005; Jan *et al.* , 2005b, 2004a; Lehnert *et al.* , 2006a, 2005, 2006b]. The standard electromagnetic package is used for Compton scattering and for photoelectric effect. The low energy package is only used for Rayleigh scattering. To speed up the simulation, X-rays and secondary electrons are not tracked; the electron energy cut is set to an equivalent of 1.0 m and the X-rays energy cut to 1 GeV.

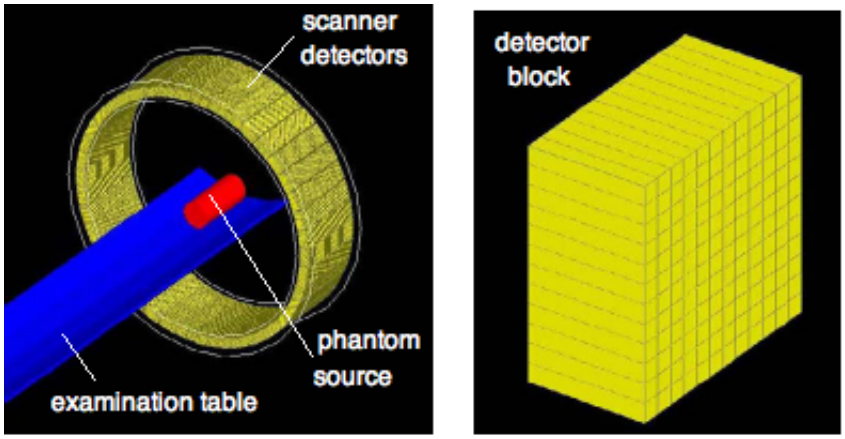

Figure 6.2: Illustration of the microPET® FOCUS geometry performed by GATE.

The simulations were performed under realistic acquisition parameters. A Gaussian distribution and an exponential distribution were used to define the background noise: the first distributions, named `energy_distrib`, is a Gaussian centered on 450 keV and of 1 keV standard deviation, while the second one is an exponential distribution, `dt_distrib`, with a power of 7.57 µs. These two distributions are used to define a noise by attributing the Gaussian distribution to the energy level of the background levels, and the exponential as the distribution of time interval between two consecutive background events. A blurring of 26% at 511 keV is applied to the energy deposed in the LSO crystals. A detected gamma is further processed only if its energy falls between 350 and 750 keV. A non-paralysabel dead time of 110.4 ns was applied on the singles events. A coincidence is defined when two gammas are detected within 6 ns, also was defined a delayed coincidence window of 6 ns with a 500 ns delay.

A treatment will be done on the regroupment of the delayed and of the prompts coincidence lines. Between two coincidences coming from these two lines and occuring within a given event, the priority is set to the delayed line, since it's inserted in the before the prompt line, and the priority is used. First, a non-paralysable dead time of 42.79 ns is applied on the delayed+prompts coincidences. Additionally, in the case where more than one coincidence can occurs for a unique Geant4 event (if more than one coincidence line are added to the coincidence pulse processor, or if multiple coincidences are treated as many subcoincidences pairs), then the whole event is rejected. Finally, the data transfer from the scanner to the hard disk was also simulated*:* a memory buffer of 8 coincidences, read at a frequency of 3.448391 MHz, in an event-by-event basis is applied on the delayed+prompt sum.

```
# P H Y S I C S #


# P R O C E S S #
/gate/physics/gamma/selectRayleigh lowenergy
/gate/physics/gamma/selectPhotoelectric standard
```

```
/gate/physics/gamma/selectCompton standard

# I N A C T I V E  S E C O N D A R Y  E L E C T R O N S #
/gate/physics/setElectronCut 1.  m

# I N A C T I V E  X - R A Y S #
/gate/physics/setXRayCut 1.  GeV
/gate/physics/setDeltaRayCut 1.  GeV

# A C Q U I S I T I O N  P A R A M E T E R S #

# D I S T R I B U T I O N S #
/gate/distributions/name energy_distrib
/gate/distributions/insert Gaussian
/gate/distributions/energy_distrib/setMean 450 keV
/gate/distributions/energy_distrib/setSigma 1 keV

/gate/distributions/name dt_distrib
/gate/distributions/insert Exponential
/gate/distributions/dt_distrib/setLambda 7.57 mus

# A D D E R #
/gate/digitizer/Singles/insert adder

# R E A D O U T #
/gate/digitizer/Singles/insert readout
/gate/digitizer/Singles/readout/setDepth 2
/gate/digitizer/Singles/insert crystalblurring
/gate/digitizer/Singles/crystalblurring/setCrystalResolutionMin 0.26
/gate/digitizer/Singles/crystalblurring/setCrystalResolutionMax 0.26
/gate/digitizer/Singles/crystalblurring/setCrystalQE 0.91
/gate/digitizer/Singles/crystalblurring/setCrystalEnergyOfReference 511.  keV
```

```
/gate/digitizer/name level1
/gate/digitizer/insert singleChain
/gate/digitizer/level1/setInputName Singles
/gate/digitizer/level1/insert deadtime
/gate/digitizer/level1/deadtime/chooseDTVolume rsector
/gate/digitizer/level1/deadtime/setDeadTime 110.4 ns
/gate/digitizer/level1/deadtime/setMode nonparalysable
/gate/digitizer/level1/insert thresholder
/gate/digitizer/level1/thresholder/setThreshold 350.  keV
/gate/digitizer/level1/insert upholder
/gate/digitizer/level1/upholder/setUphold 750.  keV

# N O I S E #
/gate/digitizer/level1/insert noise
/gate/digitizer/level1/noise/setDeltaTDistribution dt_distrib
/gate/digitizer/level1/noise/setEnergyDistribution energy_distrib

# C O I N C I D E N C E S S O R T E R #
/gate/digitizer/name delay
/gate/digitizer/insert coincidenceSorter
/gate/digitizer/delay/setInputName level1
/gate/digitizer/delay/allPulseOpenCoincGate false
/gate/digitizer/delay/setWindow 6.  ns
/gate/digitizer/delay/setOffset 500.  ns
/gate/digitizer/delay/setDepth 1
/gate/digitizer/delay/minSectorDifference 9
/gate/digitizer/delay/MultiplesPolicy takeWinnerIfAllAreGoods

/gate/digitizer/Coincidences/setInputName level1
/gate/digitizer/Coincidences/allPulseOpenCoincGate false
/gate/digitizer/Coincidences/setWindow 6.  ns
```

```
/gate/digitizer/Coincidences/setDepth 1
/gate/digitizer/Coincidences/minSectorDifference 9
/gate/digitizer/Coincidences/MultiplesPolicy takeWinnerIfAllAreGoods

/gate/digitizer/name finalCoinc
/gate/digitizer/insert coincidenceChain
/gate/digitizer/finalCoinc/addInputName Coincidences
/gate/digitizer/finalCoinc/addInputName delay
/gate/digitizer/finalCoinc/usePriority true
/gate/digitizer/finalCoinc/insert deadtime
/gate/digitizer/finalCoinc/deadtime/setDeadTime 42.79 ns
/gate/digitizer/finalCoinc/deadtime/setMode nonparalysable
/gate/digitizer/finalCoinc/deadtime/conserveAllEvent false

/gate/digitizer/name histoCoinc
/gate/digitizer/insert coincidenceChain
/gate/digitizer/histoCoinc/addInputName finalCoinc
/gate/digitizer/histoCoinc/insert buffer
/gate/digitizer/histoCoinc/buffer/setMode 0
/gate/digitizer/histoCoinc/buffer/setBufferSize 8 B
/gate/digitizer/histoCoinc/buffer/setReadFrequency 3.448391 MHz
```

6.2.3 Data Output and Reconstruction Set-Up

In GATE, there are several types of output format, which can be enabled, Table 5.1 in section 5.1.3. By default, the data output formats for all the systems used by Gate are ASCII and ROOT. In case of high statistics applications, was considered to enable only the ROOT output which contains the same information as the ASCII one, but automatically compressed (and, in addition, ready for analysis). An example of the ROOT output as described in the following command lines. During the simulation acquisition all data collection was stored in the file `moby_mouse_0.root`:

```
/gate/output/root/setFileName moby_mouse_0
/gate/output/root/setRootHitFlag 0
```

```
/gate/output/root/setRootSinglesFlag 0

/gate/output/root/setRootlevel1Flag 0

/gate/output/root/setRootCoincidencesFlag 0

/gate/output/root/setRootdelayFlag 1

/gate/output/root/setRootfinalCoincFlag 0

/gate/output/root/setRoothistoCoincFlag 1

/gate/output/root/setRootNtupleFlag 0

/gate/output/root/setSaveRndmFlag 0
```

ROOT is a framework for data processing, developed at CERN, at the heart of the research on high-energy physics [ROOT, 2010; Brun & Rademakers, 1997]. The ROOT system provides a set of object-oriented frameworks, built in C++, with all the functionality needed to handle and analyze large amounts of data in a very efficient way. Having the data defined as a set of objects, specialized storage methods are used to get direct access to the separate attributes of the selected objects, without having to touch the bulk of the data. Included in ROOT are histograming methods in an arbitrary number of dimensions, curve fitting, function evaluation, minimization, graphics and visualization classes to allow the easy setup of an analysis system that can query and process the data.

The Root output is composed of 4 histograms, one `NTuple` (*Gate*) and three `TTrees` (*Hits*, *Singles*, *Coincidences*) in which the interaction type, position and time information are stored. The 4 histograms contain the distributions of:

- `Acolinea_Angle_Distribution_deg` : the angle in degree between the two gamma of annihilation of the β^+ ;
- `Positron_Kinetic_Energy_MeV` : the energy of the β^+ ;
- `Ion_decay_time_s` : the time of the decay;
- `Positron_annihil_distance_mm` : the range of the β^+ .

In the `Ntuple` *Gate*, four similar variables are available in order to look at correlations amongst them.

Writing a C++ file, it is possible to generate a complete data analysis choosing which datasets we wish to include in the analysis that is going to be made by ROOT using its own C++ interpreter/compiler. This C++ file uses methods from ROOT classes that are included in the framework in order to provide this facility in creating specific views from the data gathered.

Figure 6.3 presents an example of a data analysis produced by the ROOT framework (the plots are saved in a `.gif` file by ROOT), for a simulation with the FOCUS system. Moreover, a set of some physical variables are calculated by the C++ file from the ROOT output, and printed in the ROOT console.

This analysis methodology was published in reference [Branco, 2005]. For the work presented here, these type of analysis was used only to verify if the results were in agreement with the results obtained for the validation of the small animal platform.

For some scanner configurations, the events may be stored either in a sinogram format or in the List Mode Format (LMF). The sinogram output module stores the coincident events from a cylindrical scanner system in a set of 2D sinograms according to the parameters set by the user. One 2D sinogram is created for each pair of crystal-rings. The sinograms are stored either in raw format or in the ecat7 format. The LMF is the format developed by the Crystal Clear Collaboration [Clear, 2010]. A library has been incorporated in Gate to read, write, and analyze the LMF format. The LMF format was originally designed for the development of small animal PET scanners for which the number of crystals is smaller than for clinical PET scanners. In particular, the maximum number of sub-volumes in a volume (e.g. the maximum number of submodules in a module) is fixed by the number of bits used to encode the sub-volume ID. All together, the final ID encoding the position of an event has to be stored in 16, 32, or 64 bits only. However, the FOCUS system outuput is a 48 bits LMF file due to the scanner geometry configuration. Chapter 8 will describe the new features that were introduced to allow its use within the GATE platform producing an output file format similar to the physical scanner.

In the LMF, the LOR of each event is separately recorded in turn, possibly with other information, such as the time and photon energy. This is an efficient form of storage for otherwise sparse data histograms (that is, few photon events and many potential LORs), but it is not amenable to analytic reconstruction methods such as FBP without first histogramming the LMF into a standard sinogram or projection data format, which can be an inefficient procedure. Alternatively, each list-mode event can be backprojected into a reconstruction matrix, which is an efficient means of data storage but incurs the disadvantages of the backprojection filtering (BPF) approach. For this reason, and because of the typically high levels of statistical noise, iterative methods are often used to reconstruct list-mode data [Kinahan *et al.* , 2004]. In this research, the simulated data were rebinned with the FORE algorithm and reconstructed using the OSEM2D method which is used in pratice with the FOCUS system. The number of subsets (16) and iterations (4) used in pratice setting was employed for the reconstruction of the simulated images. Figure 6.4 illustrates a complete simulation process, where image reconstructed is included.

The Amide's a Medical Imaging Data Examiner (AMIDE) tool was used for image display and ROI statistics analysis [Loening & Gambhir, 2003; AMIDE, 2010].

6.2.4 Experiments

The last step of the simulation consists in setting up the experiment. The beginning and end of acquisition is defined of similar form the real experiences, appealing to the commands `setTimeStart` and `setTimeStop`. The overall acquisition time can be subdivided in several time slices of fixed duration, using the command line `setTimeSlice` that defines the period of time during which it assumes the simulated system as being static. This feature is very useful in GATE, since the geometry is updated only between two time slices. This provides the possibility to take into account the

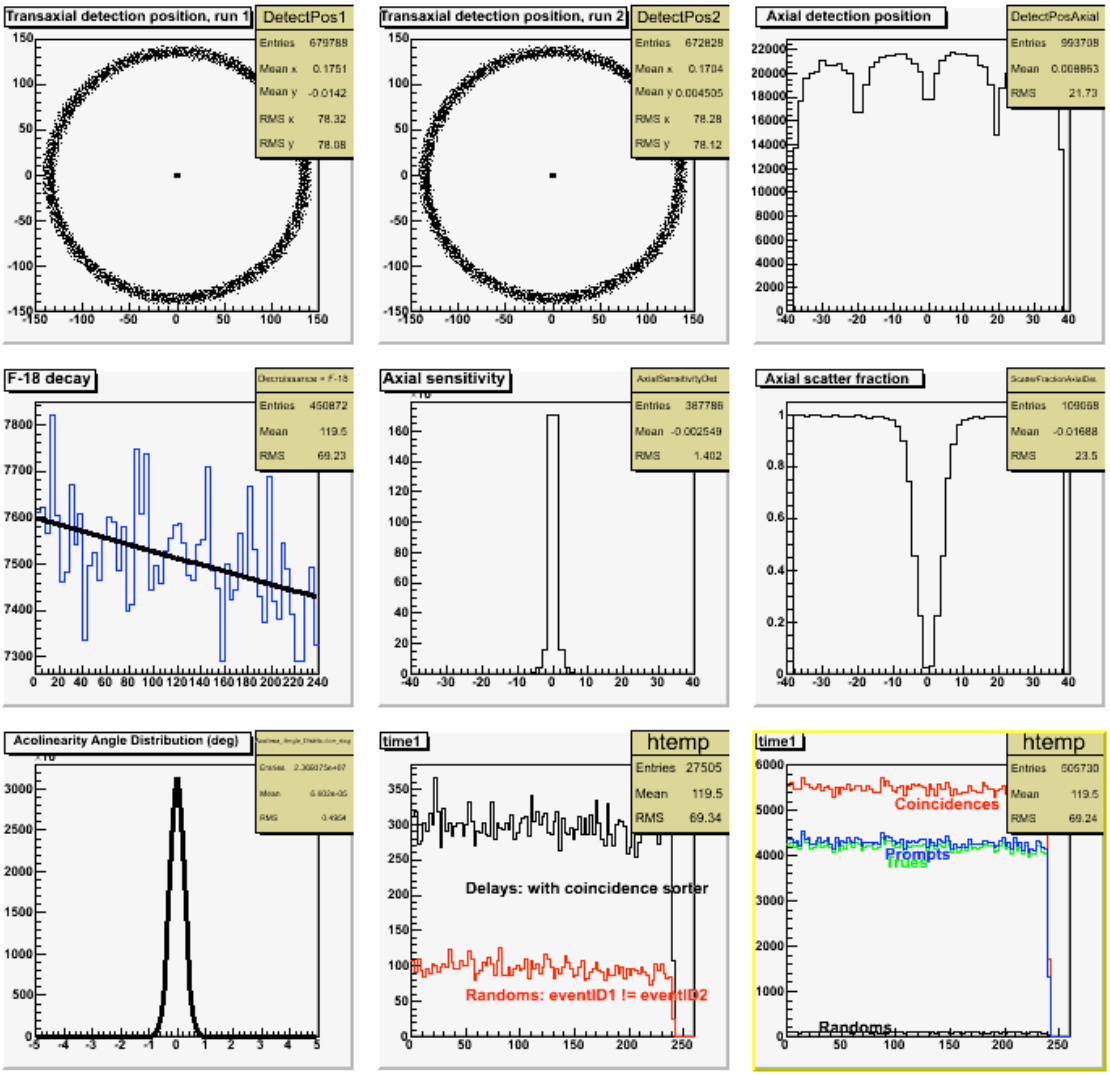

Figure 6.3: Example of a set of plots produced by a ROOT macro, for the FOCUS system. The three plots in the upper row show the detection coordinates of the annihilation photons in the system's detector heads. The first two plots (`Transaxial detection position`) are 2D histograms of the respective X and Y coordinates, one per frame. The third plot (`Axial detection position`) is a 1D histogram of the Z coordinate. In the left plot of the middle row illustrate the decay time curve of the F^{18} source. The second plot in the middle row (`Axial sensitivity`) illustrates the axial sensitivity of the scanner. For all unscattered coincidences, the axial position of the corresponding LOR is histogramed. The third plot in the middle row (`Axial scatter fraction`) shows the scatter fraction as a function of the axial position. The plot in the lower row (`Acollinearity Angle Distribution (deg)`) shows the distribution of the deviation to 180 degrees. of the angle between the two annihilation gammas. The second to last plot compare the delay coincidences generated with the real random selected in the prompts coincidences, and the last one shows the different type of decay events as a function of the time acquisition. Adapted from [Branco, 2005].

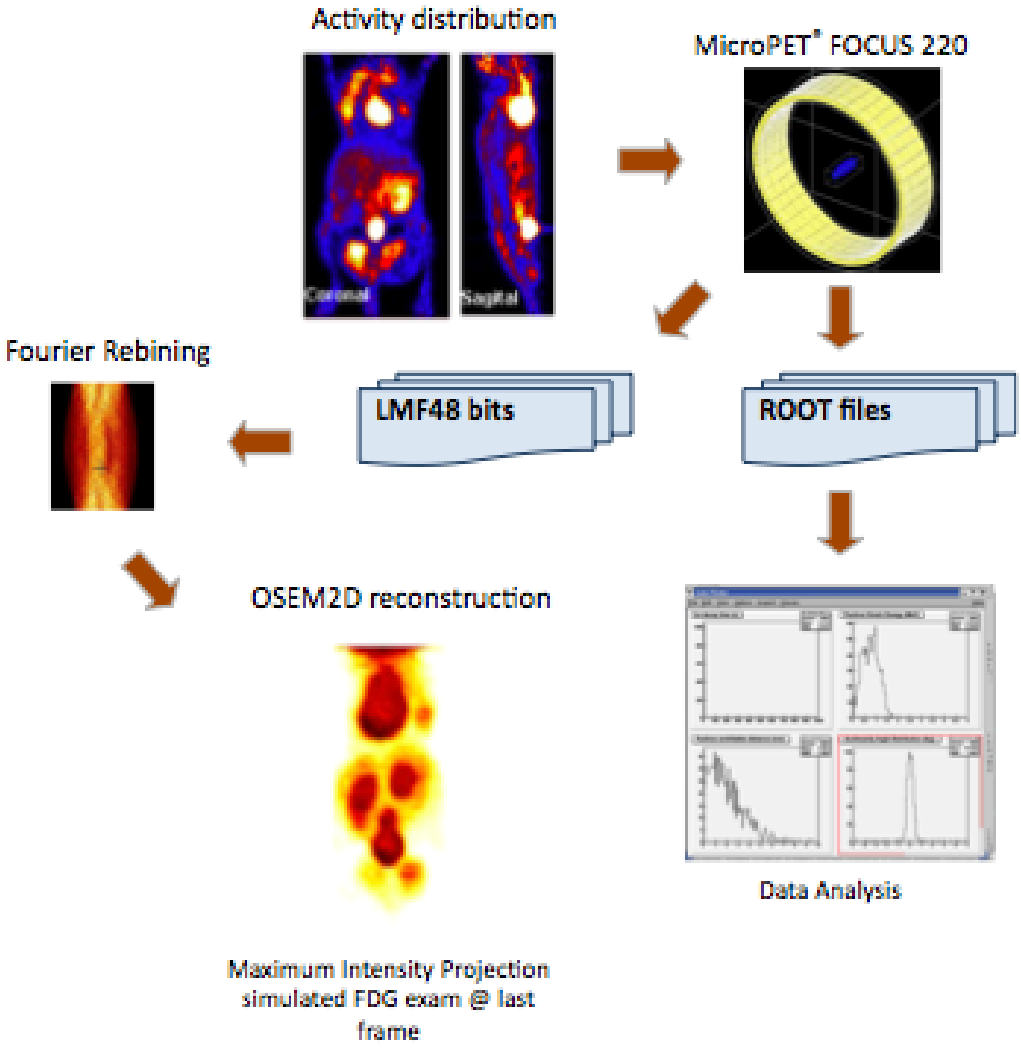

Figure 6.4: Illustration of a simulation process.

movements of the sources or the detectors by subdividing a simulation run into time slices characterized by the same geometry. The number of projections or runs of the simulation is thus defined by:

$$N_{run} = \frac{\texttt{setTimeStop} - \texttt{setTimeStart}}{\texttt{setTimeSlice}} \tag{6.1}$$

The following script lines shown an example:

```
/gate/application/setTimeSlice 90.021 s
/gate/application/setTimeStart 0 s
/gate/application/setTimeStop 90.021 s
/gate/application/startDAQ
```

6.2.5 Image Planes

In whole body imaging the sections of the body are referred to in terms of axial, coronal and sagittal planes as shown in Figure 6.5a. This terminology will be used for the mouse body image planes throughout the rest of this work.

The transverse plane (as also known as transaxial) divides the body into upper and lower parts. In Nuclear Medicine techniques, the transverse plane corresponds to the plane that is perpendicular to the axis of rotation of the scanner. By analogy, in the present work we will refer to the plane that is perpendicular to the axis of rotation of the FOCUS system as the transverse plane, Figure 6.5b.

In whole body techniques, the sagittal plane refers to the plane that divides the body or its parts into right and left sides. In the images of the FOCUS system, the sagittal plane is the plane of the mouse body that is parallel to the sagittal plane. This plane divides the body into its medial and lateral sides.

The coronal plane is the plane that is perpendicular both to the sagittal and the transverse planes. This plane divides the mouse body into its upper and lower parts.

In this section we will define the terminology that will be used for the breast image planes throughout the rest of this work.

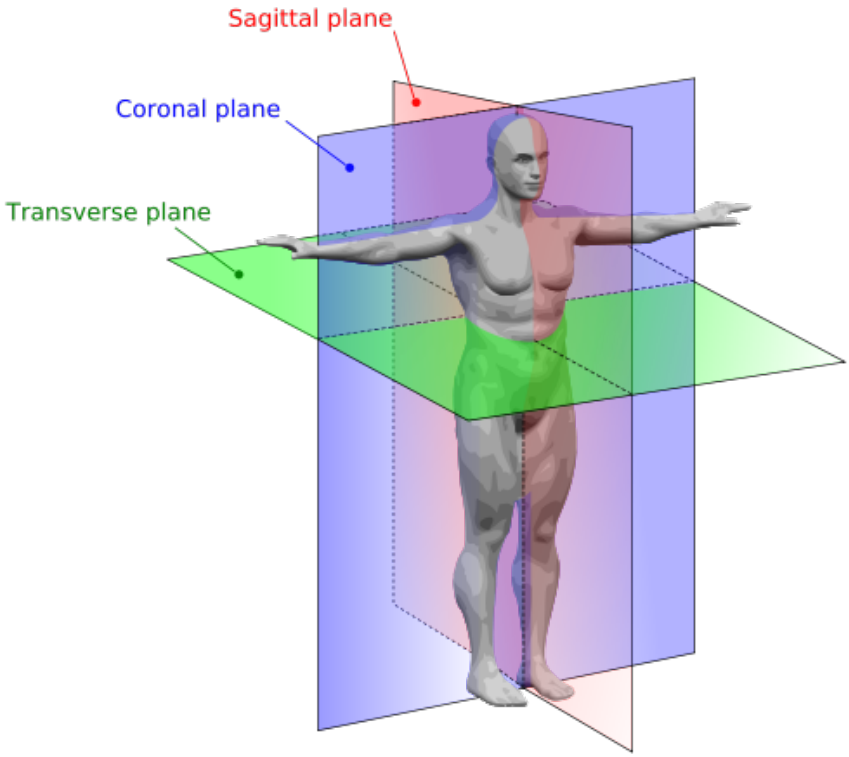

(a) Terminology for the body planes. Adapted from [Planes, 2010]

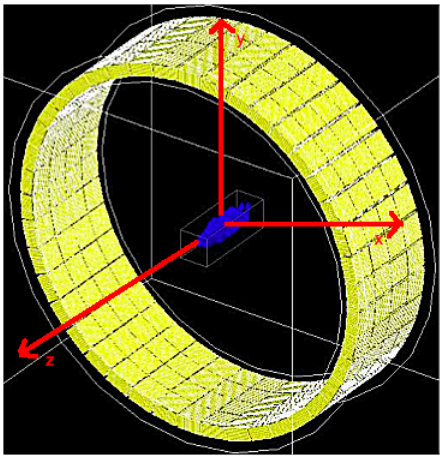

(b) The FOCUS system coordinates.

Figure 6.5: Image planes.

Part IV

Results and Discussion

Chapter 7

The Digital Mouse Phantoms

An important aspect of simulations is the possibility of having a realistic model (phantom) of the subject's anatomy and physiological functions from which imaging data can be generated using accurate models of the imaging process [Peter *et al.* , 2000; Poston *et al.* , 2002; Zubal, 1998; Ljungberg, 2004; Zaidi, 2006]. Conceptually, the purpose of a physical or computerized phantom is to represent an organ or body region of interest, to allow modelling the biodistribution of a particular radiotracer and the chemical composition of the scattering medium, which absorbs and scatters the emitted radiation in a similar manner to biological tissues. In other terms, a phantom is a mathematical model designed to represent, as accurately as possible, an organ or tissue of the body, an organ system, or the whole-body. The widespread interest in molecular imaging spurred the development of more realistic 3D to 5D computational models based on the actual anatomy and physiology of individual humans and small animals. The advantage in using such phantoms in simulation studies is that the anatomy and physiological functions are known, thus providing a gold standard or truth in order to evaluate and improve imaging devices, data acquisition techniques, and imaging processing and reconstruction methods. Moreover, computer phantoms can be altered in order to model different anatomies and pathological situations. A review of the fundamental and technical challenges of designing computational models of the human anatomy can be found in [Zaidi & Xu, 2007]. This review summarizes the latest efforts and future directions in the development of computational anthropomorphic models for application in radiological sciences.

Computerized anthropomorphic phantoms can either be defined by mathematical (analytical) functions, digital (voxel-based) volume arrays or a combination of both approaches (hybrid technique). Analytical phantoms consist of regularly shaped continuous objects defined by combinations of simple mathematical geometries (*e.g.* right circular cylinders, spheres, or disks), whereas voxel-based phantoms are mainly derived from segmented tomographic images of the anatomy obtained by either CT or MRI. Any complex activity and corresponding attenuation distributions can therefore be modelled without being confined to the use of simple geometrical shapes. Analytical phantoms, however, have the advantage of being able to model anatomical variability and dynamic organs easily. In addition, the disadvantage of the voxelized approach is that inherent errors are introduced due to the phantom voxelization. The discretization errors inherent to the voxelized representation may be reduced by finer sampling of the discretized phantoms [Ljungberg, 2004; Zaidi, 2006; Zubal,

1998]. The hybrid equation-voxel approach, combines the two approaches referenced above by allowing the mathematical description of organ boundaries from definitions extracted from voxel data [Zaidi & Tsui, 2009]. One phantom that seeks to strike a balance between realism and flexibility is the four dimensional 4D Mouse Whole-Body (MOBY) phantom [Segars *et al.* , 2004].

7.1 The Phantoms Used

Two kinds of phantoms were used for the Monte Carlo simulations performed: 4D maps generated from real data and a anthropomorphic phantom (the MOBY phantom). The 4D maps allowed the validation of the GATE platform for small animal PET studies. The simulated data from the anthropomorphic phantom allowed for the evaluation of the respiratory motion and the lung lesion quantification in small animal, in acquisition scenarios close to a real examination. In the following paragraphs we will provide a description of these phantoms.

7.1.1 Phantoms Built from Real Data

The generation of realistic mouse phantoms using real data allowed us to obtain 4D maps of the source distributions, for the case of the two different radiopharmaceuticals used in the simulations presented in this thesis: [^{18}F]-fluoride and FDG. These 4D maps have been developed through image-based segmentation using the Anatomist software [Anatomist, 2010].

Data acquisition were done at CEA/SHFJ[1] SHFJ [2010] using a microPET® FOCUS 220 system. Both data examinations were reconstructed using FORE + OSEM2D algorithms (16 subsets and 4 iterations). Data normalization and corrections for dead time, scatter and attenuation were performed.

7.1.1.1 The [^{18}F]-fluoride mouse phantom

The [^{18}F]-fluoride ion is a radioisotope with high affinity to bone structures. This positron emitting isotope can be very useful in the clinical setting because many common cancer types, such as the prostate, breast and lung cancer, have the natural potential to spread to the bony skeleton producing pathological changes in bone metabolism [Berger *et al.* , 2002; Couturier, 2004].

This exam used 400 μCi of [^{18}F]-fluoride. The acquisition started 20 minutes post injection and lasted 60 minutes. Data was binned into 4 frames of 900 s each. The resulting phantom is illustrated in Figure 7.1. It consists of an emission map composed of 101×55×95 voxels, which are of 0.47 mm along the x and y axis, and 0.80 mm along the z axis.

The data, extracted from the exam, was used to set the activity distribution in the simulation studies to values similar to those of the activity distribution present in the different mouse body structures revealed by PET. The total activity considered for a certain simulated frame was set according to the radiotracer decay[2], Figure 7.2.

[1] Service Hospitalier Frédéric Joliot (SHFJ) @ Commissariat à l'Énergie Atomique (CEA)
[2] Described by the decay equation: section 2.1.1.

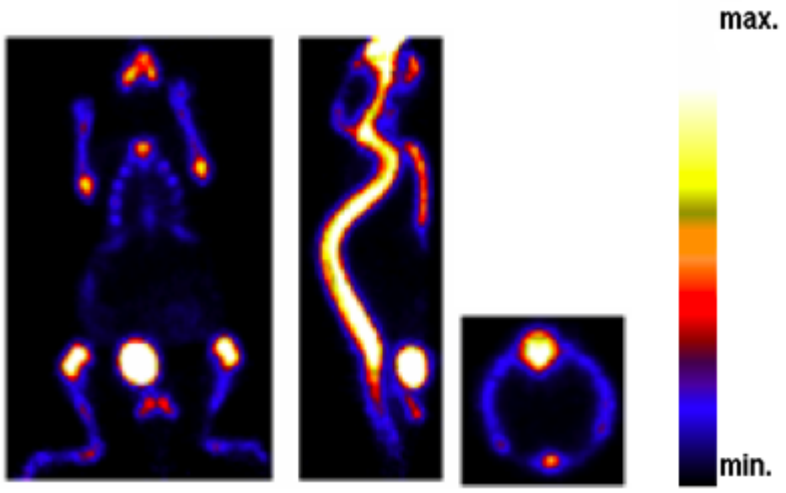

Figure 7.1: Coronal, sagital and transaxial slices for the activity distribution of [^{18}F]-fluoride mouse phantom.

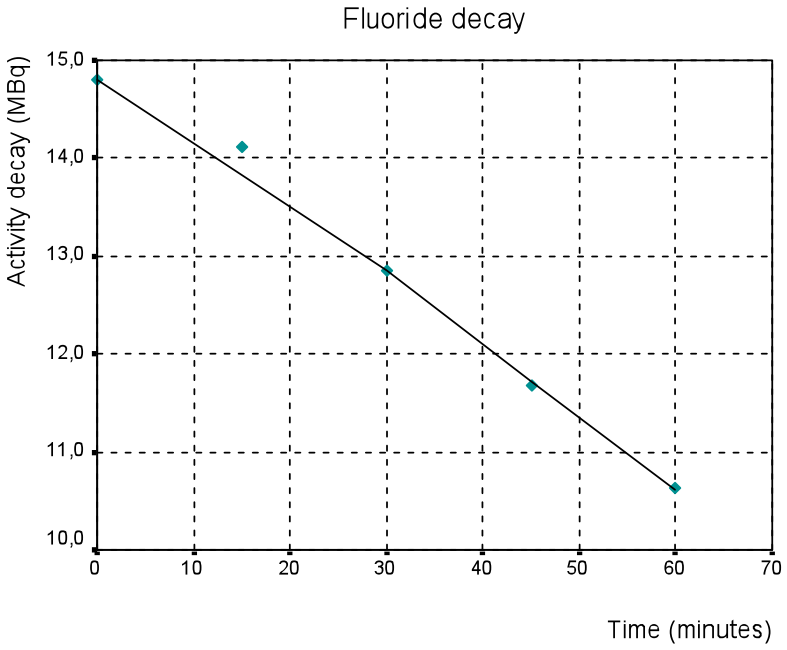

Figure 7.2: The curve shows the radioactive decay of the [^{18}F]-fluoride with a half-life of 6585.2 s, along the exam acquisition time.

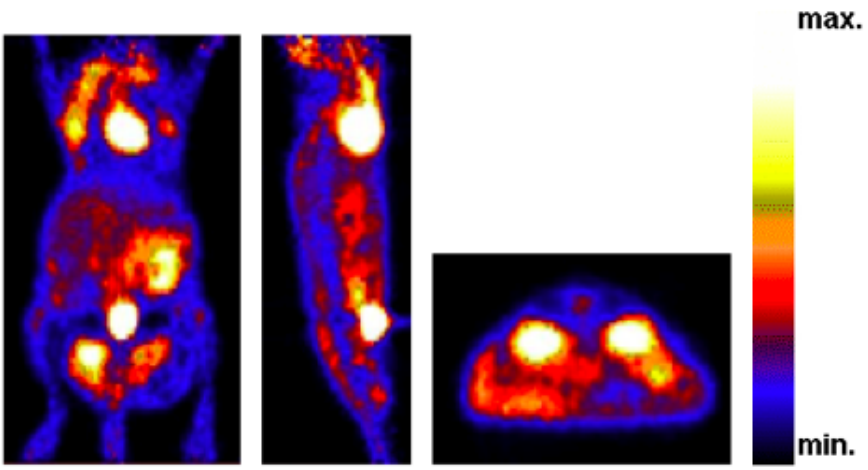

Figure 7.3: Coronal, sagital and transaxial slices for the activity distribution of the FDG mouse phantom.

7.1.1.2 FDG mouse phantom

The FDG is the most common radiotracers used for the study of cancer in the clinical setting. FDG is an analog of glucose and is taken up by living cells through the normal glucose pathway. Tumor imaging with FDG is based on the fact that malignant tumors with high metabolic rates take up greater amounts of glucose and FDG than surrounding tissues [Couturier, 2004; Larson & Schwartz, 2006].

A dynamic whole body mouse FDG exam was used to generate an emission map that consist of a matrix of 104×61×95 voxels, which are of 0.46 mm along the x and y axis, and 0.80 mm along the z axis. The mouse was injected with an activity of 220 μCi and scanned during 90 minutes. Data was binned into 18 frames (5×60 s; 5×120 s; 3×300 s; 3×600 s; 2×900 s). The resulting phantom is illustrated in Figure 7.3. The total activity considered for a certain simulated frame was set according to the radiotracer decay[3] Figure 7.4.

The microPET images were employed in order to accurately model the variable FDG distributions. The FDG biodistribution is defined by the TACs which are assigned to different body structures. The dynamic FDG mouse exam was used to compute the FDG biodistribution, needed to set the activity distribution in each organ at each point of time in the simulation studies performed. ROIs were drawn around the bladder, heart, liver, kidneys and whole body. The activity in each ROI was normalized to the total body activity in order to obtain a relative concentration in each organ at each time point. Figure 7.5 shows the TAC for each organ at each time frame. The TACs for the function model of the FDG tracer are used to set the input activity function in each structure for the whole body phantoms.

[3] Described by the decay equation: section 2.1.1.

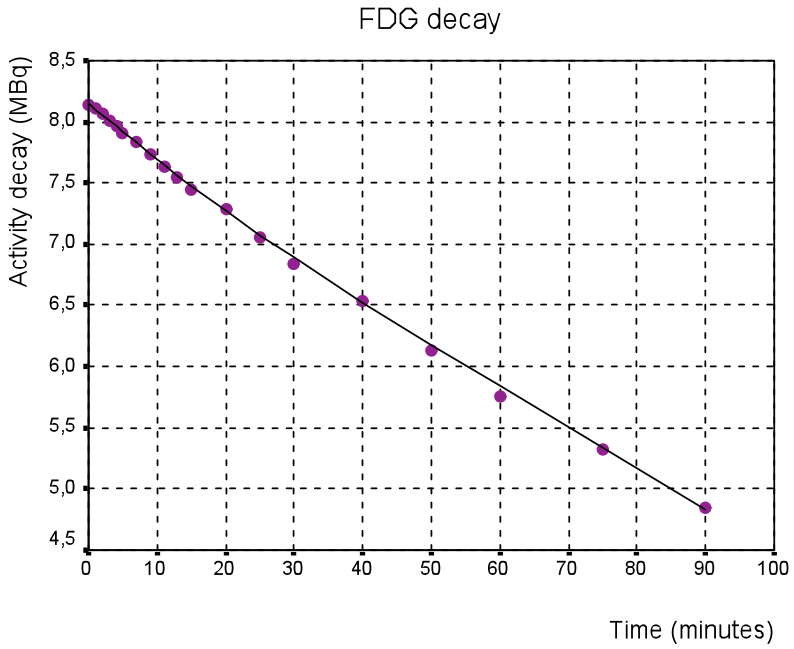

Figure 7.4: The curve shows the radioactive decay for the FDG study, with a half-life of 6585.2 s.

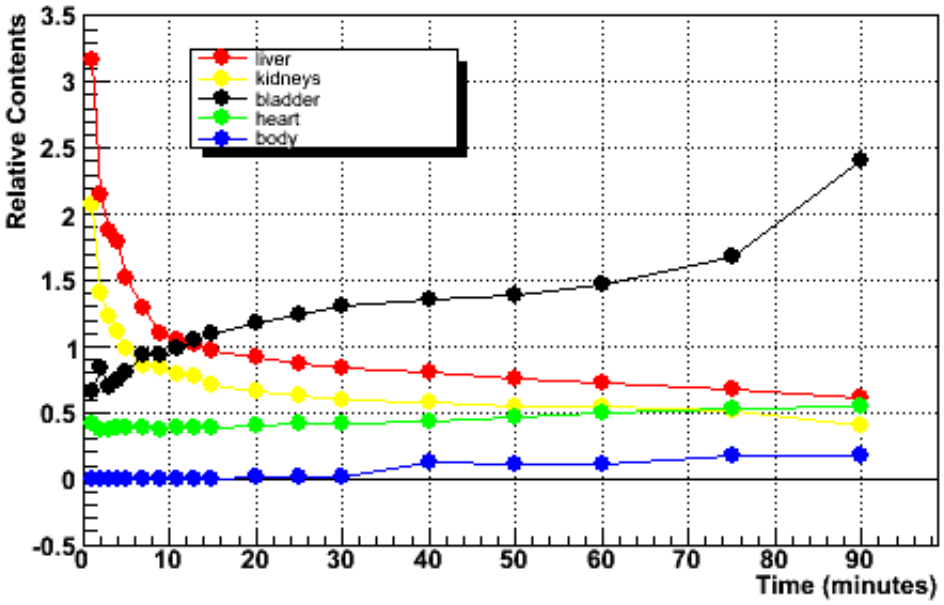

Figure 7.5: Measured TACs used as input for the FDG uptake simulation.

7.1.2 The MOBY Phantom

The MOBY[4] mouse phantom combines the realism of a voxelized phantom, with the flexibility of a mathematical phantom, based on non-uniform rational B-splines (NURBS), Figure 7.6. The organ shapes are modelled with NURBS surfaces, widely used in three dimensional computer graphics to accurately describe complex 3D surfaces, providing the foundation for a realistic model of the 3D mouse anatomy [Segars, 2001; Segars *et al.* , 2004]. The phantom software can generate voxelized representations of the mouse anatomy at any user-defined resolution. Also, organs can be set to different tissue resolutions. The execution of the MOBY program generates 3D voxelized attenuation coefficient phantoms and 3D voxelized emission phantoms. These voxelized representations can be used as input in the GATE Monte Carlo platform. The default whole body MOBY phantom consists of a matrix of 128×128×448 cubic voxels with 0.25 mm sides, Figure 7.6. A resampling was applied on the default MOBY matrix to reduce the voxel number to 40×40×124 voxels with a voxel unit size of 0.5×0.5×0.5 mm^3. This allowed to significantly reduce the computational time resulting from the particle tracking inside the simulated volume and took into account the spatial resolution of the scanner. The general parameter file for the MOBYphantom program, with the parameters chosen is shown in Appendix A.

Additionally to a 3D realistic anatomy, the MOBY phantom includes 4D models of the mouse's cardiac and respiratory motions. The organ models on the phantom were segmented from high resolution Magnetic Resonance Microscopy (MRM) data and the cardiac and respiratory motions were developed using cardiac-gated MRI and respiratory-gated MRI. Both 4D models for cardiac and respiratory motion are described by NURBS which offer a realistic description of the different motion surfaces of the different body structures. According to this model the motions are defined through control points. Both motions were parameterized allowing changes on magnitude or rates of each motion to simulate many different variations, normal and abnormal. The respiratory mechanics involve the motion of the diaphragm, heart, thoracic and lungs. During inspiration, the diaphragm contracts forcing the abdominal contents downward and forward increasing the volume of the thorax. In addition, the ribs rotate forcing the ribcage outward and upward further increasing the volume of the thoracic cavity. The lungs inflate with air due to the change in thoracic pressure. During expiration, the opposite movement occurs decreasing the thoracic volume causing the lungs to deflate. The period of the respiratory cycle for normal tidal breathing in a mouse is 0.37 seconds. The inspiration lasts 40% of the period with expiration lasting the remaining 60%. The amount of volume change in the lungs for normal tidal breathing is 0.15 mL. Figures 7.7 and 7.8 display the respiratory motion and the organs involved on it. These images indicate the ability of NURBS surfaces to model respiratory motion realistical. The complete modeling description, concerning the organ shapes, as well as the cardiac and the respiratory motion, of the phantom can be found in [Segars *et al.* , 2004].

[4]The website link to download the MOBY phantom program is [phantom, 2010], and the instructions for using the phantom can be found at [instructions, 2010; phantoms, 2010].

Figure 7.6: Anterior (left) and lateral (right) views of the MOBY digital mouse phantom. Adapted from [Segars *et al.* , 2004].

7.1.2.1 Modelling of a Stress Breathing Condition and a Tumor Motion

The MOBY respiratory motion was set up to be dependent on two time varying parameters: the change in the height of the diaphragm ($\Delta_{diaphr.}$) and the amount of chest expansion ($\Delta_{\Delta P}$). The $\Delta_{diaphr.}$ controls the upward and downward motions of the liver, stomach, spleen, heart and the kidneys while the $\Delta_{\Delta P}$ controls the motions of the organs as well as the motion of the rib cage. In the default MOBY configuration, the extent of diaphragmatic motion for normal breathing is set to be 1.0 mm while the chest expansion is 0.7 mm. These values correspond to a respiratory cycle with a period of 0.37 s. The parameter curves can be manipulated to produce different breathing patterns. By adjusting the amplitude of the time curves, heavier or lighter breathing patterns can be simulated. Also, faster or slower breathing patterns can be simulated by changing the period of the time curves. These parameters were manipulated to produce a "stress breathing" condition, in order to reproduce the respiratory motion of a mouse during a typical PET examination: the $\Delta_{diaphr.}(t)$ was set to 6.0 mm and the $\Delta_{\Delta P}(t)$ was defined to 4.2 mm. A spherical lung lesion was implemented in the middle region of the left lung and its motion modelled as a function of the non normal tidal breathing condition. The motion of a specific spot of the lung is modelled as a two-way

motion between two points in space, with same cycle of the diaphragm movement.

For a respiratory cycle with a typical period of 0.37 s, the diaphragm motion can be decided by:

$$\Delta_{diaphr.}(t) = \begin{cases} 0.5\,mm\cos\left(\frac{\pi}{0.16}t\right)+0.5 & 0 \le t \le 0.16\,s \\ 0.5\,mm\cos\left(\frac{\pi}{0.24}(0.4-t)\right)+0.5 & 0.16\,s \le t \le 0.4\,s \end{cases} \tag{7.1}$$

The $\Delta_{\Delta P}(t)$ diameter of the chest was assumed to change a maximum of N mm's sinusoidally as shown in Equation:

$$\Delta_{\Delta P}(t) = \begin{cases} -\frac{N}{2}\cos\left(\frac{\pi}{0.16}t\right)+\frac{N}{2} & 0 \le t \le 0.16\,s \\ -\frac{N}{2}\cos\left(\frac{\pi}{0.24}(0.4-t)\right)+\frac{N}{2} & 0.16\,s \le t \le 0.4\,s \end{cases} \tag{7.2}$$

The N parameter was adjusted according to the total amount of volume change in the lungs (0.15 mL for normal tidal breathing in the mouse).

Each respiratory cycle was divided into N bins (temporal frames), and one phantom was created for each of the N instances of the respiratory cycle. Based on Equations 7.1 and 7.2, a set of 10 temporal frames (gates) of 0.037 s was generated over a complete respiratory cycle of 0.37 s in addition to a non-gated data set. The 10 respiratory gated images were produced by the MOBY program for 10 different position of one respiratory cycle. The first 5 images correspond to the inhalation and the other 5 images to the exhalation process respectively. The modified MOBY phantom and the parameter curves for both respiratory and lesion motion are illustrated in Figure 7.9 and Figure 7.10.

For the studies without the inclusion of respiratory motion, simulations were carried out approximating clinical acquisitions of 15 minutes (last frame of a FDG acquisition) in order to provide whole-body images of variable statistical quality. For the simulations with respiratory motion, the acquisition time used in static simulation, T_{acqTot}, was divided by the number of respiratory cycles, N_{cycles}, and the number of bins, N_{bins}, per respiratory cycle to obtain the acquisition time at one instance (bin) of the respiratory cycle, T_{acqBin}:

$$T_{acqBin} = \frac{T_{acqTot}}{N_{cycle}N_{bins}} \tag{7.3}$$

In this way the total acquisition time remains the same for simulations with or without the inclusion of respiratory motion.

7.2 Phantom Simulation Process

Using the GATE platform, voxelized phantom or patient data can be used as inhomogeneous, anthropomorphic sources to reproduce realistic acquisitions (as stated in section 5.1.6). Using the parameterized volume method, a voxelized source can be read as an Interfile image [Staelens *et al.* , 2003]. The image gray scale is then converted into activities using a range translator. The gray

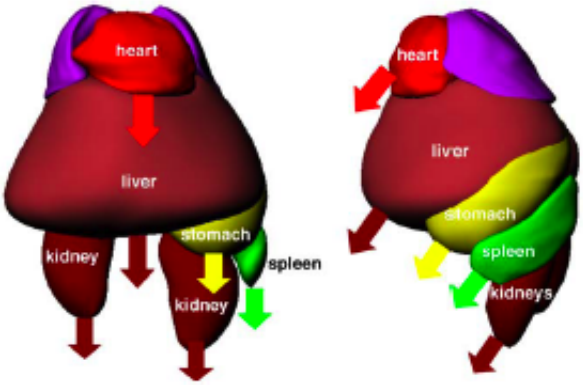

Figure 7.7: Inspiratory motions of the liver (diaphragm), stomach, spleen, heart, and kidneys simulated in the mouse phantom. Expiratory motion was simulated as the reverse of the inspiratory motion. Adapted from [Segars *et al.* , 2004].

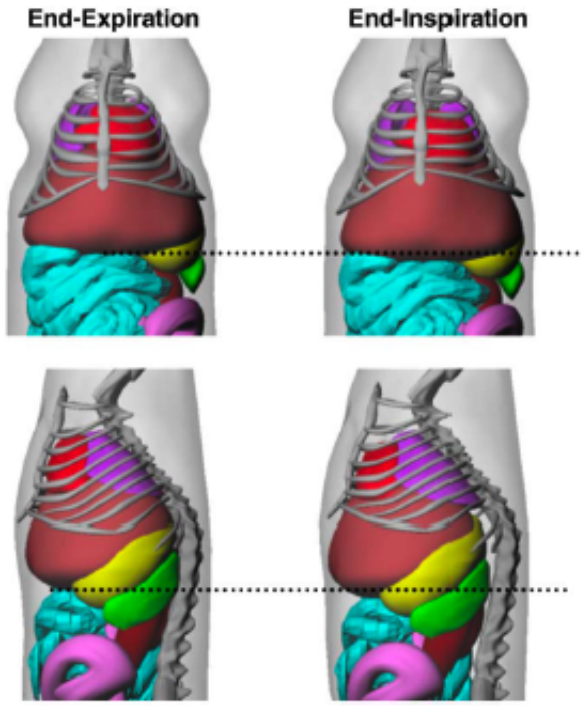

Figure 7.8: (Top) Anterior view of end-expiration (left) and end-inspiration (right) in new mouse phantom. (Bottom) Left lateral view at end-expiration (left) and end-inspiration (right). The dotted line indicates the movement of the diaphragm. Adapted from [Segars *et al.* , 2004].

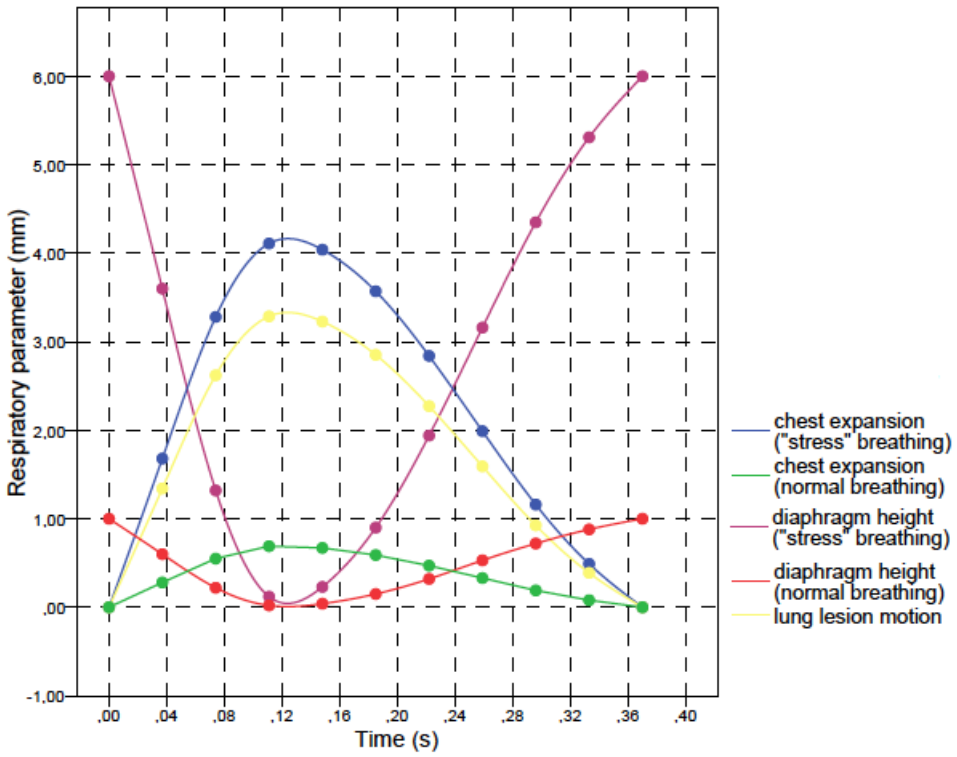

Figure 7.9: Parameter curves for both respiratory (normal and abnormal breathing condition) and lesion motion in the MOBY phantom (as a function of the non normal tidal breathing condition).

scales are therefore discretized in numerous intervals. Afterwards those activity levels are used to determine the number of primary particles for each voxel. The navigator algorithm coming with the `parameterizedBoxMatrix` determine the next voxel that the particle will enter by searching in the whole list of the voxels contained in the phantom.

An example of a macro for reading in interFile images as source distributions is detailed below, where a gamma back-to-back emission source was defined for the fluorine-18 (the annihilation photons are generated at 180 degrees). There is no confinement: the spatial distribution of emission points is specified by the shape of the source, and the angular distribution of emission angles is isotropic.

```
/gate/source/addSource voxel_mouse voxel
/gate/source/voxel_mouse/reader/insert interfile
/gate/source/voxel_mouse/interfileReader/translator/insert range
/gate/source/voxel_mouse/interfileReader/rangeTranslator/readTable
          activityRange_MOBY_FDG.dat
/gate/source/voxel_mouse/interfileReader/rangeTranslator/describe 1
/gate/source/voxel_mouse/interfileReader/readFile moby0.h33
```

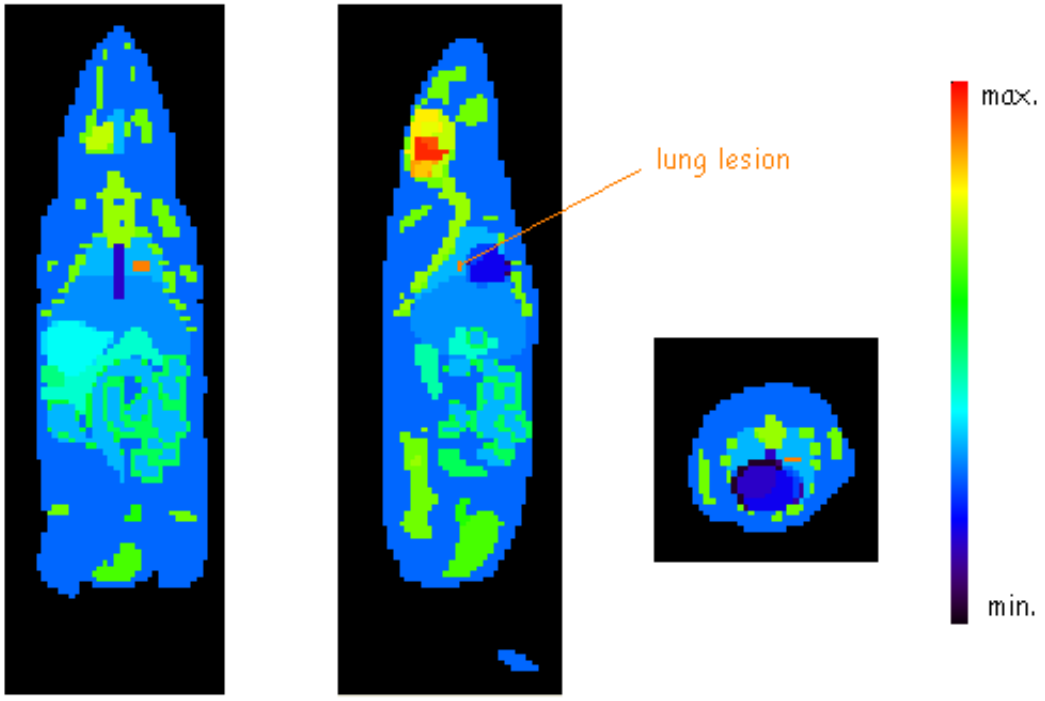

Figure 7.10: Slices of the emission map of the MOBY phantom including a spherical lesion in middle region of the left lung, generated by the MOBY program.

```
/gate/source/voxel_mouse/setPosition -14.40 -15.25 -30.75 mm
/gate/source/voxel_mouse/setType backtoback
/gate/source/voxel_mouse/gps/particle gamma
/gate/source/voxel_mouse/setForcedUnstableFlag true
/gate/source/voxel_mouse/setForcedHalfLife 6586.2 s
/gate/source/voxel_mouse/gps/energytype Mono
/gate/source/voxel_mouse/gps/monoenergy 0.511 MeV
/gate/source/voxel_mouse/gps/confine NULL
/gate/source/voxel_mouse/gps/angtype iso
/gate/source/voxel_mouse/dump 1
/gate/source/list
```

An example of the range translation table for numbers to activities (`activityRange_MOBY_FDG.dat` in the example) is shown below. The first line sets the number of subdivisions, 9, and the reamining

lines define the intervals, example $[11, 14]$, and attach a correlated activity: 76.279 Bq in this example. The resulting voxellized source has thus a discretized number of activity values (preliminar segmentation). In the case of the MOBY phantom, each organ is designated by one label which makes the definition of the activity concentration and the attenuation tissue more user friendly.

```
9
0    0    0.0
1    8     242.298
9    9    76.279
10    10    273.707
11    14    76.279
15    15    179.48
16    18    76.279
19    19    1081.367
20    69    76.279
```

Using this InterFile reader any digital phantom or patient data, stored in InterFile format, can be read in as emission distribution. The image input format is always the Interfile format as explained. In consequence, the binary matrix of the MOBY phantom (in this macro file example) is associated to a header file: `moby0.h33`. The header `moby0.h33` looks like:

```
!INTERFILE :=
;
!GENERAL DATA :=
name of data file := moby0.i33
patient name := moby
!study ID := body exam
type := Pet
study data compression := none
data encode := none
;
!GENERAL IMAGE DATA :=
!type of data := PET
```

```
imagedata byte order := LITTLEENDIAN
;
!PET STUDY (general) := ;
!process status := Reconstructed
!PET data type := Image
!number format := unsigned integer
!number of bytes per pixel := 2
number of dimensions := 3
matrix axis label [1] := x
!matrix size [1] := 55
scaling factor (mm/pixel) [1] := +0.500000e+00
matrix axis label [2] := y
!matrix size [2] := 55
scaling factor (mm/pixel) [2] := +0.500000e+00
matrix axis label [3] := z
!matrix size [3] := 124
scaling factor (mm/pixel) [3] := +0.500000e+00
!number of projections := 124
!number of slices := 124
slice thickness (pixels) := +0.500000e+00
number of time frames := 1
image scaling factor [1] := 1
data offset in bytes [1] := 0
quantification units := 1
!END OF INTERFILE :=
```

The lung lesion was defined as a spherical source. Its motion was modelled as a function of the non normal tidal breathing condition as stated above: the source position change at every frame.

```
/gate/source/addSource tumor
/gate/source/tumor/setActivity 10000.  becquerel
/gate/source/tumor/setType backtoback
```

```
/gate/source/tumor/gps/particle gamma

/gate/source/tumor/setForcedUnstableFlag true

/gate/source/tumor/setForcedHalfLife 6586.2 s

/gate/source/tumor/gps/energytype Mono

/gate/source/tumor/gps/monoenergy 0.511 MeV

/gate/source/tumor/gps/type Volume

/gate/source/tumor/gps/shape Sphere

/gate/source/tumor/gps/radius 0.375 mm

/gate/source/tumor/gps/angtype iso

/gate/source/tumor/gps/centre -2.0 -0.5 8.0 mm

/gate/source/tumor/gps/confine NULL

/gate/source/tumor/dump 1

/gate/source/list
```

GATE also offers the possibility to read in voxellized attenuation geometries following these two strategies. The gray scale is then converted to material definitions in that case using an analogous translator. The attenuation map was constructed using the same labelled phantom model as the one for the emission map. Each label of the phantom was associated with the corresponding attenuation coefficient at 511 keV, after update the GATE materials database. This file holds all the information required for Gate to assign the nuclear properties from the Geant4 data sets. Elements are the building blocks of all the materials used in Gate simulations. Elements in Gate are defined as in a periodic table. Gate stores the name, symbol, atomic number, and molar mass elements. In Gate, materials are defined as combinations of elements, and are an important parameter that Gate uses for all the particle interactions that take place during a simulation. These combinations of elements require defining four additional parameters. These are the material's name, density, constituent element(s), and their individual abundances. Detailed information about how to modify this database could be found in [Jan *et al.* , 2008].

An example of the MOBY attenuation map for GATE simulation purposes is shown by the following scripted lines:

```
/gate/world/daughters/name moby_mouse

#/gate/world/daughters/insert parameterizedBoxMatrix

/gate/world/daughters/insert compressedMatrix

/gate/moby_mouse/geometry/insertReader interfile

/gate/moby_mouse/interfileReader/insertTranslator range
```

```
/gate/moby_mouse/interfileReader/rangeTranslator/readTable
          range_moby_mouse.dat
/gate/moby_mouse/interfileReader/rangeTranslator/describe 1
/gate/moby_mouse/interfileReader/readFile moby.h33
/gate/moby_mouse/placement/setTranslation 0.  0.  0.  mm
/gate/moby_mouse/placement/setRotationAxis 1 0 0
/gate/moby_mouse/placement/setRotationAngle 0 deg
/gate/moby_mouse/attachVoxelPhantomSD
```

As phantom resolution increases, the number of voxels can become very large and a significant amount of memory may be required. The `compressedMatrix` phantom object was used instead of the `parameterizedBoxMatrix` to generate a compressed phantom where voxel size is variable. With the compression algorithm, all adjacent voxels of the same material are fused together to form the largest possible rectangular voxel. A compressed phantom uses less memory and also less cpu.

The `range_moby_mouse.dat` is detailed hereafter:

```
9
0    0    Air
1    8    Heart
9    9    Body
10    10    Liver
11    14    Body
15    15    Kidney
16    18    Body
19    19    Muscle
20    69    Body
```

The different attenuation coefficients of the organs were approximated with those of the different structures of the phantom. Information about the different attenuation coefficients can be found in [Coefficients, 2010], despite most of them was provided by Dr. William Segars and his research group [Seagers, 2010]. Complete information about this issue can be found in Appendix A. However, the goal of this reasearch do not involve the study of the attenuation impact.

Chapter 8

Enhancements to the GATE Platform

The main property of a imaging system is that its geometry hierarchy is automatically accepted by the corresponding data output formats. ASCII and ROOT output files are available for all imaging systems, within GATE. In this context, the LMF format is specified for the cylindricalPET system. The LMF contains all information for one acquisition: the records themselves, but also the data acquisition or simulation parameters. With the FOCUS system data acquisition is stored in a 48 bits LMF format (not available in GATE, as previously stated in section 6.2.3).

In this chapter we will present the reasoning behind the adaptation of the GATE platform for the output format of the microPET®Focus 220 system. The several classes and the routines that were developed to accommodate and store the acquisition data within GATE will be described.

8.1 List Mode Format

The earliest PET cameras were limited by the speed of the electronics that processed the coincidences. They could not sort the events into spatial bins (sinograms) in real time, hence they simply wrote out a list of the detector pairs of every event observed. This *list mode* form of data was generally abandoned as the speed of electronics improved. As PET scanners have advanced, a consistent trend is more and smaller detectors: the state of the art scanner in 1980 acquired 363 LORs [Townsend *et al.* , 1998], while the FOCUS 220 scanner we use has over 52 million LORs; there has been an approximately log-linear increase in LORs with time [Tai *et al.* , 2005].

While the spatial dimension has increased over the last two decades, the amount of radioactivity injected into subjects has remained constant, or even decreased due to safety concerns. Hence, with the newer PET cameras, roughly the same number of counts is distributed over a greater number of spatial elements. The end result is more and larger sinograms, though more of the sinogram elements are filled with zeros. This is a greatest concern for quantitative imaging which collects many acquisitions for a single study.

To address the problem of ever-growing sinograms with increasing spatial resolution, list mode data acquisition has been reintroduced on PET scanners. This allows a more efficient storage of

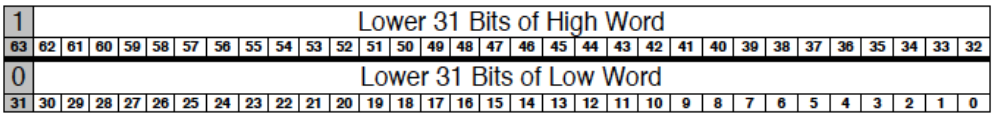

Figure 8.1: Systran listmode data packets.

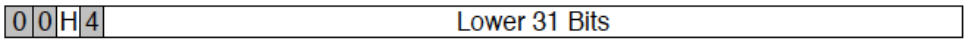

Figure 8.2: LMF 48 bits.

the data since zero-bins are not explicitly represented. It is also advantageous in that, as mentioned above, it allows definition of the temporal bins *post hoc*. Since there is often uncertainty in the exact delivery time of the tracer to the tissue of interest, the ability to change temporal bins is valuable.

8.2 The microPET® Focus LMF

The microPET systems can currently use two different listmode data transports from the tomograph to the Host PC: Systran (Fiber Optic) and 1394a (also known as Firewire). These two different data transports have different listmode data formats. All recent systems are 1394 based, and as such, only the 1394 packets are described. Translating from the Systran listmode format into the 1394 listmode format used in this document is shown below, Figure 8.3. The Systran listmode data packets are 64 bits in length. This 64 bit packet can be split into low and high 32 bit words. The most significant bit (MSB) of the low 32 bit word is always low, while the MSB of the high 32 bit word is always high, Figure 8.1.

The 1394 listmode data packets are 48 bits in length. The most significant BYTE (6th byte) of each packet is always zero. Also, the lower nibble (lower four bits) of the 5th byte is always hex 4. The 6th byte and the lower nibble of the 5th byte are used as a synchronized pattern in the listmode data stream. Figure 8.2 shows in HEX where H is part of the packet header.

Figure 8.3[1] shows how to translate the Systran packet into the 1394 format:

[1] In the packet translation, the most significant 6th byte is not shown since it is always zero, only the lower 40 bits are shown. However, the entire Systran packet is shown.

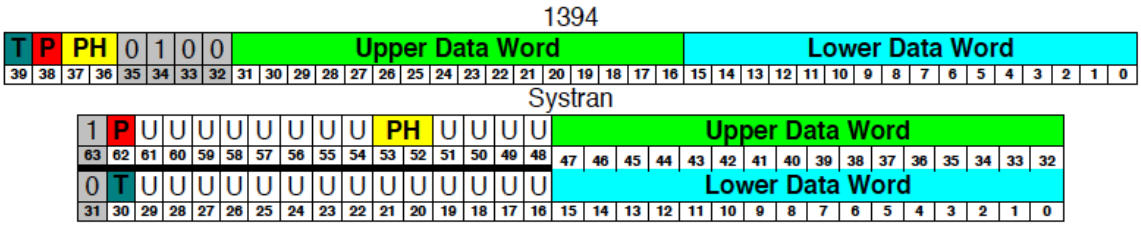

Figure 8.3: Packet translation for the microPET LMF formats.

8.3 The Class `GateToFOCUS`

A new class, `GateToFOCUS` which is responsible for the storage of the acquisition data, has been added in the output hierarchy of the GATE platform.

In order to implement a new GATE class developed for this thesis there were some alternatives that needed some careful thoughts. First, the basic idea was to use a "simple" script or a small C (or any other language) program that could read the ROOT file and then convert it to a 48 bits LMF format. In reality, this was in fact the first method used for several time in order to get the 48 bits LMF files. However, this method was not a very "clean" way of working with a full modular software like GATE and therefore there were the need to develop a new GATE class.

There were two scenarios in order to achieve this desired output. The first was to create a class with methods that were called after the ROOT file is created and concluded. This was the most obvious solution as we had already a solution that opened the ROOT file and created the LMF 48 bits file with the information saved on the former. Nevertheless this solution had a major challenge, in our opinion, as there was the need to wait for the entire simulation to finish and only after that the methods on our class could be called in order to create and build the LMF file, which could represent a significant amount of extra time in order to achieve the desired output. The second scenario was the one with the biggest level of complexity in order to be executed but which could give us the best result in the less possible time! In fact this second scenario involved the development of a C++ class with methods that are called during the simulation (like the ROOT file creation methods) and gathers the needed values from GATE simulation data.

With this scenario we reached to a solution where the processing time for the creation of LMF 48 bits file is almost negligible in comparison with the first scenario. Despite the complexity of creating such a class this was our choice in the development of an integrated solution to generate 48 bits LMF file directly from GATE. The development complexity is related not to the difficulties in programming such class but mainly to understand the whole logic of GATE implementation and output files creation. Once this was accomplished it was somewhat straightforward to implement this class in the GATE platform.

The actual code of the implemented class (`GateToFocus`) is presented in Appendix B, which will be briefly described in the next paragraphs. Also, there was the need to change the `GateOutputMgr` class in order to allow a user to state in the environment variables (`env_gate.csh` file) that it wants to use the FOCUS output during the simulation. This is accomplished by changing to 1 the `setenv G4ANALYSIS_USE_FOCUS` line in the environment, or typing `unsetenv G4ANALYSIS_USE_FOCUS`. This is reflected in the `GateOutputMgr` class which includes this new output in the array of `GateVOutputModule` pointers. When processing the simulation all the output modules included in this array of pointers will be called and get the data needed for each different output.

In the implemented class (`GateToFOCUS`) there are methods that are common with other output classes. Besides the constructor and destructor of the class, methods like `RecordBeginOf_Acquisition`, `RecordEndOfAcquisition`, `RecordBeginOfRun`, `RecordEndOfRun`, `Record_BeginOfEvent`, `RecordEndOfEvent` and `RecordStep` are the ones present in other classes as all output modules inherits from the `GateVOutputModule` and implement this new output module.

At the end of an event is the time when we start to populate our LMF 48 bits output module, calling the methods we developed especially for this class. `StoreInFOCUS` is a method that saves the coincidence in the LMF file. This method looks for the data given by the GATE simulation, mainly the values obtained by the several crystals present in the FOCUS machine, its position and time of acquisition. Other methods are called by the `StoreInFOCUS`, like `WriteInFOCUS` which writes the gather data into the LMF file in the end of the `StoreInFocus` method. As well several other methods are called which are used to execute small calculations regarding the values obtained, like `FixRSectorID`, `FixCrystalID` and `IncDecCrystalID`. Likewise other methods were implemented in order to encode the data gathered into the 48 bits format determined by the FOCUS LMF output. `InitEncode` fills the 48 bits array with the initial values, while `CoincidenceTagEncode`, `CoincidenceTypeEncode`, `TimeTagEncode`, `TimeEncode`, `HeadNumberEncode_ Gamma1`, `HeadNumberEncode Gamma2`, `X_EncodeGamma1`, `X_EncodeGamma2`, `Y_EncodeGamma1` and `Y_EncodeGamma2` are methods used to convert (i.e., encode) the data into the 48 bits format.

Like all the other output modules this new module also has a Messenger Class, the `GateToFOCUS_Messenger`, that allows to change the parameters of the object. The change of the parameters can be done by using scripted commands that are interpreted during the program execution.

8.4 Configuration of the 48 bits LMF Output

The macro command used to configure the 48 bits LMF output in GATE is:

```
/gate/output/focus/setFileName myFirst
```

to set the LMF file name, here the output file will be `myFirst.lmf`.

Moreover, in the GATE C-shell configuration script `env_gate.csh` must be defined the environment variable `G4ANALYSIS_USE_FOCUS` by the following way:

```
# Enable the use of the FOCUS output file
# Comment this line if you want to disable this output, type unsetenv or change
1 to 0
setenv G4ANALYSIS_USE_FOCUS 1
if ( ${?G4ANALYSIS_USE_FOCUS} ) then
    echo "FOCUS data output enabled"
else
```

```
    echo "FOCUS data output disabled"

endif
```

A C++ code to merge n LMF files was developed by Dr. Sébastien Jan, and used for dynamic output simulations. We merge all the LMF files in only one for the reconstuction procedure.

Chapter 9

Small Animal PET with GATE

The microPET® Focus 220 system was simulated in order to validate the use of GATE in the simulation of small animal PET. In order to do this, a model of the detection system and its geometry was developed. The accuracy of the developed detection model was tested through the comparison of simulated and measured results obtained from the FOCUS system, available at the SHFJ/CEA (Orsay, France), for a number of performance protocols including spatial resolution, counting rate and contrast recovering. Accuracy and variability of quantitative values obtained for mouse imaging using the Focus system, available at the SHFJ/CEA, can be found in [Jan *et al.* , 2004a].

Time dependence was introduced as a new feature to work with small animal imaging simulations using GATE, and the microPET®Focus 220 system. The results of those experiments have shown a good agreement between simulation and real data, leading us to conclude that the GATE platform is a relevant tool for performing small animal PET imaging simulation, under realistic conditions. Results from simulated realistic whole body studies of the mouse with [^{18}F]-fluoride and FDG, are presented, and compared to real data. The simulations were performed using the voxelized mouse phantoms obtained from real PET examinations and from the MOBY phantom. The simulation parameters are the ones already described in section 6.2.2. Positron range, attenuation, scattering and photon accolinearity were not simulated (we used a gamma/gamma emission source). This choice of parameters allowed us to produce simulated data representing an “acquisition best case scenario”. This data can therefore be taken as a gold standard when optimizing image reconstruction and image correction protocols.

9.1 Validation for the microPET® Focus Simulation

9.1.1 Spatial Resolution

For the image resolution estimation, radial and tangential FWHM were measured with a ^{18}F point source embedded in a capillary tube (0.2 mm internal diameter) and placed at different locations in the radial FOV. To validate GATE on the spatial resolution measurement, we simulated the explicit emission of the positrons by taking into account their range in water and the acolinearity of the

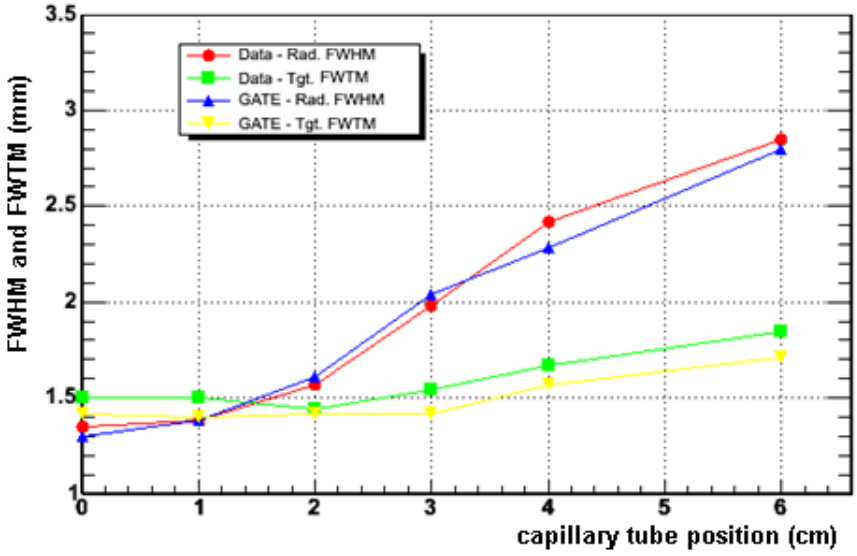

Figure 9.1: Evaluation of the FWHM and full width at the FWTM, with GATE compared with experimental values. Adapted from [Jan *et al.* , 2005b].

annihilation photons. A Gaussian blurring function is applied to the detection position of the photon within the crystal to mimic resolution degradation induced by crystal scintillation and light collection.

Figure 9.1 shows the differences between GATE simulations and experimental data for radial and tangential resolutions. The discrepancy is lower than 3%.

9.1.2 Counting Rate

To measure the counting rate performances of FOCUS, a 34 mL and 3 cm diameter cylindrical phantom was used. The phantom was uniformly filled with a ^{11}C aqueous source with an initial activity of 12 mCi. Figure 9.2 shows the defined parameters for the digitizer chain.

A comparison between simulated and experimental data for single count rate is shown in Figure 9.3. The physical background noise and the dead time of each block detector were included in the simulations. The results from simulations and measurements are in agreement for a large range of activity in the field of view (from 0 to 12 mCi).

In the lower right side of the Figure 9.3, the data are plotted for the lowest activities to demonstrate the influence of the physical background digitizer module without any activity in the FOV.

Figure 9.4 illustrates the comparison between simulated and experimental data for prompt and delay coincidences. The dead time of the coincidence processor and the data transfer from the scanner to the hard disk are also simulated. As for single counting rate, these results show a very good agreement for a large range of activity in the FOV.

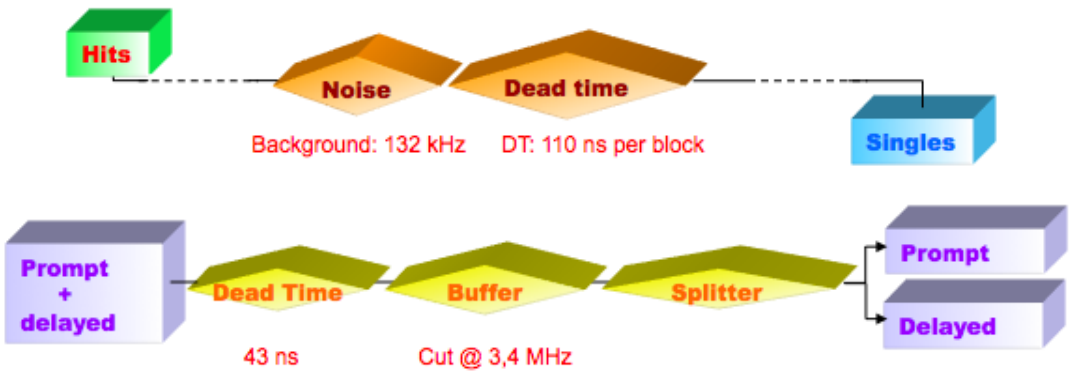

Figure 9.2: Defined parameters, in the digitizer chain, to measure the counting rate performances.

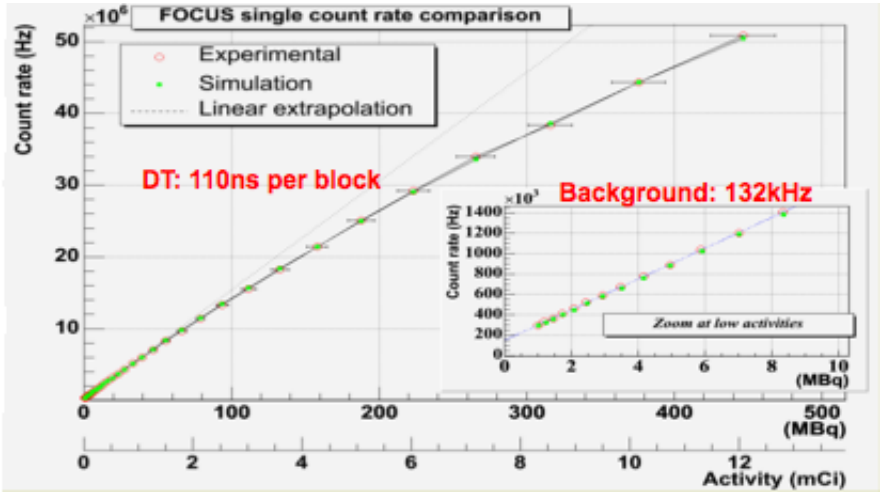

Figure 9.3: Evaluation of the counting rate, for single events, of the microPET®Focus with GATE compared with experimental values. Adapted from [Jan *et al.* , 2005b].

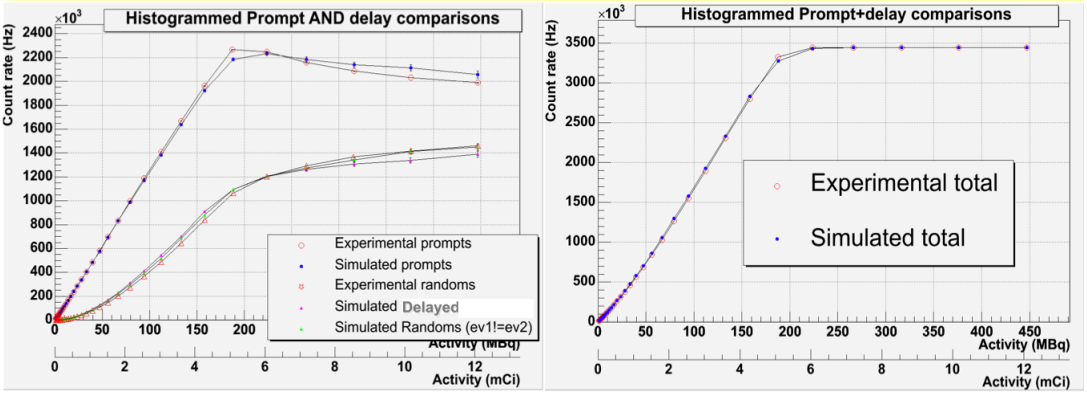

Figure 9.4: Evaluation of the counting rate, for prompt and delay coincidences, of the microPET FOCUS with GATE compared with experimental values. Adapted from [Jan *et al.* , 2005b].

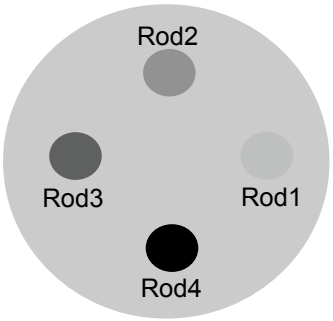

(a) Cylindrical phantom used to measure the contrast recovering of the FOCUS system.

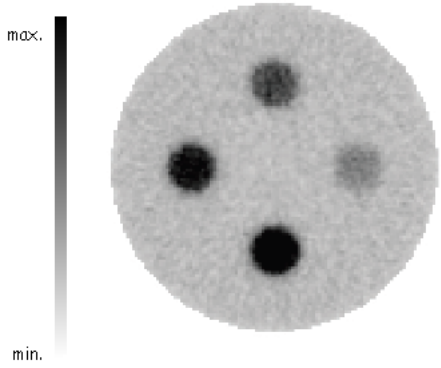

(b) Full simulation and reconstruction of a cylindrical phantom with hot inserts for contrast imaging measurement.

Figure 9.5: Contrast recovering with the FOCUS system. Adapted from [Jan *et al.* , 2005b].

9.1.3 Contrast Recovering

A 7 cm diameter cylinder with four 1 cm diameter inserts was simulated to measure the contrast recovering (CR), Figure 9.5a. The activity ratios simulated between inserts and the background are 2:1, 3:1, 4:1 and 5:1 respectively for the Rod1, Rod2, Rod3 and Rod4. Figure 9.5b shows the result after full simulation and reconstruction of this phantom. The CR results for each insert are listed in Table 9.1.

CR Rod1	96 % ± 3 %
CR Rod2	94.6 % ± 3 %
CR Rod3	93.7 % ± 3 %

Table 9.1: CR results for each rod. The activity ratio with the background is 2:1 for the Rod1, 3:1 for the Rod2, 4:1 for the Rod3 and 5:1 for the Rod4. Adapted from [Jan *et al.* , 2005b].

Organ	number of voxels (cc)	Activity (Bq/cc)
Body	30923	100.0
Bladder	134	4000.0
Rib bone	2759	1500.0
Spine bone	1405	1500.0

Table 9.2: Activity distribution in the MOBY phantom at the last frame, in the case of the [^{18}F]-fluoride.

9.2 Application for Small Animal PET Imaging

9.2.1 Bone Imaging Using [^{18}F]-Fluoride

We used the [^{18}F]-fluoride mouse exam, described in section 7.1.1, to set the activity distribution in our simulation studies for this radiopharmaceutical. This activity was defined using the real whole body mouse exam as reference.

In the case of the [^{18}F]-fluoride distribution, only the last acquisition time frame was simulated (please see Figure 7.2). This simulation corresponded to a real exam where 284 μCi are imaged by the FOCUS system during 15 minutes. Similar simulation conditions were used for the MOBY phantom. In this case, the activity distribution of [^{18}F]-fluoride was done according to Table 9.2. The simulation generated 4.0×10^{10} particles, equivalent to an injected dose of approximately 2.21 mCi imaged during 500 s. The simulation ran on a computer cluster with 50 CPUs. The computing time was approximately 10 hours. Figure 9.6 shows representative slices of real and simulated data.

To validate the accuracy of the simulations quantitative output, we compared the real data against the simulated data. We defined ROIs on the bladder, spine bone and rib bone and we normalized the activity concentration in each organ by the total activity uptake, both for real and simulated data. The results obtained after comparing simulated to real data are shown in Figure 9.7, where the statistical error measured as the ratio standard deviation over mean for all voxels considered for each organ (shown as error bars) are represented. The analysis of the relative differences between quantification values obtained for the real and the simulated data show differences of 22.7% for the bladder, 10.3% for the spine bone and 13.7% for the rib bone.

Figure 9.8 illustrates the acumulated activity obtained by simulation of the [^{18}F]-fluoride uptake using the MOBY phantom. The simulation ran on a computer cluster with 50 CPUs and lasted for approximately 21 hours.

The results obtained after comparing simulated to real data are shown in Figure 9.9, where the statistical error measured as the ratio standard deviation over mean for all voxels considered for each organ (shown as error bars) are represented. The analysis of the relative differences between quantification values obtained for the real and the simulated data show differences of 12.4% for the bladder, 18.1% for the spine bone and 19.0% for the rib bone.

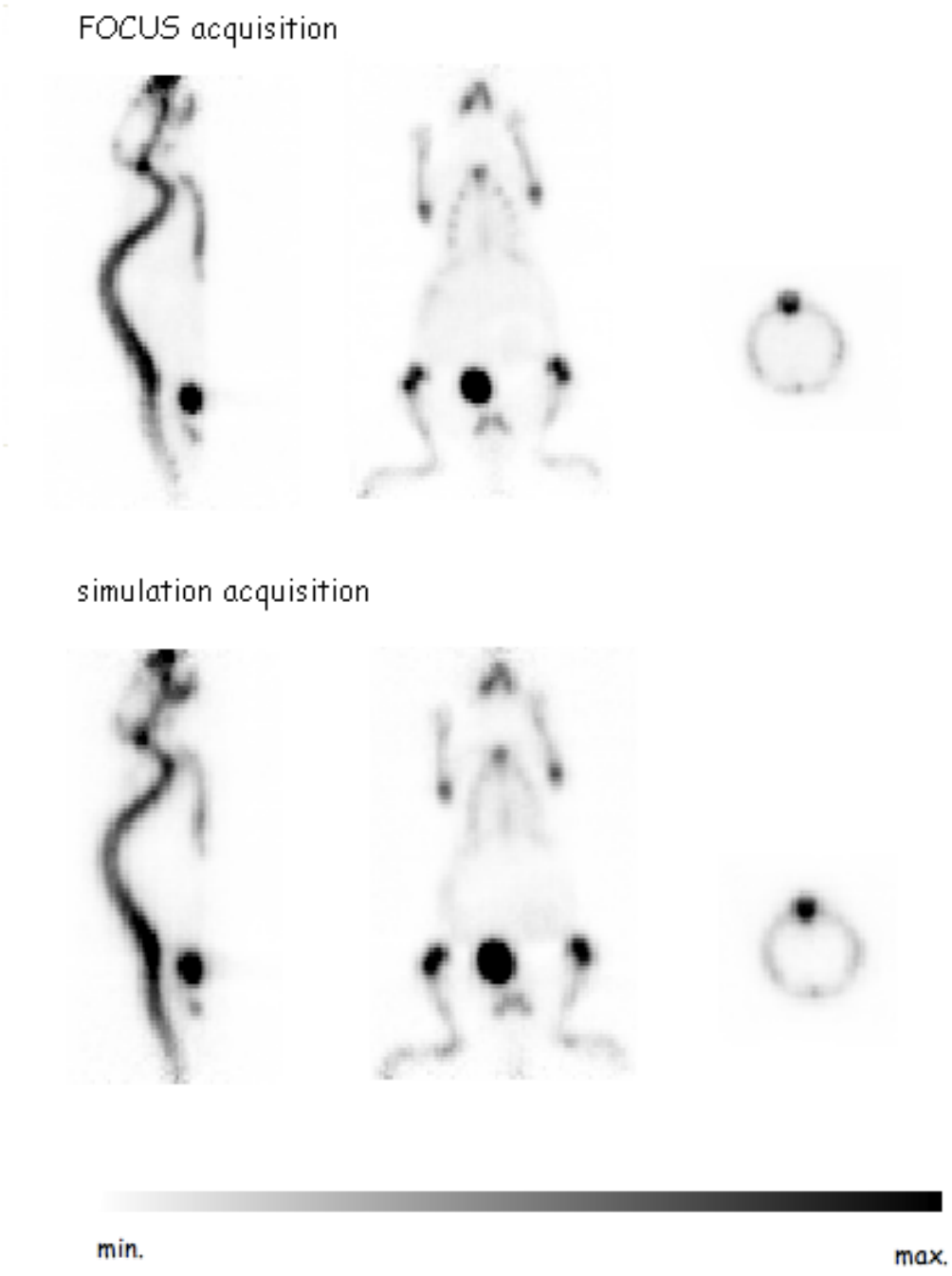

Figure 9.6: Coronal, sagital and transaxial slices representing [^{18}F]-fluoride uptake: acquired data (top) and GATE simulation using the real data phantom as input (bottom).

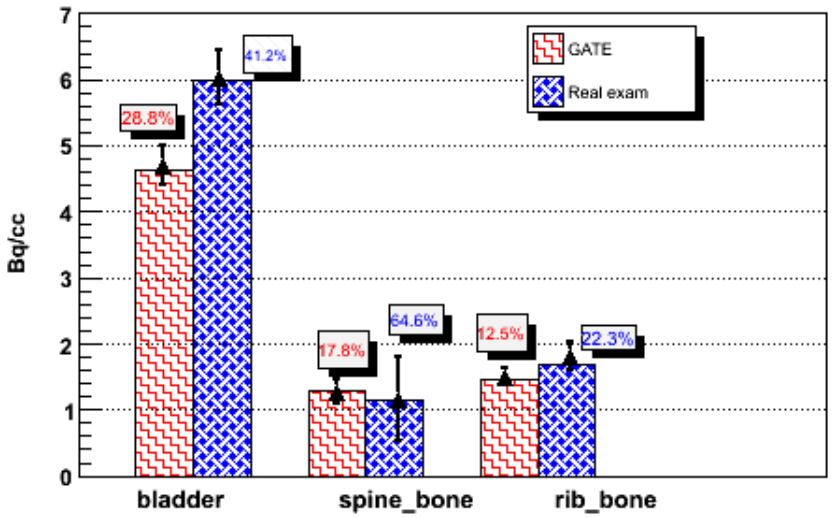

Figure 9.7: Comparison between PET image quantification using a real exam and GATE simulation, for the [^{18}F]-fluoride radiotracer with the mouse phantom generated from real data. Black bars represent the ROI statistical error measured as the ratio standard deviation over mean for all voxels considered.

Figure 9.8: Maximum Intensity Projection (MIP) of the MOBY phantom after a simulation with an activity distribution representative of the real [^{18}F]-fluoride distribution.

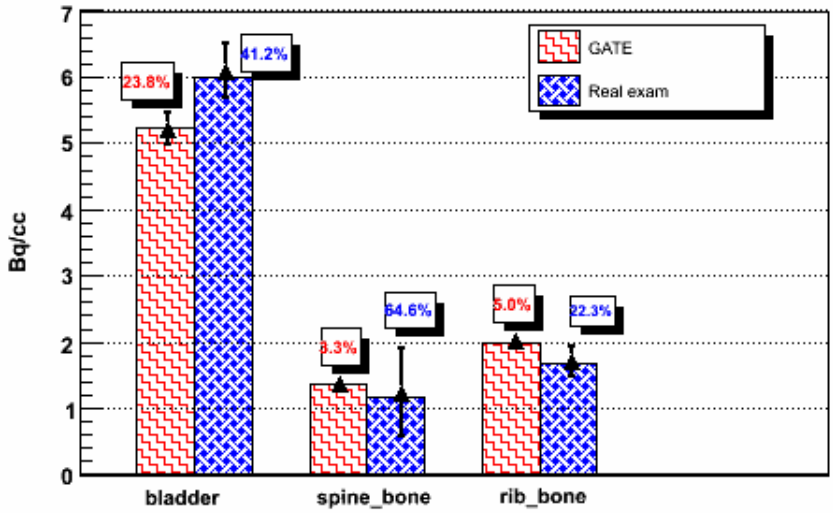

Figure 9.9: Comparison between PET image quantification and the GATE measurements, for the [^{18}F]-fluoride radiotracer with the MOBY phantom. Black bars represent the ROI statistical error measured as the ratio standard deviation over mean for all voxels considered.

9.3 Metabolic Imaging Using FDG

The FDG biodistribution is defined by the TACs which are assigned to different body structures. Figure 7.5 shows the TACs for each organ obtained for the FDG mouse exam described in section 7.1.1. We have sampled these TACs to set the activity distribution in each organ at each point in time of our simulations.

The defined activity map distribution for simulation was set to be representative of real data by assigning minimum and maximum values measured within a specific body region to intervals of voxel values in the phantom obtained from real data. The complete activity distribution for each organ structure is illustrated in Figure 9.10, expressed in %ID/cc (percentage ratio between the mean activity in each ROI and injected dose).

We simulated an acquisition time of 15 minutes, for an activity of 112 μCi at the last time frame. This resulted in tracking 3.5 $\times 10^9$ particles within GATE. Figure 9.11 compares two representative images of the mouse FDG distribution obtained from a real examination and from simulation. The simulation ran on a cluster of 10 CPUs with a global computing time of approximately 12 hours.

The accuracy of the quantitative results obtained by simulation was evaluated by comparing simulated data against real data. In order to do this, we defined ROIs on the liver, bladder, heart and kidneys. The values obtained by the use of these ROIs were normalized to the activity concentration in each organ by the total activity inside the whole body. Figure 9.12 shows the results of this comparison. In this figure, the statistical error measured as the ratio standard deviation over mean for all voxels considered for each organ (shown as error bars) are represented. The relative activity concentration obtained for the simulation data are in good agreement with the values obtained for real data.

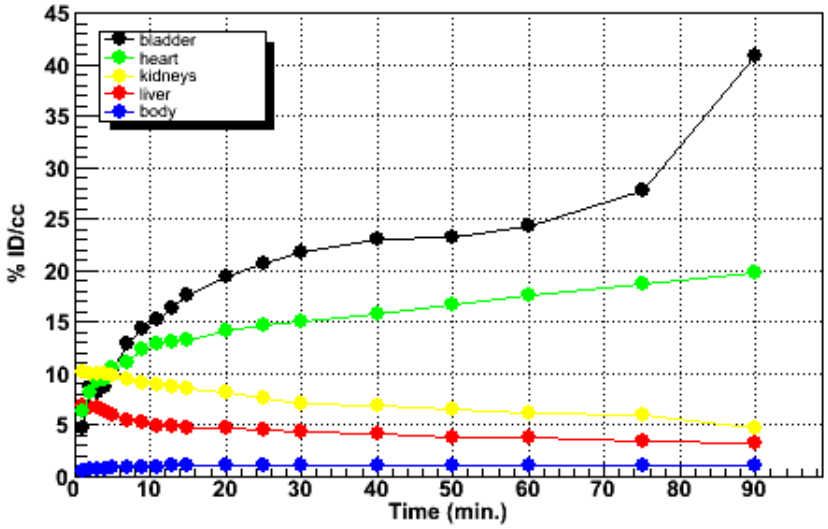

Figure 9.10: TACs used as input in the simulations for the FDG functional model, expressed in %ID/cc.

Organ	number of voxels (cc)	Activity (Bq/cc)	
		First Frame	Last Frame
Heart	548	254.7	242.3
Body	45362	0.6	76.3
Liver	3600	1963.3	273.7
Kidneys	641	1286.1	179.5
Bladder	134	410.1	1081.4

Table 9.3: Input activity distribution for the first and the last frame in the MOBY structure for the FDG.

We have also calculated the relative differences between the quantification values obtained by simulation and with the real exam. This comparison showed differences of 18.0% for the liver, 1.8% for the heart, 3.7% for the bladder and 7.5% for the kidneys. These differences may in part result from small differences on the ROIs definitions in the real exam and simulation.

A realistic FDG exam simulation was also done using the MOBY phantom. In this case, the emission map used was based on the FDG distribution, as previous stated, at the first and last time frames of a real exam. For the first frame we simulated 219 μCi for an acquisition time of 60 s which produced 4.9×10^8 particles. We simulated 131 μCi for 4.2×10^9 particles with an acquisition time of 15 minutes, corresponding to the last time frame of the real exam. The activity distribution for each organ, in each time frame, is shown on Table 9.3.

Figure 9.13 shows the results obtained for the first and last frames for the FDG simulation using MOBY. These simulations lasted for approximately 6 hours in the case of the first simulated time frame (using 6 CPUs) and approximately 14 hours for the last time frame (using 10 CPUs).

A complete simulation of a FDG exam was performed with the MOBY phantom, in order to define the TACs obtained from the simulation procedure. The simulated biodistribution obtained for the

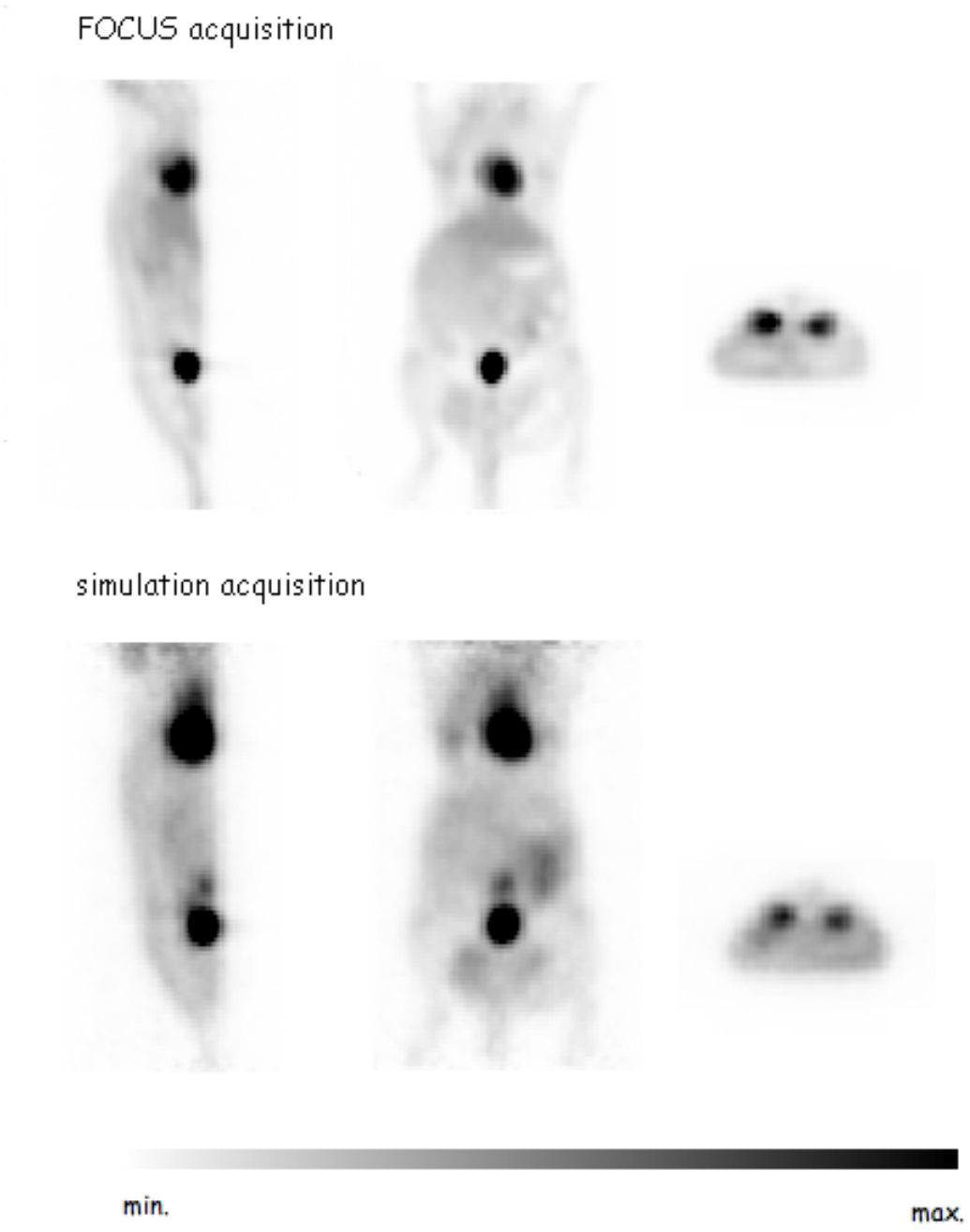

Figure 9.11: Slices from the real FDG exam (top) and the simulated exam (bottom) for the FDG mouse phantom, with an activity map distribution close to the last activity frame.

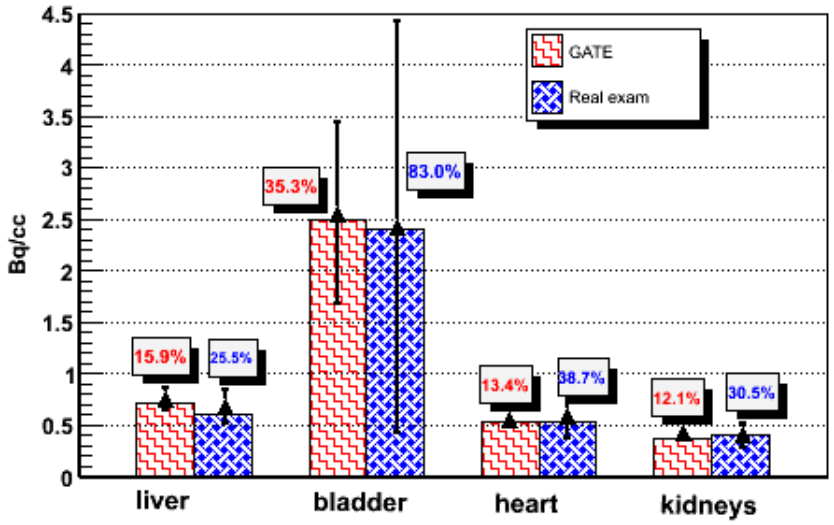

Figure 9.12: Comparison between PET image quantification and the GATE measurements, for the FDG radiotracer with the mouse phantom generated from real data. Black bars represent the ROI statistical error measured as the ratio standard deviation over mean for all voxels considered.

FDG radiotracer is shown in Figure 9.14. The analysis of the relative differences between the quantification values obtained by simulation and with the real exam is presented on Figure 9.15.

9.4 Physical Parameters Effects on the Quantification

The activity distribution was included in 6 structures of the MOBY phantom: the heart, the liver, the bladder, the kidneys, the muscle and the body. We have performed 2 sets of simulation, one with a direct gamma-gamma emission source and the other one with the inclusion of positron range and gamma accolinearity effects. Figure 9.16 shows the image obtained for each case.

To evaluate the consequences of these physical effects on the detection sensitivity and the quantitative analysis, we defined a ROI in the liver structure and we compared the activity value for the ^{18}F and the pure gamma-gamma emission source (to mimic a full correction of positron range and gamma accolinearity). The results shows that the bias on the quantification in the liver structure can be reduced by 25% for ^{18}F if corrections of physical effects are taken into account. This result is the first preliminary approach to improve the quantitative analysis in the whole-body mouse studies. More research about this issue, in the near future, should be done in order to include these corrections in the reconstruction procedure.

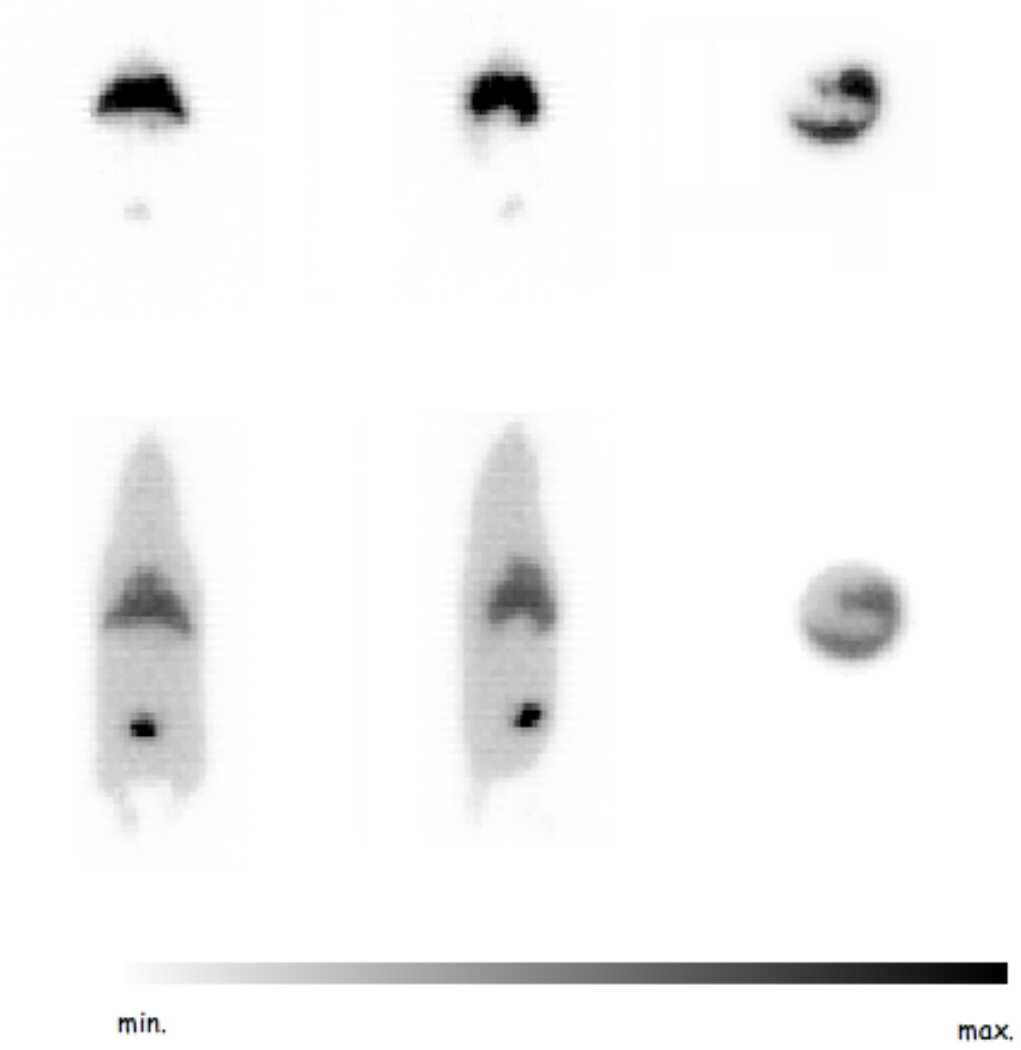

Figure 9.13: Coronal, sagital and transaxial slices for FDG simulation using MOBY: top - first activity frame (the first 60 s of the real exam), bottom - last activity frame (the last 900 s releated to the real exam).

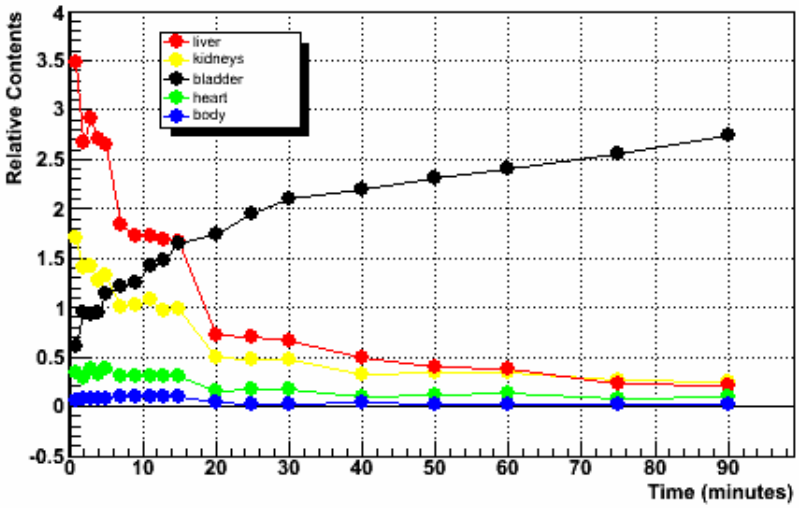

Figure 9.14: Measured TACs from a complete FDG simulation with the MOBY phantom.

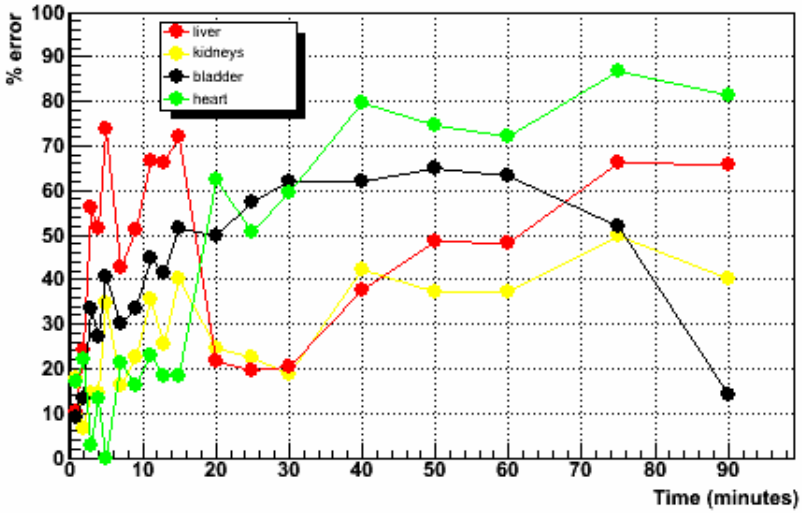

Figure 9.15: Relative differences between the quantification values obtained in the measured TACs for the MOBY phantom, and the TACs from the real FDG exam.

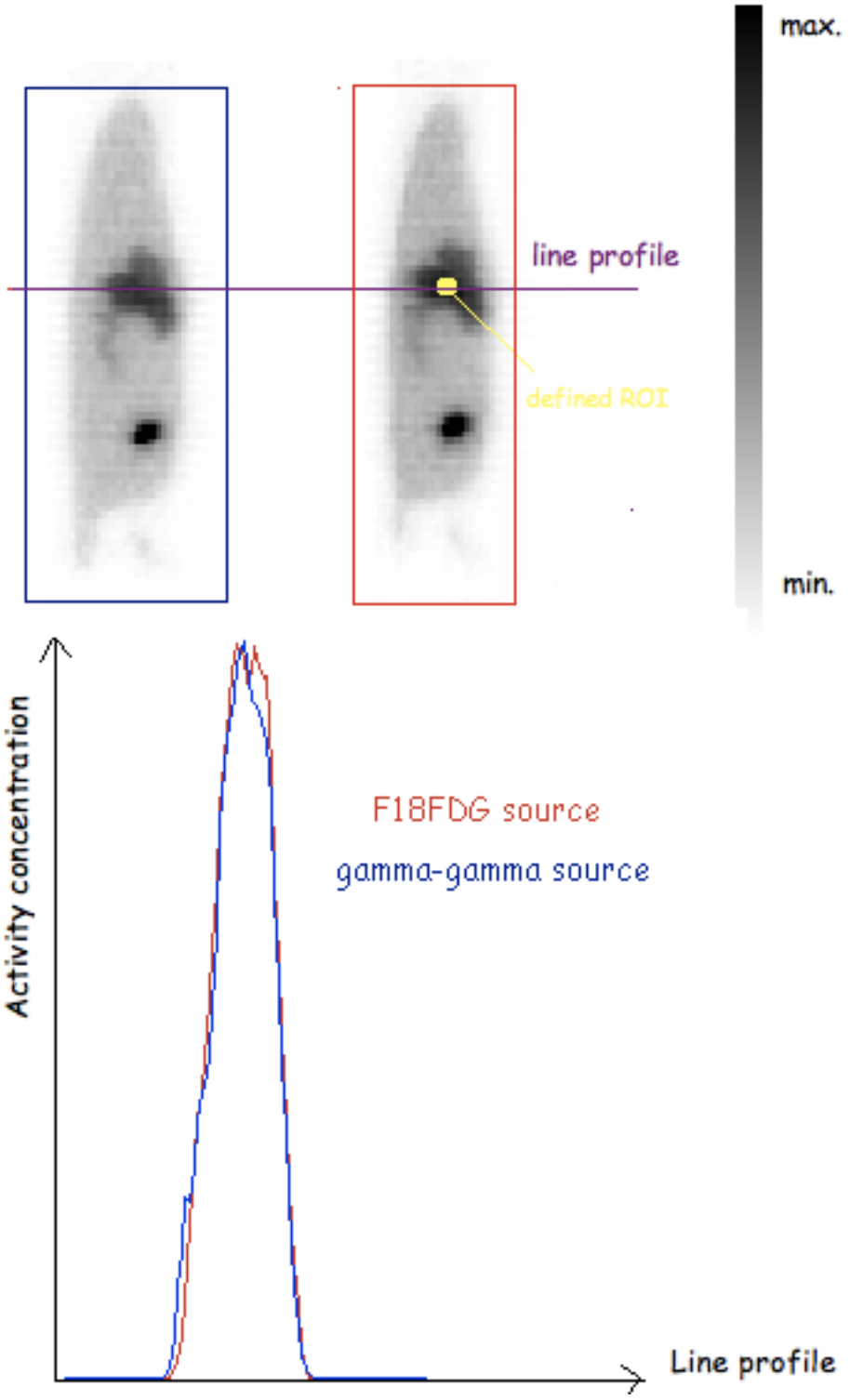

Figure 9.16: Physical parameters effects on the quantification. Left: Sagital slice of the simulated MOBY phantom with a gamma-gamma emission source. Right: Sagital slice of the simulated MOBY phantom for the ^{18}F emission source (with the inclusion of positron range and gamma acollinearity effects). Bottom: Maximum concentration profiles which illustrate the blurring or smearing effect for the ^{18}F emission source caused by the physical parameters effects.

Chapter 10

Evaluation of the Respiratory Motion in Lung Lesion Quantification

With the goal of better understanding the effect of the respiratory motion we have investigated the combined effects of target size, target-to-background activity concentration ratio and extent of respiratory motion on signal recovery of spherical lesions (targets) in 3D and 4D microPET images.

A set of static (non-gated MOBY data set without any motion associated) and dynamic (gated MOBY data set, where respiratory and lesion motions are present) FDG simulations were performed. Different lesion diameters (0.75 mm, 1.0 mm, 1.25 mm, 1.5 mm and 2.0 mm) were considered as well as different activity uptakes of FDG (0.01 μCi, 0.03 μCi, 0.05 μCi, 0.08 μCi, 1.08 μCi and 1.35 μCi), for the last time frame. The gated and non-gated MOBY emission maps are integrated into GATE as voxelized sources to assign the activity to different anatomical structures, in order to obtain static and dynamic emission data sets.

The activity distribution in all of the other organs was defined according to the last acquisition time frame for an FDG exam (determined with a typical mouse FDG PET exam). The concentration activity of the last frame (900 s of acquisition time) corresponds to 131 μCi.

The FDG biodistribution was defined by the TACs obtained from real wholebody mouse PET exams, has described previously. The activity distribution, within the MOBY phantom, was set according to the activity distribution assigned to the different whole body structures for the FDG radiotracer. In all simulation protocols, physical effects like positron range, gamma accolinearity and tissue attenuation were not taken into account in order to obtained the “best case scenario”, which could be used as defining the optimal results that could be obtain with a dedicated scanner and a specific radiotracer.

10.1 Data Analysis

Detection in PET images strongly depends on the ability to recognize the signal pattern in the presence of noisy background that in turn, is limited by the capability of the imaging system to

detect objects with very low contrast relatively to the background level and to spatially resolve a focal uptake. In the following paragraphs, the general methodology to evaluate the signal detection capability of an imaging system is presented. Although only the basic concepts on signal detection theory will be introduced, its description is important to contextualize the adopted analysis using the simulated data acquired with the microPET® Focus 220 scanner model.

The spatial resolution was measured by the FWHM. The FWHMs of reconstructed lesion images were determined along the direction of lesion movement due to respiratory motion. The image statistics were evaluated by calculating the signal-to-noise ratio (SNR) and contrast-to-noise ratio (CNR). The SNR is defined as the ratio of the average activity concentration measured in the target to the standard deviation. The higher the SNR, the less obtrusive the noise is. SNR is often defined as:

$$SNR = \frac{T}{\sigma_T} \tag{10.1}$$

The CNR was calculated as:

$$CNR = \frac{T - B}{\sqrt{\sigma_T^2 + \sigma_B^2}} \tag{10.2}$$

where T and B are the average activity concentrations measured in the target (lung lesion) and background region in the reconstructed image, respectively. $\sigma_{T,B}^2$ are the variances of these activities [Lartizien *et al.* , 2004].

In general, the "quality" of an image can be described (quantitatively) by its SNR. The SNR directly affects diagnostic and quantitative accuracy. In essence, then, a major goal of nuclear medicine equipment is to maximize the SNR in an image. The CNR refers to the ability in PET to distinguish between various contrasts in an acquired image and the inherent noise in the image. The mean signal recovery of SNR and CNR were evaluated as a function of the lesion size and the lesion activity uptake, using Equations 10.1 and 10.2.

The target-to-background ratio (TBR) is defined as the relation between the lesion activity to the background activity concentrations. The TBR values are computed using the following relation:

$$TBR = \frac{T}{B} \tag{10.3}$$

The data recorded from the ROIs were used to compute the contrast recovery (CR) and the volume recovery coefficient (VRC). The evaluation of the contrast recovery indicates how reliable the reconstructed image would be for lesion detection tasks in real situations. This result in the ability to evaluate the reconstruction algorithm used to recover a certain simulated contrast between a lesion and a background. The contrast recovery between the simulated lesions and the surrounding organs in the reconstructed images was computed using the expression:

$$CR = \frac{T - B}{T + B} \tag{10.4}$$

where T was the mean activity in the simulated spherical lesion ROI and B was the mean activity in the background region ROIs. Higher contrast values are often related with noisier images. In practice, this contrast is provided by the radiotracer's distribution. The goal of the imaging system is to preserve this contrast in the image. Contrast is maintained by avoiding blurring, which smears counts from higher activity regions into lower activity regions (and vice versa), thus reducing image contrast. In this way, spatial resolution and contrast are closely linked.

In order to determine temporal resolution, the VRC was defined as:

$$VRC = \frac{V_{measured}}{V_{true}} \tag{10.5}$$

where $V_{measured}$ is the measured lesion volume and V_{true} is the real lesion volume. To perform data analysis, and quantify VRC values, we have drawn a volume of interest (VOI) around the centroid of each lesion. The size of the drawn VOI depends on the lesion size, in order to include as many voxels as possible, to keep a good statistic, and, at the same time, to include only voxels that corresponded to the lesion. For each VOI we calculated the average number of counts in each voxel. Background values were obtained by drawing and merging circular VOIs around each lesion (within the surrounding soft tissues: lung and liver regions) and by calculating the average number of counts and the corresponding standard deviation within.

These data was also used to calculate the mean percent error in the volume for each lesion. The mean percent error between the estimated volume and the true volume of the spherical lesions was given by:

$$\%\,error = \frac{V_{measured} - V_{true}}{V_{true}} \times 100 \tag{10.6}$$

10.2 Quantification Considerations...

At the beginning of this discussion we stated that the results obtained for the higher diameter lesions (1.25 mm, 1.5 mm and 2.0 mm) in the dynamic mode (gated images) are not show due to lesion blending into the liver. Additionally, due to the limited spatial resolution of the scanner used the results obtained for the smallest lesion (0.75 mm) may be compromised by a decrease in the sensitivity of detection and thus statistics could not be accurately measured. Due to this, to evaluate the effects produced by the respiratory motion we choose to use the 1.0 mm lesion, Figure 10.1.

Concerning data analysis, a selected lesion ROI for each particular case was used to estimate T (average activity concentrations measured in the lesion) when positioned over a background region. In the present analysis, the mean lung lesion activity T was computed as the average pixel intensity in the spherical ROI located at the lesion. The ROIs were all extracted from transaxial slices of the MOBY phantom passing through the different planes containing the lesion activity. The mean background activity B was estimated as the average pixel intensity within ROIs projected into reconstructed images without the lesion data added, however surrounding the lesion location. The placement of the lesion ROI for a 1.0 mm diameter lesion and background ROIs is illustrated in Figure 10.2.

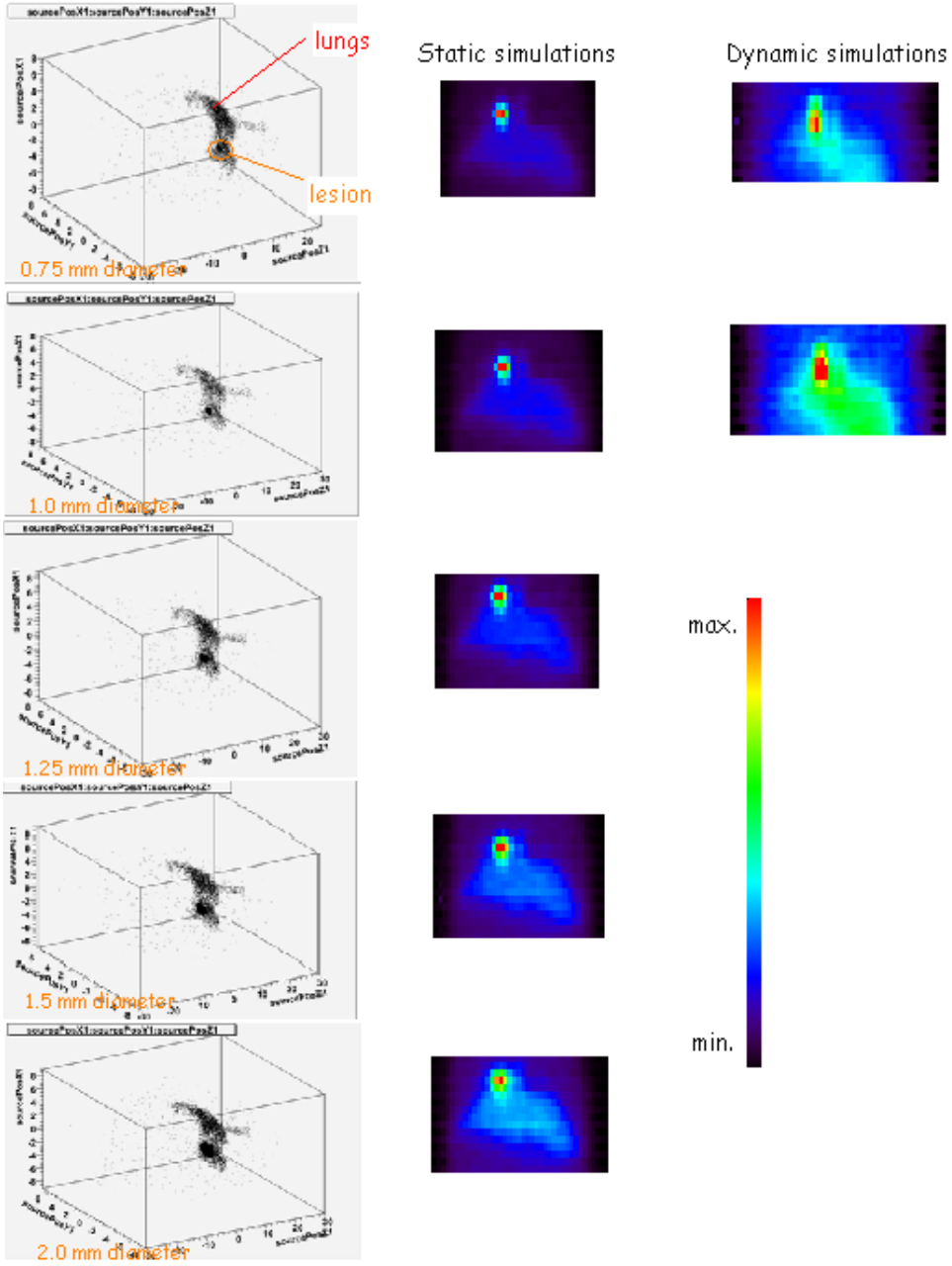

Figure 10.1: Lesion size definition. To obtain this definition there were several steps that were executed. The first was to carefully place the lesion in the lungs and not on any other organ. Secondly there was the need to try different sizes in order to define a lesion that was entirely inside the lungs. The images on the first column of the figure show this steps using ROOT. In order to achieve this outcome we had to define activity in the lesion as well as in the lungs (in a FDG exam there is no lungs activity uptake in the image). The middle column presents the images for the static FDG simulations (for the last frame), and in the rightmost column there is presented the images for the dynamic FDG simulations (for the last farme). For the higher diameter lesions (1.25 mm, 1.5 mm and 2.0 mm) in the dynamic mode images are not show due to lesion blending into the liver.

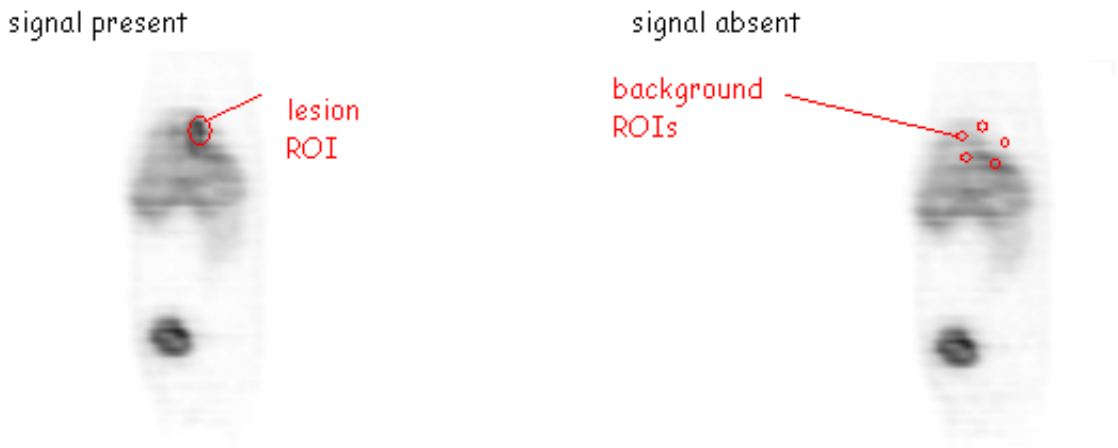

Figure 10.2: Sagital slices through the MOBY phantom containing a 1.0 mm diameter lung lesion or only background, illustrating the placement of the background and lesion ROIs used for data analysis.

	Static Simulations					Dynamic Simulations
Activity	Lesion Diameter					
(µCi)	0.75 mm	1.0 mm	1.25 mm	1.5 mm	2.0 mm	1.0 mm
0.01	12.26%	21.0%	20.58%	14.56%	18.91%	11.81%
0.03	17.16%	33.92%	25.82%	16.98%	19.41%	9.11%
0.05	20.22%	43.43%	33.66%	31.72%	24.39%	11.88%
0.08	22.80%	49.65%	39.39%	37.25%	27.64%	14.54%
1.08	24.68%	51.74%	41.85%	40.35%	32.76%	19.54%
1.35	24.82%	55.46%	43.72%	42.67%	37.73%	20.71%

Table 10.1: Statistical error obtained for the defined ROIs in the lung lesion implementation in the MOBY phantom, from the static and the dynamic simulation modes.

The statistical errors measured as the ratio standard deviation over mean for all ROIs considered for each lesion diameter, as function of the activity defined, are represented in Table 10.1. We found higher values in higher activity concentrations. This Table suggests that for the smaller lesion sizes (0.75 mm and 1.0 mm diameter) we have compromised results when compared to the statistical errors obtained for the other lesion sizesdue to limited FOCUS system resolution. In addition, lower activity concentrations (0.01 µCiand 0.03 µCi) shows the same behaviour because lower activity concentrations significantly deteriorates the lesion signal recovery. The statistical errors for the ROIs considered in static simulation was found to be 18.92% and 22.44% for the dynamic simulations.

10.3 Motion Blurring versus Spatial Resolution

"Best case scenario" images are presented in Figures 10.3 and 10.4, from static (non-gated data, without motion involved) and dynamic simulated data (gated data, where respiratory and lesion motions are present).

From Figures 10.3 and 10.4 differences between the non-gated data set (static simulation) and the gated data set (dynamic simulation) can be seen. The extent of respiratory motion is evident between the 1^{st} and the 10^{th} frames in Figure 10.4. The coronal slices shows the realistic motion of the various structures present in the thorax and upper abdomen due to the lungs expansion and contraction for the non normal tidal breathing configuration.

From the visual inspection of the static image, in Figure 10.3, the lesion is clearly shown, keeping its spherical shape. However, for the dynamic image, in the same Figure, the lesion appears blurred and elongated as a consequence of the breathing movement. Consequently, respiratory motion may preclude the accurate detection of small lung lesions.

The motion vector defined in section 7.1.2.1 (Equation 7.1) indicates more motion blurring within the transaxial plane than along axial (z) direction. Figure 10.5 shows the difference of blurring along different directions. This result also indicates, due to respiratory motion, that a sphere lesion can be blurred to a shape with different size in different directions in 3D space. Additionally, the extent of blurring along different directions will depend on the motion vector at the position in the lung.

The image spatial resolution was parameterized by the FWHM of Gaussian fits of the profiles taken over all lesions in the reconstructed images of the MOBY phantom. The results obtained for the static acquisitions are illustrated in Figure 10.6. Spatial resolution improves most significantly for the smallest lesion diameter and at the same time for higher activity uptakes.

Figure 10.7 shows the axial resolution of the lesion with 1.0 mm diameter for static and dynamic acquisitions, as a function of different FDG uptakes. It demonstrates that the blurring effect is lower for static acquisitions. It also demonstrates that when the FDG uptake increases the blurring decreases for dynamic and static acquisitions and consequently improve spatial resolution.

10.4 Lesion Detectability

Signal-to-noise (SNR) ratios are indicators of the visual utility of an image for detection purposes. The SNR directly affects diagnostic and quantitative accuracy [Sain & Barrett, 2003]. The SNR describes the relative "strength" between the desired information and the noise in the image. The higher the SNR, the less obtrusive the noise is. The value SNR = 5 is the conventional value of detectability used in radiology, and as also been used in emission tomography images. Lesions for which $T - B > 5\sigma_B$ can be considered 100% visible [Cherry *et al.* , 2003b; Graham & Links, 2007]. SNR values for the lower lesion activity concentration are in the vast majority of situations higher than the 100% detectability limit.

Figure 10.8 show that the SNR depends strongly both on the lesion diameter and on the activity concentration. Nevertheless, the plots presented show that, for the highest activity values, most

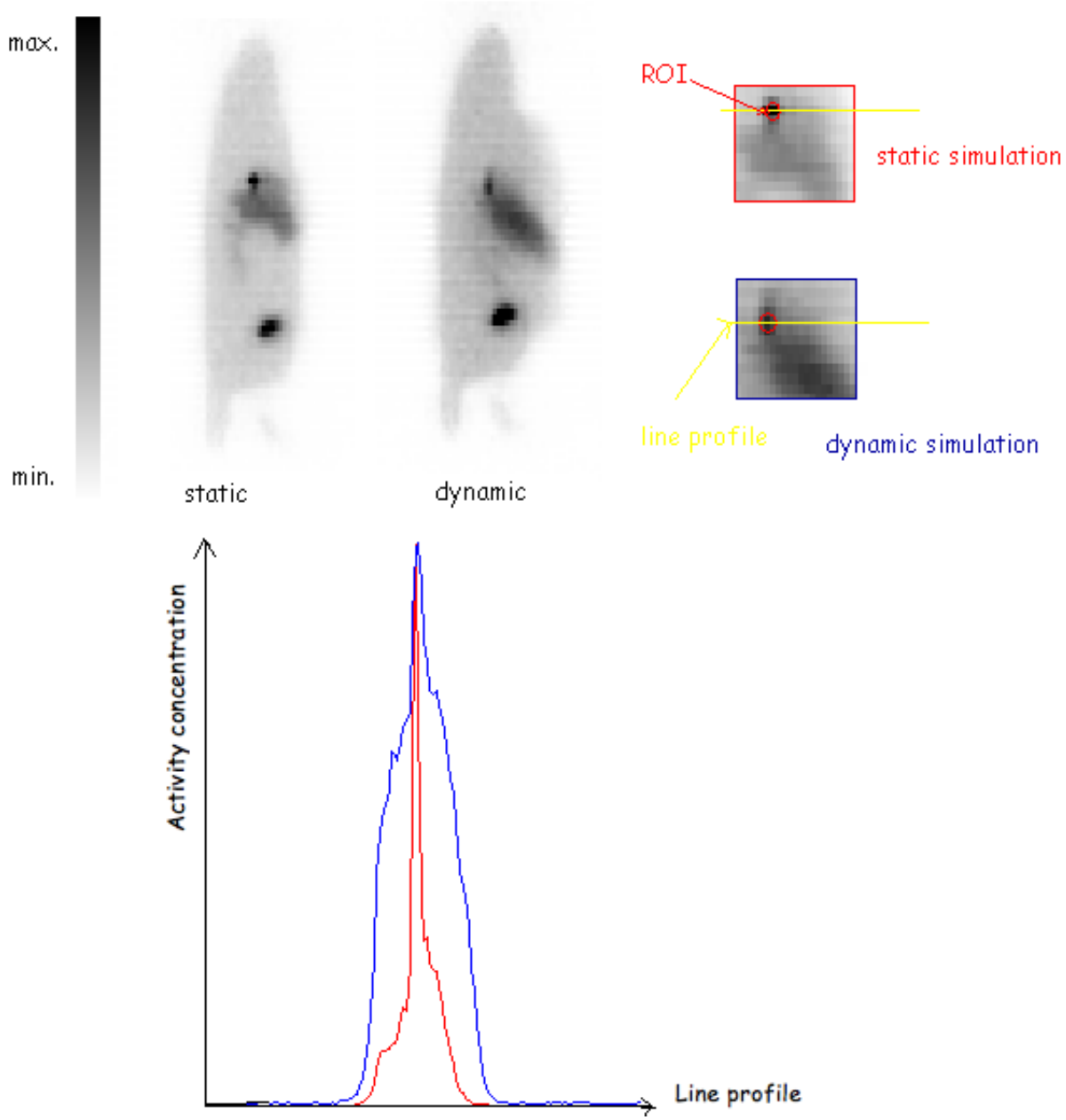

Figure 10.3: Sagital slices, of the reconstructed MOBY phantom, for a static acquisition, where no motion was simulated, and for the simulation of a dynamic acquisition, where respiratory and lesion motions were considered, with a lung lesion of 1.0 mm diameter and an FDG uptake of 0.05 μCi. The maximum concentration profiles from 3D and 4D simulated exams: where the blurring or smearing effect induced by respiratory motion are represented in the right.

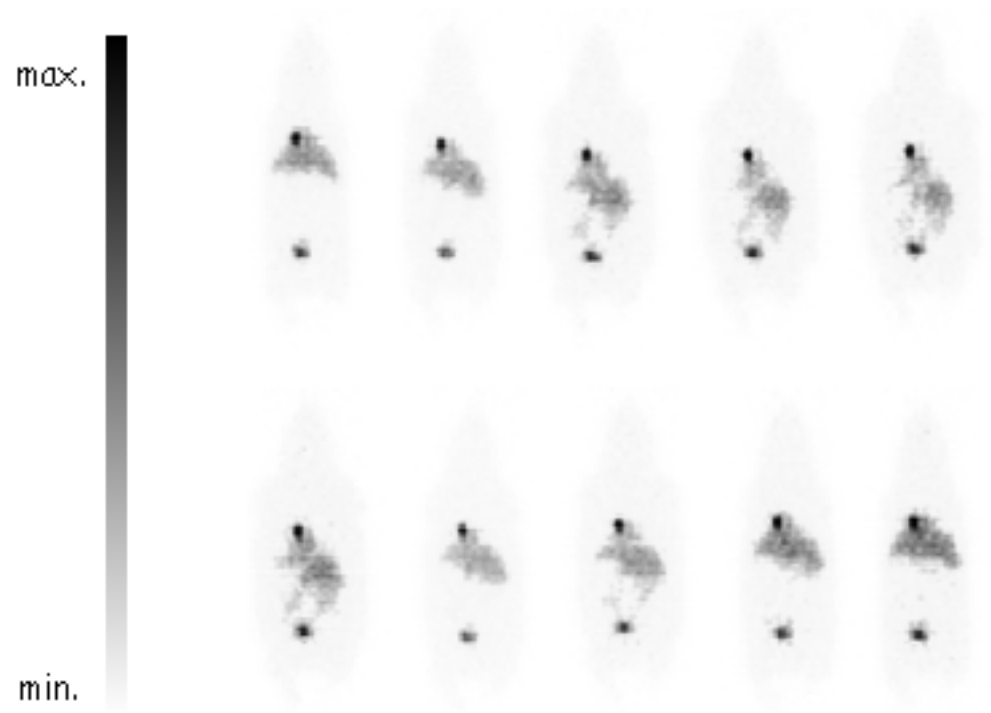

Figure 10.4: Coronal slices of the MOBY phantom corresponding to the simulation of a “stress” condition breathing motion (see section 7.1.2.1) including a lung motion lesion of 1.5 mm diameter and an FDG uptake of 1.35 μCi. These coronal slices represent one respiratory cycle for an FDG exam in the last time frame. The dynamic 3D emission assumed an event collection during 900 s, where 5.65×10^9 particles were generated.

Figure 10.5: Transaxial, coronal and sagital slices of the reconstructed lung lesion, in the MOBY phantom, with 2.0 mm diameter and an FDG uptake of 0.08 μCi. No motion was simulated.

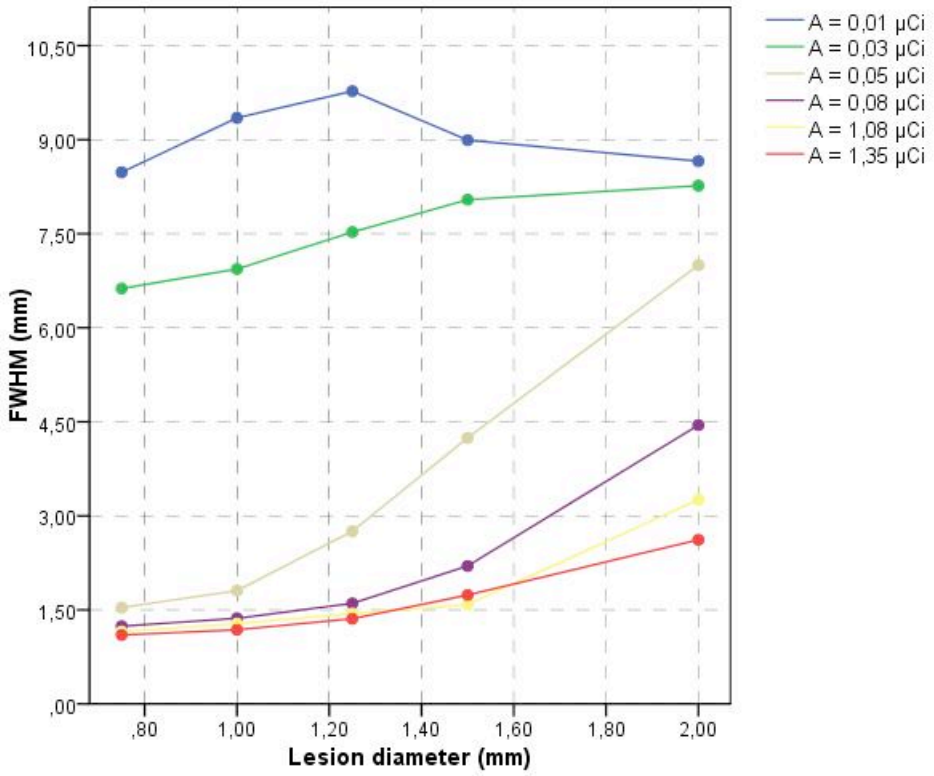

Figure 10.6: FWHM of the line spread function through the lesion centroid as a function of the lesion diameter defined for the static acquisitions schemes.

of the lesions converge to SNR values that are below the line of 100% visibility. In the case of higher activity concentrations, the smallest lesion diameter tend to converge to SNR values close to the 100% detectability line against SNR values that are significantly below that value for highest lesion diameter. However, according to the reconstructed images, the lesions with the considered diameters for all activity concentration ratios are all observable by visual inspection (some difficulties appear for the smallest lesions with lower activity concentrations, and the largest due to the lesion blending in the surrounding organs). This seems to indicate that the SNR = 5 criterion, from conventional radiology, might not be a good detectability criterion for emission tomography images. Keeping this in mind, we will, nevertheless, use this criterion as a reference for the quality of the images with respect to its SNR ratio.

Figure 10.8 shows the plot of the SNR ratio against lesion diameter for all activity concentrations considered. Table 10.2 shows the SNR for static and dynamic acquisitions as a function of different activity concentrations for the 1.0 mm diameter lesion. The results summarize what was previously devised: the SNR is as lower as higher is the activity concentration, and is as higher as higher is the lesion diameter. Although this conclusion is contra intuitive for the results obtained in the smallest lesion, this is a direct consequence of the sensitivity lost caused the spatial resolution: signal recovery can be hindered by the limited spatial resolution of the microPET scanner (partial volume effect). Concerning the relation between SNR and the activity concentration, we expected to recover higher SNR values with the increase in the activity concentration. In fact we get a higher

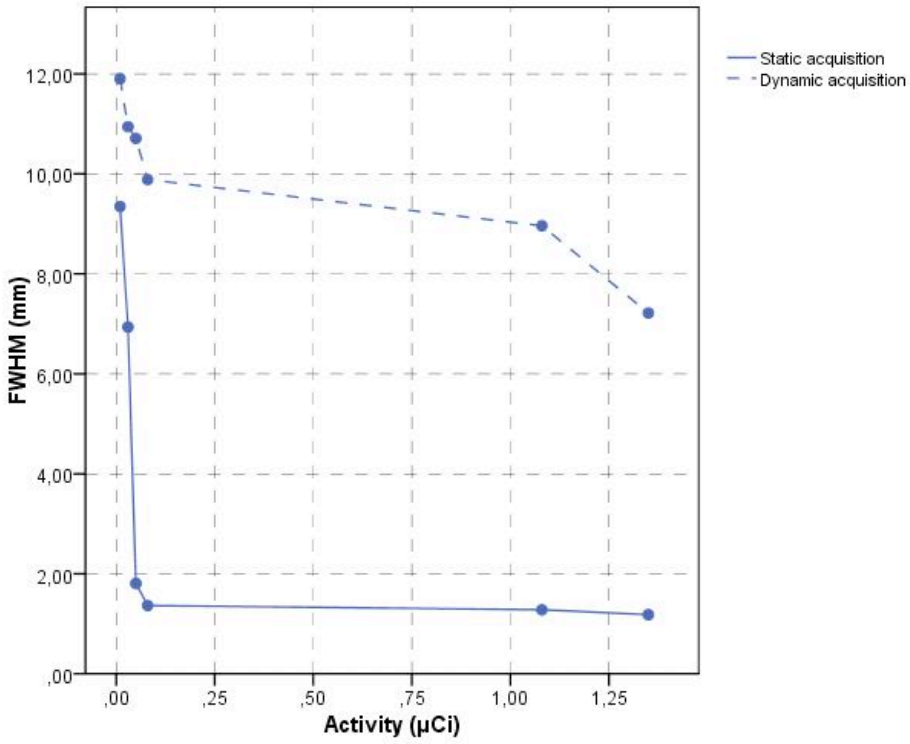

Figure 10.7: FWHM of the line spread function through the lesion centroid as a function of the FDG activity defined for static and dynamic acquisitions schemes, for the 1.0 mm diameter lesion. Data from dynamic acquisitions are represented by dashed curves and static acquisition data are represented by solid curves.

signal as a function of the lesion activity increase but we also obtained higher noise values which results in an increase of the SNR value for lower lesion FDG concentration.

Despite of the increase in the mean signal recovery, as a function of the FDG concentration increase, the standard deviation had also a significant increase. This result in a decrease of the SNR recovers values. We get the same behaviour for the CNR values as a function of the activity concentration. These results can also be explained through the results obtained for the spatial resolution versus the motion blurring (see section 10.3).

In respect to the CNR, when the size of a lesion is substantially larger than the limiting spatial resolution it can influence the detection ability, especially if the lesion has low contrast. The CNR is displayed in Figure 10.9 as a function of the lesion diameter, and for different activity uptakes. Overall, CNR improves significantly as lesion contrast decreases and lesion size increases.

We need to have into account the same line of the results inspection: caused by the small size of lesions relative to scanner resolution (partial-volume effect) we got higher CNR values for the smallest lesion.

Table 10.2 summarizes SNR and CNR values in the lesion with 1.0 mm diameter as a function of the FDG activity concentration. The first columns show the CNR and the SNR from the non-gated images of the phantom in a static mode. The other results correspond to data obtained from the

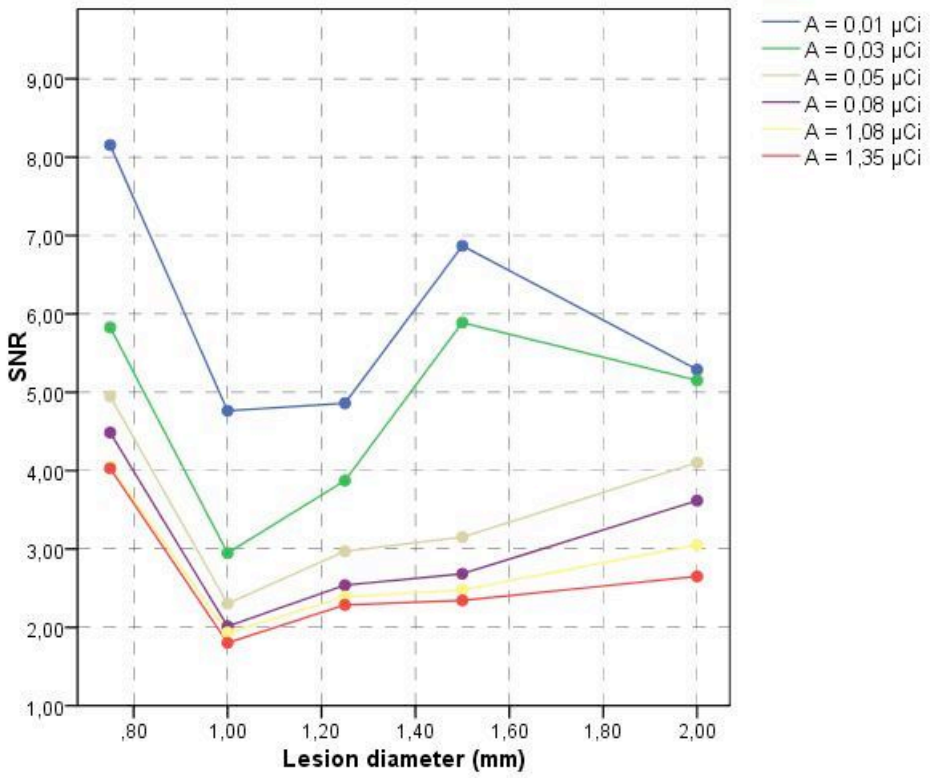

Figure 10.8: SNR of the 0.01 µCi, 0.03 µCi, 0.05 µCi, 0.08 µCi, 1.08 µCi and 1.35 µCi FDG uptakes for the spherical lesions as a function of the lesion diameter. Results obtained for the static simulations.

gated images of the phantom in the dynamic mode. The dynamic simulations results in larger overestimations of SNR due to poor counting statistics and high image noise. This effect is more significant as the lesion activity concentration decreases, as it is shown in Table 10.2. However, the same table shows a slight improvement in CNR recovery for the dynamic acquisitions as the lesion activity increases. Respiratory motion has less of an effect on the peak lesion signal and thus could explain the improvement on the dynamic CNR results.

We expected improvements on the SNR and the CNR data as a function of the increase of the FDG activity (higher activities always provide better SNR and CNR). This is due to the fact that we defined the lesion motion as a function of the no normal tidal breathing and thus with a largest magnitude of motion. Because there is a higher motion in this condition then it is expected that we will get an improved signal recovery for the lower contrast lesions. As discussed before, the values obtained for the other dynamic acquisitions sets are quantitatively changed due to the lesion blending into the liver (in the case of the largest diameter lesions) and are not used in the comparative set. We decided to remove the comparative set for the smallest lesion because the statistical results may be compromise by the limited spatial resolution of the microPET® FOCUS 220.

Figure 10.10 illustrates the relationship between contrast and activity concentration, TBR, as a function of the lesion diameter. The higher the contrast the higher is the detectability. Figure 10.11 shows the TBR plot for a set of dynamic and static acquisitions as a function of the FDG activity

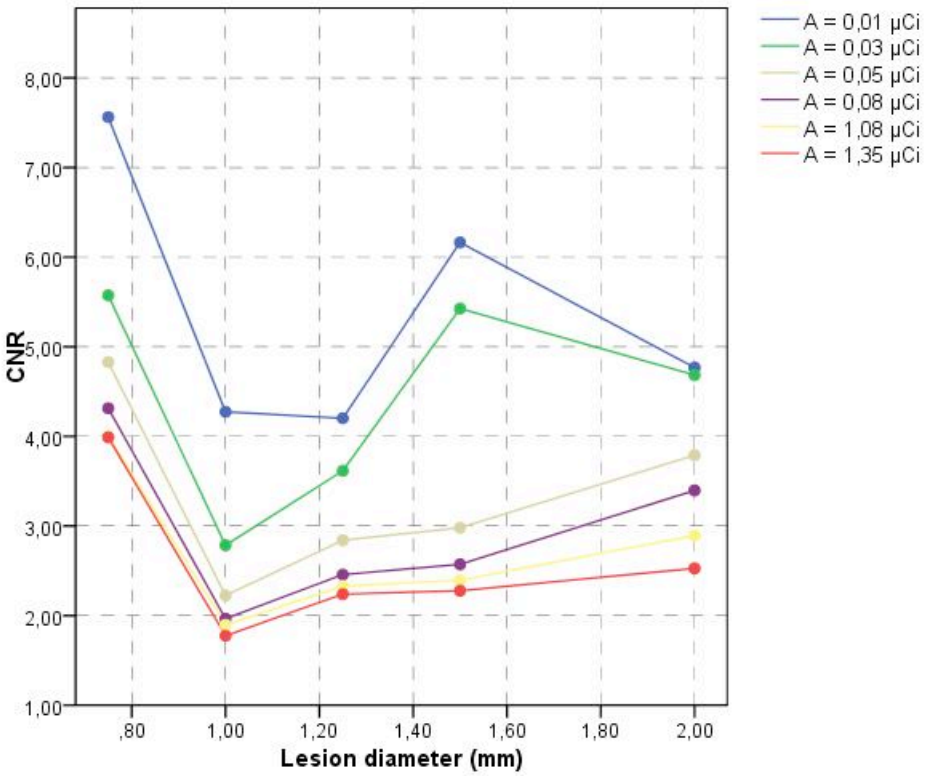

Figure 10.9: CNR of the 0.01 µCi, 0.03 µCi, 0.05 µCi, 0.08 µCi, 1.08 µCi and 1.35 µCi FDG uptakes for the spherical lesions as a function of the lesion diameter. Results obtained for the static simulations.

Activity	Static Simulations		Dynamic Simulations	
(µCi)	CNR	SNR	CNR	SNR
0.01	4.274	4.764	0.213	8.465
0.03	2.785	2.948	2.405	10.975
0.05	2.225	2.303	2.407	8.419
0.08	1.966	2.014	2.920	6.880
1.08	1.897	1.933	2.823	5.117
1.35	1.766	1.803	2.968	4.829

Table 10.2: SNR and CNR values in the lesion with 1.0 mm diameter as a function of the FDG activity concentration. The first columns show the CNR and the SNR from the images of the phantom in a static mode. The other results correspond to data obtained from the images of the phantom in the dynamic mode.

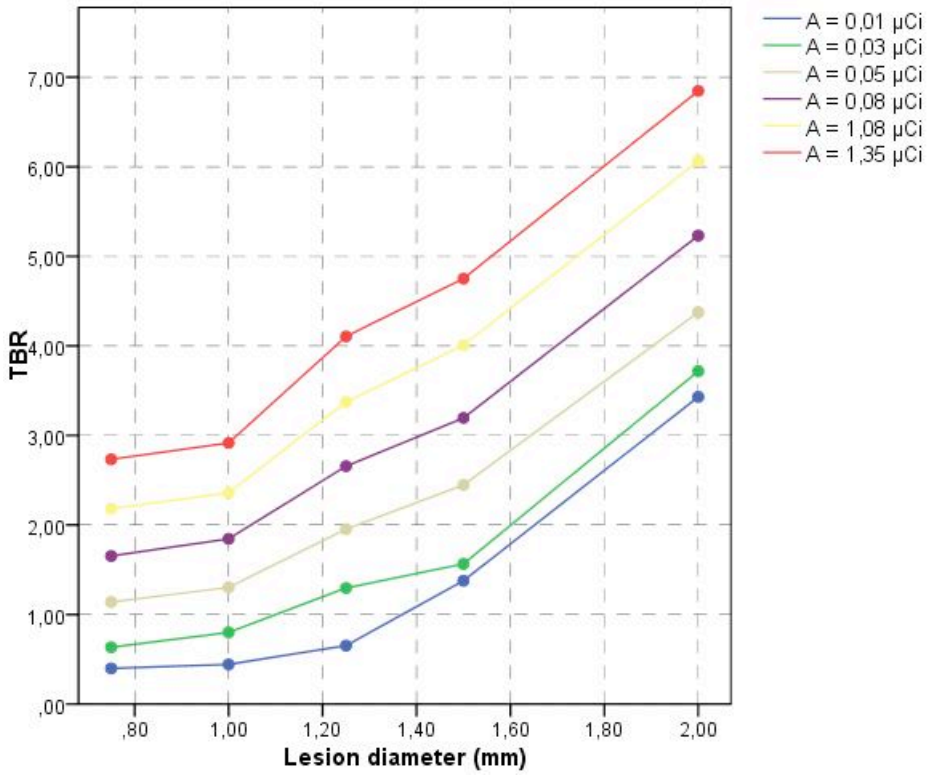

Figure 10.10: TBR of the 0.01 µCi, 0.03 µCi, 0.05 µCi, 0.08 µCi, 1.08 µCi and 1.35 µCi FDG uptakes for the spherical lesions as a function of the lesion diameter. Results obtained for the static simulations.

concentration, for the lesion diameter of 1.0 mm. The curves show that the TBR increases as the activity concentration increases. Moreover, and as expected, the figure also illustrates that we achieved lower TBR values for the images of the moving lesions.

10.5 Evaluation of the Contrast Recovery and Volume Recovery Coefficient

The Figure 10.12 shows the trends of the contrasts recovery, in the static acquisition simulations, against lesion diameter, for all the lesion activity uptakes considered. As it can be seen in these plots, the contrast recovery values obtained in these studies are always high, even for the smallest lesion diameter. These plots highlight the fact that the contrast recovery depends more strongly on the lesion diameter than it depends on the lesion to background considered. In fact, for a given diameter, the contrast recovery is approximately the same for all the different activity uptakes. The strong dependence on lesion diameter illustrates a significant partial volume effect.

Figure 10.13 illustrates the CR of a set of dynamic and static acquisitions as a function of the FDG activity concentration for the 1.0 mm diameter lesion. The line of the simulated contrast is also shown in the plot as an horizontal red line for comparison. We found higher CR values from the

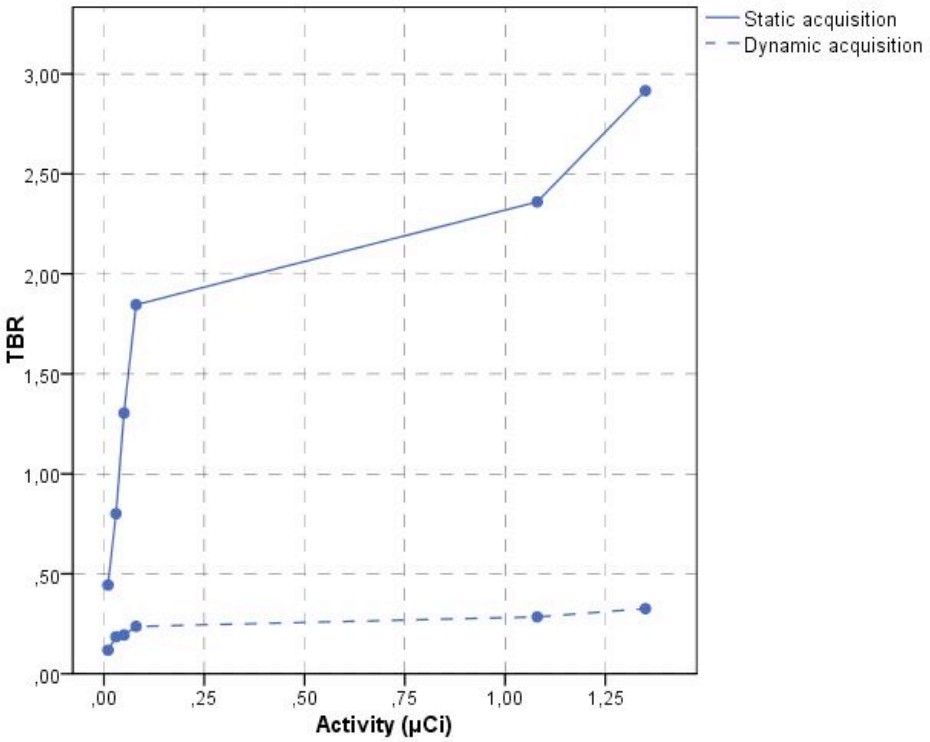

Figure 10.11: TBR of a set of a dynamic and a static acquisition as a function of the FDG activity concentration for the 1.0 mm diameter lesion. Data from dynamic acquisitions are represented with the dashed curve and static acquisition data are represented by the solid curve.

dynamic data against the static data. We expected that the motion decrease the contrast in the reconstructed images, while images from static acquisitions can largely recover the signal lost due to motion. These results are influenced from the ROIs defined in the background level. However, the mean signal recover is higher in static data when compared to the dynamic data. These results suggest that the ROIs approach for the background level used probably was not the best choice (despite of the approach used in pre-clinical practice).

Table 10.3 summarizes the VRC as a function of the lesion diameter, for static and dynamic acquisitions. As expected, with dynamic acquisitions the volumes of sphere were overestimated due to the smearing effect resulting from motion. For static acquisitions the VRC values are close to 1.0, which means that values were correctly recovered. The table also shows the mean percent errors in volume estimates measured on the simulated lesions as a function of the real lesion volume.

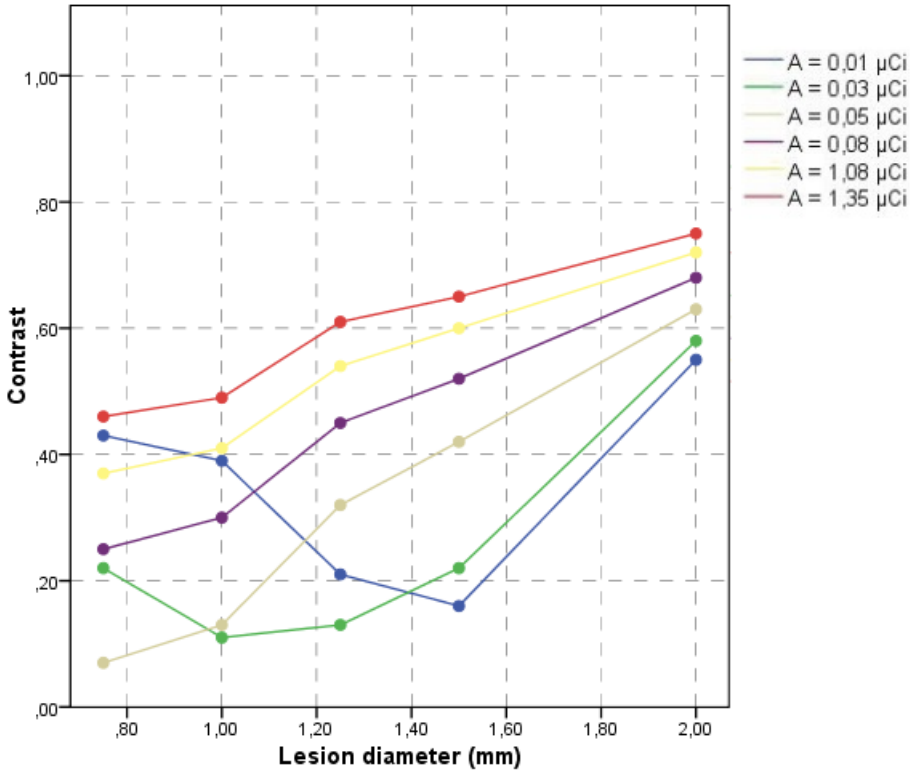

Figure 10.12: Contrast of the 0.01 µCi, 0.03 µCi, 0.05 µCi, 0.08 µCi, 1.08 µCi and 1.35 µCi FDG uptakes for the spherical lesions as a function of the lesion diameter. Results obtained for the static simulations.

Lesion Diameter	Static Simulations		Dynamic Simulations	
(mm)	VRC	% error	VRC	% error
0.75	1.629	61.30	3.259	225.88
1.00	1.120	12.02	2.930	192.98
1.25	1.098	9.83	N/A	N/A
1.50	0.987	1.27	N/A	N/A
2.00	0.995	0.54	N/A	N/A

Table 10.3: VRC in the static and dynamic acquisitions as a function of the lesion diameter. The mean percent errors in volume estimates measured on simulated lesions as a function of the real lesion volume are also shown. (Note: N/A - ”not available” - is this context means that the VRC value was not possible to measure due to the blurring and to the smearing effect resulting from the respiratory motion.)

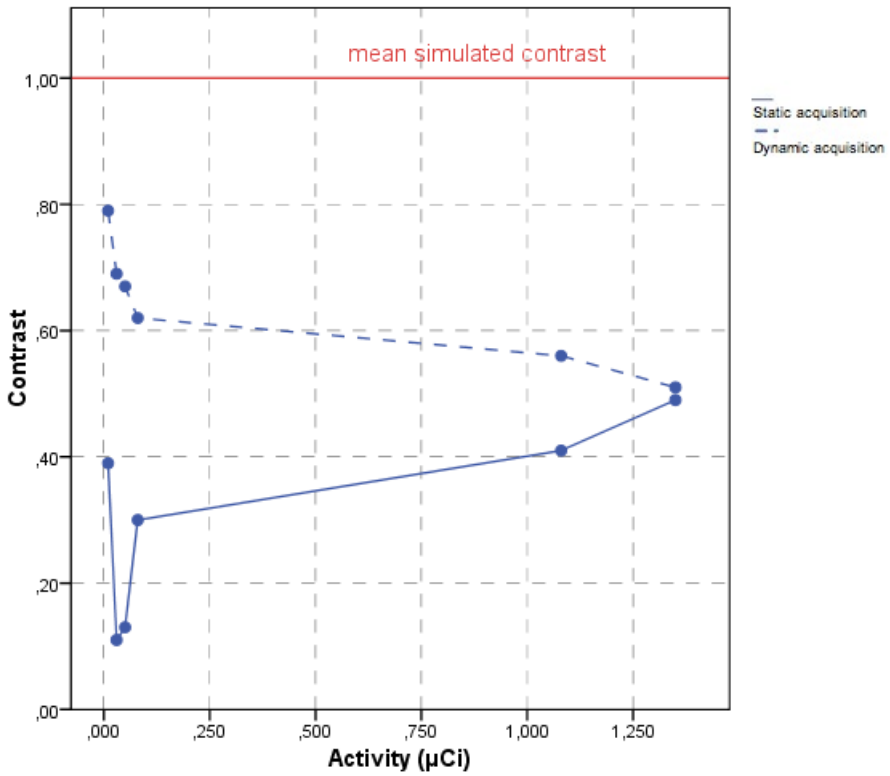

Figure 10.13: Contrast recover of a set of dynamic and static acquisitions as a function of the FDG activity concentration for the 1.0 mm diameter lesion. Data from dynamic acquisitions are represented by the dashed curve and static acquisition data are represented by the solid curve. The red line represents the mean simulated contrast.

Part V

Main Discussion and Conclusions

Chapter 11

Main Discussion and Conclusions

This final chapter will review and discuss the main results obtained in this thesis and suggestions and perspectives for future work will be presented. For the sake of clarity, the discussion will be divided into sections corresponding to each of the chapters contained in Part IV of this document.

11.1 The Digital Mouse Phantoms

Chapter 7 presents our developments towards computational phantoms to use in small animal imaging research. The phantoms generated from image segmentation of pre-clinical acquisitions were used to evaluate the results obtained from simulated data.

The phantoms produced imaging data comparable to that obtained from pre-clinical acquisitions with the FOCUS system.

We conclude that NURBS are an efficient and flexible way to describe the anatomy and physiology of a realistic 4D digital mouse phantom - the MOBY phantom. With its realistic model of the mouse anatomy and respiratory motion, the phantom provides a unique and useful tool in molecular imaging research. The MOBY phantom has enormous potential for the research of new instrumentation, image acquisition strategies, as well as image processing and reconstruction methods in molecular imaging.

11.2 Enhancements to the GATE Platform

In Chapter 8 we presented the reasoning followed to enable the GATE platform dealing with data output from the microPET® Focus 220 system. The implemented class is now allowing us to obtain the same output that we have with the real FOCUS system. In this way, we can now use the software used in pre-clinical practice to reconstruct the simulated data.

11.3 Small Animal PET with GATE

In Chapter 9, we compared the performances of the GATE platform against the microPET® Focus 220 system in order to validate the use of the simulated model for quantitative analysis. We presented the first results on the realistic simulation of small animal metabolic studies using the microPET® Focus 220 system. The work presented reflects the potential of using GATE to simulate small animal exams and exempts the obtained results from effects related to the image reconstruction algorithms used (they were the same for real and simulated data) and physical effects (they were corrected on real images and they were not simulated on GATE).

We chose to use a two-fold approach for our simulations. On one hand, we have built realistic phantoms from real data and on the other hand we have used a voxelized realistic mouse phantom, the MOBY phantom. Comparing the output of the simulations with real data allowed us to evaluate the limitations of using GATE using a dual strategy. An important aspect of simulation is to have a realistic model (phantom) of the subject's anatomy and physiological functions from which imaging data can be generated using accurate models of the imaging process. The advantage in using such phantoms for simulation studies is that the anatomy and physiological functions are known. Moreover, computer phantoms can be altered in order to model different anatomies and pathological situations.

We produced Monte Carlo simulations for the [^{18}F]-fluoride radiotracer uptake using the mouse phantom generated from acquired data and also using the MOBY phantom. The [^{18}F]-fluoride tracer normally accumulates at the bones and highlights the skeletal system of the animal. Simulations performed reproduce the same pattern. Furthermore, the relative activity concentrations for the simulation data are in good agreement with the same measurements for the real values. The analysis of the relative differences between quantification values obtained for the real and the simulated data that may in part result from small differences on the definition of ROIs between real and simulated data. Even so, the maximum difference obtained is 22.7% in the case of the bladder. Additionally, the statistical error measured as the ratio standard deviation over mean for all voxels considered for each organ show that the variability from simulated results is lower than the measurements obtained from the real exams. This difference most probably result from a sub-optimal correction of these effects on real data.

Simulation of small animal metabolic imaging using FDG was also done. FDG is taken up by cells to the same extent as glucose but is not fully metabolized. Evident accumulation of FDG in the mouse body can be seen in vivo especially in the brain, heart, kidneys and bladder, 60 minutes after injection. Unlike glucose, FDG is excreted by the kidneys into the bladder.

We have simulated the first and the last time frames of an FDG dynamic exam, using the MOBY phantom, in order to evaluate the uptake variability of the tracer during the exam. As we saw, the differences between the activity distribution for the liver and the heart are very small, disabling a clear separation between the two organs. This fact results from the specific description of the organs inside the MOBY phantom, since in MOBY the liver lies slightly in front of the hearth. Despite this, the activity simulated distribution are in good agreement with the FDG biodistribution. In the last frame it is possible to see higher accumulated activity inside the bladder, when compared with what happens in the first frame, something which is expected in a usual dynamic FDG exam.

The accuracy of the quantitative results obtained by simulations was evaluated by comparing simulated data against real data, for the simulation with the acquired mouse phantom. The relative activity concentrations obtained for the simulation data are in good agreement with the values obtained for real data. As for the case of [^{18}F]-fluoride, the statistical error measured as the ratio standard deviation over mean for all voxels considered for each organ show that the variability from simulated results is lower than the measurements obtained from the real exams. This difference most probably results from a sub-optimal correction of these effects on real data.

Additionally, the use of realistic phantoms generated from acquired data results on visual differences between the image resolution of real data and simulated data. These differences are due to the presence of an additional image blurring on simulated data, resulting from the fact that its input already reflects all the image acquisition and processing chain characteristic of the scanner used.

Overall, the good agreement between simulation and the real acquisitions leads us to conclude that GATE platform is an important tool to perform mouse PET imaging simulation when assessing [^{18}F]-fluoride and FDG distributions.

In spite the encouraging results obtained, these studies have some limitations. The simulations are generally long and difficult to perform without a very well equipped computer structure. The production of the realistic images, including attenuation information (using the phantoms attenuation maps to set the different body structures and the correspondent attenuation information) and physical effects (using the isotope decay instead a gamma-gamma emission source), was done only to evaluate the consequence of these physical effects on image quantification. We show that the corrections of physical effects such as positron range and gamma-gamma accolinearity may reduce the bias, on the small animal quantitative analysis using ^{18}F labelled radioisotopes, by 25%.

11.4 Evaluation of the Respiratory Motion in Lung Lesion Quantification

The location and detection of lesions in thoracic and abdominal mouse imaging can be affected by the respiratory motion due to displacement of the organs during the normal breathing. This effect should be taken into account when searching lesions and quantifying lesion tracer uptake in highly deforming structures such as the lungs. In Chapter 10 we have presented the evaluation of the effect of the respiratory motion on lung lesion quantification in small animal PET studies.

The FWHMs of reconstructed lesion images were determined alongside with the direction of movement due to respiratory motion for static and dynamic acquisitions. The results demonstrate how the respiratory motion would affect the blurring of a lung lesion along the direction of movement.

As expected, contrast-to-noise ratio (CNR) recovery improves for static acquisitions. The static images have a slightly greater CNR recovery compared to the dynamic images, which is due to the loss of resolution in the motion images. CNR recovery also improves as lesion size increases and lesion contrast decreases.

The results illustrates that the signal-to-noise ratio (SNR) deteriorate for motion data. Results for higher diameter lesions in the lung were influenced by lesion blending into the liver. However,

results for the 1.0 mm lesion shown better SNR data induced by the respiratory motion. Concerning the static acquisitions we found better SNR for lower FDG uptakes and higher lesion sizes. The CR depends more strongly on the lesion diameter than it depends on the lesion to background considered. Better temporal resolution (volume recover) was found in the non-gated data.

As discussed before, respiratory motion leads to reduced contrast and quantitative accuracy in terms of recovered contrast activity concentration and functional volumes. Several methodologies proposed for reducing the effects of respiratory motion have been based on the development of respiratory gated acquisitions [Visvikis *et al.* , 2006a; Nehmeh *et al.* , 2002; Dawood *et al.* , 2006; Detorie & Dahlbom, 2006; Lamare *et al.* , 2007a; Dawood *et al.* , 2008; Bettinardi, 2009; Lamare *et al.* , 2007b; Detorie & Dahlbom, 2008]. However, in general, 4D PET images have low counting statistics and high image noise compared to static 3D PET images. Since the same number of coincidence events in 3D PET is divided into many different respiratory phase bins or time frames, the number of coincidence events per image bin is considerably reduced. This leads to higher image noise in 4D PET images, resulting in an even lower SNR of the reconstruction. Therefore, there is a trade-off between image noise and temporal resolution. Long duration time per frame gives low noise but blurred images resulting from the loss of temporal resolution [Park *et al.* , 2008; Zhu *et al.* , 2002]. In order to determine the effect of the number of gating bins on image noise and temporal resolution, sets of 4D simulations will be performed for the MOBY phantom following the same line of reasoning of these studies.

Some other limitations of our research are related to the phantom's anatomy and breathing cycle. In future studies different phantoms anatomy can improve our quantitative evaluation. In our work, we produced a stress breathing condition on the respiratory motion cycle of the phantom, whereas variations in respiratory cycle from an animal to another and in time may also influence the observed effects. Moreover, variations in the amplitude of the diaphragm motion also influence the results. A reference to a real examination can be helpful to compare the results obtained. Therefore, there is still the need for a method that takes into account the effect of respiratory motion without, at the same time, affecting the quantification analysis on the reconstructed images. For that reason, this work is being complemented by accessing the impact of such motion in the quantification analysis using a dynamic VOI, placed around the centroid of each lesion, in 4D imaging studies.

11.5 Perspectives for Future Work

This research contributes to evaluating the respiratory motion effect in the quantification of micro-PET images. A complete evaluation should also consider real dynamic FDG examinations that need to be compared against the results presented in this thesis. Moreover, the production of realistic images, where attenuation information (using the phantoms attenuation maps to set the different body structures and the correspondent attenuation information) and physical effects (using the isotope decay instead a gamma/gamma emission source) are included, was not done. Although this was not among the main goals of this work, its inclusion would allow evaluating the consequence of these physical effects on image sensitivity and quantification. Since the physical effects are not taken into account, further investigation is needed to accurately evaluate these effects on image quantification.

We have used the OSEM algorithm for image reconstruction with fixed parameters (16 subsets and 4 iterations). These parameters are normally used in pre-clinical standard protocols. However, there are several other image reconstruction algorithms and parameters including smoothing filters and the number of subsets and iterations that could affect the results (namely, lesion quantification may be inaccurate depending on the reconstruction algorithms used), but have not been addressed in this study. Further studies are required to investigate the effect of these parameters on signal and volume recovery.

In this research we have always used the same breathing condition to simulate respiratory motion. However, image quantification is influenced by the amplitude and pattern of respiratory motion. This suggests that it may be beneficial to simulate different breathing motion conditions to obtain a reasonable estimate on image quantification under clinical conditions.

Background activity is unavoidable and it causes significant noise and contrast loss in PET images [Tai & Laforest, 2005]. The effect of background activity concentration will be analyzed in the next phases of this research.

11.6 Concluding Remarks

This work is based on the use of a complete implemented PET simulation system dedicated for small animal PET imaging using GATE. We showed that the GATE platform can simulate realistic small animal PET acquisitions under realistic conditions to improve the quantitative analysis in mouse body studies. Moreover, the implemented system has contributed to the evaluation of the degradation on lesion lesion detection due to normal breathing, and hopefully shed some additional light on dealing with this problem while performing human exams.

Appendix A

MOBY files

A.1 general.samp.par

The general parameters file (general.samp.par) for the generated MOBY phantom used in this research, is shown in the following program lines:

```
0 :  activity_phantom_each_frame (1=save phantom to file, 0=don't save)

0 :  attenuation_coeff_phantom_each_frame (1=save phantom to file, 0=don't save)

1 :  activity_phantom_average (1=save , 0=don't save)

1 :  attenuation_coeff_phantom_average (1=save, 0=don't save)

1 :  motion_option (0=beating heart only, 1=respiratory motion only, 2=both motions)

0.37 :  output_period (SECS) (if <= 0, then output_period=time_per_frame*output_frames)

0.037 :  time_per_frame (SECS)

10 :  output_frames (# of output time frames )

0.1 :  hrt_period (SECS) (length of beating heart cycle; normal = 0.1s)

0.0 :  hrt_start_phase_index (range=0 to 1; ED=0, ES=0.4)

0.37 :  resp_period (SECS) (length of respiratory cycle; normal breathing = 0.37s)

0.0 :  resp_start_phase_index (range=0 to 1, full exhale=0, full inhale=0.455)

1.0 :  max_diaphragm_motion (extent in mm's of diaphragm motion; normal breathing = 1 mm)

0.7 :  max_AP_expansion (extent in mm's of the AP expansion of the chest; normal breathing = 0.7 mm)

14.96 :  body_long_axis (sets body transverse axis - scales everything except lungs and heart with it) (normal
= 26.7 mm)

14.01 :  body_short_axis (sets body AP axis - scales everything except lungs, heart, and ribcage with it)
(normal = 25.0 mm)

50.1 :  body_height (sets height (excluding tail) - scales everything except lungs, heart, and ribcage with
it) (normal = 91.0 mm)

13.45 :  rib_long_axis (sets ribcage transverse axis - scales lungs with it and repositions the heart) (normal
= 24.0 mm)

11.77 :  rib_short_axis (sets ribcage AP axis - scales lungs with it and repositions the heart) (normal =
21.0 mm)
```

11.21 : rib_height (sets height of ribcage - scales lungs with it and repositions the heart) (normal 20.0 mm)

0.45 : thickness of small intestine wall (normal = 0.8 mm)

0.28 : thickness of large intestine wall (normal = 0.5 mm)

1 : hrt_scale (scales heart in 3D - 1.0 is original70 mouse heart)

4.71 : hrt_lv_length (sets the length of the LV - entire heart is scaled with the LV) (orig. mouse heart = 8.4 mm)

0.50 : hrt_lv_radius (sets the ave. radius of the LV - entire heart is scaled with the radius) (orig. heart = 0.9 mm)

0.15 : height of liver dome (normal mouse = 0.27 mm)

0.0056 : intv in cm (thickness of body tissue around the heart and liver; normal = 0.01)

0.05 : pixel width (cm);

40 : array size;

1 : subvoxel_index (=1,2,3,4 -> 1,8,27,64 subvoxels/voxel, respectively);

52 : start_slice;

176 : end_slice;

1 : increment between slices;

60.0 : zy_rotation (beta) in deg.;

30.0 : xz_rotation (phi) in deg.;

-150.0 : yx_rotation (psi) in deg.;

0.0 : x translation in cm;

0.0 : y translation in cm;

0.0 : z translation in cm;

1 : apical_thinning (1 = present, otherwise not present);

0.0 : valve thickness in cm (0= no valve);

0.3 : av_step(cm): step width for smooth change between Atr & Ven (0=none);

0 : total_rotation (deg);

0 : activity units (1= scale by voxel volume; 0= don't scale);

SETTING ORGAN ACTIVITIES

---

0 : myoLV_time_curve (1= activity determined by a time-activity curve; 0= fixed activity)

1 : hrt_myoLV_act - fixed activity in left ventricle myocardium if above option is 0

sample_act.txt : myoLV_act_filename - name of file containing time-activity curve for LV myocardium

---

0 : myoRV_time_curve (1= activity determined by a time-activity curve; 0= fixed activity)

2 : hrt_myoRV_act - activity in right ventricle myocardium

sample_act.txt : myoRV_act_filename - name of file containing time-activity curve for RV myocardium

---

0 : myoLA_time_curve (1= activity determined by a time-activity curve; 0= fixed activity)

3 : hrt_myoLA_act - activity in left atrium myocardium

sample_act.txt : myoLA_act_filename - name of file containing time-activity curve for LA myocardium

```
-------------------------------------------------------------------------
0 :  myoRA_time_curve (1= activity determined by a time-activity curve; 0= fixed activity)
4 :  hrt_myoRA_act - activity in right atrium myocardium
sample_act.txt :  myoRA_act_filename - name of file containing time-activity curve for RA myocardium
-------------------------------------------------------------------------
0 :  bldplLV_time_curve (1= activity determined by a time-activity curve; 0= fixed activity)
5 :  hrt_bldplLV_act - activity in left ventricle chamber (blood pool)
sample_act.txt :  bldplLV_act_filename - name of file containing time-activity curve for LV blood pool
-------------------------------------------------------------------------
0 :  bldplRV_time_curve (1= activity determined by a time-activity curve; 0= fixed activity)
6 :  hrt_bldplRV_act - activity in right ventricle chamber (blood pool)
sample_act.txt :  bldplRV_act_filename - name of file containing time-activity curve for RV blood pool
-------------------------------------------------------------------------
0 :  bldplLA_time_curve (1= activity determined by a time-activity curve;
0= fixed activity) 7 :  hrt_bldplLA_act - activity in left atria chamber (blood pool)
sample_act.txt :  bldplLA_act_filename - name of file containing time-activity curve for LA blood pool
-------------------------------------------------------------------------
0 :  bldplRA_time_curve (1= activity determined by a time-activity curve; 0= fixed activity)
8 :  hrt_bldplRA_act - activity in right atria chamber (blood pool)
sample_act.txt :  bldplRA_act_filename - name of file containing time-activity curve for RA blood pool
-------------------------------------------------------------------------
0 :  body_time_curve (1= activity determined by a time-activity curve; 0= fixed activity)
9 :  body_activity (background activity) ;
sample_act.txt :  body_act_filename - name of file containing time-activity curve for body
-------------------------------------------------------------------------
0 :  liver_time_curve (1= activity determined by a time-activity curve; 0= fixed activity)
10 :  liver_activity;
sample_act.txt :  liver_act_filename - name of file containing time-activity curve for liver
-------------------------------------------------------------------------
0 :  lung_time_curve (1= activity determined by a time-activity curve; 0= fixed activity)
11 :  lung_activity;
sample_act.txt :  lung_act_filename - name of file containing time-activity curve for lungs
-------------------------------------------------------------------------
0 :  st_wall_time_curve (1= activity determined by a time-activity curve; 0= fixed activity)
12 :  st_wall_activity; (stomach wall)
sample_act.txt :  st_wall_act_filename - name of file containing time-activity curve for stomach wall
-------------------------------------------------------------------------
0 :  st_cnts_time_curve (1= activity determined by a time-activity curve; 0= fixed activity)
13 :  st_cnts_activity; (stomach contents)
sample_act.txt :  st_cnts_act_filename - name of file containing time-activity curve for stomach contents

-------------------------------------------------------------------------
```

```
0 :  pancreas_time_curve (1= activity determined by a time-activity curve; 0= fixed activity)
14 :  pancreas_activity; (pancreas)
sample_act.txt :  pancreas_act_filename - name of file containing time-activity curve for pancreas
-------------------------------------------------------------------------
0 :  kidney_time_curve (1= activity determined by a time-activity curve; 0= fixed activity)
15 :  kidney_activity;
sample_act.txt :  kidney_act_filename - name of file containing time-activity curve for kidneys
-------------------------------------------------------------------------
0 :  spleen_time_curve (1= activity determined by a time-activity curve; 0= fixed activity)
16 :  spleen_activity;
sample_act.txt :  spleen_act_filename - name of file containing time-activity curve for spleen
-------------------------------------------------------------------------
0 :  small_intestine_time_curve (1= activity determined by a time-activity curve; 0= fixed activity)
17 :  small_intestine_activity; sample_act.txt :
small_intestine_act_filename - name of file containing time-activity curve for small intestine
-------------------------------------------------------------------------
0 :  large_intestine_time_curve (1= activity determined by a time-activity curve; 0= fixed activity)
18 :  large_intestine_activity; sample_act.txt :
large_intestine_act_filename - name of file containing time-activity curve for large intestine
-------------------------------------------------------------------------
0 :  bladder_time_curve (1= activity determined by a time-activity curve; 0= fixed activity)
19 :  bladder_activity; sample_act.txt :
bladder_act_filename - name of file containing time-activity curve for bladder
-------------------------------------------------------------------------
0 :  vas_deferens_time_curve (1= activity determined by a time-activity curve; 0= fixed activity)
20 :  vas_def_activity;
sample_act.txt :  vas_def_act_filename - name of file containing time-activity curve for vas deferens
-------------------------------------------------------------------------
0 :  testicular_time_curve (1= activity determined by a time-activity curve; 0= fixed activity)
21 :  testicular_activity;
sample_act.txt :  testicular_act_filename - name of file containing time-activity curve for testes
-------------------------------------------------------------------------
0 :  rib_time_curve (1= activity determined by a time-activity curve; 0= fixed activity)
22 :  rib_activity;
sample_act.txt :  rib_act_filename - name of file containing time-activity curve for ribs
-------------------------------------------------------------------------
0 :  spine_time_curve (1= activity determined by a time-activity curve; 0= fixed activity)
23 :  spine_activity;
sample_act.txt :  spine_act_filename - name of file containing time-activity curve for spine
-------------------------------------------------------------------------
0 :  brain_backgrnd_time_curve (1= activity determined by a time-activity curve; 0= fixed activity)
```

24 : brain_backgrnd_activity;

sample_act.txt : brain_backgrnd_act_filename - name of file containing time-activity curve for brain background

---

0 : neo_white_time_curve (1= activity determined by a time-activity curve; 0= fixed activity)

25 : neo_white_activity;

sample_act.txt : neo_white_act_filename - name of file containing time-activity curve for neocortical white matter

---

0 : neo_gray_time_curve (1= activity determined by a time-activity curve; 0= fixed activity)

26 : neo_gray_activity;

sample_act.txt : neo_gray_act_filename - name of file containing time-activity curve for neocortical gray matter

---

0 : cere_white_time_curve (1= activity determined by a time-activity curve; 0= fixed activity)

27 : cere_white_activity;

sample_act.txt : cere_white_act_filename - name of file containing time-activity curve for cerebellum white matter

---

0 : cere_gray_time_curve (1= activity determined by a time-activity curve; 0= fixed activity)

28 : cere_gray_activity;

sample_act.txt : cere_gray_act_filename - name of file containing time-activity curve for cerebellum gray matter

---

0 : cere_nuc_time_curve (1= activity determined by a time-activity curve; 0= fixed activity)

29 : cere_nuc_activity;

sample_act.txt : cere_nuc_act_filename - name of file containing time-activity curve for cerebellum nuclei

---

0 : thal_time_curve (1= activity determined by a time-activity curve; 0= fixed activity)

30 : thal_activity;

sample_act.txt : thal_act_filename - name of file containing time-activity curve for thalamus

---

0 : hippocamp_time_curve (1= activity determined by a time-activity curve; 0= fixed activity)

31 : hippocamp_activity;

sample_act.txt : hippocamp_act_filename - name of file containing time-activity curve for hippocampus

---

0 : thyroid_time_curve (1= activity determined by a time-activity curve; 0= fixed activity)

32 : thyroid_activity;

sample_act.txt : thyroid_act_filename - name of file containing time-activity curve for the thyroid

---

511. : radionuclide energy in keV (range 1-1000 keV) ; for attn. map only

---

A.2 Attenuation Coefficients

The following lines shows the new materials included on the GATE database, related to the MOBY anatomy.

On the first line the density (with units) is defined by `d=material density units` and is separated by a semi-colon from the number of constituents in the material defined by `n=number of elements`. On the second and subsequent lines the individual elements and their mass fractions are defined by `+el:name=name of element ; f=mass fraction`, where the sum of the mass fractions should be one.

```
Body:  d=1.00 g/cm3 ; n=2
       +el:  name=Hydrogen ; f=0.111898
       +el:  name=Oxygen ; f=0.888102

Muscle:  d=1.05 g/cm3 ; n=11
       +el:  name=Hydrogen ; f=0.102
       +el:  name=Carbon ; f=0.143
       +el:  name=Nitrogen ; f=0.034
       +el:  name=Oxygen ; f=0.71
       +el:  name=Sodium ; f=0.001
       +el:  name=Phosphor ; f=0.002
       +el:  name=Sulfur ; f=0.003
       +el:  name=Chlorine ; f=0.001
       +el:  name=Potassium ; f=0.004
       +el:  name=Calcium ; f=0.0
       +el:  name=Scandium ; f=0.0

LungMoby:  d=0.26 g/cm3 ; n=9
       +el:  name=Hydrogen ; f=0.103
       +el:  name=Carbon ; f=0.105
       +el:  name=Nitrogen ; f=0.031
       +el:  name=Oxygen ; f=0.749
       +el:  name=Sodium ; f=0.002
       +el:  name=Phosphor ; f=0.002
       +el:  name=Sulfur ; f=0.003
       +el:  name=Chlorine ; f=0.003
       +el:  name=Potassium ; f=0.002
```

SpineBone: d=1.42 g/cm^3 ; n=11

+el: name=Hydrogen ; f=0.063

+el: name=Carbon ; f=0.261

+el: name=Nitrogen ; f=0.039

+el: name=Oxygen ; f=0.436

+el: name=Sodium ; f=0.001

+el: name=Magnesium ; f=0.001

+el: name=Phosphor ; f=0.061

+el: name=Sulfur ; f=0.003

+el: name=Chlorine ; f=0.001

+el: name=Potassium ; f=0.001

+el: name=Calcium ; f=0.133

RibBone: d=1.92 g/cm^3 ; n=11

+el: name=Hydrogen ; f=0.034

+el: name=Carbon ; f=0.155

+el: name=Nitrogen ; f=0.042

+el: name=Oxygen ; f=0.435

+el: name=Sodium ; f=0.001

+el: name=Magnesium ; f=0.002

+el: name=Phosphor ; f=0.103

+el: name=Sulfur ; f=0.003

+el: name=Calcium ; f=0.225

+el: name=Scandium ; f=0.0

+el: name=Titanium ; f=0.0

Adipose: d=0.95 g/cm^3 ; n=7

+el: name=Hydrogen ; f=0.114

+el: name=Carbon ; f=0.598

+el: name=Nitrogen ; f=0.007

+el: name=Oxygen ; f=0.278

+el: name=Sodium ; f=0.001

+el: name=Sulfur ; f=0.001

+el: name=Chlorine ; f=0.001

Blood: d=1.06 g/cm^3 ; n=11

+el: name=Hydrogen ; f=0.102

```
        +el:  name=Carbon ; f=0.11
        +el:  name=Nitrogen ; f=0.033
        +el:  name=Oxygen ; f=0.745
        +el:  name=Sodium ; f=0.001
        +el:  name=Phosphor ; f=0.001
        +el:  name=Sulfur ; f=0.002
        +el:  name=Chlorine ; f=0.003
        +el:  name=Potassium ; f=0.002
        +el:  name=Iron ; f=0.001
        +el:  name=Cobalt ; f=0.0

Heart:  d=1.05 g/cm3 ; n=11
        +el:  name=Hydrogen ; f=0.104
        +el:  name=Carbon ; f=0.139
        +el:  name=Nitrogen ; f=0.029
        +el:  name=Oxygen ; f=0.718
        +el:  name=Sodium ; f=0.001
        +el:  name=Phosphor ; f=0.002
        +el:  name=Sulfur ; f=0.002
        +el:  name=Chlorine ; f=0.002
        +el:  name=Potassium ; f=0.003
        +el:  name=Calcium ; f=0.0
        +el:  name=Scandium ; f=0.0

Kidney:  d=1.05 g/cm3 ; n=11
        +el:  name=Hydrogen ; f=0.103
        +el:  name=Carbon ; f=0.132
        +el:  name=Nitrogen ; f=0.03
        +el:  name=Oxygen ; f=0.724
        +el:  name=Sodium ; f=0.002
        +el:  name=Phosphor ; f=0.002
        +el:  name=Sulfur ; f=0.002
        +el:  name=Chlorine ; f=0.002
        +el:  name=Potassium ; f=0.002
        +el:  name=Calcium ; f=0.001
        +el:  name=Scandium ; f=0.0
```

Liver: d=1.06 g/cm^3 ; n=11

+el: name=Hydrogen ; f=0.102

+el: name=Carbon ; f=0.139

+el: name=Nitrogen ; f=0.03

+el: name=Oxygen ; f=0.716

+el: name=Sodium ; f=0.002

+el: name=Phosphor ; f=0.003

+el: name=Sulfur ; f=0.003

+el: name=Chlorine ; f=0.002

+el: name=Potassium ; f=0.003

+el: name=Calcium ; f=0.0

+el: name=Scandium ; f=0.0

Lymph: d=1.03 g/cm^3 ; n=11

+el: name=Hydrogen ; f=0.108

+el: name=Carbon ; f=0.041

+el: name=Nitrogen ; f=0.011

+el: name=Oxygen ; f=0.832

+el: name=Sodium ; f=0.003

+el: name=Sulfur ; f=0.001

+el: name=Chlorine ; f=0.004

+el: name=Argon ; f=0.0

+el: name=Potassium ; f=0.0

+el: name=Calcium ; f=0.0

+el: name=Scandium ; f=0.0

Pancreas: d=1.04 g/cm^3 ; n=11

+el: name=Hydrogen ; f=0.106

+el: name=Carbon ; f=0.169

+el: name=Nitrogen ; f=0.022

+el: name=Oxygen ; f=0.694

+el: name=Sodium ; f=0.002

+el: name=Phosphor ; f=0.002

+el: name=Sulfur ; f=0.001

+el: name=Chlorine ; f=0.002

+el: name=Potassium ; f=0.002

+el: name=Calcium ; f=0.0

```
       +el:  name=Scandium ; f=0.0

Intestine:  d=1.03 g/cm3 ; n=11
       +el:  name=Hydrogen ; f=0.106
       +el:  name=Carbon ; f=0.115
       +el:  name=Nitrogen ; f=0.022
       +el:  name=Oxygen ; f=0.751
       +el:  name=Sodium ; f=0.001
       +el:  name=Phosphor ; f=0.001
       +el:  name=Sulfur ; f=0.001
       +el:  name=Chlorine ; f=0.002
       +el:  name=Potassium ; f=0.001
       +el:  name=Calcium ; f=0.0
       +el:  name=Scandium ; f=0.0

Skull:  d=1.61 g/cm3 ; n=11
       +el:  name=Hydrogen ; f=0.05
       +el:  name=Carbon ; f=0.212
       +el:  name=Nitrogen ; f=0.04
       +el:  name=Oxygen ; f=0.435
       +el:  name=Sodium ; f=0.001
       +el:  name=Magnesium ; f=0.002
       +el:  name=Phosphor ; f=0.081
       +el:  name=Sulfur ; f=0.003
       +el:  name=Calcium ; f=0.176
       +el:  name=Scandium ; f=0.0
       +el:  name=Titanium ; f=0.0

Cartilage:  d=1.10 g/cm3 ; n=11
       +el:  name=Hydrogen ; f=0.096
       +el:  name=Carbon ; f=0.099
       +el:  name=Nitrogen ; f=0.022
       +el:  name=Oxygen ; f=0.744
       +el:  name=Sodium ; f=0.005
       +el:  name=Phosphor ; f=0.022
       +el:  name=Sulfur ; f=0.009
       +el:  name=Chlorine ; f=0.003
```

```
       +el:  name=Argon ; f=0.0
       +el:  name=Potassium ; f=0.0
       +el:  name=Calcium ; f=0.0

Brain:  d=1.04 g/cm3 ; n=11
       +el:  name=Hydrogen ; f=0.107
       +el:  name=Carbon ; f=0.145
       +el:  name=Nitrogen ; f=0.022
       +el:  name=Oxygen ; f=0.712
       +el:  name=Sodium ; f=0.002
       +el:  name=Phosphor ; f=0.004
       +el:  name=Sulfur ; f=0.002
       +el:  name=Chlorine ; f=0.003
       +el:  name=Potassium ; f=0.003
       +el:  name=Calcium ; f=0.0
       +el:  name=Scandium ; f=0.0

Spleen:  d=1.06 g/cm3 ; n=11
       +el:  name=Hydrogen ; f=0.103
       +el:  name=Carbon ; f=0.113
       +el:  name=Nitrogen ; f=0.032
       +el:  name=Oxygen ; f=0.741
       +el:  name=Sodium ; f=0.001
       +el:  name=Phosphor ; f=0.003
       +el:  name=Sulfur ; f=0.002
       +el:  name=Chlorine ; f=0.002
       +el:  name=Potassium ; f=0.003
       +el:  name=Calcium ; f=0.0
       +el:  name=Scandium ; f=0.0
```

Appendix B

GateToFOCUS New Class

B.1 GateToFOCUS.cc

```
/*----------------------
GATE - Geant4 Application for Tomographic Emission OpenGATE Collaboration
This software is distributed under the terms of the GNU Lesser General Public Licence (LGPL)

See GATE/LICENSE.txt for further details
----------------------*/


#include "GateToFOCUS.hh"
#include "GateToFOCUSMessenger.hh"
#include "globals.hh"
#include "G4Run.hh"
#include "G4Step.hh"
#include "G4Event.hh"
#include "G4ios.hh"
#include <iomanip>
#include "GateOutputMgr.hh"


// ####
// #### Constructor / destructor
// ####
GateToFOCUS::GateToFOCUS(const G4String& name, GateOutputMgr* outputMgr, DigiMode digiMode)

:  GateVOutputModule(name,outputMgr,digiMode)
```

```
{
m_verboseLevel = 1;
m_fileName = name + ".lst";
m_FOCUSMessenger = new GateToFOCUSMessenger(this);
m_gRandom = new TRandom(0);
}


GateToFOCUS::~GateToFOCUS()
{
delete m_gRandom;
delete m_FOCUSMessenger;
if (m_verboseLevel > 0)
G4cout << "GateToFOCUS deleting..." << G4endl;
}
// ####
// #### Output module
// ####
void GateToFOCUS::RecordBeginOfAcquisition()
{
if (m_verboseLevel > 2)
G4cout << "GateToFOCUS::RecordBeginOfAcquisition" << G4endl;
m_outFile = fopen(m_fileName, "wb");
if (m_outFile == NULL && m_verboseLevel > 0)
G4cout << "GateTOFOCUS::RecordBeginOfAcquisition:  cannot open " << m_fileName << " for writting"
<< G4endl;
}


void GateToFOCUS::RecordEndOfAcquisition()
{
if (m_verboseLevel > 2)
G4cout << "GateToFOCUS::RecordEndOfAcquisition" << G4endl;
if (m_outFile != NULL)
fclose(m_outFile);
}


void GateToFOCUS::RecordBeginOfRun(const G4Run* )
{
```

```
if (m_verboseLevel > 2)
G4cout << "GateToFOCUS::RecordBeginOfRun" << G4endl;
}

void GateToFOCUS::RecordEndOfRun(const G4Run* )
{
if (m_verboseLevel > 2)
G4cout << "GateToFOCUS::RecordEndOfRun" << G4endl;
}

void GateToFOCUS::RecordBeginOfEvent(const G4Event* )
{
if (m_verboseLevel > 2)
G4cout << "GateToFOCUS::RecordBeginOfEvent" << G4endl;
}

void GateToFOCUS::RecordEndOfEvent(const G4Event* )
{
if (m_verboseLevel > 2)
G4cout << "GateToFOCUS::RecordEndOfEvent" << G4endl;

if (m_outFile == NULL)
return;

const GateCoincidenceDigiCollection* CDC = GetOutputMgr()->GetCoincidenceDigiCollection("Coincidences");

if (!CDC)
{
if (m_verboseLevel > 2)
G4cout << "GateToFOCUS::RecordEndOfEvent::GateCoincidenceDigiCollection not found" << G4endl;

return;
}

size_t n_digi = CDC->entries();
for (size_t i_digi=0 ; i_digi < n_digi ; i_digi++)
```

```
StoreInFOCUS((*CDC)[i_digi]);
}

void GateToFOCUS::RecordStep(const G4Step* )
{
if (m_verboseLevel > 2)
G4cout << "GateToFOCUS::RecordStep" << G4endl;
}

void GateToFOCUS::SetFileName(const G4String aName)
{
m_fileName = aName;

if (m_verboseLevel > 0)
G4cout << "GateToFOCUS::SetFileName::  new name = " << aName << G4endl;
}
// ####
// #### Save the coincidences in the file
// ####
void GateToFOCUS::StoreInFOCUS(GateCoincidenceDigi *digi)
{
char data[EventSize];

GatePulse *gPulse1 = &(digi->GetPulse(0));
GatePulse *gPulse2 = &(digi->GetPulse(1));

Double_t time1 = gPulse1->GetTime();
Double_t time2 = gPulse2->GetTime();

if (m_verboseLevel > 2)
G4cout << "GateToFOCUS::StoreInFOCUS: time1 = " << time1 << ", time2 = " << time2 << G4endl;

Int_t crystalID1 = gPulse1->GetComponentID(CRYSTAL_DEPTH);
Int_t crystalID2 = gPulse2->GetComponentID(CRYSTAL_DEPTH);

if (m_verboseLevel > 2)
```

```
G4cout << "GateToFOCUS::StoreInFOCUS: crystalID1 = " << crystalID1 << ", crystalID2 = " << crystalID2
<< G4endl;


Int_t moduleID1 = gPulse1->GetComponentID(MODULE_DEPTH);

Int_t moduleID2 = gPulse2->GetComponentID(MODULE_DEPTH);


if (m_verboseLevel > 2)

G4cout << "GateToFOCUS::StoreInFOCUS: moduleID1 = " << moduleID1 << ", moduleID2 = " << moduleID2
<< G4endl;


Int_t eventID1 = gPulse1->GetEventID();

Int_t eventID2 = gPulse2->GetEventID();


if (m_verboseLevel > 2)

G4cout << "GateToFOCUS::StoreInFOCUS: eventID1 = " << eventID1 << ", eventID2 = " << eventID2
<< G4endl;


Int_t rsectorID1 = gPulse1->GetComponentID(RSECTOR_DEPTH);

Int_t rsectorID2 = gPulse2->GetComponentID(RSECTOR_DEPTH);


if (m_verboseLevel > 2)

G4cout << "GateToFOCUS::StoreInFOCUS: rsectorID1 = " << rsectorID1 << ", rsectorID2 = " << rsectorID2
<< G4endl;

// ####

// #### time

// ####

Int_t StartTime = int(time1*1000);


if (StartTime != 0)

{

InitEncode(data);

TimeTagEncode(data, TimeMarker);

TimeEncode(data, StartTime);

WriteInFOCUS(data);

}

// ####

// #### coincidence data
```

```
// ####
InitEncode(data);
CoincidenceTagEncode(data,Event48Bit);

if (eventID1 != eventID2)
CoincidenceTypeEncode(data,Delayed);

unsigned headID1;
unsigned headID2;

rsectorID1 = FixRSectorID(rsectorID1, &headID1);
rsectorID2 = FixRSectorID(rsectorID2, &headID2);

unsigned Y1_crystalID = (moduleID1 * 12) + (int(crystalID1 / 12) + 1) - 1;
unsigned Y2_crystalID = (moduleID2 * 12) + (int(crystalID2 / 12) + 1) - 1;
unsigned X1_crystalID = (rsectorID1 * 12) + ((crystalID1 + 1) - 12 * (int(crystalID1 / 12)))
- 1;
unsigned X2_crystalID = (rsectorID2 * 12) + ((crystalID2 + 1) - 12 * (int(crystalID2 / 12)))
- 1;

float Tag_1 = m_gRandom->Gaus(0,0.9);

if (Tag_1 > 0.6 || Tag_1 < -0.6)
{
IncDecCrystalID(2, Y1_crystalID);
IncDecCrystalID(3, Y2_crystalID);
IncDecCrystalID(3, X1_crystalID);
IncDecCrystalID(3, X2_crystalID);
}

Y1_crystalID = FixCrystalID(Y1_crystalID, 0, 47);
Y2_crystalID = FixCrystalID(Y2_crystalID, 0, 47);
X1_crystalID = FixCrystalID(X1_crystalID, 0, 251);
X2_crystalID = FixCrystalID(X2_crystalID, 0, 251);

if (headID1 == 1)
```

```
{
HeadNumberEncodeGamma1(data, headID1);
HeadNumberEncodeGamma2(data, headID2);

Y_EncodeGamma1(data,Y1_crystalID);
Y_EncodeGamma2(data,Y2_crystalID);
X_EncodeGamma1(data,X1_crystalID);
X_EncodeGamma2(data,X2_crystalID);
}
else
{
HeadNumberEncodeGamma1(data, headID2);
HeadNumberEncodeGamma2(data, headID1);

Y_EncodeGamma1(data,Y2_crystalID);
Y_EncodeGamma2(data,Y1_crystalID);
X_EncodeGamma1(data,X2_crystalID);
X_EncodeGamma2(data,X1_crystalID);
}

WriteInFOCUS(data);
}

void GateToFOCUS::WriteInFOCUS(char *data)
{
if (m_outFile != NULL)
fwrite(data, sizeof(char), EventSize, m_outFile);
}

Int_t GateToFOCUS::FixRSectorID(Int_t rsectorID, unsigned *HeadID)
{
if (rsectorID > 0)
rsectorID = rsectorID - 1;
else
rsectorID = 41;
```

```
if (rsectorID >=0 && rsectorID <= 20)
*HeadID = 1;
else
*HeadID = 0;

if (rsectorID < 21)
rsectorID = 20 - rsectorID;
else
rsectorID = 41 - rsectorID;

return rsectorID;
}

Int_t GateToFOCUS::FixCrystalID(Int_t crystalID, Int_t min, Int_t max)
{
if (crystalID < min) crystalID = 0;
else
if (crystalID > max) crystalID = max;

return crystalID;
}

Int_t GateToFOCUS::IncDecCrystalID(Int_t random, Int_t crystalID)
{
float Tag_2 = m_gRandom->Integer(random);

if (Tag_2 == 0) crystalID = crystalID + 1;
else
crystalID = crystalID - 1;

return crystalID;
}
// ####
// #### Functions to encode
// ####
void GateToFOCUS::InitEncode(char *data)
```

```
{
data[0] = 0x00;
data[1] = 0x00;
data[2] = 0x00;
data[3] = 0x00;
data[4] = 0x44;
data[5] = 0x00;
}

int GateToFOCUS::CoincidenceTagEncode(char *data, int EventTag)
{
if (EventTag == Event48Bit)
{
data[4] = data[4];
return SuccessEncode;
}
else
return FailureEncode;
}

int GateToFOCUS::CoincidenceTypeEncode(char *data, int CoincidenceType)
{
if (CoincidenceType == Delayed)
{
data[4] = data[4] & 0x0F;
return SuccessEncode;
}
else if (CoincidenceType == Prompt)
{
data [4] = data[4];
return SuccessEncode;
}
else
return FailureEncode;
}
```

```
int GateToFOCUS::TimeTagEncode(char *data, int EventTag)
{
if (EventTag == TimeMarker)
{
data[4] = data[4] | 128;
data[3] = data[3] | 128;
return SuccessEncode;
}
else
return FailureEncode;
}

int GateToFOCUS::TimeEncode(char *data, unsigned TimeID)
{
data[0] = data[0] | (TimeID&0xFF);
data[1] = data[1] | ((TimeID&0xFF00)>>8);
data[2] = data[2] | ((TimeID&0xFF0000)>>16);
data[3] = data[3] | ((TimeID&0x1F000000)>>21);
return SuccessEncode;
}

int GateToFOCUS::HeadNumberEncodeGamma1(char *data, unsigned HeadID)
{
data[2] = data[2] | (HeadID & 0x01)<<7;
return SuccessEncode;
}

int GateToFOCUS::HeadNumberEncodeGamma2(char *data, unsigned HeadID)
{
data[0] = data[0] | (HeadID & 0x01)<<7;
return SuccessEncode;
}

int GateToFOCUS::X_EncodeGamma1(char *data, unsigned X_crystalID)
{
data[2] = data[2] | (X_crystalID & 0x7F);
```

```
data[3] = data[3] | (X_crystalID & 0x80)>>1;
return SuccessEncode;
}

int GateToFOCUS::X_EncodeGamma2(char *data, unsigned X_crystalID)
{
data[0] = data[0] | (X_crystalID & 0x7F);
data[1] = data[1] | (X_crystalID & 0x80)>>1;
return SuccessEncode;
}

int GateToFOCUS::Y_EncodeGamma1(char *data, unsigned Y_crystalID)
{
data[3] = data[3] | (Y_crystalID & 0x3F);
return SuccessEncode;
}

int GateToFOCUS::Y_EncodeGamma2(char *data, unsigned Y_crystalID)
{
data[1] = data[1] | (Y_crystalID & 0x3F);
return SuccessEncode;
}
```

B.2 GateToFOCUS.hh

```
/*----------------------
GATE - Geant4 Application for Tomographic Emission OpenGATE Collaboration
This software is distributed under the terms of the GNU Lesser General Public Licence (LGPL)

See GATE/LICENSE.txt for further details
----------------------*/

#ifndef GateToFOCUS_H
#define GateToFOCUS_H

#ifdef G4ANALYSIS_USE_FOCUS
```

```
#include "GateVOutputModule.hh"
#include "GateCoincidenceDigi.hh"

#include <TRandom.h>

#define Event48Bit 1
#define TimeMarker 2
#define BlockSingles 3
#define UnknownWord 0
#define EventSize 6
#define GammaSize 4
#define Prompt 10
#define Delayed 11
#define SuccessEncode 20
#define FailureEncode 21

class GateToFOCUSMessenger;

class GateToFOCUS : public GateVOutputModule
{
public:

GateToFOCUS(const G4String& name, GateOutputMgr* outputMgr, DigiMode digiMode);

virtual ~GateToFOCUS();

void RecordBeginOfAcquisition();
void RecordEndOfAcquisition();
void RecordBeginOfRun(const G4Run *);
void RecordEndOfRun(const G4Run *);
void RecordBeginOfEvent(const G4Event *);
void RecordEndOfEvent(const G4Event *);
void RecordStep(const G4Step *);
void RecordVoxels(GateVGeometryVoxelStore *) {};
```

```
const G4String& GetFileName() {return m_fileName;}

void SetFileName(const G4String aName);


private:


G4String       m_fileName;

FILE*       m_outFile;

TRandom*       m_gRandom;

GateToFOCUSMessenger*       m_FOCUSMessenger;


void StoreInFOCUS(GateCoincidenceDigi *digi);

void WriteInFOCUS(char *data);

Int_t FixRSectorID(Int_t rsectorID, unsigned *HeadID);

Int_t GateToFOCUS::FixCrystalID(Int_t crystalID, Int_t min, Int_t max);

Int_t IncDecCrystalID(Int_t random, Int_t crystalID);


void InitEncode(char *data);

int CoincidenceTagEncode(char *data, int EventTag);

int CoincidenceTypeEncode(char *data, int CoincidenceType);

int TimeTagEncode(char *data, int EventTag);

int TimeEncode(char *data, unsigned TimeID);

int HeadNumberEncodeGamma1(char *data, unsigned HeadID);

int HeadNumberEncodeGamma2(char *data, unsigned HeadID);

int X_EncodeGamma1(char *data, unsigned X_crystalID);

int X_EncodeGamma2(char *data, unsigned X_crystalID);

int Y_EncodeGamma1(char *data, unsigned Y_crystalID);

int Y_EncodeGamma2(char *data, unsigned Y_crystalID);

};


#endif

#endif
```

B.3 GateToFOCUSMessenger.cc

```
/*----------------------
GATE - Geant4 Application for Tomographic Emission OpenGATE Collaboration
This software is distributed under the terms of the GNU Lesser General Public Licence (LGPL)

See GATE/LICENSE.txt for further details
----------------------*/


#ifdef G4ANALYSIS_USE_FOCUS


#include "GateToFOCUSMessenger.hh"
#include "GateToFOCUS.hh"
#include "GateOutputMgr.hh"
#include "G4UIcmdWithAString.hh"


GateToFOCUSMessenger::GateToFOCUSMessenger(GateToFOCUS* gateToFOCUS)
:  GateOutputModuleMessenger(gateToFOCUS)
, m_gateToFOCUS(gateToFOCUS)
{
G4String cmdName;


cmdName = GetDirectoryName() + "setFileName";


SetFileNameCmd = new G4UIcmdWithAString(cmdName, this);
SetFileNameCmd->SetGuidance("Set the name of the output file (FOCUS binary file)");
SetFileNameCmd->SetParameterName("Name",false);
}


GateToFOCUSMessenger::~GateToFOCUSMessenger()
{
delete SetFileNameCmd;
}


void GateToFOCUSMessenger::SetNewValue(G4UIcommand* command, G4String newValue)
{
```

```
if (command == SetFileNameCmd)
m_gateToFOCUS->SetFileName(newValue);
else
GateOutputModuleMessenger::SetNewValue(command, newValue);
}
#endif
```

B.4 GateToFOCUSMessenger.hh

```
/*----------------------
GATE - Geant4 Application for Tomographic Emission OpenGATE Collaboration
This software is distributed under the terms of the GNU Lesser General Public Licence (LGPL)

See GATE/LICENSE.txt for further details
----------------------*/


#ifndef GateToFOCUSMessenger_h
#define GateToFOCUSMessenger_h 1


#ifdef G4ANALYSIS_USE_FOCUS


#include "GateOutputModuleMessenger.hh"


class GateToFOCUS;
class G4UIcmdWithAString;


class GateToFOCUSMessenger:  public GateOutputModuleMessenger
{
public:
GateToFOCUSMessenger(GateToFOCUS* gateToFOCUS);
~GateToFOCUSMessenger();
void SetNewValue(G4UIcommand*, G4String);
protected:
GateToFOCUS* m_gateToFOCUS;
G4UIcmdWithAString* SetFileNameCmd;
};
#endif
#endif
```

B.5 GateOutputMgr.cc

Inside the output manager some code lines had to be included:

```
#include "GateToFOCUS.hh"
(...)
#ifdef G4ANALYSIS_USE_FOCUS
GateToFOCUS* gateToFOCUS = new GateToFOCUS("focus", this,m_digiMode);
AddOutputModule((GateVOutputModule*)gateToFOCUS);
#endif
```

B.6 GNUmakefile

The GNUmakefile has to be changed in order to compile the new implemented class:

```
# FOCUS
ifdef G4ANALYSIS_USE_FOCUS
CPPFLAGS += -DG4ANALYSIS_USE_FOCUS
endif
```

Appendix C

Publications and Comunications

The work developed throughout this thesis gave origin to the following publications:

C.1 List of Publications

S. Branco (2009). Evaluation of the respiratory motion effect on small animal PET images. Proceedings of the II ECCOMAS Thematic Conference on Computational Vision and Medical Image Processing: VipIMAGE 2009, Taylor & Francis: 389-394.

S. Branco and S. Jan (2009). Quantitative Evaluation of Respiratory motion in Small Animal PET Imaging. [Abstracts of the Annual Congress of the EANM 2009, Barcelona, Spain]. European Journal of Nuclear Medicine and Molecular Imaging: 36(2): S412.

S. Branco, S. Jan and P. Almeida (2008). Respiratory Motion Modeling in Small Animal PET Using GATE. IEEE Nuclear Science Symposium Conference Record: 4948-4953.

A. E. Spinelli, G. Fiacchi, D. D'Ambrosio, S. Branco, R. Franchi, S. Boschi and M. Marengo (2008). Iterative Reconstruction of Small Animal PET Images Using Spatially Variant System Point Spread Function and MAP with Anatomical Priors. IEEE Nuclear Science Symposium Conference Record.

S. Branco, S. Jan and P. Almeida (2008). Respiratory motion in small animal PET using Monte Carlo simulations [Abstracts of the Annual Congress of the EANM 2008, Munich, Germany]. European Journal of Nuclear Medicine and Molecular Imaging 35(2): S175.

Branco, S., Jan, S. and Almeida, P. (2008). Small Animal Simulation Studies using the microPET® FOCUS system and the GATE platform. International Journal for Computational Vision and Biomechanics 1(2): 141-149.

S. Branco, S. Jan and P. Almeida (2007). Monte Carlo Simulations Studies in Small Animal PET using GATE. IEEE Nuclear Science Symposium Conference Record: 3994-3997.

S. Branco, S. Jan and P. Almeida (2007). Molecular imaging of small animals PET using Monte Carlo simulations [Abstracts of the Annual Congress of the EANM 2007, Copenhagen, Denmark]. European Journal of Nuclear Medicine and Molecular Imaging 34(2): S227.

S. Branco, S. Jan and P. Almeida (2007). Monte Carlo Simulations in Small Animal PET Imaging [Imaging 2006 conference Proceeding]. Nuclear Instruments and Methods in Physics Research A 580:1127-1130.

Branco, S., Jan, S. and Almeida, P. (2007). Molecular Imaging of Small Animals PET using Monte Carlo Simulations. Revista do Departamento de Electrónica, Telecomunicações e Informática da Universidade de Aveiro 4(7): 845-848.

Branco, S., Jan, S. and Almeida, P. (2007). Monte Carlo Simulations Studies in Small Animal PET. Computational Modelling of Objects Represented in Images. Fundamentals, Methods and Applications: Proceedings of the International Symposium CompIMAGE 2006, Taylor & Francis: 111-115.

C.2 List of Comunications

C.2.1 Oral communications

S. Branco. Evaluation of the respiratory motion effect on small animal PET images. VipIMAGE2009 – II ECCOMAS Thematic Conference on Computational Vision and Medical Image Processing (2009). Porto.

S. Branco, S. Jan and P. Almeida. Respiratory motion in small animal PET using Monte Carlo simulations. EANM'08 – Annual Congress of the European Association of Nuclear Medicine (2008). Munich.

S. Branco, S. Jan e P. Almeida. Simulações Monte Carlo em PET de pequenos animais. XI Congresso Nacional de Medicina Nuclear (2007). Porto.

S. Branco, S. Jan and P.Almeida. Molecular imaging of small animals PET using Monte Carlo simulations. EANM'07 – Annual Congress of the European Association of Nuclear Medicine (2007). Copenhagen.

Branco, S., Jan, S. e Almeida, P. Simulação de modelos animais em PET utilizando o método Monte Carlo. V Encontro Nacional das Ciências e Tecnologias da Saúde (2006). Lisboa.

Branco, S., Jan, S. and Almeida, P. Monte Carlo Simulations Studies in Small Animal PET. CompImage - Computational modelling of objects represented in images: Fundamentals, methods and applications (2006). Coimbra.

Branco, S., Jan, S. and Almeida, P. Monte Carlo Simulations of Small Animal PET. New Trends on PET (2006). Saint Petersburg.

C.2.2 Invited Oral communications

S. Branco, S. Jan e P. Almeida. Small Animal PET studies using GATE. OpenGATE meeting (2007). Paris.

C.2.3 Posters in conferences

S. Branco and S. Jan. Quantitative Evaluation of Respiratory motion in Small Animal PET Imaging. EANM'09 – Annual Congress of the European Association of Nuclear Medicine (2009). Barcelona.

S. Branco, S. Jan and P. Almeida. Respiratory Motion Modeling in Small Animal PET Using GATE. Nuclear Science Symposium and Medical Imaging Conference & 16th International Workshop on Room Temperature Semiconductor Detectors (2008). Dresden.

A. E. Spinelli, G. Fiacchi, D. D'Ambrosio, S. Branco, S. Boschi, R. Franchi and M. Marengo. Small animal iterative PET image reconstruction using system point spread function modeling and MAP with anatomical priors. Nuclear Science Symposium and Medical Imaging Conference & 16th International Workshop on Room Temperature Semiconductor Detectors (2008). Dresden.

S. Branco, S. Jan and P. Almeida. Monte Carlo Simulations Studies in Small Animal PET using GATE. Nuclear Science Symposium and Medical Imaging Conference (2007). Hawaii.

Branco, S., Jan, S. and Almeida, P. Molecular Imaging of Small Animals PET using Monte Carlo Simulations. Workshop on Medical Instrumentation Signal and Imaging (2007). Aveiro.

Branco, S., Jan, S. and Almeida, P. Molecular Imaging of Small Animals with PET Monte Carlo Simulations. Workshop on Behaviour Pathologies: Biological Approaches (2007). Oeiras.

Branco, S., Jan, S. and Almeida, P. Monte Carlo Simulations in Small Animal PET. International Conference on Imaging Techniques in Subatomic Physics, Astrophysics, Medicine, Biology and Industry - Imaging 2006 (2006). Stockholm.

C.3 Scientific Committee

Special Track *Computational Bioimaging* at the 6th International Symposium on Visual Computing (ISVC 2010). Las Vegas.

Special Track *Computational Bioimaging* at the 5th International Symposium on Visual Computing (ISVC 2009). Las Vegas.

VipIMAGE2009 – II ECCOMAS Thematic Conference on Computational Vision and Medical Image Processing. Porto.

C.4 Conference Chair

Thematic session *Small Animal Imaging: Trends and Techniques* at the VipIMAGE2009 – II ECCOMAS Thematic Conference on Computational Vision and Medical Image Processing. Porto.

C.5 Organizing Committee

Thematic session *Small Animal Imaging: Trends and Techniques* at the VipIMAGE2009 – II ECCOMAS Thematic Conference on Computational Vision and Medical Image Processing. Porto.

C.6 Honours and Awards

Conference Trainee Grant based on the scientific excellence contribution submitted to the 2008 IEEE Nuclear Science Symposium and Medical Imaging Conference & 16th International Workshop on Room Temperature Semiconductor Detectors (NSS/MIC/RTSD). Dresden.

Highlight lecture of the EANM'08 – Annual Congress of the European Association of Nuclear Medicine. Munich.

Conference Trainee Grant given by Fundação Calouste Gulbenkian, based on the scientific excellence contribution submitted to the EANM'08 – Annual Congress of the European Association of Nuclear Medicine.

Bibliography

Agostinelli, S., Allison, J., Amako, K., Apostolakis, J., Araujo, H., Asai, P. Arce M., Axen, D., Banerjee, S., Barrand, G., Behner, F., Bellagamba, L., Boudreau, J., Broglia, L., Brunengo, A., Burkhardt, H., Chauvie, S., Chuma, J., Chytracek, R., Cooperman, G., Cosmo, G., Degtyarenko, P., DellÕAcqua, A., Depaola, G., Dietrich, D., Enami, R., Feliciello, A., Ferguson, C., Fesefeldt, H., Folger, G., Foppiano, F., Forti, A., Garelli, S., Giani, S., Giannitrapani, R., Gibin, D., Cadenas, J.J. Gomez, Gonzalez, I., Abril, G. Gracia, Greeniaus, G., Greiner, W., Grichine, V., Grossheim, A., Guatelli, S., Gumplinger, P., Hamatsu, R., Hashimoto, K., Hasui, H., Heikkinen, A., Howard, A., Ivanchenko, V., Johnson, A., Jones, F.W., Kallenbach, J., Kanaya, N., Kawabata, M., Kawabata, Y., Kawaguti, M., Kelner, S., Kent, P., Kimura, A., Kodama, T., Kokoulin, R., Kossov, M., Kurashige, H., Lamanna, E., Lampen, T., Lara, V., Lefebure, V., Lei, F., Liendl, M., Lockman, W., Longo, F., S. Magni, M. Maire, Medernach, E., Minamimoto, K., de Freitas, P. Mora, Morita, Y., Murakami, K., Nagamatu, M., Nartallo, R., Nieminen, P., Nishimura, T., Ohtsubo, K., Okamura, M., OÕNeale, S., Oohata, Y., Paech, K., Perl, J., Pfeiffer, A., Pia, M. G., Ranjard, F., Rybin, A., Sadilov, S., Salvo, E. Di, Santin, G., Sasaki, T., Savvas, N., Sawada, Y., Scherer, S., Sei, S., Sirotenko, V., Smith, D., Starkov, N., Stoecker, H., Sulkimo, J., Takahata, M., Tanaka, S., Tcherniaev, E., Tehrani, E. Safai, Tropeano, M., Truscott, P., Uno, H., Urban, L., Urban, P., Verderi, M., Walkden, A., Wander, W., Weber, H., Wellisch, J.P., Wenaus, T., Williams, D.C., Wright, D., Yamada, T., Yoshida, H., & Zschiesche, D. 2003. Geant4 - a simulation toolkit. *Nuclear instruments and methods in physics research a*, **506**, 250–303. 4.5, 5.1.4, 5.1.4.3

Allison, J., Amako, K., Apostolakis, J., Araujo, H., Dubois, P. Arce, Asai, M., Barrand, G., Capra, R., Chauvie, S., Chytracek, R., Cirrone, G. A. P., Cooperman, G., Cosmo, G., Cuttone, G., Daquino, G. G., Donszelmann, M., Dressel, M., Folger, G., Foppiano, F., Generowicz, J., Grichine, V., Guatelli, S., Gumplinger, P., Heikkinen, A., Hrivnacova, I., Howard, A., Incerti, S., Ivanchenko, V., Johnson, T., Jones, F., Koi, T., Kokoulin, R., Kossov, M., Kurashige, H., Lara, V., Larsson, S., Lei, F., Link, O., Longo, F., Maire, M., Mantero, A., Mascialino, B., I. McLaren, P. Mendez Lorenzo, Minamimoto, K., Murakami, K., Nieminen, P., Pandola, L., Parlati, S., Peralta, L., Perl, J., Pfeiffer, A., Pia, M. G., Ribon, A., Rodrigues, P., Russo, G., Sadilov, S., Santin, G., Sasaki, T., Smith, D., Starkov, N., Tanaka, S., Tcherniaev, E., Tome, B., Trindade, A., Truscott, P., Urban, L., Verderi, M., A.Walkden, P.Wellisch, J., C.Williams, D., Wright, D., & Yoshida, H. 2006. Geant4 developments and applications. *Ieee transactions on nuclear science*, **53**(1), 270–278. 5.1.4

Amako, K., Guatelli, S., Ivanchenko, V., Mascialino, B., Murakami, K., Pandola, L., Parlati, S., Pia, M. G., Piergentili, M., Sasaki, T., & Urban, L. 2004. Validation of geant4 electromagnetic physics versus protocol data. *Ieee nuclear science symposium conference record*, **4**, 2115–2119. 5.1.4

AMIDE. 2010. *http://amide.sourceforge.net/*. 6.2.3

Anatomist. 2010. *http://brainvisa.info/*. 7.1.1

Andreo, P. 1991. Monte carlo techniques in medical radiation physics. *Physics in medicine and biology*, **36**(7), 861–920. 1, 4, 4, 4.1

Andreo, P., & Ljungberg, M. 1998. *Monte carlo calculations in nuclear medicine: Applications in diagnostic imaging*. Institute of Physics Publishing. Chap. General Monte Carlo Codes for use in Medical Radiation Physics, pages 37–52. 1, 4.5

Apostolakis, J., Giani, S., Maire, M., Nieminen, P., Pia, M.G., & Urban, L. 1999. Geant4 low energy electromagnetic models for electrons and photons. *Cern-open-99-034 and infn/ae-99/18*. 5.1.4.2

Archambault, L., Beaulieu, L., Carrier, J. F., Castrovillari, F., Chauvie, S., Foppiano, F., Ghiso, G., Guatelli, S., Incerti, S., Lamanna, E., Larsson, S., Lopes, M. C., Peralta, L., Pia, M. G., Rodrigues, P., Tremblay, V. H., & Trindade, A. 2003. Overview of geant4 applications in medical physics. *Ieee nuclear science symposium*, **3**, 1743–1746. 5.1.1

Assie, Karine, Breton, Vincent, Buvat, Irene, Comtat, Claude, Jan, Sebastien, Krieguer, Magalie, Lazaro, Delphine, Morel, Christian, Rey, Martin, Santin, Giovanni, Simon, Luc, Staelens, Steven, Strul, Daniel, Vieira, Jean-Marc, & de Walle, Rik Van. 2004. Monte carlo simulation in pet and spect instrumentation using gate. *Nuclear instruments and methods in physics research a*, **527**, 180–189. 4.5, 5

Association, National Electrical Manufacturers. 2001. Nema standards publication nu 2-2001: Performance measurements of positron emission tomographs. *National electrical manufacturers association*. 2.4

Badawi, R. D., & Marsden, P. K. 1999. Developments in component-based normalization for 3d pet. *Physics in medicine and biology*, **44**(2), 571–594. 2.5.2

Badawi, R. D., Ferreira, N. C., Kohlmyer, S. G., Dahlbom, M., Marsden, P. K., & Lewellen, T. K. 2000. A comparison of normalization effects on three whole-body cylindrical 3d pet systems. *Physics in medicine and biology*, **45**(11), 3253–3266. 2.5.2

Bailey, D. 1998. *The theory and practice of 3d pet*. Kluwer Academic Publishers. Chap. Quantitative Procedures in 3D PET, pages 55–109. 2.5.1, 2.5.2, 2.5.3, 2.5.4

Bailey, D. 2003. *Positron emission tomography: Basic science and clinical practice*. Springer. Chap. Data Acquisition and Performance Characterization in PET, pages 69–90. 2.2.3, 2.3.2, 2.4.1, 2.4.2, 2.4.3, 2.4.4

Bailey, D. L. 2005. *Positron emission tomography: Basic sciences*. Springer. Chap. Data Acquisition and Performance Characterization in PET, pages 41–62. 2.2.3, 2.3.2, 2.3.3, 2.3.5, 2.4.1, 2.4.2, 2.4.3

Bailey, D. L., Karp, J. S., & S., S. Surti. 2003. *Positron emission tomography: Basic science and clinical practice*. Springer. Chap. Physics and Instrumentation in PET, pages 41–67. 2.1.1, 2.1.2, 2.1.2, 2.1.3, 2.1.3.2, 2.2.1, 2.2.2, 2.2.2

Bailey, D. L., Karp, J. S., & Surti, S. 2005. *Positron emission tomography: Basic sciences*. Springer. Chap. Physics and Instumentation in PET, pages 13–39. 2.1.1, 2.1.2, 2.1.2, 2.1.3, 2.1.3.2, 2.2.1, 2.2.2, 2.2.2, 2.4.4

Bajc, M., Jonson, B., & Steinert, H. C. 2007. *Clinical nuclear medicine*. Springer. Chap. Lung, pages 118–146. 1

Balaban, Robert S., & Hampshire, Victoria A. 2001. Challenges in small animal noninvasive imaging. *Institute for laboratory animal research*, **42**(3), 248–262. 3.1

Bao, Q., Newport, D., Chen, M., Stout, D. B., & Chatziioannou, A. F. 2009. Performance evaluation of the inveon dedicated pet preclinical tomograph based on the nema nu-4 standards. *The journal of nuclear medicine*, **50**(3), 401–408. 3.2.3

Barca, G., Castrovillari, F., Chauvie, S., Cuce, D., Foppiano, F., Ghiso, G., Guatelli, S., Lamanna, E., Lopes, M.C., Peralta, L., Pia, M.G., Rodrigues, P., Trindade, A., & Veltri, M. 2003. A powerful simulation tool for medical physics applications: Geant4. *Nuclear physics b Ð proceedings supplements*, **125**, 80–84. 4.5

Bataille, F., Comtat, C., Jan, S., & Trebossen, R. 2004. Monte carlo simulation for the ecat hrrt using gate. *Ieee mic conference records*, **4**, 2570–2574. 5.2

Beenhouwer, Jan De, Kruecker, Dirk, Staelens, Steven G., Ferrer, Ludovic, Chatziioannou, Arion F., & Rannou, Fernando R. 2005. Distributed computing platform for pet and spect simulations with gate. *Ieee nuclear science symposium conference record*, **3**, 2437–2440. (document), 5.10, 5.11, 5.12, 5.3.4

Beenhouwer, Jan De, Staelens, Steven, Ferrer, Ludovic, D'Asseler, Yves, Lemahieu, Ignace, & Rannou, Fernando R. 2007. Cluster computing software for gate simulations. *Medical physics*, **34**(6), 1926–1933. 5.3.4

Ben-Haim, Simona, & Ell, Peter. 2009. 18f-fdg pet and pet/ct in the evaluation of cancer treatment response. *The journal of nuclear medicine*, **50**(1), 88–99. 2

Berger, Frank, Lee, Yu-Po, Loening, Andreas M., Chatziioannou, Arion, Freedland, Stephen J., Leahy, Richard, Lieberman, Jay R., Belldegrun, Arie S., Sawyers, Charles L., & Gambhir, Sanjiv S. 2002. Whole-body skeletal imaging in mice utilizing micropet: optimization of reproducibility and applications in animal models of bone disease. *European journal of nuclear medicine*, **29**(9), 1225–1236. 7.1.1.1

Bettinardi, V. 2009. Number of partitions (gates) needed to obtain motion-free images in a respiratory gated 4d-pet/ct study as a function of the lesion size and motion displacement. *Medical physics*, **36**(12), 5547–5558. 11.4

Blasberg, R. 2002. Pet imaging of gene expression. *European journal of cancer*, **38**, 2137–2146. 3.4

Blasberg, R., & Tjuvajev, J. G. 2002. In vivo molecular-genetic imaging. *Journal of cellular biochemistry supplement*, **39**, 172–183. 3.4

Boellaard, Ronald, OÕDoherty, Mike J., Weber, Wolfgang A., Mottaghy, Felix M., Lonsdale, Markus N., Stroobants, Sigrid G., Oyen, Wim J. G., Kotzerke, Joerg, Hoekstra, Otto S., Pruim, Jan, Marsden, Paul K., Tatsch, Klaus, Hoekstra, Corneline J., Visser, Eric P., Arends, Bertjan, Verzijlbergen, Fred J., Zijlstra, Josee M., Comans, Emile F. I., Lammertsma, Adriaan A., Paans, Anne M., Willemsen, Antoon T., Beyer, Thomas, Bockisch, Andreas, Schaefer-Prokop, Cornelia, Delbeke, Dominique, Baum, Richard P., Chiti, Arturo, & Krause, Bernd J. 2009. Fdg pet and pet/ct: Eanm procedure guidelines for tumour pet imaging: version 1.0. *European journal of nuclear medicine and molecular imaging*, 1–20. 2.3.4

Bomanji, J., Costa, D., & Ell, P. 2001. Clinical role of positron emission tomography in oncology. *The lancet oncology*, **2**(3), 157–164. 1

Branco, Susana. 2005. *Implementacao de um sistema para simulacao por monte carlo de pet aplicada aos pequenos animais.* M.Phil. thesis, Faculdade de Ciencias da Universidade de Lisboa. (document), 6.2.3, 6.3

Brasse, David, Kinahan, Paul E., Lartizien, Carole, Comtat, Claude, Casey, Mike, & Michel, Christian. 2005. Correction methods for random coincidences in fully 3d whole-body pet: impact on data and image quality. *Journal of nuclear medicine*, **46**(5), 859–867. 2.5.5

Brun, R., & Rademakers, F. 1997. Root Ð a object oriented data analysis framework. *Nuclear instruments and methods in physics research a*, **389**, 81–86. 6.2.3

Bruyant, P. P. 2002. Analytic and iterative reconstruction algorithms in spect. *The journal of nuclear medicine*, **43**(10), 1343–1358. (document), 2.15, 2.6.2

Buvat, I., & Castiglioni, I. 2002. Monte carlo simulations in spet and pet. *The quarterly journal of nuclear medicine*, **46**(1), 48–61. 1, 4, 4.5

Buvat, I., & Lazaro, D. 2006. Monte carlo simulations in emission tomography and gate: an overview. *Nuclear instruments and methods in physics research a*, **569**, 323–329. 1, 4.5

Buvat, Irene. 2007. Quantification in emission tomography: Challenges, solutions, and performance. *Nuclear instruments and methods in physics research a*, **571**, 10–13. 1

Buvat, Irene, Castiglioni, Isabella, Feuardent, Juliette, & Gilardi, Maria-Carla. 2005. Unified description and validation of monte carlo simulators in pet. *Physics in medicine and biology*, **50**, 329–346. 1, 4.5

Casey, M. E., & Nutt, R. 1986. A multicrystal two dimensional bgo detector system for positron emission tomography. *Ieee transactions on nuclear science*, **33**(1), 460–463. 2.2.3

Casey, M. E., Gadagkar, H., & Newport, D. 1995. A component based method for normalization in volume pet. *Proceedings of the 3rd int. meeting on fully three-dimensional image reconstruction in radiology and nuclear medicine*, 67–71. 2.5.2

CCRT. 2010. *http://www-ccrt.cea.fr*. 5.3.1

Chatziioannou, A. F. 2002a. Molecular imaging of small animals with dedicated pet tomographs. *European journal of nuclear medicine*, **29**(1), 98–114. (document), 3.1.5, 3.3, 3.3

Chatziioannou, A. F. 2002b. Pet scanners dedicated to molecular imaging of small animal models. *Molecular imaging and biology*, **4**(1), 47–63. (document), 1, 3.1.5, 3.3, 3.5

Chatziioannou, Arion F. 2005. Instrumentation for molecular imaging in preclinical research. *Proceedings of the american thoracic society*, **2**, 533–536. 3.4

Chauvie, S., Grichine, V., Gumplinger, P., Ivanchenko, V., Kokoulin, R., Magni, S., Maire, M., Nieminen, P., G.Pia, M., Rybin, A., & Urban, L. 2000. Geant4 electromagnetic physics. *Infn/ae-00/07*. 5.1.4

Chauvie, S., Grichine, V., Gumplinger, P., Ivanchenko, V., Kokoulin, R., Magni, S., Maire, M., Nieminen, P., G.Pia, M., Rybin, A., & Urban, L. 2001. Geant4 low energy electromagnetic physics. *Proceedings of chep2001, beijing*. 5.1.4

Cherry, S. R. 2004. In vivo molecular and genomic imaging: new challenges for imaging physics. *Physics in medicine and biology*, **49**, R13–R48. 1, 3.4

Cherry, S. R. 2009. Multimodality imaging: Beyond pet/ct and spect/ct. *Seminars in nuclear medicine*, **39**, 348–353. 1

Cherry, S. R., & Chatziioannou, A. F. 2004. *Emission tomography: The fundaments of pet and spect*. Elsevier. Chap. Small Animal PET Systems, pages 213–228. 3.1, 3.1.6, 3.3

Cherry, S. R., & Dahlbom, M. 2006. *Pet: Physics, instrumentation and scanners*. Springer. (document), 2.1.1, 2.1.2, 2.1.3.1, 2.2, 2.4.1, 2.10, 2.5, 2.5.3, 2.5.4, 2.5.5, 2.5.7, 2.14

Cherry, S. R., & Gambhir, S. S. 2001. Use of positron emission tomography in animal research. *Institute for laboratory animal research*, **42**(3), 219–232. 1, 3.4

Cherry, S. R., Shao, Y., Siegel, S., Silverman, R. W., Meadors, K., Young, J., Jones, W. F., Newport, D., Mooyers, C., Mumcuoglu, E. U., Chatziioannou, A., Farquhar, T., Andreaco, M., Paulus, M., Binkley, D., Nutt, R., & Phelps, M. E. 1997. Micropet: A high resolution pet scanner for imaging small animals. *Ieee transactions on nuclear science*, **44**(3), 1161–1166. 3.3

Cherry, S. R., Sorenson, J. A., & Phelps, M. E. 2003a. *Physics in nuclear medicine*. Saunders. 2.1.2, 2.1.3.1, 2.3.2, 2.4.2, 2.5, 2.5.2, 2.5.3, 2.5.4, 2.5.5, 2.5.6, 2.7

Cherry, S. R., Sorenson, J. A., & Phelps, M. E. 2003b. *Physics in nuclear medicine*. Saunders. Chap. Image Quality in Nuclear Medicine, pages 253–272. 10.4

Christian, P. E. 2007a. *Nuclear medicine and pet/ct: Technology and techniques*. Mosby Elsevier. Chap. PET Instrumentation, pages 314–343. 2

Christian, P. E. 2007b. *Nuclear medicine and pet/ct: Technology and techniques*. Mosby Elsevier. Chap. Physics of Nuclear Medicine, pages 39–58. 2.1.1

Cirrone, G. A. P., Cuttone, G., Donadio, S., Grichine, V., Guatelli, S., Gumplinger, P., Ivanchenko, V., Maire, M., Mantero, A., Mascialino, B., Nieminen, P., Pandola, L., Parlati, S., Pfeiffer, A., Pia, M. G., & Urban, L. 2003. Precision validation of geant4 electromagnetic physics. *Ieee nuclear science symposium conference record*, **N23-2**. 5.1.4

Clear, Crystal. 2010. *http://crystalclear.web.cern.ch/crystalclear/*. 6.2.3

CLHEP. 2010. *http://proj-clhep.web.cern.ch/proj-clhep/*. 5.3.3

Coefficients, Attenuation. 2010. *http://physics.nist.gov/physrefdata/xraymasscoef/tab2.html*. 7.2

Couturier, O. 2004. Fluorinated tracers for imaging cancer with positron emission tomography. *European journal of nuclear medicine and molecular imaging*, **31**(8), 1182–1206. 1, 7.1.1.1, 7.1.1.2

Dawood, Mohammad, Lang, Norbert, Jiang, Xiaoyi, & Schafers, Klaus P. 2006. Lung motion correction on respiratory gated 3-d pet/ct images. *Ieee transactions of medical imaging*, **25**(4), 476–485. 11.4

Dawood, Mohammad, Buther, Florian, Jiang, Xiaoyi, & Schafers, Klaus P. 2008. Respiratory motion correction in 3-d pet data with advanced optical flow algorithms. *Ieee transactions on medical imaging*, **27**(8), 1164–1175. 11.4

Defrise, M., & Kinahan, P. E. 1998. *The theory and practice of 3d pet*. Kluwer Academic Publishers. Chap. Data acquisition and image reconstruction for 3D PET, pages 11–53. 2.4.3, 2.6.3

Defrise, M., Kinahan, P. E., & J., C. J. Michel C. 2003. *Positron emission tomography: Basic science and clinical practice*. Springer. Chap. Image Reconstruction Algorithms in PET, pages 91–114. (document), 2.6.3, 2.19

Defrise, M., Kinahan, P. E., & Michel, C. J. 2005. *Positron emission tomography: Basic sciences*. Springer. Chap. Image Reconstruction Algorithms in PET, pages 63–91. (document), 2.6.1.1, 2.6.1.2, 2.6.3, 2.19

Defrise, Michel, & Gullberg, Grant T. 2006. Image reconstruction. *Physics in medicine and biology*, **51**, R139–R154. 2.6

Defrise, Michel, Kinahan, P. E., Townsend, D. W., Michel, C., Sibomana, M., & Newport, D. F. 1997. Exact and approximate rebinning algorithms for 3-d pet data. *Ieee transactions on medical imaging*, **16**(2), 145–158. 2.6.3

Derenzo, S. E., Moses, W. W., Huesman, R. H., & Budinger, T. F. 1993. *Quantification of brain function: Tracer kinetics and image analysis in brain pet.* Elsevier. Chap. Critical instrumentation issues for <2 mm resolution, high sensitivity brain PET., pages 25–40. 2.4.1

Detorie, N., & Dahlbom, M. 2006. Motion correction for respiratory gated pet images. *Ieee nuclear science symposium conference record*, 3273–3277. 11.4

Detorie, Nicole C., & Dahlbom, Magnus. 2008. Quantitative evaluation of reconstruction algorithms for motion compensated pet. *Nuclear science symposium conference record*, 5366–5372. 11.4

EGS. 2010. *http://www2.slac.stanford.edu/vvc/egs/*. 4.5

EGS4. 2010. *http://www.irs.inms.nrc.ca/egs4/get_egs4.html*. 4.5

Engine, Sun Grid. 2010. *http://gridengine.sunsource.net/*. 5.3.2

Fahey, F. H. 2002. Data acquisition in pet imaging. *Journal of nuclear medicine technology*, **30**(2), 39–49. 2.3.3

Ferreira, Nuno C. 2001. *Contribuicao para a quantificacao em tomografia por emissao de positroes no modo 3d*. Ph.D. thesis, Faculdade de Medicina da Universidade de Coimbra. 2.3.4, 2.5.2

Gambhir, S. S. 2002. Molecular imaging of cancer with positron emission tomography. *Nature reviews*, **2**, 683–693. (document), 1, 3.4

Gambhir, S. S., Barrio, R., Herschman, H. R., & Phelps, M. E. 1999. Assays for noninvasive imaging of reporter gene expression. *Nuclear medicine and biology*, **26**, 481–490. 3.4

Gambhir, S. S., Herschman, H. R., Cherry, S. R., Barrio, J. R., Satyamurthy, N., Toyokuni, T., Phelps, M. E., Larson, S. M., Balaton, J., Finn, R., Sadelain, M., Tjuvajev, J., & Blasberg, R. 2000. Imaging transgene expression with radionuclide imaging technologies. *Neoplasia*, **2**(1-2), 118–138. 3.4

GATE. 2010a. *http://www.opengatecollaboration.org*. 1, 4.5, 5, 2

GATE. 2010b. *http://wiki.opengatecollaboration.org/*. 5, 5.1.6, 5.3.3

Geant4. 2010. *http://geant4.web.cern.ch/geant4/*. 4.5

GPS, Geant4. 2010. *http://reat.space.qinetiq.com/gps/new_gps_sum_files/gps_sum.htm*. 5.1.5

Graham, L. S., & Links, J. M. 2007. *Nuclear medicine and pet/ct: Technology and techniques*. Mosby Elsevier. Chap. Instrumentation, pages 59–104. 10.4

Green, Leeta A., Gambhir, Sanjiv S., Srinivasan, Ashok, Banerjee, Pranab K., Hoh, Carl K., Cherry, Simon R., Sharfstein, Susan, Barrio, Jorge R., Herschman, Harvey R., & Phelps, Michael E. 1998. Noninvasive methods for quantitating blood time-activity curves from mouse pet images obtained with fluorine-18-fluorodeoxyglucose. *The journal of nuclear medicine*, **39**(4), 729–734. 3.1.5

Gropp, William, Lusk, Ewing, Ashton, David, Balaji, Pavan, Buntinas, Darius, Butler, Ralph, Chan, Anthony, Goodell, David, Krishna, Jayesh, Mercier, Guillaume, Ross, Rob, Thakur, Rajeev, & Toonen, Brian. 2008 (April). *Mpich2 userÕs guide*. Version 1.0.7 edn. Mathematics and Computer Science Division, Argonne National Laboratory. 5.3.2

Guerra, A. D., & Belcari, N. 2007. State-of-the-art of pet, spect and ct for small animal imaging. *Nuclear instruments and methods in physics research a*, **583**, 119–124. 3.3

Guhlke, S., Verbruggen, A. M., & Vallabhajosula, S. 2007. *Clinical nuclear medicine*. Springer. Chap. Radiochemistry and Radiopharmacy, pages 34–76. 1, 2.7

Gunter, D. L. 2004. *Emission tomography: The fundaments of pet and spect*. Elsevier. Chap. Collimator Design for Nuclear Medicine, pages 153–168. 2.3.5

Haynor, D. R. 1998. *Monte carlo calculations in nuclear medicine: Applications in diagnostic imaging*. Institute of Physics Publishing. Chap. Variance Reduction Techniques, pages 13–24. 4.4

Herschman, H. 2003. Micro-pet imaging and small animal models of disease. *Current opinion in immunology*, **15**, 378–384. 3.4

Huang, Sung-Cheng, Wu, Hsiao-Ming, Shoghi-Jadid, Kooresh, Stout, David B., Chatziioannou, Arion, Schelbert, Heinz R., & Barrio, Jorge R. 2004. Investigation of a new input function validation approach for dynamic mouse micropet studies. *Molecular imaging & biology*, **6**(1), 34–46. 3.1.5

Hume, Susan P., & Jones, Terry. 1998. Positron emission tomography (pet) methodology for small animals and its application in radiopharmaceutical preclinical investigation. *Nuclear medicine & biology*, **25**, 729–732. 3.4

Humm, John L., Rosenfeld, Anatoly, & Guerra, Alberto Del. 2003. From pet detectors to pet scanners. *European journal of nuclear medicine and molecular imaging*, **30**(11), 1574–1597. 2.2.1, 2.2.2, 2.2.3

Hutchins, Gary D., Miller, Michael A., Soon, Victor C., & Receveur, Timothy. 2008. Small animal pet imaging. *Institute for laboratory animal research*, **49**(1), 54–65. 3.1

Hutton, B. F., Nuyts, J., & Zaidi, H. 2006. *Quantitative analysis in nuclear medicine imaging*. Springer Publishing. Chap. Iterative Reconstruction Methods, pages 107–140. 2.6.2, 2.6.2

Infiniband. 2010. *http://www.infinibandta.org/*. 5.3.1

Installation, GATE. 2010a. *http://www.opengatecollaboration.org/download-source.html*. 5.3.3

Installation, Geant4. 2010b. *http://geant4.web.cern.ch/geant4/support/download.shtml*. 5.3.3

instructions, MOBY. 2010. *http://www.bme.unc.edu/ wsegars/moby_instructions.htm*. 4

Inveon, Siemens Medical. 2010. *http://www.medical.siemens.com/webapp/wcs/stores/servlet /productdisplay q_catalogid e_-11 a_cattree e_100010,1007660,1011525,1029715 a_langid e_-11 a_productid e_200657 a_storeid e_10001.htm*. 3.2.3

Jacobson M., Levkovitz R., Ben-Tal A. Thielemans K. Spinks T. Belluzzo D. Pagani E. V. Bettinardi Gilardi M. C. Zverovich A., & G., Mitra. 2000. Enhanced 3d pet osem reconstruction using inter-update metz filtering. *Physics in medicine and biology*, **45**(8), 2417–2439. (document), 2.11

Jan, S., Boisgard, R., Fontyn, Y., Eroukhmanoff, C., Comtat, C., & Trebossen, R. 2004a. Accuracy and variability of quantitative values obtained for mouse imaging using the micropet focus. *Nuclear science symposium conference record*, **5**, 2934–2937. 6.2.2, 9

Jan, S., Santin, G., Strul, D., Staelens, S., Assie, K., Autret, D., Avner, S., Barbier, R., Bardies, M., Bloomfield, P. M., Brasse, D., Breton, V., Bruyndonckx, P., Buvat, I., Chatziioannou, A. F., Choi, Y., Chung, Y. H., Comtat, C., Donnarieix, D., Ferrer, L., Glick, S. J., Groiselle, C. J., D. Guez, P. F. Honore, Cavata, S. Kerhoas, Kirov, A. S., Kohli, V., Koole, M., Krieguer, M., van der Laan, D. J., Lamare, F., Largeron, G., Lartizien, C., Lazaro, D., Maas, M. C., Maigne, L., Mayet, F., Melot, F., Merheb, C., Pennacchio, E., Perez, J., Pietrzyk, U., Rannou, F. R., Rey, M., Schaart, D. R., Schmidtlein, C. R., Simon, L., Song, T. Y., Vieira, J. M., Visvikis, D., de Walle, R. Van, Wieers, E., & Morel, C. 2004b. Gate: a simulation toolkit for pet and spect. *Physics in medicine and biology*, **49**(19), 4543–4561. (document), 1, 4.5, 5, 5.1

Jan, S., Comtat, C., Strul, D., Santin, G., & Trebossen, R. 2005a. Monte carlo simulation for the ecat exact hr+ system using gate. *Ieee transactions on nuclear science*, **52**(3), 627–633. 5.2

Jan, S., Desbree, A., Pain, F., Guez, D., Comtat, C., Gurden, H., Kerhoas, S., Laniece, P., Lefebvre, F., Mastrippolito, R., & Trebossen, R. 2005b. Monte carlo simulation of the micropet focus system for small rodents imaging applications. *Ieee nuclear science symposium conference record*, **3**, 1653–1657. (document), 1, 5.2, 6.2.2, 9.1, 9.3, 9.4, 9.5, 9.1

Jan, S., Santin, G., Strul, D., Staelens, S., Assie, K., Autret, D., Avner, S., Barbier, R., Bardies, M., Bloomfield, P. M., Brasse, D., Breton, V., Bruyndonckx, P., Buvat, I., Chatziioannou, A. F., Choi, Y., Chung, Y. H., Comtat, C., Donnarieix, D., Ferrer, L., Glick, S. J., Groiselle, C. J., D. Guez, P. F. Honore, Cavata, S. Kerhoas, Kirov, A. S., Kohli, V., Koole, M., Krieguer, M., van der Laan, D. J., Lamare, F., Largeron, G., Lartizien, C., Lazaro, D., Maas, M. C., Maigne, L., Mayet, F., Melot, F., Merheb, C., Pennacchio, E., Perez, J., Pietrzyk, U., Rannou, F. R., Rey, M., Schaart, D. R., Schmidtlein, C. R., Simon, L., Song, T. Y., Vieira, J. M., Visvikis, D., de Walle, R. Van, Wieers, E., & Morel, C. 2007 (September). *Gate installation guide*. Versions 3.1.2 edn. OpenGATE Collaboration. 5.3.3

Jan, S., Santin, G., Strul, D., Staelens, S., Assie, K., Autret, D., Avner, S., Barbier, R., Bardies, M., Bloomfield, P. M., Brasse, D., Breton, V., Bruyndonckx, P., Buvat, I., Chatziioannou, A. F., Choi, Y., Chung, Y. H., Comtat, C., Donnarieix, D., Ferrer, L., Glick, S. J., Groiselle, C. J., D. Guez, P. F. Honore, Cavata, S. Kerhoas, Kirov, A. S., Kohli, V., Koole, M., Krieguer, M., van der Laan, D. J., Lamare, F., Largeron, G., Lartizien, C., Lazaro, D., Maas, M. C., Maigne, L., Mayet, F., Melot, F., Merheb, C., Pennacchio, E., Perez, J., Pietrzyk, U., Rannou, F. R., Rey, M., Schaart, D. R., Schmidtlein, C. R., Simon, L., Song, T. Y., Vieira, J. M., Visvikis, D., de Walle, R. Van, Wieers, E., & Morel, C. 2008 (August). *Gate users guide*. Version 4.0.0 edn. OpenGATE Collaboration. (document), 5, 5.1, 5.2, 5.1.6, 5.3, 5.1.9.2, 5.7, 7.2

Jan, S., Santin, G., Strul, D., Staelens, S., Assie, K., Autret, D., Avner, S., Barbier, R., Bardies, M., Bloomfield, P. M., Brasse, D., Breton, V., Bruyndonckx, P., Buvat, I., Chatziioannou, A. F., Choi, Y., Chung, Y. H., Comtat, C., Donnarieix, D., Ferrer, L., Glick, S. J., Groiselle, C. J., D. Guez, P. F. Honore, Cavata, S. Kerhoas, Kirov, A. S., Kohli, V., Koole, M., Krieguer, M., van der Laan, D. J., Lamare, F., Largeron, G., Lartizien, C., Lazaro, D., Maas, M. C., Maigne, L., Mayet, F., Melot, F., Merheb, C., Pennacchio, E., Perez, J., Pietrzyk, U., Rannou, F. R., Rey, M., Schaart, D. R., Schmidtlein, C. R., Simon, L., Song, T. Y., Vieira, J. M., Visvikis, D., de Walle, R. Van, Wieers, E., & Morel, C. 2009 (June). *Gate users guide*. Version 5.0.0 edn. OpenGATE Collaboration. 5.1.6

Jan, Sebastien, Collot, Johann, Gallin-Martel, Marie-Laure, Martin, Philippe, Mayet, Frederic, & Tournefier, Edwige. 2003. Gepetos: A geant4 monte carlo simulation package for positron emission tomography. *Ieee transactions on nuclear science*, **52**(1), 1–5. 5.1.1

Jeavons, A. P., Chandler, R. A., & Dettmar, C. A. R. 1999. A 3d hidac-pet camera with sub-millimetre resolution for imaging small animals. *Ieee transactions on nuclear science*, **46**(3), 468–473. 3.3

Kane, S. 2009. *Introduction to physics in modern medicine*. Taylor & Francis. 1

Kappor, V., McCook, B., & Torok, F. S. 2004. An introduction to pet-ct imaging. *Radiographics*, **24**(2), 523–543. (document), 2.20

Kerhoas-Cavata, Sophie, & Guez, David. 2006. Modeling electronic processing in gate. *Nuclear instruments and methods in physics research a*, **569**, 330–334. 5.1.9

Kinahan, P. E., Hasegawa, B. H., & Beyer, T. 2003. X-ray-based attenuation correction for positron emission tomography/computed tomography scanners. *Seminars in nuclear medicine*, **33**(3), 166–179. 2.1.3.3, 2.5.3

Kinahan, P. E., Defrise, M., & Clackdoyle, R. 2004. *Emission tomography: The fundaments of pet and spect*. Elsevier. Chap. Analytic Image Reconstruction Methods, pages 421–442. 2.6.1.1, 2.6.1.2, 6.2.3

Knoess, Christof, Siegel, Stefan, Smith, Anne, Newport, Danny, Richerzhagen, Norbert, Winkeler, Alexandra, Jacobs, Andreas, Goble, Rhonda N., Graf, Rudolf, Wienhard, Klaus, & Heiss, Wolf-Dieter. 2003. Performance evaluation of the micropet r4 scanner for rodents. *European journal of nuclear medicine and molecular imaging*, **30**(5), 737–747. 3.3

Knoll, G. F. 2000. *Radiation detection and measurement*. Wiley. 5.1.9.2

Kornblum, Harley I., Araujo, Dalia M., Annala, Alexander J., Tatsukawa, Keith J., Phelps, Michael E., & Cherry, Simon R. 2000. In vivo imaging of neuronal activation and plasticity in the rat brain by high resolution positron emission tomography (micropet). *Nature biotechnology*, **18**, 655–660. 3.4

Kubota, K. 2001. From tumor biology to clinical pet: A review of positron emission tomography (pet) in oncology. *Annals of nuclear medicine*, **15**(6), 471–486. 1

Laforest, R. 2005. *Siemens medical solutions - special edition molecular imaging*. Siemens Medical Solutions. Chap. Small Animal PET Imaging for the Study of Diseases and Drug Development, pages 19–24. 3.4

Lalush, D. S., & Wernick, M. N. 2004. *Emission tomography: The fundaments of pet and spect*. Elsevier. Chap. Iterative Image Reconstruction, pages 443–472. (document), 2.17, 2.6.2, 2.6.2

Lamare, F., Turzo, A., Bizais, Y., Rest, C. Cheze Le, & Visvikis, D. 2006. Validation of a monte carlo simulation of the philips allegro/gemini pet systems using gate. *Physics in medicine and biology*, **51**, 943–962. 5.2

Lamare, F., Carbayo, M. J. Ledesma, Cresson, T., Kontaxakis, G., Santos, A., Rest, C. Cheze Le, Reader, A. J., & Visvikis, D. 2007a. List-mode-based reconstruction for respiratory motion correction in pet using nonrigid body transformations. *Physics in medicine and biology*, **52**, 5187–5204. 11.4

Lamare, F., Cresson, T., Savean, J., Rest, C. Cheze Le, Reader, A. J., & Visvikis, D. 2007b. Respiratory motion correction for pet oncology applications using affine transformation of list mode data. *Physics in medicine and biology*, **52**, 121–140. 11.4

Lammertsma, A. A. 2004. Role of human and animal pet studies in drug development. *International congress series*, **1265**, 3–11. 3.4

Larobina, Michele, Brunetti, Arturo, & Salvatore, Marco. 2006. Small animal pet: A review of commercially available imaging systems. *Current medical imaging reviews*, **2**, 187–192. 3.3

Larson, Steven M., & Schwartz, Lawrence H. 2006. 18f-fdg pet as a candidate for qualified biomarker: Functional assessment of treatment response in oncology. *The journal of nuclear medicine*, **47**(6), 901–903. 1, 7.1.1.2

Lartizien, C., Kinahan, P., & Comtat, C. 2004. A lesion detection observer study comparing 2-dimensional versus fully 3-dimensional whole-body pet imaging protocols. *Journal of nuclear medicine*, **45**, 714–723. 10.1

Lazaro, D., Buvat, I., Loudos, G., Strul, D., Santin, G., Giokaris, N., Donnarieix, D., Maigne, L., Spanoudaki, V., Styliaris, S., Staelens, S., & Breton, V. 2004. Validation of the gate monte carlo simulation platform for modeling a csi(tl) scintillation camera dedicated to small-animal imaging. *Physics in medicine and biology*, **49**, 271–285. 5.1.1

Lazaro, Delphine. 2003. *Validation de la plate-forme de simulation gate en tomographie d emission monophotonique et application au developpement d un algorithme de reconstruction 3d complete*. Ph.D. thesis, Universite Blaise Pascal. (document), 4.2, 5.6

Lecomte, R. 2004. Technology challenges in small animal pet imaging. *Nuclear instruments and methods in physics research a*, **527**, 157–165. (document), 3.2

Lehnert, Wencke, Meikle, Steven R., Siegel, Stefan, Bailey, David, Banati, Richard, & Rosenfeld, Anatoly B. 2005. Evaluation of transmission methodology for the micropet focus 220 animal scanner. *Ieee nuclear science symposium conference record*, 2519–2523. 6.2.2

Lehnert, Wencke, Meikle, Steven R., & Newport, Danny F. 2006a. Count rate performance and dead time in singles transmission scanning for the micropet focus 220 scanner. *Ieee nuclear science symposium conference record*, 2484–2487. 6.2.2

Lehnert, Wencke, Meikle, Steven R., Siegel, Stefan, Newport, Danny, Banati, Richard B., & Rosenfeld, Anatoly B. 2006b. Evaluation of transmission methodology and attenuation correction for the micropet focus 220 animal scanner. *Physics in medicine and biology*, **51**, 4003–4016. 6.2.2

Levin, C. 2004. *Emission tomography: The fundaments of pet and spect*. Elsevier. Chap. Basic Physics of Radionuclide Imaging, pages 53–88. 2.1.2, 2.1.3.1, 2.1.3.2

Lewellen, T., & Karp, J. 2004. *Emission tomography: The fundaments of pet and spect*. Elsevier. Chap. PET Systems, pages 179–194. (document), 2, 2.9, 2.3.5, 2.5

Lewellen, T. K. 2008. Recent developments in pet detector technology. *Physics in medicine and biology*, **53**, R287–R317. (document), 2.3

Lewis, H. W. 1950. Multiple scattering in an infinite medium. *Physical review*, **78**, 526–529. 5.1.4.1

Lewis, Jason S., Achilefu, S., Garbow, J. R., Laforest, R., & Welch, M. J. 2002. Small animal imaging: current technology and perspectives for oncological imaging. *European journal of cancer*, **38**, 2173–2188. 3.4

Lewitt, R. M., & Matej, S. 2003. Overview of methods for image reconstruction from projections in emission computed tomography. *Proceedings of the ieee*, **91**(10), 1588–1611. 2.5.1

Libraries, Geant4. 2010. *http://www-nds.iaea.org/*. 5.1.4.2

Ljungberg, M. 1998. *Monte carlo calculations in nuclear medicine: Applications in diagnostic imaging*. Institute of Physics Publishing. Chap. Introduction to the Monte Carlo Method, pages 1–12. 1, 4, 4.2, 4.2.3

Ljungberg, M. 2004. *Emission tomography: The fundaments of pet and spect*. Elsevier. Chap. Simulation Techniques and Phantoms, pages 551–563. 1, 4, 4.2.3, 7

Loening, A. M., & Gambhir, S. S. 2003. Amide: A free software tool for multimodality medical image analysis. *Molecular imaging*, **2**(3), 131–137. 6.2.3

MacLaren, Duncan C., Toyokuni, Tatsushi, Cherry, Simon R., Barrio, Jorge R., Phelps, Michael E., Herschman, Harvey R., & Gambhir, Sanjiv S. 2000. Pet imaging of transgene expression. *Society of biological psychiatry*, **48**, 337–348. 3.4

Manual, Geant4 Physics Reference. 2010. *http://geant4.web.cern.ch/geant4/g4usersdocuments/usersguides/physicsreferencemanual/html/physicsreferencemanual.html*. 5.1.4

Mawlawi, O., & Townsend, D. W. 2009. Multimodality imaging: an update on pet/ct technology. *European journal of nuclear medicine and molecular imaging*, **36**, S15–S29. 1

MCNP. 2010. *http://mcnp-green.lanl.gov/*. 4.5

Meikle, S. R., & Badawi, R. D. 2003. *Positron emission tomography: Basic science and clinical practice*. Springer. Chap. Quantitative Techniques in PET, pages 115–146. 2.5, 2.5.2, 2.5.3, 2.5.4, 2.5.5, 2.5.6, 2.5.7

Meikle, S. R., & Badawi, R. D. 2005. *Positron emission tomography: Basic sciences*. Springer. Chap. Quantitative Techniques in PET, pages 93–126. 2.5, 2.5.2, 2.5.3, 2.5.4, 2.5.5, 2.5.6

Melcher, C. L. 2000. Scintillation crystals for pet. *The journal of nuclear medicine*, **41**(6), 1051–1055. 2.2.1

Merheb, C., Petegnief, Y., & Talbot, J. N. 2007. Full modelling of the mosaic animal pet system based on the gate monte carlo simulation code. *Physics in medicine and biology*, **52**(3). 5.2

Michel, C., Eriksson, L., Rothfuss, H., & Bendriem, B. 2006. Influence of crystal material on the performance of the hirez 3d pet scanner: A monte-carlo study. *Eee nuclear science symposium conference record*, **4**, 1528–1531. 5.2

microPET FOCUS, Siemens Medical. 2010. *http://www.medical.siemens.com/webapp/wcs/stores/servlet/productdisplay q_catalogid e_-11 a_cattree e_100010,1007660,1011525,1029715 a_langid e_-11 a_productid e_200675 a_storeid e_10001.htm*. (document), 6.1, 6.1, 6.1

Microsystems, Sun. 2007 (May). *Sun n1 grid engine 6.1 user's guide*. Version 6.1 edn. Sun Microsystems. 5.3.2

MPICH2. 2010. *http://www.mcs.anl.gov/research/projects/mpich2/*. 5.3.2

Myers, R. 2001. The biological application of small animal pet imaging. *Nuclear medicine and biology*, **28**, 585Ð593. 3.3, 3.4

Myers, R., & Hume, S. 2002. Small animal pet. *European neuropsychopharmacology*, **12**, 545–555. 3.3

Nehmeh, Sadek A., Erdi, Yusuf E., Ling, Clifton C., Rosenzweig, Kenneth E., Schoder, Heiko, Larson, Steve M., Macapinlac, Homer A., Squire, Olivia D., & Humm, John L. 2002. Effect of respiratory gating on quantifying pet images of lung cancer. *Journal of nuclear medicine*, **43**(7), 876–881. 1, 11.4

Nutt, Ronald. 2002. The history of positron emission tomography. *Molecular imaging and biology*, **4**(11), 11–26. 1

of a PET exam, MIP. 2010. *http://tech.snmjournals.org/cgi/content-nw/full/33/2/69/f2*. 2.1b

Ollinger, J. M. 1995. Detector efficiency and compton scatter in fully 3d pet. *Ieee signal processing magazine*, **42**(4), 1168–1173. 2.5.2

Ollinger, J. M., & Fessler, J. A. 1997. Positron emission tomography. *Ieee signal processing magazine*, **14**(1), 43–55. 2

Park, S.-J., Southekal, S., Purschke, M., Junnarkar, S. S., Pratte, J.-F., Stoll, S. P., Woody, C. L., Schlyer, D. J., & Vaska, P. 55. Digital coincidence processing for the ratcap conscious rat brain pet scanner. *Ieee transactions on nuclear science*, **2008**(1), 510–515. 3.2.1

Park, Sang-June, Ionascu, Dan, Killoran, Joseph, Mamede, Marcelo, Gerbaudo, Victor H., Chin, Lee, & Berbeco, Ross. 2008. Evaluation of the combined effects of target size, respiratory motion and background activity on 3d and 4d pet/ct images. *Physics in medicine and biology*, **53**, 3661–3679. 11.4

PENELOPE. 2010. *http://www.nea.fr/html/dbprog/*. 4.5

Peter, J., Tornai, M. P., & Jaszczek, R. J. 2000. Analytical versus voxelized phantom representation for monte carlo simulation in radiological imaging. *Ieee transactions on medical imaging*, **19**, 556–564. 1, 7

phantom, MOBY. 2010. *http://www.bme.unc.edu/ wsegars/phantom.html*. 4

phantoms, William Seagers. 2010. *http://dmip.rad.jhmi.edu/people/faculty /paul/segars_research.htm*. 4

Phelps, M. E. 2000. Positron emission tomography provides molecular imaging of biological processes. *Proceedings of the national academy of sciences of the united states of america*, **97**(16), 9226–9233. 2, 3.4

Pichler, B. J., & Ziegler, S. I. 2004. *Emission tomography: The fundaments of pet and spect*. Elsevier. Chap. Photodetectors, pages 255–267. 2.2.2

Planes, Anatomical. 2010. *http://www.wikipedia.org/*. 6.5a

Pomper, M. G. 2001. Molecular imaging: An overview. *Academic radiology*, **8**(11), 1141–1153. 3.4

Pomper, Martin G., & Hammoud, Dima A. 2004. Positron emission tomography in molecular imaging. *Ieee engineering in medicine and biology magazine*, **July**/**August**, 28–37. 2

Poston, J. W., Bolch, W., & Bouchet, L. 2002. *Therapeutic applications of monte carlo calculations in nuclear medicine*. Institute of Physics Publishing. Chap. Mathematical models of the human anatomy, pages 108–132. 1, 7

Powsner, R. A., & Powsner, E. R. 2006. *Essential nuclear medicine physics*. Blackwell Publishing. (document), 2.1.3, 2.4, 2.5, 2.8

R., R. Taschereau, & Chatziioannou, A. F. 2005. Fdg-pet image-based dose distribution in a realistic mouse phantom from monte carlo simulations. *Ieee nuclear science symposium conference record*, **3**, 1633–1636. 5.1.6

RatCAP. 2010. *http://www.chemistry.bnl.gov/ratcap/*. 3.2.1

RDM, Geant4. 2010. *http://www.space.qinetiq.com/geant4/rdm.html*. 5.1.5

Riemann, B., Schafers, K. P., Schober, O., & Schafers, M. 2008. Small animal pet in preclinical studies: opportunities and challenges. *Quarterly journal of nuclear medicine and molecular imaging*, **52**(3), 215–221. 1, 3.4

Rodrigues, Pedro, Moura, Rui, Ortigao, Catarina, Peralta, Luis, Pia, Maria Grazia, Trindade, Andreia, & Varela, Joao. 2004. Geant4 applications and developments for medical physics experiments. *Ieee transactions on nuclear science*, **51**(4), 1412–1419. 5.1.1

Rogers, D. W. O. 2006. Fifty years of monte carlo simulations for medical physics. *Physics in medicine and biology*, **51**, R287–R301. 1

ROOT. 2010. *http://root.cern.ch*. 6.2.3

Rousset, O. G., & Zaidi, H. 2006. *Quantitative analysis in nuclear medicine imaging*. Springer Publishing. Chap. Correction for Partial Volume Effects in Emission Tomography, pages 236–271. 2.5.7

Rowland, D. J. 2002. Molecular imaging: The application of small animal positron emission tomography. *Journal of cellular biochemistry supplement*, **39**, 110–115. 3.4

Rowland, D. J., & R., S. R. Cherry S. 2008. Small-animal preclinical nuclear medicine instrumentation and methodology. *Seminars in nuclear medicine*, **38**(3), 209–222. 1, 3.3, 3.4

Rubins, Daniel J., Meadors, A. Ken, Yee, Simon, Melega, William P., & Cherry, Simon R. 2001. Evaluation of a stereotactic frame for repositioning of the rat brain in serial positron emission tomography imaging studies. *Journal of neuroscience methods*, **107**, 63–70. 3.2.2

Saha, G. B. 2005. *Basics of pet imaging: Physics, chemistry, and regulations*. Springer. (document), 2.4, 2.4.4, 2.13, 2.5.3, 2.5.7, 2.18, 2.7, 2.4, 2.7.1

Sain, John D., & Barrett, Harrison H. 2003. Performance evaluation of a modular gamma camera using a detectability index. *The journal of nuclear medicine*, **44**(1), 58–66. 10.4

Salvat, F., Fernandez-Varea, J. M., Sempau, J., & Mazurier, J. 1999. Pratical aspects of monte carlo simulation of charged particle transport: Mixed algorithms and variance reduction techniques. *Radiat environ biophys*, **38**, 15–22. 4.4

Sanchez-Crespo, A., & Larsson, S. A. 2006. The influence of photon depth of interaction and non-collinear spread of annihilationphotons on pet image spatial resolution. *European journal of nuclear medicine*, **33**(8), 940–947. 2.4.1

Sanchez-Crespo, Alejandro, Andreo, Pedro, & Larsson, Stig A. 2004. Positron flight in human tissues and its influence on pet image spatial resolution. *European journal of nuclear medicine and molecular imaging*, **31**(1), 44–51. 2.1.1

Santin, G., Strul, D., Lazaro, D., Simon, L., Krieguer, M., Martins, M. Vieira, Breton, V., & Morel, C. 2003. Gate, a geant4-based simulation platform for pet and spect integrating movement and time management. *Ieee transactions on nuclear science*, **50**(5), 1516–1521. 5.1.8, 5.4a, 5.4b

Schelbert, H. R. 2003. Pet imaging in small animals. *Journal of nuclear cardiology*, **10**(5), 513–520. 3.4

Schmidtlein, C. Ross, Kirov, Assen S., Nehmeh, Sadek A., Erdi, Yusuf E., Humm, John L., Amols, Howard I., Bidaut, Luc M., Ganin, Alex, Stearns, Charles W., McDaniel, David L., & Hamacher, Klaus A. 2006. Validation of gate monte carlo simulations of the ge advance/discovery ls pet scanner. *Medical physics*, **33**(1), 198–208. 5.2

Schoder, Heiko, Erdi, Yusuf E., Larson, Steven M., & Yeung, Henry W. D. 2003. Pet/ct: a new imaging technology in nuclear medicine. *European journal of nuclear medicine and molecular imaging*, **30**(10), 1419–1437. 2.3.3

Schwarz, S. W., & Anderson, C. J. 2007. *Nuclear medicine and pet/ct: Technology and techniques*. Mosby Elsevier. Chap. Radiochemistry and Radiopharmacology, pages 165–192. 2.7

Seagers, William. 2010. *http://dmip.rad.jhmi.edu/people/faculty/paul/*. 7.2

Segars, W. P. 2001. *Development and application of the new dynamic nurbs-based cardiac-torso (ncat) phantom*. Ph.D. thesis, The University of North Carolina at Chapel Hill. 7.1.2

Segars, William. P., Tsui, Benjamin M.W., Frey, Eric C., Johnson, G. Allan, & Berr, Stuart S. 2004. Development of a 4-d digital mouse phantom for molecular imaging research. *Molecular imaging and biology*, **6**(3), 149–159. (document), 1, 7, 7.1.2, 7.6, 7.7, 7.8

SHFJ. 2010. *http://www-dsv.cea.fr/dsv/instituts/institut-d-imagerie-biomedicale-i2bm/unites-de-recherche/service-hospitalier-frederic-joliot-shfj-p.-merlet*. 7.1.1

Shukla, A. K., & Kumar, Utham. 2006. Positron emission tomography: An overview. *Journal of medical physics*, **31**(1), 13–21. 2

SIMIND. 2010. *http://www.radfys.lu.se/simind/*. 4.5

Simon, Luc, Strul, Daniel, Santin, Giovanni, Krieguer, Magalie, & Morel, Christian. 2004. Simulation of time curves in small animal pet using gate. *Nuclear instruments and methods in physics research a*, **527**, 190–194. 5.1.8, 5.1.9.2

SimSET. 2010. *http://depts.washington.edu/simset/html/simset_main.html*. 4.5

Sorenson, J. A., & Phelps, M. E. 1987. *Physics in nuclear medicine*. Saunders. 2.1.3.1, 2.3.2

SORTEO. 2010. *http://sorteo.cermep.fr/*. 4.5

Staelens, S., Santin, G., Strul, D., Koole, M., Vandenberghe, S., D'Asseler, Y., Breton, V., Morel, C., Lemahieu, I., & de Walle, R. Van. 2003. Monte carlo simulations of interfile based emission and attenuation maps for clinical applications. *Journal of nuclear medicine*, **44**(5), 292P. 7.2

Staelens, S., Beenhouwer, J. De, Kruecker, D., Maigne, L., Rannou, F., Ferrer, L., D'Asseler, Y., Buvat, I., & Lemahieu, I. 2006. Gate: improving the computational efficiency. *Nuclear instruments and methods in physics research section a: Accelerators, spectrometers, detectors and associated equipment*, **529**(2), 341–345. 5.3, 5.3.4

Staelens, Steven. 2004. *Monte carlo simulations for system modeling in emission tomography*. Ph.D. thesis, Faculteit Toegepaste Wetenschappen - Universiteit Gent. (document), 5.5

Strother, S. C., Casey, M. E., & Hoffman, E. J. 1990. Measuring pet scanner sensitivity: relating countrates to image signal-to-noise rations using noise equivalent counts. *Ieee transactions on nuclear science*, **37**(2), 783–788. 2.4.3

Strul, D., Santin, G., Lazaro, D., Breton, V., & Morel, C. 2003. Gate (geant4 application for tomographic emission): a pet/spect general-purpose simulation platform. *Nuclear physics b Ð proceedings supplements*, **125**, 75–79. 4.5, 5.1.8

Tai, Y.-C., & Laforest, R. 2005. Instrumentation aspects of animal pet. *Annual review of biomedical engineering*, **7**, 255–285. 1, 3.1, 3.3, 11.5

Tai, Y. C., Chatziioannou, A., Siegel, S., Young, J., Newport, D., Goble, R. N., Nutt, R. E., & Cherry, S. R. 2001. Performance evaluation of the micropet p4: a pet system dedicated to animal imaging. *Physics in medicine and biology*, **46**, 1845–1862. 3.3

Tai, Yuan-Chuan, Ruangma, Ananya, Rowland, Douglas, Siegel, Stefan, Newport, Danny F., Chow, Patrick L., & Laforest, Richard. 2005. Performance evaluation of the micropet focus: A third-generation micropet scanner dedicated to animal imaging. *Journal of nuclear medicine*, **46**, 455–463. 3.3, 6.1, 6.2.2, 8.1

Tarantola, G., Zito, F., & Gerundini, P. 2003. Pet instrumentation and reconstruction algorithms in whole-body applications. *The journal of nuclear medicine*, **44**(5), 756–769. 2.3.2, 2.4, 2.4.4, 2.5.3

Taschereau, R., & Chatziioannou, A. F. 2007. Monte carlo simulations of absorbed dose in a mouse phantom from 18-fluorine compounds. *Medical physics*, **34**(3), 1026–1036. 5.1.6

Townsend, D. W., & Bendriem, B. 1998. *The theory and practice of 3d pet*. Kluwer Academic Publishers. Chap. Introduction to 3D PET, pages 1–10. 2.5.2, 2.5.3, 2.5.4, 2.5.5, 2.5.6

Townsend, D. W., Isoardi, R. A., & Townsend, D. W. 1998. *The theory and practice of 3d pet*. Springer. Chap. Volume Imaging Tomographs, pages 111–132. 8.1

Townsend, David W., Carney, Jonathan P.J., Yap, Jeffrey T., & Hall, Nathan C. 2004. Pet/ct today and tomorrow. *The journal of nuclear medicine*, **45**(1), 4S–14S. 1

Tsai, Y.-S. 1974. Pair production and bremsstrahlung of charged leptons. *Review of modern physics*, **46**(4), 815–851. 5.1.4.2

Tsui, B. M. W., & Frey, E. C. 2006. *Quantitative analysis in nuclear medicine imaging*. Springer Publishing. Chap. Analytic Image Reconstruction Methods in Emission Computed Tomography, pages 82–106. 2.6.1.1, 2.6.1.2

Turkington, T. G. 2001. Introduction to pet instrumentation. *Journal of nuclear medicine technology*, **29**(1), 4–11. 2.1.3.1, 2.3.3

Valk, P. E., Delbeke, D., Bailey, D. L., Townsend, D. W., & Maisey, M. N. 2006. *Positron emission tomography: Clinical practice*. Springer. 2.7

Vallabhajosula, Shankar. 2007. 18f labeled positron emission tomographic radiopharmaceuticals in oncology: An overview of radiochemistry and mechanisms of tumor localization. *Seminars in nuclear medicine*, **37**, 400–419. 2.7

Vandervoort, Eric, Camborde, MarieÐLaure, Jan, Sebastien, & Sossi, Vesna. 2005. Monte-carlo modeling of the micropet r4 small animal pet scanner for coincidence-mode emission and singles-mode transmission data acquisition. *Ieee nuclear science symposium conference record*, **5**, 2449–2453. 5.2

Vandervoort, Eric, Camborde, Marie-Laure, Jan, Sebastien, & Sossi, Vesna. 2007. Monte carlo modelling of singles-mode transmission data for small animal pet scanners. *Physics in medicine and biology*, **52**, 3169Ð3184. 5.2

Vaska, P., Woody, C., Schlyer, D., Pratte, J.-F., Junnarkar, S., Southekal, S., Stoll, S., Schulz, D., Schiffer, W., Alexoff, D., Lee, D., Patel, V., Purschke, M., Lee, W., Fried, J., Lenz, W., Krishnamoorthy, S., Maramraju, S., Kriplani, A., Radeka, V., OÕConnor, P., Lecomte, R., & Fontaine, R. 2007. The design and performance of the 2nd-generation ratcap awake rat brain pet system. *Ieee nuclear science symposium conference record*, **6**, 4184–4184. 3.2.1

Vassaux, G., & Wassink, T. G. 2003. In vivo noninvasive imaging for gene therapy. *Journal of biomedicine and biotechnology*, **2**, 92–101. 3.4

Visvikis, D. 2004. Feasibility of image derived respiratory gating of fdg pet datasets. *European journal of nuclear medicine and molecular imaging*, **31**, S230. 1

Visvikis, D., Turzo, A., Bizais, Y., & Rest, C. Cheze-Le. 2004. Technology related parameters affecting quantification in positron emission tomography imaging. *Nuclear medicine communications*, **25**, 637–641. 1

Visvikis, D., Lamare, F., Bruyant, P., Boussion, N., & Rest, C. Cheze Le. 2006a. Respiratory motion in positron emission tomography for oncology applications: Problems and solutions. *Nuclear instruments and methods in physics research a*, **569**, 453–457. 1, 11.4

Visvikis, D., Bardies, M., Chiavassa, S., Danford, C., Kirov, A., Lamare, F., Maigne, L., Staelens, S., & Taschereau, R. 2006b. Use of the gate monte carlo package for dosimetry applications. *Nuclear instruments and methods in physics research a*, **569**, 335–340. 5.1.6

Wang, Yuchuan, Seidel, Jurgen, Tsui, Benjamin M. W., Vaquero, Juan J., & Pomper, Martin G. 2006. Performance evaluation of the ge healthcare explore vista dual-ring small-animal pet scanner. *The journal of nuclear medicine*, **47**(11), 1891–1900. 3.3

Weber, S., & Bauer, A. 2004. Small animal pet: aspects of performance assessment. *European journal of nuclear medicine and molecular imaging*, **31**(11), 1545–1555. 3.1.6

Weissleder, Ralph, & Mahmood, Umar. 2001. Molecular imaging. *Radiology*, **219**(2), 316–333. 3.4

Wernick, M. N., & Aarsvold, J. N. 2004. *Emission tomography: The fundaments of pet and spect*. Elsevier. Chap. Introduction to Emission Tomography, pages 11–23. (document), 1, 2, 2.1.2, 2.3.4, 2.16

Wilkinson, F. 2004. *Emission tomography: The fundaments of pet and spect*. Elsevier. Chap. Scintillators, pages 229–254. 2.2.1

Wilson, M. A. 1998. *Textbook of nuclear medicine*. Lippincott-Raven Publishers. 2.6.1.2

Woody, C., Dzhordzhadze, V., Fontaine, R., Junnakar, S., Kandasamy, A., Kriplani, A., Krishnamoorthy, S., Lecomte, R., OÕConnor, P., Page, C., Pratte, J.-F., Purschke, M., Radeka, V., Rampil, I., Schlyer, D., Shokouhi, S., Southekal, S., Stoll, S., Vaska, P., Villanueva, A., & Yu, B. 2004. The ratcap conscious small animal pet tomograph. *Ieee nuclear science symposium conference record*, **4**, 2334–2338. 3.2.1

Zaidi, H. 1999. Relevance of accurate monte carlo modeling in nuclear medical imaging. *Medical physics*, **26**(4), 574–608. 1, 4, 4, 4.2, 4.4, 4.5

Zaidi, H. 2006. *Quantitative analysis in nuclear medicine imaging*. Springer Publishing. Chap. Monte Carlo Modeling in Nuclear Medicine Imaging, pages 358–390. (document), 1, 4.1, 4, 7

Zaidi, H., & Hasegawa, B. H. 2006a. *Quantitative analysis in nuclear medicine imaging*. Springer Publishing. Chap. Overview of Nuclear Medical Imaging: Physics and Instrumentation, pages 1–34. 2

Zaidi, H., & Hasegawa, B. H. 2006b. *Quantitative analysis in nuclear medicine imaging*. Springer Publishing. Chap. Attenuation Correction Strategies in Emission Tomography, pages 167–204. 2.5.3

Zaidi, H., & Koral, K. F. 2006. *Quantitative analysis in nuclear medicine imaging*. Springer Publishing. Chap. Scatter Correction Strategies in Emission Tomography, pages 205–235. 2.5.4

Zaidi, H., & Sgouros, G. 2002. *Therapeutic applications of monte carlo calculations in nuclear medicine*. Institute of Physics Publishing. 1, 4

Zaidi, H., & Tsui, B. M. W. 2009. Review of computational anthropomorphic anatomical and physiological models. *Proceedings of the ieee*, **97**(12), 1938–1953. 1, 7

Zaidi, H., & Xu, X. G. 2007. Computational anthropomorphic models of the human anatomy: The path to realistic monte carlo modeling in radiological sciences. *Annual review of biomedical engineering*, **9**, 471–500. 1, 7

Zanzonico, P. 2004. Positron emission tomography: a review of basic principles, scanner design and performance, and current systems. *Seminars in nuclear medicine*, **34**(2), 87–111. (document), 1, 2.1.2, 2.2.1, 2.2.2, 2.6, 2.2.3, 2.4.1, 2.4.3, 2.5.2, 2.5.3, 2.5.4, 2.5.5, 2.5.6

Zanzonico, P., & Heller, S. 2007. *Clinical nuclear medicine*. Springer. Chap. Physics, Instrumentation, and Radiation Protection, pages 1–33. 1

Zeng, G. L. 2001. Image reconstruction - a tutorial. *Computerized medical imaging and graphics*, **25**, 97–103. 2.6

Zhu, Zhiyu, Tsui, Benjamin M.W., & Segars, Williams P. 2002. A simulation study of the effect of gating scheme on respiratory motion blurring in fdg lung pet. *Ieee nuclear science symposium conference record*, 1554–1558. 11.4

Zubal, G., & Harrell, C. 1991. *Information processing in medical imaging*. Springer. Chap. Voxel based Monte Carlo calculations of nuclear medicine images and applied variance reduction techniques, pages 23–33. 4.4

Zubal, I. G. 1998. *Monte carlo calculations in nuclear medicine: Applications in diagnostic imaging*. Institute of Physics Publishing. Chap. Anthropomorphic Phantoms, pages 25–36. 1, 7

Note: Each one of the bibliographic references shown above ends with an indication on where it's cited in this document, e.g., the numbers 2.4.3 and 3.1.6 references the section 4.3 of chapter 2 and section 1.6 of chapter 3 respectively.